MODELING AND SIMULATION OF STRUCTURAL STABILITY, THERMAL EXPANSION AND ANHARMONICITY OF 2D MATERIALS

By

ANEES P

(Enrolment No. PHYS02201104011)

Indira Gandhi Centre for Atomic Research, Kalpakkam, India.

A thesis submitted to the

Board of Studies in Physical Sciences

In partial fulfillment of requirements

For the Degree of

DOCTOR OF PHILOSOPHY

of

HOMI BHABHA NATIONAL INSTITUTE

February, 2017

Homi Bhabha National Institute

Recommendations of the Viva Voce Board

As members of the Viva Voce Committee, we certify that we have read the dissertation prepared by **Anees P** entitled **"Modeling and simulation of structural stability, thermal expansion and anharmonicity of 2D materials"** and recommend that it may be accepted as fulfilling the thesis requirement for the award of Degree of Doctor of Philosophy.

______________________________ Date: Oct 27, 2017
(Chairman- Dr. G. Amarendra)

______________________________ Date: 27/10/2017
(Guide/Convener- Dr. B. K. Panigrahi)

______________________________ Date: 27/10/2017
External Examiner- Prof. G. P. Das

______________________________ Date: 27/10/2017
Member 1: Dr. Sharat Chandra

______________________________ Date: 27/10/2017
Member 2: Dr. T. R. Ravindran

Final approval and acceptance of this thesis is contingent upon the candidate's submission of the final copies of the thesis to HBNI.

I hereby certify that, I have read this thesis prepared under my direction and recommend that it may be accepted as fulfilling the thesis requirement

Date: 27/10/2017
Place: Kalpakkam

Dr. B. K. Panigrahi

(Guide)

STATEMENT BY AUTHOR

This dissertation has been submitted in partial fulfillment of requirements for an advanced degree at Homi Bhabha National Institute (HBNI) and is deposited in the Library to be made available to borrowers under rules of the HBNI.

Brief quotations from this dissertation are allowable without special permission, provided that accurate acknowledgment of source is made. Requests for permission for extended quotation from or reproduction of this manuscript in whole or in part may be granted by the Competent Authority of HBNI when in his or her judgment the proposed use of the material is in the interests of scholarship. In all other instances, however, permission must be obtained from the author.

Date: **27/10/2017**
Place: Kalpakkam

Anees P

DECLARATION

I, hereby declare that the investigation presented in the thesis has been carried out by me. The work is original and has not been submitted earlier as a whole or in part for a degree/diploma at this or any other Institution/University

Anees P

List of Publications

PUBLICATIONS

(a) Published in journals

1. *Ab initio* study on stacking sequences, free energy, dynamical stability and potential energy surfaces of graphite structures, **P. Anees**, M. C. Valsakumar, Sharat Chandra, and B. K. Panigrahi, *Model. Simul. Mater. Sci. Eng.*, **2014**, *22*, 035016

2. Temperature dependent phonon frequency shift and structural stability of free standing graphene: A spectral energy density analysis, **P. Anees**, M. C. Valsakumar, and B. K. Panigrahi, *2D Mater.,* **2015***,* *2*, 035014

3. Effect of strong phonon-phonon coupling on temperature dependent structural stability and frequency shift of 2D h-BN, **P. Anees**, M. C. Valsakumar, and B. K. Panigrahi, *Phys. Chem. Chem. Phys.,* **2016**, *18*, 2672

4. Anharmonicity of optic modes in monolayer MoS_2, **P. Anees**, M. C. Valsakumar, and B. K. Panigrahi, *Appl. Phys. Lett.***,** **2016**, *108*, 101902

5. Delineating the role of ripples on thermal expansion of 2D honeycomb materials: graphene, 2D h-BN and monolayer(ML)-MoS_2, **P. Anees**, M. C. Valsakumar, and B. K. Panigrahi, *Phys. Chem. Chem. Phys.,* **2017,** *19*, 10518

(b) Manuscript under preparation

6. A spectral energy density based package to extract the temperature dependent phonon dispersion, frequency shift, linewidth and coupling of normal modes, **P. Anees**, M. C. Valsakumar, and B. K. Panigrahi

(c) Other publications

(i) Published in conference proceedings:

1. High temperature phonon dispersion in graphene using classical molecular dynamics simulations, **P. Anees**, M. C. Valsakumar and B.K Panigrahi. *AIP Conf. Proc.* **2014,** *1591*, 1070

(ii) Papers presented in national/international conferences:

1. Effect of temperature on stability of bilayer graphite structures : Lattice dynamics and molecular dynamics study, **P. Anees**, M.C. Valsakumar, Sharat Chandra and B.K. Panigrahi, Asia Sweden Meeting on understanding Functional Materials From Lattice Dynamics (ASMFLD), 9-6 January, **2014**, IIT-Guwahati, Assam, India

2. Extracting temperature dependent phonon frequency shift, linewidth and coupling of normal modes using classical molecular dynamics simulations, **P. Anees**, M.C. Valsakumar and B.K. Panigrahi, (Invited talk), symposium on molecular simulations (Anessur rahaman Day), 24 August, **2014**, University of Hyderabad, India

3. Temperature dependent phonon frequencies in monolayer MoS_2, **P. Anees**, M.C. Valsakumar and B.K. Panigrahi, Multiscale Modeling of Materials and Devices (MMMD), 30 October - 2 November, **2014**, BARC, Mumbai, India (Best poster Award)

4. Delineating the role of ripples on thermal expansion properties of free-standing graphene, **P. Anees**, M.C. Valsakumar and B.K. Panigrahi, International conference on ”Nanoscience, Nanotechnology & Advanced Materials” (NANOS-2015), 14-17 December, **2015**, GITAM University, Visakhapatnam, India

(d) Publications not included in the thesis

1. Computation of thermal conductivity: A non-equilibrium approach, **P. Anees**, K. Gururaj, and M. C. Valsakumar. A*IP Conf.Proc.*, **2012,** *1447*, 1011

2. Phase stability and lattice dynamics of ammonium azide under hydrostatic compression, N. Yedukondalu, G. Vaitheeswaran, **P. Anees** and M. C. Valsakumar, *Phys. Chem. Chem. Phys.*, **2015**, *17*, 29210

3. Crystal structure and bonding characteristics of transformation products of bCC β in Ti-Mo alloys, M. Sabeena, S. Murugesan, **P. Anees**, E. Mohandas and M. Vijayalakshmi, *J. Alloy. Comp.,* **2017,** *705,* 769

(e) Workshop/school attended

1. Workshop on “Materials Modeling and Simulation”, 27-31 December, **2010**, University of Hyderabad, India

2. Psi-K Quantum-ESPRESSO school on *ab initio* thermal transport, 27-30 June, **2016**, Université Pierre et Marie Curie - Paris, France

Anees P

I dedicate this thesis to

my beloved Father and Mother

&

***to my grandparents* (*late*).**

Their continuous love, encouragements, prayers and
blessings make me able to chase my dreams

Acknowledgements

In achieving every goal, there will be collective efforts of many people. It would not have been possible for me to accomplish this challenging task without the constant support and encouragement of certain people. Acknowledging each one of them is a special privilege.

First of all, I would like to express my sincere gratitude to my research guide ***Dr. B. K. Panigrahi*** *for his constant encouragement and support. He has provided enormous support and freedom for me to carryout my work. His timely support and guidance helped me to drive the work and complete the thesis. He has taken enormous effort and care to make the thesis in proper shape.*

I profusely thank ***Shri M.C. Valsakumar sir*** *who was instrumental in accomplishing this challenging task. His constant encouragement, mentoring, teaching and parental caring groomed me as a research scientist. I always admire his wonderful teaching, which instigate my passion towards the condensed matter physics. I would say that, I am one of the luckiest student to learn various aspects of computational physics from him. I would also like to extent my sincere thanks to* ***Mrs. Leela Valsakumar*** *for her care and affection during my visit to their home.*

I thank to all my DC members, ***Dr. G. Amarendra*** *(chairman),* ***Dr. Sharat Chandra*** *and* ***Dr. T. R. Ravindran*** *for serving as DC members. Their valuable suggestions and creative criticism helped me to cross the obstacles and move ahead. I thank the former (**Dr. B. V. R. Tata**) and the present (**Dr. N. V. Chandra Shekar**) Dean, HBNI, for their encouragement and support. I also thank the former and the present directors of IGCAR and MSG for giving me an opportunity to work in the area of computational materials science which I enjoy the most.*

I take this opportunity, to thank ***Dr. S. Mathijaya*** *and* ***Dr. Sharat Chandra*** *for their guidance and support. I also thank them for careful reading of the thesis* *and for their valuable comments. I thank* ***Dr. K. Gururaj*** *for introducing me the MD simulation in the beginning of my career. I would like to give a bunch of thanks to my colleagues* ***Gurpreet Kaur*** *and* ***Manan Dholakia*** *for their great companionship, help, support and providing lively research atmosphere. I also extend my sincere thanks to* ***Mr. Jegadeesan*** *for introducing me the bash scripting and other aspects of Linux based systems.*

It is my immense pleasure to thank all my friends, ***Karthickeyan****,* ***Srinivasan, Radhakrishna, Soumee Chakraborty, Dr. Subratha, Dr. Sivadasan, Dr. K. Vinod, Radhikesh, Irshad, Alok, K. T. Chavan, Akshaya****,* ***Rajitha and all other friends in MSG and IGCAR*** *for their friendship and creating cordial working environment. I would also like to express my sincere thanks to my* ***training school batch mates*** *and* ***AFC football club members*** *for their kindness and making my stay cherished in Kalpakkam.*

I am thankful forever to ***Dr. Rajini P Antony*** *for her unconditional support and encouragement. I am highly indebted to her for teaching me various aspects of research. I thank her for all emotional support she had provided. I also acknowledge her for careful reading of thesis which helped me to minimize the typos.*

Finally, and most importantly, I thank to all ***my family members****. My parents' love, support and inspiration guided me throughout my life. They taught me how to overcome the obstacles, how to be patient in difficulties, and how to strive towards the goals. I am lucky to have wonderful brothers and sister, and I am grateful to them for their love and care for me.*

SYNOPSIS

Graphene has got enormous attention due its fascinating electronic, mechanical and thermal properties and it is proposed as a promising candidate for next generation electronic industry. The main pitfall in graphene based electronics is the absence of finite band gap in its electronic band structure. After successful isolation of graphene in 2004, the search for other 2D layered materials has geared up in past few years. The 2D hexagonal (h)-BN and monolayer (ML)-MoS_2 are other interesting 2D layered materials with finite band gap.

Knowledge of structural, thermal and vibrational properties of these materials is essential to fabricate sophisticated electronic devices. However, it is difficult to understand the above mentioned phenomena at atomistic level by experimentation. Computer simulations can be used to understand the fundamental issues associated with thermal and vibrational properties at atomistic level. A*b initio* simulation employs the quasi-harmonic approximation (QHA) to compute the thermal and vibrational properties at finite temperature. The QHA works well at intermediate temperatures and it may not be suitable at high temperature because of the phonon–phonon interactions, which are not included in QHA. As the temperature increases, more and more phonon modes are excited and anharmonicity of the crystal becomes more pronounced. To incorporate the third order phonon scattering processes, anharmonic lattice dynamics methods are used. Both QHA and anharmonic LD fails to incorporate the full anharmonicity of materials, and also they can include only few hundreds of atoms, hence they can't model the effects of long wavelength ripples on surfaces of 2D materials. Since molecular dynamics (MD) simulations incorporate the anharmonicity of the interatomic potential without truncating it and also it can handle systems having millions of atoms, it will be a natural choice to model the high temperature thermal and vibrational properties. To compute the vibrational properties of materials at finite temperatures, a spectral energy density (SED) based method is adapted and coupled with classical MD simulation package LAMMPS which is the highlight of this thesis.

The structural, thermal and vibrational properties of graphite, graphene, 2D h-BN and ML-MoS_2 are studied in detail using *ab initio* and classical MD simulations. The thesis comprises seven chapters and the content of each chapter is given in a nutshell below.

CHAPTER-1: Introduction

This chapter gives a brief overview of structural, thermal and vibrational properties of aforementioned 2D materials. The literature status and motivation of the thesis is deliberated. Further, the challenges and scope of the thesis are brought out at end of this chapter.

CHAPTER-2: Computational and Theoretical methods

The computational and theoretical methods employed in this thesis are discussed in this chapter. The details of density functional theory (DFT) and classical molecular dynamics (MD) simulations are discussed in brief. The detailed theoretical derivation, implementation and validation of SED method is given at end of this chapter

CHAPTER-3: Stacking sequences and dynamical stability of graphite structures

In this chapter the structure and stability of several plausible stacking sequences in the graphite (in addition to the standard AB-hexagonal and ABC-rhombohedral structures) are studied using *ab initio* and classical MD simulations.

CHAPTER-4: Temperature dependent structural stability and phonon frequency shift of graphene

This chapter discusses the temperature dependent structural stability, frequency shift, linewidth and coupling of normal modes of vibrations of free-standing graphene obtained using SED method. The role of thermally excited ripples on thermal expansion properties of graphene is delineated by explicitly carrying out 3D and 2D classical MD simulations.

CHAPTER-5: Effect of strong phonon-phonon coupling on structural and

vibrational properties of 2D h-BN

2D h-BN is iso-structural to graphene, in chapter-4, the structural, thermal and vibrational properties of graphene are discussed in depth. This chapter is devoted to analyze the similar properties of 2D h-BN and the results are compared with graphene.

CHAPTER-6: Thermal expansion, structural stability and anharmonicity of monolayer (ML-MoS$_2$)

Monolayer (ML)-MoS$_2$, is another honeycomb lattice structure, posses a special S-Mo-S symmetric sandwich structure which makes it differ from graphene and 2D h-BN. The prime focus of this chapter is to analyze the structural stability, thermal expansion and anharmonicity of ML-MoS$_2$. The results are compared with graphene and 2D h-BN.

CHAPTER-7: Conclusions and future outlook

This is the final chapter of the thesis and it discusses the key findings of this study and scope for future work. The structural, thermal and vibrational properties of 2D materials are discussed and compared. To get better insights and also for further developments, few recommendations are given at end of this chapter.

Contents

List of Figures

List of Tables

Lists of abbreviations

a-lattice - In-plane lattice parameter
BO - Born-Oppenheimer
CA - Ceperly-Alder
CVD - Chemical vapor deposition
DFT - Density functional theory
DFPT - Density functional Perturbation theory
EAM - Embedded atom method
FBZ - First Brillouin zone
GGA - Generalized gradient approximation
HEG - homogeneous electron gas
HK - Hohenberg-Kohn
ICDD - International centre for diffraction data
KS - Kohn-Sham
LAMMPS - Large-scale atomic/molecular massively parallel simulator
LCBOP - Long-range bond-order potential for carbon
LDA - Local density approximation
LD - Lattice dynamics
LJ - Lennard-Jones
LTEC - Linear thermal expansion coefficient
MC - Monte Carlo
MD - Molecular dynamics
ML/FL - Monolayer/Fewlayer
NEB - Nudged elastic band
NVE - Number of particle(N), volume(V) and energy(E) are fixed
NVT - Number of particle(N), volume(V) and temperature(T) are fixed
NPT - Number of particle (N), pressure(P) and temperature(T) are fixed
PAW - Projector augmented wave
PBC - Periodic boundary condition
PBE - Perdew-Burke-Ernzerhof
PDOS- Phonon density of states
PP - pseudo-potential
PWSCF - Plane-wave self-consistent field
QHA - Quasi-harmonic approximation
QH-LD - Quasi-harmonic lattice dynamics
REBO - Reactive empirical bond order
SED - Spectral energy density
SW - Stillenger-Weber
TF - Thomas-Fermi
VACF - Velocity-velocity auto-correlation function
VASP - Vienna *ab initio* simulation package

vdW - Van der Waals
XC - Exchange correlation
2D - 2 dimension
3D - 3 dimension

Designation of phonon modes

The phonon modes are designated according to their polarizations. The letter L, T and Z are used to designate longitudinal, transverse and out-of-plane modes. The letter A and O are used to label acoustic and optic modes respectively.

LA - Longitudinal acoustic
TA - Transverse acoustic
ZA - Out-of-plane acoustic (bending mode)
ZO - Out-of-plane optic
LO - Longitudinal optic
TO - Transverse optic
LO/TO - degenerate LO and TO modes at Γ point

Chapter 1

Introduction

This chapter gives a brief overview of properties and applications of 2D materials. The electronic properties of graphene, 2D hexagonal (h)-BN and monolayer (ML)-MoS_2 are outlined. Their structural, thermal and vibrational properties are deliberated. Finally, the objective of the thesis are brought out at end of this chapter.

1.1 2D materials: An overview

Two-dimensional (2D) materials are a class of materials, consisting of a limited number of crystalline layers of atomic thickness [1]. They exhibit electronic properties that differ drastically from their bulk counterpart due to the confinement of charge carriers into a plane [1]. Some of the 2D materials can exist in nature as stack of individual sheets, such as graphene in graphite, and hence they can be easily exfoliated into single sheet. Some others do not exist as layered crystals in nature, they can be derived only through chemical route, and many of them are not stable in ambient conditions [2]. One characteristic feature of almost all 2D materials is that, they possess a strong in-plane bond, and show relatively weak van der Waals (vdW) interaction along direction normal to the 2D sheet, hence the name 2D materials [2].

The research on 2D materials blossomed over a decade ago with the isolation of graphene in 2004 [3], and has resulted in amazing discoveries. The bulk form of carbon such as graphite and diamond have been known to mankind for hundreds of years. The zero dimensional bucky-balls and one dimensional carbon nanotubes (CNT) were discovered in late 1980's and early 1990's respectively. After that, researchers started attempt to isolate the 2D form of graphite which led to the discovery of graphene. Most of the carbon nanostructures are made up of 2D graphene sheet, hence it is known as the mother of all graphitic materials [4]. The graphene sheet can be wrapped in to 0D bucky-balls, rolled up into 1D CNT and stacked into bulk graphite (Figure 1.1).

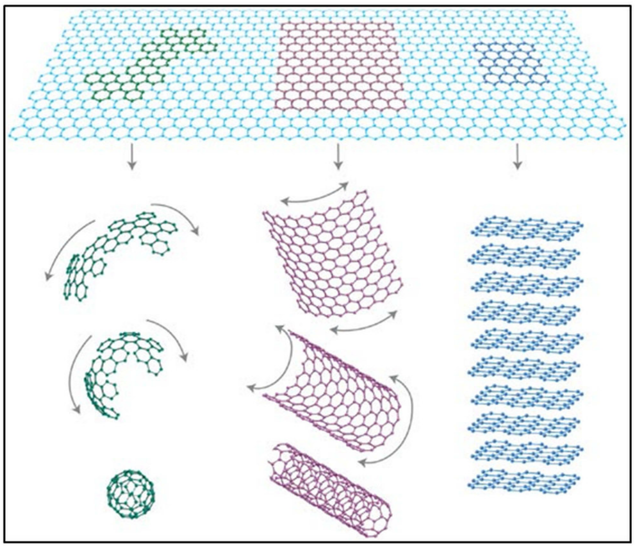

Figure 1.1 – Graphene is the 2D building block for all other carbon materials with different dimensionalities. It can be wrapped to form 0D C_{60} fullerene(left); rolled up into 1D CNT (middle) and stacked to bulk graphite (right); (image reproduced from reference [4]).

The field of 2D materials has grown enormously in past few years, still then many questions needs to be answered. Below what thickness one can call a thin crystal as 2D material ?. Several authors [5–7], analyzed this issue by exploring the electronic properties of trilayer graphene, and showed that, both thickness (number of layers) and the stacking arrangement is important in determining their electronic properties. Whether a crystal of particular thickness can be called 2D material or not, may depend on the specific compound and the physical phenomena considered [1]. When the thickness of a compound decreases, significant change in its electronic properties can occur at a thickness of about tens of monolayers [1]. In certain cases, further decreasing the thickness can cause unexpected changes in its electronic properties, hence, when exactly a thin crystal can be considered as a 2D material is ambiguous, and it is still under debate [1]. This ambiguity can be illustrated with graphene. Monolayer graphene is a zero-gap semiconductor and shows linear dispersion around K point in the Brillouin zone (BZ) [4, 8]. The bilayer graphene is a zero-gap semiconductor with quadratic energy dispersion [8]. The band structure of bilayer graphene can be tuned electrostatically, application of a perpendicular electric field can lead to a band gap opening [8]. Experiments [5–7] shows that ABC-trilayer graphene is physically distinct from all other multilayer graphene. The energy dispersion is cubic in ABC-trilayer graphene rather linear (like monolayer) or quadratic (like bilayer). The unique electronic properties of ABC-trilayer graphene with respect to all other multilayer graphene makes it a distinct 2D material.

After successful isolation of graphene, the search for other 2D materials was geared up in past few years. Since there exist hundreds of layered materials, in principle, one can think of cleaving them in to single layer using the same simple Scotch-tape experiment[3], but this task is not so straightforward [9]. Many 2D crystals proposed theoretically are still far from reality, because they corrode, decompose, segregate and so forth at ambient conditions [10]. The high thermal and chemical stability of 3D crystal is essential for the survival of its 2D counterpart. Graphite meets both conditions, that allows graphene to exist under ambient conditions, the same is true for other stable 2D crystals such as hexagonal (h) boron nitride (BN) and molybdenum disulphide (MoS_2) [9].

Graphite, h-BN and MoS_2 are widely used as solid lubricant, and their monolayers are extensively studied. Though the structural, chemical and electronic properties of tungsten disulphide (WS_2), tungsten diselenide (WSe_2) and molybdenum diselenide ($MoSe_2$) are similar to MoS_2, their monolayers are not studied in detail, probably because of their less abundance in nature [9]. Figure 1.2 shows the current members of 2D materials family. The materials that belong to the blue-shaded regions are stable monolayers at ambient conditions. The materials which are probably stable in air are shaded in green, materials in the pink shaded regions are unstable in air, but they may become stable in inert atmosphere. The gray-shaded materials are exfoliated to monolayer from their bulk, but no further information is available about these materials other than atomic force microscopy (AFM) results[9]. Apart from this, there exist entire periodic table of crystalline solids and compounds each having different electronic, optical and mechanical properties, and the possibility to separate them into single-atomic or few-atomic layer thick 2D crystals still remains open. Even though a wide spectrum of stable 2D materials are available today, the prime focus of this thesis is on graphene, 2D h-BN and monolayer(ML)-MoS_2 because of their novel properties and potential applications in different sectors.

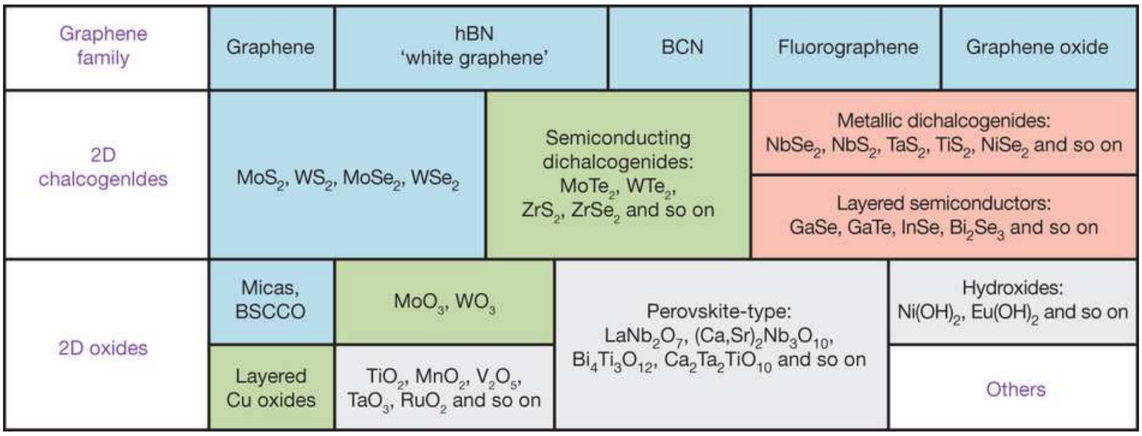
<table>
<tr><td>Graphene family</td><td>Graphene</td><td>hBN
'white graphene'</td><td>BCN</td><td>Fluorographene</td><td>Graphene oxide</td></tr>
<tr><td rowspan="2">2D chalcogenides</td><td rowspan="2" colspan="2">MoS_2, WS_2, $MoSe_2$, WSe_2</td><td rowspan="2">Semiconducting dichalcogenides: $MoTe_2$, WTe_2, ZrS_2, $ZrSe_2$ and so on</td><td colspan="2">Metallic dichalcogenides: $NbSe_2$, NbS_2, TaS_2, TiS_2, $NiSe_2$ and so on</td></tr>
<tr><td colspan="2">Layered semiconductors: GaSe, GaTe, InSe, Bi_2Se_3 and so on</td></tr>
<tr><td rowspan="2">2D oxides</td><td>Micas, BSCCO</td><td>MoO_3, WO_3</td><td rowspan="2" colspan="2">Perovskite-type: $LaNb_2O_7$, $(Ca,Sr)_2Nb_3O_{10}$, $Bi_4Ti_3O_{12}$, $Ca_2Ta_2TiO_{10}$ and so on</td><td>Hydroxides: $Ni(OH)_2$, $Eu(OH)_2$ and so on</td></tr>
<tr><td>Layered Cu oxides</td><td>TiO_2, MnO_2, V_2O_5, TaO_3, RuO_2 and so on</td><td>Others</td></tr>
</table>

Figure 1.2 – **2D materials family**. Blue-shaded regions are stable monolayers at ambient conditions (room temperature in air). Green-shade- materials are probably stable in air; pink shade-materials are unstable in air, but they may become stable in inert atmosphere. Gray-shade-materials are exfoliated to monolayer from their bulk, but no further information are available about these materials (image reproduced from reference [9]).

1.1.1 2D materials based disruptive technologies

Technologies, in general, advances either as incremental or as quantum leap. In order to become disruptive, a new technology should bring an improvement in order of magnitudes instead of incremental [11]. 2D materials are expected to have major impact in technological applications and have a chance to become next disruptive technologies due to their novel properties [11]. Among 2D materials, graphene has got enormous attention due to its superior electronic [4], thermal [12] and mechanical properties [13]. Figure 1.3 shows graphene's properties and its possible application areas. The mobility of charge carriers in graphene is 100,000 cm^2/V-Sec [4], which is two order of magnitude higher than that of Si (1,400 cm^2/V-Sec), hence the charge carriers in graphene travels 10-100 times faster than in Si at room temperatures. The high carrier mobility, high thermal conductivity ($> \sim$2000 to 5300 W/m-K [12]) and high flexibility of graphene makes it a promising candidate to replace or complement the Si based electronic industry. Due to the potential electronic properties, graphene is used to fabricate high-frequency devices, touch screens, ultra-sensitive sensors and nano-electromechanical systems (NEMS) [11]. Graphene's ability to transmit (97.7 %) light [14] and its high electrical conductivity makes it an appealing candidate to device high performance light emitting diodes (LEDs), flexible touch-screens and photo-detectors. Graphene has many other intriguing properties, being one atom thick, flexible and chemically inert, it can be used to make thin membranes/gas barriers. The high Young's modulus ($\sim$1,100 Gpa) and fracture strength ($\sim$125 Gpa) [13] of graphene can be utilized to make high strength and light weight composites. The flexibility of graphene enables it to substitute the brittle indium tin oxide (ITO) in the manufacturing of flexible displays and touch screen [11].

The 2D hexagonal boron nitride (h-BN), which is structurally analogous to graphene, is a wide gap semiconductor with a band gap of $\sim$5.8 eV [15], and hence it is a promising material in opto-electronic industry [15–17]. The graphene/h-BN hybrid structures are also devised to have better performance [18]. Graphene deposited on SiO_2 substrate lacks the intrinsic properties of free-standing graphene due to scattering from impurities [19, 20] and surface roughness [21–23]. The h-BN, which geometrically supports graphene due to its identical structure, is hence used as a substrate which retains the quality of the suspended graphene sheets [24].

Atomically thin MoS_2 is another emerging 2D material with fascinating optical, electrical and mechanical properties [25, 26]. Being an intrinsic semiconductor with a finite band gap (∼1.9 eV) [25] makes this material a promising candidate in electronic and opto-electronic industry [27]. The ML-MoS_2 has been isolated in 2005, but it gained much attention few-years back, when researchers made field effect transistors (FETs) using ML-MoS_2 with extraordinary performance[27]. Its room temperature carrier mobility and on/off ratio are comparable to that of graphene nano-ribbons [27]. A recent experiment demonstrates a high thermo-electric energy conversion using ML-MoS_2 [28]

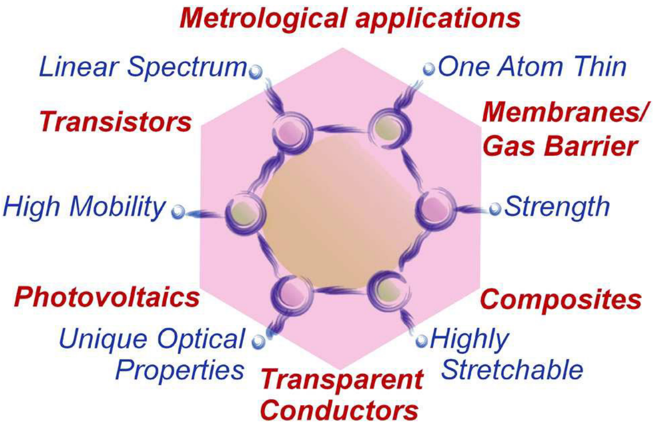

Figure 1.3 – An overview of properties and application of graphene (image reproduced from reference [11]).

1.2 Structural and electronic properties of graphene, 2D h-BN and ML-MoS_2

Graphene is a 2D crystal with carbon atoms arranged in a honeycomb structure (Figure 1.4). The 2D honeycomb lattice is not a Bravais lattice, because two neighboring sites are not equivalent. The 2D Bravais lattice of honeycomb structure is defined using a rhombus (Figure 1.4), the corresponding primitive lattice vectors are

$$\begin{pmatrix} \bar{a} \\ \bar{b} \end{pmatrix} = a \begin{pmatrix} \frac{\sqrt{3}}{2} & -\frac{1}{2} \\ \frac{\sqrt{3}}{2} & \frac{1}{2} \end{pmatrix} \begin{pmatrix} \hat{x} \\ \hat{y} \end{pmatrix} \tag{1.1}$$

where $|\bar{a}| = |\bar{b}| = a$, the in-plane lattice parameter. This particular choice of lattice vectors make an angle 60^o between $\bar{a}$ and $\bar{b}$. The in-plane lattice parameter is defined as $a = \sqrt{3}R_{c-c} = 2.46$ Å, where $R_{c-c} = 1.42$ Å, is the distance between nearest neighbor (nn) carbon atoms. In this configuration, the two basis atoms are situated at (1/3, 1/3, 0) and (2/3, 2/3, 0), respectively. Once the primitive vectors are defined in real space, the corresponding reciprocal lattice vectors ($\bar{A}_j$) can be obtained using the relation $\bar{a}_j.\bar{A}_j = 2\pi\delta_{ij}$

$$\begin{pmatrix} \bar{A} \\ \bar{B} \end{pmatrix} = \frac{2\pi}{a} \begin{pmatrix} \frac{1}{\sqrt{3}} & -1 \\ \frac{1}{\sqrt{3}} & 1 \end{pmatrix} \begin{pmatrix} \hat{x} \\ \hat{y} \end{pmatrix} \tag{1.2}$$

The angle between $\bar{A}$ and $\bar{B}$ is 120^o. The first Brillouin zone (FBZ) is shown in figure 1.4, which is also hexagonal in shape. The Γ, M, K and K' are high symmetry points in FBZ. The Γ point is at the center of FBZ where the wave-vector ($\bar{q}$) is zero. The corners of hexagon are called K points (also known as Dirac points), these are very special points in the electronic band structure of graphene. The conduction and valence band touch each other at K points (Figure 1.5) and shows linear dispersion ($E = \hbar k v_F$), as a consequence, the quasi-particles in graphene behaves as if they were massless Dirac particles, with a Fermi velocity $v_f \approx \frac{C}{300}$ [4, 8]. The linear dispersion around K point stimulate a new "Fermi-Dirac" physics. Another interesting consequence of linear dispersion is the anomalous room temperature quantum-Hall effect [4].

One of the potential drawbacks of graphene is the absence of a finite band-gap in its electronic band structure, which limits its use as an alternate to silicon based electronics. Due to this special electronic band structure, graphene based FETs shows low on off ratios. Several attempts have been made to obtain a finite band gap on graphene's electronic band structure, which includes, substrate induced band gap opening, chemical substitution doping, quantum confinement (nanoribbons) and hybrid structures (BCN-structures) [29]. In a multilayer graphene, the stacking order provides a new degree of freedom to tune the electronic band structure [7]. Bao *et al* [7] made a detailed study on stacking-dependent band-gap and electronic transport in ABA (Bernal) and ABC (rhombohedral) stacked graphene. At Dirac point, the ABA stacked graphene is semi-metallic, at the same time, the ABC stacked graphene shows a band gap opening (∼6 meV)[7].

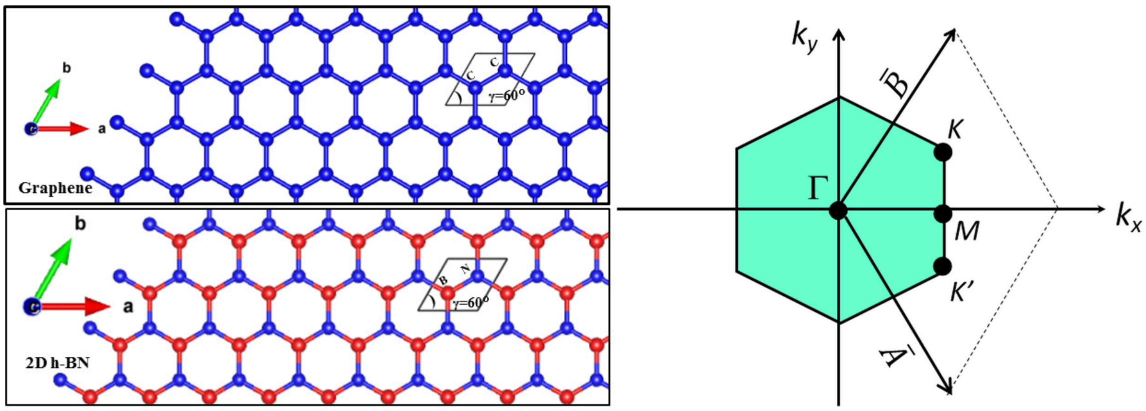

Figure 1.4 – (left) The unitcell of graphene and 2D h-BN is defined using a rhombus containing two basis atoms. The primitive lattice vectors are $\bar{a} = a(\frac{\sqrt{3}}{2}, -\frac{1}{2}, 0)$, $\bar{b} = a(\frac{\sqrt{3}}{2}, \frac{1}{2}, 0)$ and $\bar{c}$=(0, 0, c). (right) The first Brillouin zone (FBZ), which is also hexagonal in shape. The Γ, M, K and K' are the high symmetry points in FBZ, $\bar{A}$ and $\bar{B}$ are the reciprocal lattice vectors.

In 2D h-BN, instead of carbon atoms, B and N atoms are alternatively occupied at the corners of hexagons (Figure 1.4), therefore its sublattices are chemically not equivalent. This make the electronic properties of 2D h-BN completely different from that of graphene. Recent *ab initio* calculation predict a band gap of 4.67 eV [30], (which is 1 eV less than the experimental values [15]), and also shows a direct to indirect transition along K-Γ direction (indicated using red arrow). Due to the large electronegativity difference between the B and N atoms, the π-band wavefunction is located near the N atom and the π^*-band wave function is located near the B atom. The localization of π-band wavefunction near the N atom makes the 2D h-BN a wide band semiconductor [31]. In graphene, the two basis atoms are equivalent, hence the π and π^* band wavefunctions are degenerate at the K point, leading to linear dispersion.

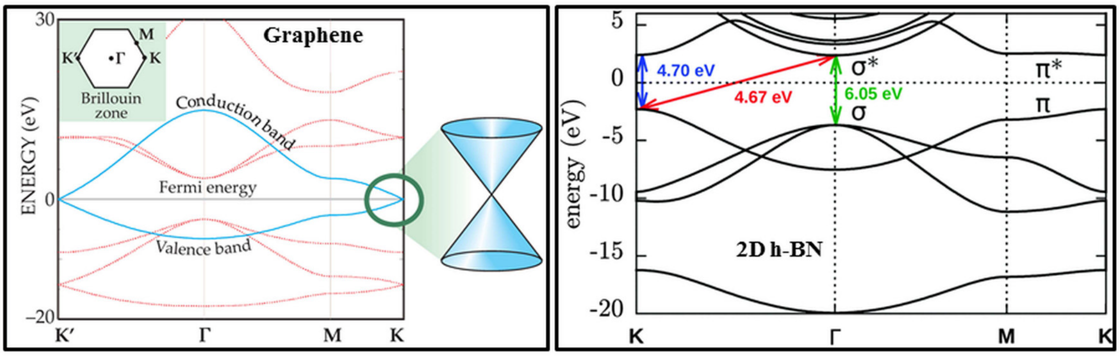

Figure 1.5 – The electronic band structure of graphene (image reproduced from reference [32]) and 2D h-BN (image reproduced from reference [30]). The conduction and valence band touch each other at K points in graphene, while there is a band gap opening at the K points in 2D h-BN. The 2D h-BN shows direct to indirect transition along K-Γ direction (indicated using red arrow), and its fundamental band gap is 4.67 eV.

ML-MoS_2 belongs to transition metal dichalcogenides (TMDs) family, and posses a hexagonal symmetry as graphene and 2D h-BN (Figure 1.6). Unlike graphene and 2D h-BN, each MoS_2 layer is formed by stacking two hexagonal planes of S atoms and an intercalated hexagonal plane of Mo atoms bound with the S atoms in a trigonal prismatic arrangement [33]. The unitcell of ML-MoS_2 is also defined using a rhombus with three basis atoms, and their coordinates are, Mo (2/3, 2/3, 0.500), S1 (1/3, 1/3, 0.603) and S2 (1/3, 1/3, 0.394). Kuc *et al* [34] calculated the electronic band structure of bulk, bi-layer and ML-MoS_2 (Figure 1.7). For bulk and bilayer MoS_2, the valence band maximum (VBM) and the conduction band minimum (CBM) are situated at Γ point and the midway between the Γ and K point, respectively. When thickness reduces from 2L to ML, both VBM and CBM shifted to K point, and shows an indirect to direct band gap transition. The unique electronic properties of ML-MoS_2 arises from the d-orbital related interaction [34, 35]. The conduction band at K point is composed of d-orbital of Mo atoms, since Mo atoms are located at the middle of S-Mo-S layer, they have minimal interlayer coupling. At the same time, states near Γ-point and the points of indirect band gap stems from the linear combination of d-orbital of Mo atom and p_z orbital of S atom. Hence there will be a strong interlayer coupling at these points and their energy is very sensitive to number of layers [35].

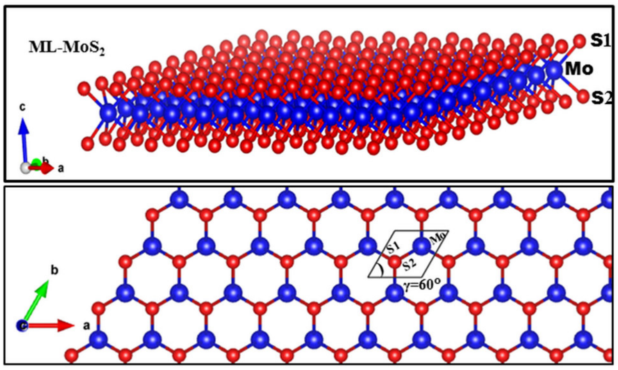

Figure 1.6 – (top) The side view of ML-MoS$_2$; Mo atomic layer sandwiched between the two S atom layers in a trigonal prismatic fashion. (bottom) top view of ML-MoS$_2$; The honeycomb lattice contains one Mo atom and two S atoms located at the corners of hexagons.

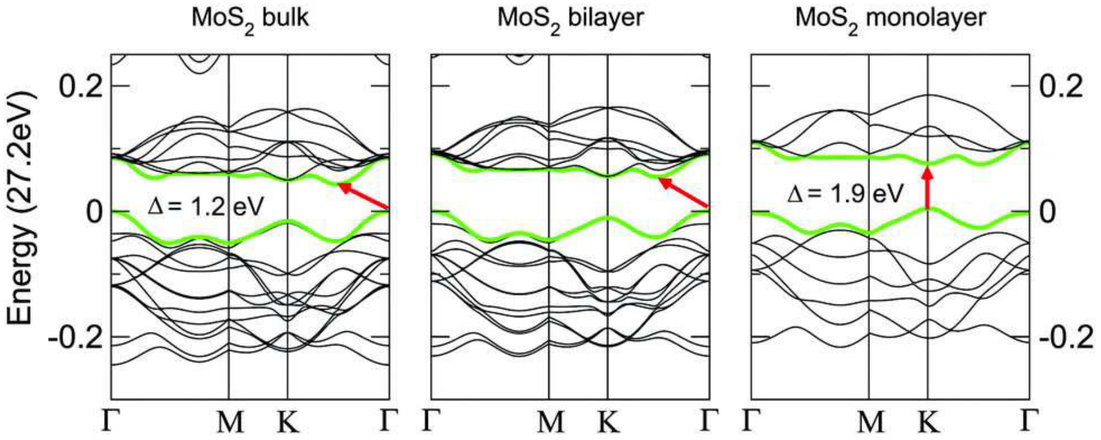

Figure 1.7 – The electronic band structure of bulk, bilayer and monolayer MoS$_2$. The top and bottom of valence and conduction bands are highlighted in green color. The indirect to direct band gap transition from bulk to monolayer is indicated by red arrow (image reproduced from reference [36]).

1.3 Thermal and vibrational properties of graphene, 2D h-BN and ML-MoS$_2$

The 2D materials based technologies can bring down the size of the electronic devices considerably low. Heat removal is a crucial issue in such miniaturized and nano-size electronic devices due to increased level of dissipated power [12]. Knowledge on thermal and vibrational properties of materials are essential to design high quality devices with better heat dissipation capability. However, it is difficult to understand the above mentioned phenomena at atomistic level by experimentation. Computer simulations can be used in such situations to understand the fundamental issues associated with thermal and vibrational properties at atomistic level. To comprehend the current state-of-art, the thermal and vibrational properties of graphene, 2D h-BN and ML-MoS_2 are briefly reviewed in the following sections.

1.3.1 Thermodynamic stability of 2D crystals

The thermodynamic stability of strict 2D crystal is a long standing debate in condensed-matter theory. In 1930's, Landau and Peierls claimed that strictly 2D crystals are thermodynamically unstable and could not survive as free-standing crystals [37, 38]. Their theory predicted that, at finite temperatures, the divergent contribution of thermal fluctuations in 2D crystal lattice causes the displacement of atoms that is comparable to that of interatomic distances. Later, this arguments were extended by Mermin and Wagner, who have formulated the so called Mermin-Wagner theorem [39], which states that, the long wavelength thermal fluctuation would destroy the long range order in 2D crystals at finite temperatures. In support of this argument, it has been found that the melting point of thin films rapidly decreases with decrease in thickness and it start to decompose when thickness is of the order of dozens of atomic layers [40]. Because of this reason, atomic monolayers can exist only as an integral part of bulk 3D structures, usually grown epitaxially on the top of substrates having matching lattice constants [40]. This was the scenario until the discovery of graphene in 2004. In the case of graphene, the strong coupling between the in-plane stretching and out-of-plane bending modes will suppress the thermal fluctuations, and makes the 2D crystals stable with strong height fluctuation on the surfaces known as ripples [41]. Meyer *et al* [42] studied the structure of individual graphene sheets, which are freely suspended in a micro fabricated scaffold in vacuum or air. Their transmission electron microscopy images shows that the suspended graphene sheets are not perfectly flat; the microscopic corrugations of 2D graphene sheets are conspicuous, and the out-of-plane deformations reach 1 nm. These corrugations are prominent in graphene, becomes smaller in bilayer graphene and disappears in bulk graphite, indicates that the corrugations are intrinsic to graphene sheets [42].

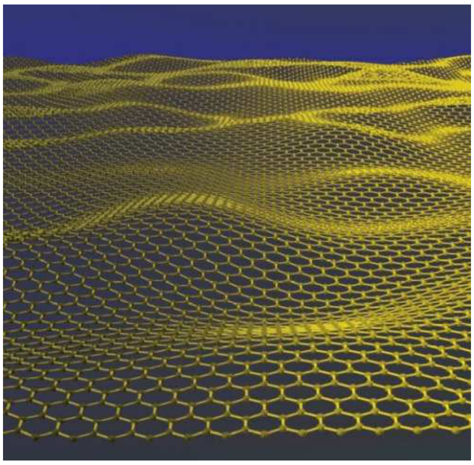

Figure 1.8 – An artist's impression of ripples in graphene's surface (Image reproduced from, university of Manchester- Jannik Meyer/AFP/Getty Images).

1.3.2 Thermal expansion

Even though tremendous efforts have been made to investigate thermal transport in graphene both experimentally and theoretically, the complete picture is not yet clear and the overall scenario still remains complex [12, 43]. Mounet and Marzari [44] made first detailed study on structural, thermal and vibrational properties of diamond, graphite and graphene in the framework of density functional theory (DFT) via quasi-harmonic approximation (QHA). In their study, the authors found that the in-plane lattice parameter ($\boldsymbol{a}$-lattice) of graphite shows negative thermal expansion in the temperature range of 0 K - 600 K, and its minimum value is around room temperature. This feature is absent in diamond and much more apparent in graphene, where $\boldsymbol{a}$-lattice shows thermal contraction upto 2300 K, and it is three times larger than graphite. In 2008, Zakharchenko *et al* [45] studied the thermal expansion of graphene using Monte Carlo (MC) simulations, which allows to go beyond the quasi-harmonic calculations and enables to incorporate the anharmonic effects. They found that the thermal expansion coefficient of graphene is negative upto 900 K and positive thereafter. Their results are in qualitative agreement with Mounet and Marzari [44] upto 500 K, but shows strong deviations at higher temperatures. The authors conclude that, the QHA works reasonably well for bulk crystals, but it fails in strong anharmonic crystals like graphene. Later, Pozzo *et al* [46] performed *ab initio* molecular dynamics (MD) simulations and found that, the $\boldsymbol{a}$-lattice of free-standing graphene is contracting with an increase in temperature (upto 2000 K). At the same time, the same graphene sheet supported on Ir (111) substrate, the $\boldsymbol{a}$-lattice shows thermal expansion instead of contraction [46]. Jiang *et al* [47] used Green's function technique and reported that the linear thermal expansion coefficient (LTEC) is very sensitive to substrate layer interaction. A weak substrate-layer interaction can cause a significant change in the value of LTEC, and if the substrate effects are strong enough, the LTEC can become positive in the whole computed temperature range [47]. The above discrepancies among the various simulations arises due to the difference in the incorporation of anharmonicity in those calculations, its effects are usually very strong in 2D crystals.

From the experimental front, Bao *et al* [48] reported the negative thermal expansion of graphene in the temperature range 200 K - 350 K. Later, Singh *et al* [49] measured the thermal expansion coefficient of graphene by monitoring the variation of frequency of resonance of suspended graphene electro-mechanical resonators and found it to be negative in the temperature range of 30 K - 300 K. Yoon *et al* [50] used temperature dependent Raman spectroscopy to study the thermal expansion coefficient of graphene and found that it remains negative in the measured temperature range of 200 K - 400 K. They constrained their thermal expansion measurement upto 400 K as above this temperature graphene sheet slips on SiO_2 substrate surface because the tensile strain increases significantly over the weak Van der Waals (vdW) force which pins the sheet on the substrate [50]. The situation is likely to be true for 2D h-BN also. Hence, high temperature Raman data are not available to compare with the theoretical predictions.

Due to the overwhelmingly attractive properties and novel applications, substantial amount of research have been pumped towards graphene. However, the thermophysical properties of 2D h-BN and ML-MoS$_2$ are not explored in detail so far. Yates *et al* [51] measured the thermal expansion of pyrolytic BN in the temperature range of 80 K - 780 K using a interferometric experimental set up. Their data show that the LTEC remain negative in the whole measured temperature range and attains a minimum value around 230 K ($-2.95 \times 10^{-6} K^{-1}$). The authors compared their results with the pyrolytic graphite, and found that the LTEC is more negative in pyrolytic BN. After graphene's discovery, researchers started to revisit the thermal expansion of 2D h-BN. Sevik [52] studied the thermal expansion of graphene, 2D h-BN and ML-MoS$_2$ using QHA. They found that the LTEC of graphene and 2D h-BN are more negative than that of their bulk counter part. At low temperature, there is a remarkable difference between the LTEC of these two materials. Unlike graphene and 2D h-BN, the $\boldsymbol{a}$-lattice of ML-MoS$_2$ shows a positive thermal expansion in the whole computed temperature range (0 K - 1500 K) [52, 53] and it has been measured earlier in bulk-MoS$_2$ using X-ray powder diffraction [54, 55].

1.3.3 Vibrational properties

In order to interpret the structural and thermal properties of 2D materials, an understanding of lattice vibrational modes is essential. In general, lattice vibrational modes are obtained using lattice dynamics (LD) methods. For a crystal containing N basis atoms, there will be 3N modes of vibrations. Among 3N modes, three modes are always acoustic (A) corresponding to to three rigid translational motion of crystal, and the remaining 3N-3 are optic (O) modes. For acoustic modes, the atoms in the unitcell move in same phase, whereas for optic modes they move out of phase.

1.3.3.1 Phonons in 2D honeycomb structures

The unitcell of graphene contains two basis atoms, hence there will be six modes of vibrations (three acoustic + three optic). Figure 1.9 shows the phonon dispersion (the relationship between the phonon frequency/energy and the phonon wave-vector **q**) of graphene and graphite. In the long wavelength limit, one can distinguish three kinds of modes, (1) longitudinal (L) modes, in which atoms move in the direction of **q**; (2) transverse (T) modes, in which atoms move in 2D plane, in a direction perpendicular to **q**; (3) out-of-plane modes (Z), where the atoms move along out-of-plane direction. Graphite, the bulk counterpart of graphene contains 4 basis atoms, leading to 12 modes of vibrations (three acoustic + nine optic). The phonon modes designated with prime (say LO') indicates that the two equivalent atoms in a layer vibrate in phase but they are vibrating with a phase difference of 180° with respect to the two atoms in the neighbouring layer. Since graphene contains only one layer, the primed optic mode do not appear in graphene [44]. For frequencies above 400 cm^{-1}, the modes are doubly degenerate, because of weak inter-sheet interaction [56]. The in-plane modes are identical in both graphene and graphite. Below 400 cm^{-1}, the phonon branches of graphite deviate noticeably from graphene sheet (Figure 1.9). The phonon branches of graphite split in to acoustic (corresponds to the in-phase vibration of equivalent atoms of neighbouring layer) and optic branches (corresponds to the out of phase vibration of equivalent atoms in the neighbouring layer) below 400 cm^{-1} [56].

In 2D materials, there is a clear distinction between the in-plane and out-of-plane modes. The term out-of-plane mode is used to denote the modes, where the atom movement is perpendicular to the 2D sheet (labeled using letter Z). The LA and TA modes show linear dispersion near the Γ point, whereas the ZA modes [44, 56] shows quadratic dispersion, the latter being a characteristic feature of phonon dispersion of 2D layered materials [57, 58], which is observed in neutron scattering experiments

[59]. The quadratic dispersion of ZA mode is due to the D_{6h} point-group symmetry [60]. In the long wave length limit, the ZA mode causes bending of the surfaces due to thermally excited ripples in the sheets, hence it is known as bending modes.

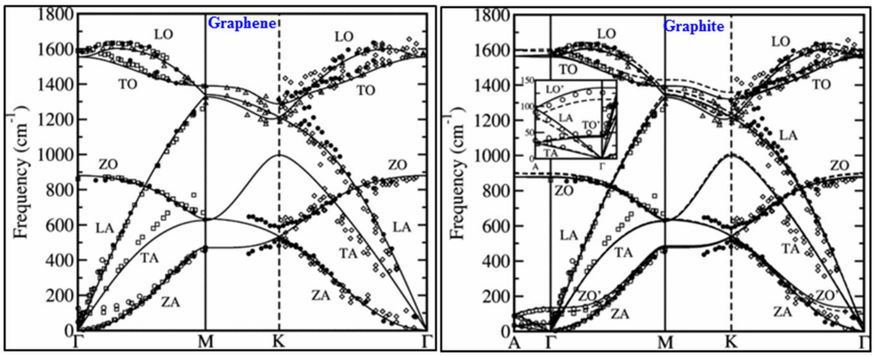

Figure 1.9 – The phonon dispersion of graphene and graphite. The solid and dashed lines are GGA and LDA *ab initio* calculations, respectively. The experimental data are shown as symbols. The quadratic dispersion of ZA mode is clearly visible in both graphene and graphite. The phonon dispersion of graphite deviate noticeably from graphene below 400 cm^{-1}(image reproduced from reference [44]).

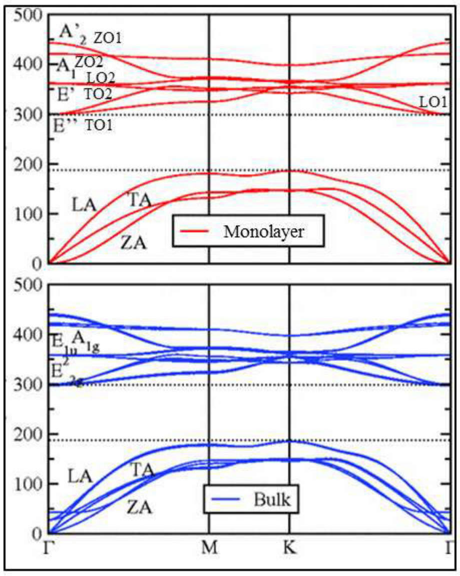

Figure 1.10 – Phonon dispersion of bulk and ML-MoS$_2$. The unitcell of ML-MoS$_2$ is composed of three basis atoms, hence there will be nine modes of vibrations (three acoustic + six optic). The optic branches of ML-MoS$_2$ are designated using both group theory based notations (A_2'', E', A_1', E'') and their polarizations $(ZO1, LO2/TO2, ZO2, LO1/TO1)$ (image reproduced from reference [33]).

The unitcell of 2D h-BN contains 2 basis atoms, which leads to six modes of vibrations as in the case of graphene. The designation of these modes are identical to that of graphene, and their frequencies differ from the graphene because of the difference in masses of basis atoms. In ML-MoS$_2$, the unitcell is composed of three basis atoms, hence there will be nine modes of vibrations (three acoustic + six optic, Figure 1.10). The designation of acoustic modes are identical to that of graphene and 2D h-BN. Since there are six optic modes their designation will be slightly different from graphene and 2D h-BN. More detailed description will be given in respective chapter.

1.3.3.2 Literature survey-graphene

The harmonic and quasi-harmonic lattice dynamics methods are extensively used to obtain the phonon frequencies and then the thermodynamic properties of graphite and graphene [44, 56]. Wirtz *et al* [56] made a detailed first principle study on phonon dispersion of graphite and graphene. In their study, they analyzed the effect of exchange correlation (XC) functional on the phonon dispersion. The authors found that generalized gradient approximation (GGA) underestimates the phonon frequencies by 2 % with respect to local density approximation (LDA) and the agreement with experiments became more satisfactory. Mounet and Marzari [44] calculated the phonon dispersion for hexagonal (ABABA.. stack) and rhombohedral (ABCABC... stack) graphite and graphene using *ab initio* simulations. They observed that stacking has negligible effects for all phonon branches lying above 400 cm^{-1}. Phonon dispersion of hexagonal and rhombohedral graphite are different only along the out-of-plane direction ($\Gamma-$A). To obtain the thermodynamic quantities such as thermal expansion, specific heat and temperature dependent elastic constants, the authors employed QHA. Later, many authors studied the thermal and vibrational properties of graphite, few-layer and single layer graphene using *ab initio* simulations within QHA [52, 61–63].

The anharmonic effect is usually very strong in 2D crystals and it becomes more pronounced at high temperatures. The coupling between the phonon modes will have significant effects on structural, thermal and vibrational properties at finite temperatures. The effects of anharmonicity on thermal and vibrational properties of graphene have been studied using DFPT [43, 64, 65]. Most notably, Bonini *et al* [64] investigated the effect of anharmonicity on phonon frequency shift and phonon linewidth in graphene and graphite. The authors found that the width of the E_{2g} (this nomenclature is based on group theoretical classification; experimentalists designate it as the G peak) phonon mode decreases with increasing temperature due to strong electron-phonon coupling. On the other hand, the frequency of this mode shows a down-shift with increasing temperature in spite of contraction of the lattice. Recently, Paulatto *et al* [65] developed a method based on the 2n+1 theorem within the framework of DFPT to compute the anharmonic scattering coefficients for processes involving three phonons having arbitrary wave-vectors.

Being fast and non-destructive characterization tool, Raman spectroscopy will be the first choice for experimentalist to study the vibrational properties of graphene and allied 2D materials [66]. Calizo *et al* [67] studied the effect of temperature on the G peak of single and few-layer graphene on Si/SiO$_2$ substrate by Raman spectroscopy and observed a down-shift in frequency in the temperature range of 123 K - 198 K. Later, Lin *et al* [68] conducted Raman scattering experiments on un-supported vertical graphene sheets to eliminate the substrate effect. The authors found that while the frequency shift observed by them is consistent with the results of first principle calculations, the phonon linewidth shows an opposite trend. Modification of phonon dispersion due to the strain effect by the substrate has to be taken into account in temperature dependent Raman studies of graphene on Si/SiO$_2$ substrate. This strain effect caused by the substrate prevents a direct comparison of Raman spectra with the results of calculations which pertain to a free-standing graphene. Yoon *et al* [50] tried to eliminate the substrate effect in the thermal expansion coefficient obtained using Raman spectroscopy and found that there are significant differences between the results of calculations and experimental data near the room temperature. The discrepancies between the different Raman studies are related to presence of defects in the sample, low excitation power on sample surface and drift of the laser spot [67].

Raman and other optical scattering spectroscopy techniques are limited to probe zone center (Γ-point) phonons. This can be illustrated as follows. The wave-vector of incident photon is $\bar{k} = \frac{2\pi}{\lambda}$, for a typical value λ=500 nm, $\bar{k} \simeq 10^5$cm^{-1}. The size of BZ is of the order of $\frac{\pi}{a} \approx 10^8$ cm^{-1}. The $\bar{k}$ is smaller than the size of BZ by a factor of $\simeq 10^3$. The theory of scattering demands that, the wave-vector of incident photon should be of the same order of scattering medium (say phonon, its wave vector is $\bar{q}$). Since the value of $\bar{k}$ is much smaller than the radius of BZ, only those phonons with small $\bar{q}$ (long wave length phonons) will participate in light scattering. More precisely, this type of scattering probes only region close to the centre of zone [69].

To obtain the entire phonon dispersion, in-elastic neutron scattering techniques are used. The energy/wave length of thermal neutron ($\sim$25 meV/1-2 Å) is of the same order of magnitude of phonons. Hence, thermal neutron scattering is an ideal tool to probe the phonon spectra and dynamics of the scattering medium [70]. The in-elastic x-ray scattering techniques are also used to determine the phonon dispersion. The relative advantage of neutron scattering over x-ray is that, the energy of thermal neutron is of the same order of phonon frequency, hence there will be an appreciable shift in phonon frequency, which can be determined with great accuracy [69]. The electron energy loss spectroscopy (EELS) is another tool to obtain the phonon dispersion, which are used to probe the surface phonons. In EELS, the low energy electrons are in-elastically scattered from the surface phonons, whose energy $\sim 10^{-3}$ eV to 1 eV. The neutron, x-ray and electron scattering techniques have been widely used to obtain the phonon dispersion of graphite [59, 71–75] and graphene [76–80].

1.3.3.3 Literature survey-2D h-BN and ML-MoS$_2$

As pointed out earlier, graphene's fascinating properties intrigued extensive research on other novel 2D materials. Consequently, in past few years enormous studies have been done to understand the vibrational and thermodynamic properties of 2D h-BN and ML-MoS$_2$. Topsakal *et al* [81] performed *ab initio* simulations to study the structural, electronic and vibrational properties of all allotropic forms of BN. Michel *et al* [82] employed empirical force constant model to derive the phonon dispersion of multilayer BN. Later, Slotman *et al* [83] studied the thermal expansion, bending rigidity and energetics of point defects using classical MD simulations. Singh *et al* [84] studied the thermomechanical properties of 2D h-BN using atomistic simulations. The vibrational properties of BN nanotubes have been studied in early 2000 [85, 86]. Sànchez *et al* [85], reported the phonon dispersion, density of states and elastic constants of single-walled nanotube and 2D h-BN using tight binding methods. The vibrational properties of BN nanotubes of different diameter and chiralities are studied using *ab initio* lattice dynamics calculation [86]. Experimentally, the vibrational properties of bulk h-BN are studied four decades ago [87, 88]. The phonon modes of bulk h-BN at the Γ point in the BZ is studied using IR [87] and first order Raman scattering techniques [87, 88]. Electron energy loss spectroscopy (EELS) has been used to get the phonon dispersion of 2D h-BN on Ni(111) substrate [89, 90]. Serrano *et al* [91], studied the vibrational properties of h-BN using in-elastic x-ray scattering and complemented with *ab initio* calculations.

After the discovery of ML-MoS_2 based field effect transistors (FETs) [27], the research on monolayers of MoS_2 and other transition metal dichalcogenides has grown exponentially [92]. Similar to graphene and 2D h-BN, LD methods are widely employed to obtain the vibrational properties of ML-MoS_2 [33, 52, 93, 94]. Ataca *et al* [93], investigated the LD properties of bulk and ML-MoS_2 using DFT. They studied the effect of vdW interaction on structure, energetics and phonon dispersion of bulk MoS_2. Due to the absence of vdW interaction, some Raman active modes are softer in ML-MoS_2 [93]. Sánchez *et al* [33], studied the behaviour of Raman active E^1_{2g} and A_{1g} as a function of layer number using *ab initio* calculations. They found that A_{1g} mode frequency increases with layer number, while E^1_{2g} mode shows reverse trend. Later, Cai *et al* [94], calculated the Grüneisen parameter and Umklapp scattering limited relaxation time of phonons in ML-MoS$_2$ using DFPT.

Raman spectroscopy has been widely used to study the vibrational properties of ML/FL MoS$_2$ [95–101]. Lee *et al* [95], made first detailed study on ML and FL MoS$_2$ using AFM and Raman spectroscopy. Two Raman active modes E^1_{2g} and A_{1g} are very sensitive to thickness of MoS$_2$. The frequency of E^1_{2g} mode falls with thickness, while A_{1g} mode frequency increases. Later, many authors studied the evolution of Raman active modes with layer number [92, 95, 97]. The temperature evolution of E^1_{2g} and A_{1g} modes are studied using temperature dependent Raman spectroscopy [98–101]. These studies shows a red shift of E^1_{2g} and A_{1g} mode with an increase temperature [98, 99]. Recently, Robinson *et al* [102] reported the effect of supporting substrate on the Raman shift of E^1_{2g} and A_{1g} modes. The excitation laser power can induce a local temperature change which can also alter the Raman spectra [103].

1.4 Objective of the thesis

We reviewed the structural, thermal and vibrational properties of different 2D materials (graphene, 2D h-BN and ML-MoS$_2$) in section 1.3. The main issues in the field of 2D materials and the objective of the thesis are as follows.

1. The structural, thermal and vibrational properties of 2D materials are investigated in detail using harmonic and quasi-harmonic LD methods (section 1.3.3). In harmonic LD, the effects of anharmonicity are completely ignored. The finite temperature properties are modeled using the tedious QHA[1]. The QHA works well at intermediate temperatures and it may not be suitable at high temperature because of the non inclusion of phonon–phonon interactions. As the temperature increases more and more phonon modes are excited and anharmonicity of the crystal becomes more pronounced. To probe the higher order anharmonicity, a few efforts have been made using anharmonic LD based techniques (section 1.3.3). The higher order phonon effects are neglected in anharmonic LD based methods by truncating the crystal lattice

---

[1] more details about LD, QHA and anharmonic LD methods will be given in chapter-2, section 2.3

potential energy at third order in the displacement of the atoms from their equilibrium position, therefore some crucial information may miss in the case of strong anharmonic crystals.

2D materials, being strong anharmonic in nature, the higher order phonon processes are important and cannot be neglected [68]. Under such circumstances MD simulations becomes a natural choice; it can incorporate the anharmonicity of interatomic potentials fully without any approximations. Ling Ti Kong [104] proposed a method to compute the phonon dispersion and phonon DOS directly from MD simulations at finite temperatures. These method seems to be an extension of QHA to MD simulations, hence couldn't capture the true anharmonic properties of materials. Moreover this method will not provide the information about mode resolved phonon frequencies and linewidth. In the present thesis, the above tasks have been achieved by adapting a spectral energy density (SED) based method. Several in-house codes have been developed and coupled with classical MD simulation package LAMMPS.

2. The thermally excited ripples are inevitable in 2D crystals, which makes them stable at finite temperature (section 1.3.1). These ripples can affect the thermo-physical properties of 2D materials significantly. Most of the researchers used *ab initio* simulation in conjunction with QHA to obtain the thermal expansion properties. In QHA, the 2D sheets are considered to be flat, hence the effects of ripples cannot be incorporated. *Ab initio* MD simulation can be used to incorporate the effects of ripples, but within the *ab initio* MD frame work one cannot include more than few hundreds of atoms in the simulation cell (due to the lack of computational resources), which seems to be in-adequate to incorporate the long wavelength ripples. From the experimental perspective, most of the measurements are made on 2D sheet supported on a substrate or over a trench. These measurements are extremely challenging due to the strain effects, and may not be able to capture the intrinsic thermal expansion properties of free-standing 2D sheets with complete effects of ripples. Since classical

MD simulations can incorporate millions of atoms and also computation can be done with free-standing sheets containing ripples, detailed MD study needs to be undertaken to understand the role of ripples on the thermal expansion of 2D crystals at finite temperatures.

In light of above facts, we set the objective of the present thesis as follows; understand the structural, thermal and vibrational properties of 2D materials with full anharmonicity. In order to achieve these tasks, systematic studies have been done using the *ab initio* and classical MD simulations (in conjunction with SED method), and the significant results obtained are presented in the thesis. The remaining part of the thesis is organized as follows. The computational and theoretical methods employed in this thesis are discussed in **chapter 2**. The detailed theoretical derivation, implementation and benchmarking of SED method is given at end of **chapter-2**. The dynamical (structural) stability of stacking altered graphite structures are analyzed using *ab initio* and classical MD simulations, and presented in **chapter-3**. The SED method is used to calculate temperature dependent structural stability, thermal expansion, frequency shift and coupling of normal modes of vibrations of graphene and 2D h-BN, and the results are discussed in **chapter-4&5**, respectively. **Chapter-6** focuses on the anharmonicity of optic phonon modes of ML-MoS_2. The temperature dependent structural stability and thermal expansion of ML-MoS_2 are also addressed in this chapter. Finally the conclusion and scope for the further studies are brought out in **chapter-7**.

Chapter 2

Computational and theoretical methods

This chapter discusses the computational and theoretical methods employed in this thesis. The general aspects of density functional theory (DFT) and classical molecular dynamics (MD) simulations are discussed. To probe the complete anharmonicity in materials, a spectral energy density based (SED) formalism is adapted. Several in-house codes are developed and coupled with classical MD simulation package LAMMPS. The theoretical derivation, implementation and validation of SED method is discussed in detail.

2.1 Density Functional Theory (DFT)

Density Functional Theory (DFT) is the most successful and widely used quantum mechanical modeling method in condensed matter physics and materials science. With the advancement of powerful computers, DFT based simulations became routine, and it is widely used to predict the various physical properties of materials, which comprises not only bulk solids but also low dimensional materials, interfaces, nanoparticles, complex molecules and proteins. The basic idea behind DFT is that the wave-function of many-body interacting system is replaced with a single scalar quantity known as charge-density, which reduces the complexity of 3N degrees of freedom of the system in to only three spatial coordinates.

2.1.1 Hamiltonian for a condensed matter system and Born-Oppenheimer approximation

The ground state properties of a many-body system (such as collection of atoms, molecules or a solid) can be obtained by solving the time independent Schrödinger equation

$$\hat{H}\Psi = E\Psi \tag{2.1}$$

where $\hat{H}$ is the non-relativistic Hamiltonian for a many-body system (say a solid) contains N nuclei and n(ZN) electrons and it is written as follows

$$\hat{H} = \hat{T}_N(\mathbf{R}) + \hat{T}_e(\mathbf{r}) + \hat{V}_{eN}(\mathbf{r}, \mathbf{R}) + \hat{V}_{ee}(\mathbf{r}) + \hat{V}_{NN}(\mathbf{R}) \tag{2.2}$$

$$\hat{H} = -\hbar^2 \sum_I \frac{\nabla_I^2}{2M_I} - \frac{\hbar^2}{2m} \sum_i \nabla_i^2 - \sum_{iI} \frac{Z_I e^2}{|\mathbf{r_i} - \mathbf{R_I}|} + \frac{e^2}{2} \sum_{i \neq j} \frac{1}{|\mathbf{r_i} - \mathbf{r_j}|} + \frac{e^2}{2} \sum_{I \neq J} \frac{Z_I Z_J}{|\mathbf{R_I} - \mathbf{R_j}|} \tag{2.3}$$

where $\mathbf{r} = \{r_1, r_2, r_3 .....r_n\}$ are electron coordinates and $\mathbf{R} = \{R_1, R_2, R3, ...R_N\}$ are the nuclear coordinates. The first two term represent the kinetic energy of the nuclei and electrons. The third term corresponds to electron-nucleus Coulomb interaction. The last two terms are the electron-electron and nucleus-nucleus Coulomb interaction. The Hamiltonian $\hat{H}$ acts on many particle wave function $\Psi(\mathbf{R}, \mathbf{r})$ which depends on both nucleus and electron coordinates.

Due to heavy mass, nuclei moves much slower than electrons. Hence nuclei can be considered as fixed particles and electrons are moving relative to them, electrons can respond to nuclei motions almost instantaneously. This is known as Born-Oppenheimer (BO) approximation [105]. As a consequence of BO approximation the first term in equation 2.3, kinetic energy of nuclei is considered as zero and the fifth term will be a constant function. The BO approximation decouples the nuclear and electronic coordinates and allows one to solve the Schrödinger equation for the wave functions of electrons alone which are moving in an external potential $\hat{V}_{eN} \equiv \hat{V}_{ext}$. Under BO approximation the modified Hamiltonian can be written as

$$\hat{H} = \hat{T}_e + \hat{V}_{ee} + \hat{V}_{ext} \tag{2.4}$$

BO approximation simplifies the many-body problem into a many electron problem, but still difficult to find an exact solution. The first stepping stone towards DFT is the Thomas-Fermi (TF) model [106, 107]. In this model the total electronic energy is expressed in terms of the electron density $\rho(\mathbf{r})$ rather than the wave function. TF model used a heuristic approach, in which the various contributions towards the total electronic energy such as kinetic energy, exchange and correlations were taken from the homogeneous electron gas. The approximation used in TF model is so crude and hence it fails in many cases, especially in the cases of solids and molecules, where TF model fails to describe the bonding between the atoms [108]. Though the TF model fails to describe the properties of solids, it paves the way towards the modern DFT by introducing the concept of electron density.

2.1.2 The Hohenberg-Kohn theorems and Kohn Sham equation

The basis of the modern DFT is Hohenberg-Kohn (HK) theorem [109–111]. Hohenberg and Kohn proved that the total energy of an electron gas is a unique functional of electron density. The minimum value of the total energy functional is the ground state energy and the corresponding density is the single particle ground state density. Once the ground state electron density is known all other properties of the system can be computed. Pauli's exclusion principle demands that the many-electron wave function should be anti-symmetric. The anti-symmetry of the wave function keeps the electrons of same spin spatially apart and thus reduce the Coulomb energy of the electronic system. This reduction in energy of electronic system due to anti-symmetry of wave function is called exchange energy [112]. The exchange energy is computed straightforwardly using Hartree-Fock method [110]. The electrons having opposite spin can also be spatially separated at the expense of increasing the kinetic energy. In this case the Coulomb energy of system is reduced at the cost of increasing kinetic energy of electrons, this is known as correlation energy [112]. The difference between the many-body electronic energy and energy computed in Hartree-Fock methods will give the correlation energy.

Though HK theorem reduces the complexity of many-body problem using electron density as a basic variable, still there is no direct way to deduce the exact kinetic energy from the electron density. This limitation is overcome in Kohn-Sham (KS) approach [110, 113]. The Kohn and Sham put HK theorem into practical usage, in this formulation the interacting many-body electronic system mapped onto a fictitious system of non-interacting electrons moves in an effective potential due to all other electrons.

In order to understand the Kohn and Sham formulation, we can re-write the many-electron Hamiltonian (equation 2.4) in term of its corresponding energy functional

$$E[\rho] = T_e[\rho] + E_{ee}[\rho] + E_{ext}[\rho] \tag{2.5}$$

where $T_e[\rho] = \langle\Psi(\rho)|\hat{T}|\Psi(\rho)\rangle$ is the kinetic energy of interacting system; $E_{ee}[\rho] = \langle\Psi(\rho)|\hat{V}_{ee}|\Psi(\rho)\rangle$ is the Coulomb repulsion energy and $E_{ext}[\rho]$ is the energy functional corresponding to electron-ion interaction. To have an intuitive understanding on how exchange-correlation functional is introduced, the equation 2.5 is re-written by adding and subtracting the non-interacting kinetic energy functional $T_0[\rho]$ and Hartree functional $E_H[\rho]$ as follows

$$\begin{aligned} E[\rho] &= T_e[\rho] + T_0[\rho] - T_0[\rho] + E_{ee}[\rho] + E_H[\rho] - E_H[\rho] + E_{ext}[\rho] && (2.6) \\ &= T_0[\rho] + E_H[\rho] + E_{ext}[\rho] + \{T_e[\rho] - T_0[\rho] + E_{ee}[\rho] - E_H[\rho]\} && (2.7) \end{aligned}$$

Here the energy functional remains the same. The basic idea in Kohn and Sham formulation is that, if one can find a non-interacting system of same electron density as of interacting system, then the kinetic energy of non-interacting system can be calculated exactly using the following equation [110]

$$T_0 \quad = \quad \frac{-\hbar^2}{2m}\sum_{i}^{N_s}\langle\Phi|\nabla^2|\Phi\rangle \tag{2.8}$$

where Φ is used to denote the the wave-function of non-interacting particles instead of Ψ, and this will be usually represented as the Slater determinant of occupied orbitals

$$\Phi = \frac{1}{\sqrt{N_s!}}SD[\phi_1(\mathbf{r}1)\phi_2(\mathbf{r}2).....\phi_{N_s}(\mathbf{r}_{N_s})] \tag{2.9}$$

and yield the electron density as

$$\rho(\mathbf{r}) = \sum_{i}^{N_s}\big|\phi_i(\mathbf{r})\big|^2 \tag{2.10}$$

KS formulation again brings back the wave function into picture to calculate the kinetic energy. The kinetic energy computed in this formalism is not the exact kinetic energy of interacting system, which is due to the fact that the true many-body wave function is not a Slater determinant [110]. The correlation term in kinetic energy is not take into account in this scheme. The other terms in equation 2.7 are Hartree energy, $E_H(\rho) = \int \frac{\rho(\mathbf{r})\,\rho(\mathbf{r}')}{|\mathbf{r}-\mathbf{r}'|}d\mathbf{r}\,d\mathbf{r}'$, and the Coulomb repulsion in KS scheme can be written as, $E_{ee}(\rho) = \langle\Phi|\hat{V}_{ee}|\Phi\rangle$. Advantage of the re-arrangement of equation 2.7 is that the first three terms can be calculated exactly. The quantity inside the curly bracket in equation 2.7, contains the effects of correlation contribution to kinetic energy, $\Big(T_c(\rho) = T_e(\rho) - T_0(\rho)\Big)$, exchange energy, $\Big(E_X(\rho) = \langle\Phi|\hat{V}_{ee}|\Phi\rangle - E_H(\rho)\Big)$ and the Coulombic correlation $\Big(E_C(\rho) = \langle\Psi(\rho)|\hat{V}_{ee}|\Psi(\rho)\rangle - \langle\Phi|\hat{V}_{ee}|\Phi\rangle = \langle\Psi(\rho)|\hat{V}_{ee}|\Psi(\rho)\rangle - E_H(\rho) - E_X(\rho)\Big)$, and which is known as exchange correlation energy $E_{XC}(\rho)$. The $E_{XC}(\rho) = \langle\Psi(\rho)|\hat{T}+\hat{V}_{ee}|\Psi(\rho)\rangle - \langle\Phi|\hat{T}+\hat{V}_{ee}|\Phi\rangle$, will account for the difference between the exact ground state energy and energy computed in Hartree-Fock approximation, and using the non-interacting kinetic energy $T_0[\rho]$. Now in KS formulation the energy functional and its corresponding Hamiltonian (KS-Hamiltonian) can be written as

$$E[\rho] = T_0[\rho] + E_H[\rho] + E_{ext}[\rho] + E_{XC}[\rho] \tag{2.11}$$

$$\hat{H}_{KS} = \hat{T}_0 + \hat{V}_H(\mathbf{r}) + \hat{V}_{ext}(\mathbf{r}) + \hat{V}_{XC}(\mathbf{r}) \tag{2.12}$$

where $\hat{T}_0$ is the kinetic energy operator of a single electron, $\hat{V}_H(\mathbf{r})$ is the Hartree potential given by $\hat{V}_H(\mathbf{r}) = \frac{\delta E_H[\rho(\mathbf{r})]}{\delta\rho(\mathbf{r})} = \int \frac{\rho(\mathbf{r}')}{|\mathbf{r}-\mathbf{r}'|}d\mathbf{r}'$. The exchange-correlation potential is given by $\hat{V}_{XC}(\mathbf{r}) = \frac{\delta E_{XC}[\rho(\mathbf{r})]}{\delta\rho(\mathbf{r})}$.

Only the minimum value of KS functional has physical meaning. At the minimum, the KS energy functional is equal to the ground state energy of the system [112]. One has to find out a set of wave functions ϕ_i which minimize the KS energy functional. These wave functions can be obtained from the self consistent solution to the KS equations

$$\left[-\frac{\hbar^2}{2m}\nabla^2 + V_{KS}(\mathbf{r})\right]\phi_i(\mathbf{r}) = \epsilon_i\phi_i(\mathbf{r}) \tag{2.13}$$

where $V_{KS}(\mathbf{r}) = V_{ext}(\mathbf{r}) + V_H(\mathbf{r}) + V_{XC}(\mathbf{r})$, ϕ_i is the wave function of electronic state i, and ϵ_i is the KS eigenvalue. Both $V_H(\mathbf{r})$ and $V_{XC}(\mathbf{r})$ depends on charge density, which in turn depends on ϕ_i (equation 2.10). Hence the KS equation must be solved in a self consistent manner. It is worth to note that the KS eigenvalues are not the energies of single particle energy states, and total energy of electronic system is not the sum of the eigenvalues of all occupied states $E_{tot} \neq \sum_i^{occ.} \epsilon_i$. Similarly the KS wave-functions ϕ_i are not single particle wave-functions of electrons.

In KS theory, the many body effects are introduced through the exchange-correlation (XC) functional. But the exact functional form of XC functional is not known up to now, certain approximations have been made to compute XC functional, which works reasonably well for most of the solid state systems. The following sections briefly discuss the most popular and widely used XC functionals.

2.1.3 Local Density Approximation (LDA)

LDA [114–116] is the simplest and most widely used approximation to compute the XC functional. In LDA, the XC functional is constructed by assuming that the XC energy at a point $\mathbf{r}$ is equal to the XC energy of a homogeneous electron gas (HEG) of the same density at the point $\mathbf{r}$. The total XC functional can be written as

$$E_{XC}^{LDA}[\rho] = \int \rho(\mathbf{r})\varepsilon_{XC}^{homo}(\rho(\mathbf{r}))d\mathbf{r} \tag{2.14}$$

In this scheme, the exchange part of the functional is expressed as the exact expression of HEG. The analytic representation of correlation varies in different versions, of which most popular one is Ceperly-Alder (CA) [114] . Other popular versions are Vosko-Wilk-Nusiar (VWN) [117], Perdew-Zunger (PZ) [116] and Perdew-Wang (PW) [118].

2.1.4 Generalized Gradient Approximation (GGA)

LDA works well for the systems where the electron density varies slowly. In the real systems, the spatial distribution of electron density is not homogeneous and it varies rapidly. In such situation the XC energy of inhomogeneous system varies significantly from that of HEG. The above limitation has been overcome in GGA [119, 120] , in which the XC functional is calculated by taking the contributions from both electron density $\rho(\mathbf{r})$ and its gradient $\nabla\rho(\mathbf{r})$. In GGA, the XC energy can be expressed as

$$E_{XC}^{GGA}[\rho] = \int \rho(\mathbf{r})\varepsilon_{XC}^{homo}\Big(\rho(\mathbf{r}), \nabla\rho(\mathbf{r})\Big)d\mathbf{r} \tag{2.15}$$

As in LDA, there exists many flavors of GGA, the three most widely used GGAs are proposed by Becke (B88) [121], Perdew-Wang (PW91) [120] and Perdew, Burke and Ernzerhof (PBE) [122]. Generally GGA works better than LDA and predicts accurately the bond length, binding energy and lattice constant, especially for system with rapidly varying charge density. In certain cases (some ionic crystal, layered materials) GGA over corrects the LDA results and overestimate the lattice parameters, which deviates from the experimental data. There are no universal XC functionals, the choice of XC has to be made carefully and judiciously depending upon the physical problem.

2.1.5 Solving Kohn-Sham equations

The KS equation (equation 2.13) must be solved self consistently to obtain the exact density and energy of a ground state system, this is usually done using some self-consistent iteration schemes. The procedure is to start with initial guess of charge density, which is generally constructed from the superposition of atomic electron density. Once the initial charge density is available the effective KS potential, $V_{KS}(\mathbf{r})$ can be calulated, and then solve KS equation to obtain the single particle energies and wave-functions. Now calculate the new charge density from the KS wave-function obtained, and check the self-consistency condition. If self-consistency is not achieved, mix the new density obtained with old one and repeat the cycle until the self-consistency is achieved. Once self-consistency is achieved various physical quantities such as total energy, force, stress, electron density of states and band structure etc., can be calculated.

At this level, to solve the KS equation (equation 2.13), one has to make certain choices, *1. To write a wave-function for infinite number of electrons in the system moving in a static potential; 2. To represent single particle KS orbitals; 3. To represent electron-ion interaction*$\big(V_{ext}(\mathbf{r})\big)$*;*

2.1.5.1 *periodic boundary conditions - Bloch's theorem*

In KS scheme the many-electron problem is mapped into a single electron problem and exchange-correlation effects are treated with certain approximations. Still it is a tedious job to solve KS equation for a non-interacting system which contains infinite number of electrons. System containing a large number of atoms will have infinite number of electrons, therefore wave function must be calculated for each of these electrons in the system. This problem can be tackled with the help of Bloch's theorem (more details can be found in any elementary solid state physics book [123, 124]).

Bloch's theorem maps the calculation of wave-function for all electrons in an infinite solid onto a calculation of wave-function for a finite number of electrons in the unitcell. It is not necessary to calculate the electronic wave-function everywhere in space. It is sufficient to know the solution in the unitcell, and it differs in the neighboring cell by a phase factor $e^{i\mathbf{k}.\mathbf{a}}$ due to periodic boundary condition [110]. In principle the calculation needs to be done at infinite number of **k** points in the first Brillouin zone (BZ). Computationally, it is forbidden to do the calculations with infinite **k** points. This can be tackled using the **k** point sampling techniques. Many physical properties, such as, density of states, band structure are calculated by integrating over the entire BZ. Such integrations can be performed by summing over finite number of **k** points in the BZ, and they are called **k** point mesh. Some special techniques have been made to choose the special **k** points in the BZ appropriately, and thereby increases the computational efficiency, among them Monkhorst-Pack [125] and Chadi-Cohen [126] schemes are widely used.

2.1.5.2 *Choice of basis set- To represent the single particle KS orbitals*

To solve the KS equation (equation 2.13), a mathematical description for the KS orbital ϕ_i is required. Most convenient method is express the wave-function in terms of Fourier expansion using a plane wave basis set.

$$\phi_i^{(k)} = \frac{1}{\sqrt{\Omega}} \sum_{\mathbf{G}=0}^{\infty} C_{ik}(\mathbf{G})\, e^{i(k+\mathbf{G}).\mathbf{r}} \tag{2.16}$$

where Ω is the supercell volume, **G** is the reciprocal lattice vector and k is the wave vector in the first Brillouin zone. The plane wave basis set is mostly preferred due to its mathematical simplicity and it spans the entire Hilbert space. The practical advantage of plane wave basis set is that it can be easily implemented into a computational code, and also the evaluation of $H\phi_i$ becomes exceedingly efficient using Fast Fourier Transforms. In principle one has to use an infinite basis set to represent the electronic wave functions. However, in practice, we can use a finite basis set. The plane wave with small kinetic energy is more important than that of plane waves with large kinetic energy. Hence the plane wave basis set can be truncated to incorporate only those plane waves whose energy is less than that of a cut-off value (E_{cut}). The size of basis set affects the accuracy of calculation, hence series of convergence test has to be done to fix the cut-off energy. Apart from the plane wave basis set, there are certain other choices to represent the electronic wave-functions such as, *extended basis sets, localized basis sets, mixed basis set and Augmented basis set,* the details can be found in reference [110].

2.1.5.3 *Pseudo-potential methods - To represent the electron-ion interaction*

The electrons attached to the atoms can be classified into core electrons and valence electrons. The core electrons are tightly bound to the nuclei and do not participate in bonding. Therefore most of the physical properties of solids depend on valence electron configuration than the core-electron. The core states are localized in the vicinity of the nucleus, hence valence states shows rapid oscillations near the core region to maintain the orthogonality conditions, which is required by the exclusion principle. An extremely large number of plane waves are required to expand the core orbitals and to follow the rapid oscillations of valence electrons near the core region [112]. If we treat all the electrons explicitly, the computational effort increases enormously. The above difficulty is overcome by pseudo-potential method [127], which allows to use a smaller basis set to expand the electronic wave functions. In pseudo-potential method, we eliminate the core-core and core-nucleus interactions and replace the strong Coulomb potential with a much weaker *pseudo-potential (PP).* This models the core-valence and valence-nucleus interactions; the valence electron wave-functions, which oscillates rapidly near the core region are described by a *pseudo-wave-function* with significantly fewer nodes. Figure 2.1 illustrates the concept of pseudization. The pseudo-potential $\left(V_{pseudo}\right)$ matches with all electron potential $\left(V\right)$ beyond the cutoff radius (r_c) and it removes the singularity of V near to origin. The upper part shows that all electron wave-function Ψ and its pseudo counter part Ψ_{pseudo}, which is smooth and nodeless near the core region.

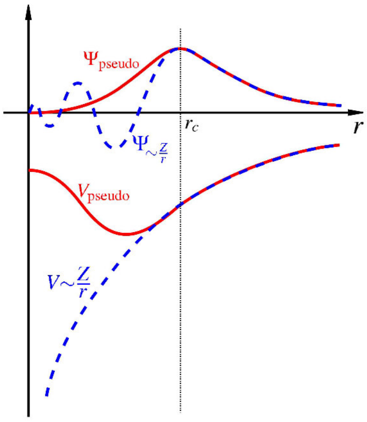

Figure 2.1 – The schematic representation of all electron potential and pseudo potentials, and their corresponding wave-functions [128].

There are different kinds of *PPs,* which have been implemented in DFT codes, among them most popular *PPs* are norm-conserving, ultrasoft and projector augmented wave (PAW) [129, 130]. Detailed description of these *PPs* can be found elsewhere [110, 111]. In the present study, only PAW potential is used, which has been employed in Vienna *Ab initio* Simulation Package (VASP) [131].

2.1.6 Lattice dynamics using *ab initio* methods

In this thesis, chapter 3 discusses the dynamic stability of different graphite structure using lattice dynamics calculations. The lattice dynamics properties can be obtained either from linear response calculations or from frozen phonon method within *the ab initio* framework. A brief discussion of the above two method is given below.

1) Hellmann-Feynman theorem and Density Functional Perturbation Theory (DFPT) : One has to compute the first and second derivative of Born-Oppenheimer energy surface to obtain the equilibrium geometry and vibrational frequencies of the system. The above task can be accomplished using Hellmann-Feynman theorem [132, 133] , which states that the first derivative of the eigenvalue of a Hamiltonian,

H_λ, depends on parameter λ, is given by the expectation value of the derivative of the Hamiltonian;

$$\frac{\partial E_\lambda}{\partial \lambda} = \left\langle \Psi_\lambda \middle| \frac{\partial H_\lambda}{\partial_\lambda} \middle| \Psi_\lambda \right\rangle \tag{2.17}$$

where Ψ_λ is the eigenfunction of H_λ corresponding to the eigenvalue E_λ ($H_\lambda \Psi_\lambda = E_\lambda \Psi_\lambda$). In BO approximation the electronic Hamiltonian (H_{BO}) depends on ionic co-ordinates parametrically.

$$H_{BO} = -\hbar^2 \sum_I \frac{\nabla_I^2}{2M_I} - \frac{\hbar^2}{2m} \sum_i \nabla_i^2 - \sum_{iI} \frac{Z_I e^2}{|\mathbf{r_i} - \mathbf{R_I}|} + \frac{e^2}{2} \sum_{i \neq j} \frac{1}{|\mathbf{r_i} - \mathbf{r_j}|} + \frac{e^2}{2} \sum_{I \neq J} \frac{Z_I Z_J}{|\mathbf{R_I} - \mathbf{R_j}|} \tag{2.18}$$

Where the last term in the equation 2.18 is electrostatic interaction between the ions (E_I) and it is essential in the total energy calculations. E_I is only a classical additive in the electronic structure theory. The force acting on I^{th} nucleus in the electronic ground state can be written as [134]

$$\mathbf{F}_I = -\frac{\partial E(\mathbf{R})}{\partial \mathbf{R}_I} = -\left\langle \Psi(\mathbf{R}) \middle| \frac{\partial H_{BO}(\mathbf{R})}{\partial \mathbf{R}_I} \middle| \Psi(\mathbf{R}) \right\rangle \tag{2.19}$$

where $\Psi(\mathbf{r}, \mathbf{R})$ is the electronic ground state wave function of the BO Hamiltonian, which depends on $\mathbf{R}$ via electron-ion interaction, that couples to the electronic degrees of freedom only through electron charge density. Hence in this case the Hellmann-Feynman theorem can be written as

$$\mathbf{F}_I = -\int \rho \frac{\partial V_{ext}}{\partial \mathbf{R}_I} d\mathbf{r} - \frac{\partial E_I(\mathbf{R})}{\partial \mathbf{R_I}} \tag{2.20}$$

where ρ is the ground state electronic charge density corresponding to the nuclear configuration $\mathbf{R}$ and $V_{ext} = \sum_{iI} \frac{Z_I e^2}{|\mathbf{r_i} - \mathbf{R_I}|}$ is the electron-ion interaction. The force constant matrix (Hessian of BO potential energy surface) is obtained by taking the second derivative of Hellmann-Feynaman forces (equation 2.20) with respect to the nuclear co-ordinates,

$$\frac{\partial^2 E(\mathbf{R})}{\partial \mathbf{R_I} \partial \mathbf{R_J}} \equiv -\frac{\partial \mathbf{F_I}}{\partial \mathbf{R_J}} = \int \frac{\partial \rho}{\partial \mathbf{R_J}} \frac{\partial V_{ext}}{\partial \mathbf{R_I}} d\mathbf{r} + \int \rho \frac{\partial^2 V_{ext}}{\partial \mathbf{R_I}\, \partial \mathbf{R_J}} + \frac{\partial^2 E_I(\mathbf{R})}{\partial \mathbf{R_I}\, \partial \mathbf{R_J}} \tag{2.21}$$

The equation 2.21 states that the calculation of force constant matrix requires the knowledge of ground state electronic charge density ρ and its linear response to nuclear distortion $\frac{\partial \rho}{\partial \mathbf{R_I}}$ [134]. Applicability of this method extends to many other fields depending upon the nature of perturbations. A perturbation in ionic co-ordinates, magnetic field, lattice vectors and electric field will give the responses as force constant matrix, NMR frequency, elastic constants and di-electric constants respectively. Even-though DFPT calculations are efficient and accurate, it is computationally demanding in the case of many complex systems.

2) Frozen phonon method: This is a primitive method, here the force constants are determined by explicitly displacing the atoms from their equilibrium configurations and compute the force on every atom using Hellmann-Feynman theorem. This method is quicker and easy to implement, hence widely used. The main drawback of this method is that, displacing the atoms creates the forces not only between the atoms within the unitcell but also with their periodic images. To avoid this, calculations has to be done with big supercells which is computationally expensive [134].

2.2 Molecular dynamics

MD is a technique to study the time evolution of a system of particles. In order to use MD methods one has to define a set of rules that governs the interaction between the atoms in the system. These interaction can be derived either from *ab initio* calculations (*ab initio* MD) or from empirical potentials (classical MD). In *ab initio* MD, though the interaction between the atoms are derived quantum mechanically, the atomic motion still obeys the laws of classical mechanics. *Ab initio* MD simulations are computationally demanding, and it is applicable to systems containing less than ∼100 atoms and simulations for durations less than ∼100 ps. Because of these limitations classical MD simulation scheme is adapted in the present work.

2.2.1 Basics of MD simulations

In MD simulations, the time evolution of a system of interacting particle is obtained by solving the equation of motion [135, 136] ,

$$\mathbf{F_i} = m_i \mathbf{a}_i = m_i \frac{d^2 \mathbf{r_i}}{dt^2}, \tag{2.22}$$

where $\mathbf{F_i}$ is the force acting on i^{th} atom due to the interaction with other particle in the system; m_i, $\mathbf{r_i}$ and $\mathbf{a}_i$ are the mass, position vector and acceleration of the particle i respectively, and t stands for the time. The force $\mathbf{F}_i$ acting on the particle is obtained from the negative gradient of the total potential energy of the system $U(\mathbf{r_1}, \mathbf{r_2},, ...\mathbf{r_N})$,

$$\mathbf{F_i} = -\nabla_i U(\mathbf{r_1}, \mathbf{r_2}, ...\mathbf{r_N}) \tag{2.23}$$

In order to solve the equation 2.22 the information about the total potential energy of the system is required. Hence before starting MD simulation one has to choose a proper interatomic potential which is capable of describing the system properties reasonably well. Once the initial conditions (eg. initial positions and velocities of all particles) and interatomic potential is defined the equations of motion can be solved numerically to obtain the position $\big(\mathbf{r}(t)\big)$ and velocities $\big(\mathbf{v_i}(t)\big)$ of all particles as a function of time. MD does not require any prior knowledge of the system and it is a fully deterministic method; state of the system at any future time can be predicted from its current state.

2.2.2 Work-flow in MD simulations

MD simulations are analogous to real experiments in many aspects. In real experiments, first we prepare a sample of interest. Thereafter this sample will be connected to an instrument say for example with a thermostat or a high pressure diamond anvil cell to maintain the sample under a certain temperature and pressure. Once the sample is equilibrated into a desired value, various physical quantities can be measured. MD simulations also follows the similar scheme. A typical MD simulation consists the following steps: [136–138]

2.2.2.1 A. Initialize the system

A1. Create a simulation cell: Before starting the simulation one has to set up a simulation cell of the system of interest. The particles are arranged inside a simulation cell of size $S_x\times S_y \times S_z$. It is also possible to set up a simulation cell with non-orthogonal axes. In classical MD, there are three types of boundary conditions to deal with surface atoms, such as, free, fixed and periodic. Free boundary conditions works well for molecules and nano-clusters in vacuum. For a continuous medium this does not work, the atoms are left hanging on the surface and creates surface effects. In fixed boundary condition the atoms at boundary are fixed, hence it is completely un-physical, sometimes it can be used with large sacrificial regions. The PBC are most popular and widely used, in which the simulation cells are infinitely repeated across the borders. PBC conditions helps to study the properties of a bulk system with lesser number of atom in such a way that the atoms experiences the same force as if they are inside the bulk. PBC eliminates the surface effects, at the same time it will cause artificial interaction across the cell borders. To avoid the above problem a proper convergence test needs to be done to fix the cell size. More details can be found in the references [136–138].

A2. Provide the initial position and velocities of the particle: Once a simulation cell is defined, one has to assign the initial positions and velocities to the particles. The particles are arranged on a lattice as per the crystal structure. This will be the ground state structure (T = 0 K) of the material with the given potential. Initial velocities are taken either zero or from a Maxwell-Boltzmann distribution. At ground state the net force acting on the particles would be zero because of symmetry, therefore atoms would sit indefinitely at their equilibrium position. Under this situation equation of motion won't do anything different apart from evolving exactly the same way. To avoid this, some randomization must be done in the starting sample [139]. This can be achieved in the following way. 1) small random displacements are added to lattice positions; in this case special care has to be taken to avoid the overlap of atomic cores. 2) The initial velocities are taken from the Maxwell distribution at a given temperature. In doing so, the system will have a linear momentum corresponding to the translational motion, this is eliminated by subtracting the linear momentum component from the velocity of each particle.

A3. Select a time step: In MD, the equation of motion is solved using time integration algorithms. All these algorithms are based on finite difference method, where time is discretized on a grid and the time step $\triangle t$ is the distance between the grid. If one knows the position and its derivative at time t the integrating algorithm will give the same quantities at later time $t + \triangle t$ [139]. The common and important concept in various algorithms is time step $\triangle t$. If time step is too large particles will move too far and lead to instability, reversely for a small time step it will not be efficient due to long simulation times. To ensure the numerical stability and conservation of energy, one has to choose a time step which is one order smaller than that of the fastest process in the system. A practical rule-of-thumb is that the particles should not move more than $\frac{1}{20}$th of the nearest neighbour distances. In practice, the time step should be kept as $\triangle t < 4\, fs$, to ensure the stability of algorithm [136, 138].

2.2.2.2 B. Integrate Newton's equations of motion

B1. Selecting the appropriate interatomic potential: To compute the force between the atoms using equation 2.23 an interatomic potential function is required. The accuracy of the MD simulation results depends on the quality of interatomic potential used. While selecting a potential, one should consider the following characteristic features; 1) accuracy, 2) transferability (capable of computing various other properties for which it was not fit) and 3) computational speed [140]. The potential energy of a system of N-particle can be expressed as [135, 139],

$$U(\mathbf{r_1},\, \mathbf{r_2},....\mathbf{r_N}) = \sum_i U_1(\mathbf{r_i}) + \sum_i \sum_{i<j} U_2(\mathbf{r_i}, \mathbf{r_j}) + \sum_i \sum_{i<j} \sum_{j<k} U_3(\mathbf{r_i}, \mathbf{r_j}, \mathbf{r_k}) + ... \quad (2.24)$$

The first term U_1 represents the external potential and depends on the each particles co-ordinates. The second term U_2 is the pair-potential term which depends only on the distance between the two atoms. The third term U_3 will come into picture when the interaction between the two atoms is modified with the presence of a third atom. The clause $i < j$ (for two body) and $i < j < k$(for three body) is used to avoid the double counting between the bonds. Based on above expression the potentials can be broadly classified as pair-potential (contains only U_2 term) and many-body potential (U_3 and higher terms are incorporated).

Pair-potentials: The most commonly used pair-potential to model the properties of a simple system is Lennard-Jones (LJ) potential, and its functional form is

$$U(\mathbf{r}_{ij}) = 4\epsilon\Big[\Big(\frac{\sigma}{\mathbf{r}_{ij}}\Big)^{12} - \Big(\frac{\sigma}{\mathbf{r}_{ij}}\Big)^{6}\Big] \quad (2.25)$$

where ϵ is the depth of the potential energy well and its value is equal to $2^{\frac{1}{6}}\sigma$ for the equilibrium particle separation. The first term represents the repulsion between the atoms when they are brought closer to each other. The second term is the long range attractive contribution. The LJ potential gives good description for van der Waals interaction in inert gases and molecular systems. The functional forms of other commonly used pair potentials in MD simulations are listed below in table 2.1 [140]

Table 2.1 – The functional form and applicability of commonly used pair-potentials in MD simulations

Name	Functional form	Applicability
Hard sphere	$U(\mathbf{r}_{ij}) = \begin{cases} \infty & \mathbf{r_{ij}} < \mathbf{r}_0 \\ 0 & \mathbf{r_{ij}} > \mathbf{r}_0 \end{cases}$	Theoretical investigation of some idealized problems
Coulomb	$U(\mathbf{r}_{ij}) = \frac{q_i q_j}{\mathbf{r}_{ij}}$	Coulomb interaction between the charged particles
Morse	$U(\mathbf{r}_{ij}) = \epsilon\left[e^{-2\alpha(\mathbf{r_{ij}}-\mathbf{r_0})} - 2e^{-\alpha(\mathbf{r_{ij}}-\mathbf{r_0})}\right]$	More suitable when attractive interaction comes from a chemical bond
Buckingham	$U(\mathbf{r}_{ij}) = Ae^{-\frac{\mathbf{r_{ij}}}{\mathbf{R_{BM}}}} - \frac{B}{\mathbf{r_{ij}^6}}$	Suitable for simulating the bombardment of energetic ions or atoms

The pair potentials is used to describe the properties of many systems accurately. However, they possess severe limitations, notably, pair-potentials do not have environment dependence and hence they wrongly predict the bond energies for many transition metals. The vacancy formation energies of many metals are severely overestimated in pair-potential based calculations. Pair-potentials also fails to describe the deviation of elastic constants from the Cauchy relations in cubic crystals ($C_{12} = C_{44}$). All these limitations are due to the fact that many-body effects are not incorporated in pair-potentials. The above discrepancies were resolved to some extent with the development of embedded atom (EAM) method [141, 142]. The main attraction of EAM based potential is that it can explain the variation of bond strength with coordination. In this thesis EAM potential is not used, hence a detailed description of it is not provided here. More details can be found in the references [141–143]

Potentials for covalently bonded systems: The present thesis focus on structural, vibrational and thermal properties of different 2D materials, where the predominant bonding is covalent in nature. The Stillenger-Weber (SW) potential [144] is the first successful potential constructed to model the covalent bonding in diamond lattice (eg. Si, Ge, C and GaAs). In SW potential the total system potential energy can be written as

$$U(\mathbf{r_1}, \mathbf{r_2}, ...\mathbf{r_N}) = \sum_{i} \sum_{i<j} U_2(\mathbf{r_i}, \mathbf{r_j}) + \sum_{i} \sum_{i<j} \sum_{j<k} U_3(\mathbf{r_i}, \mathbf{r_j}, \mathbf{r_k}) \tag{2.26}$$

The two body term is

$$U_2(\mathbf{r}_{ij}) = \begin{cases} A\Big(B\mathbf{r_{ij}}^{-\mathbf{p}} - \mathbf{r_{ij}}^{-\mathbf{q}}\Big) exp\Big[\frac{c}{(\mathbf{r_{ij}} - \mathbf{r_c})}\Big] & \mathbf{r_{ij}} < \mathbf{r}_c \\ 0 & \mathbf{r_{ij}} > \mathbf{r}_c \end{cases}$$

Where A, B, p and q are constants. The first term is very similar to Lennard-Jones form, and the second term is a cutoff function that smoothly terminate the potential at a distance $\mathbf{r_c}$. The three body term models the angular dependence and can be written as the sum of functions of each of the three angles of a triplet i, j, k.

$$U_3(\mathbf{r_{ij}}, \mathbf{r_{ik}}, \mathbf{r_{jk}}) = h(\mathbf{r_{ij}}, \mathbf{r_{ik}}, \theta_{jik}) + h(\mathbf{r_{ji}}, \mathbf{r_{jk}}, \theta_{ijk}) + h(\mathbf{r_{ki}}, \mathbf{r_{kj}}, \theta_{ikj})$$

where θ_{jik} is the angle centered on atom i and h is a function with parameters λ, γ, β:

$$h(\mathbf{r_{ij}}, \mathbf{r_{ik}}, \theta_{jik}) = \lambda exp\left[\frac{\gamma}{\mathbf{r_{ij}} - \mathbf{r_c}} + \frac{\gamma}{r_{ik} - \mathbf{r_c}}\right] (cos(\theta_{jik}) - \beta)^2$$

For tetrahedral structure the value of $\beta = cos(109.47^o) = -\frac{1}{3}$. The angle-j term ($h_{ijk}$) and angle-k term ($h_{ikj}$) can be computed by permuting the indices accordingly. The parameters used in the original study of Stillinger and Weber were obtained by fitting the radial distribution function, melting temperature to the experimental data by assuming that diamond lattice is the lowest energy structure [144]. The original SW parameters are, $A = 7.049556277$, $B = 0.6022245584$, $p = 4$, $q = 0$, $r_c = 1.80$, $\lambda =$

21, $\gamma = 1.20$ [144]

SW potential is popular because of its simplicity and fairly good description of Si in diamond lattice. However, it possess severe limitations such as transferability problem. The three body term will explain only one equilibrium configuration (angle 109.47°). The SW potential cannot give a proper description in the case of carbon, that have three equilibrium configurations with angles 180°, 120° and 109.47°. Later, more realistic potentials were developed to explain the properties of group IV elements (Si, Ge and C) based on the concept of bond-strength dependence on bonding environment (known as bond order potentials), among them the most popular ones are Tersoff [145] potential (for Si& Ge) and Brenner-potential[146] for C. In this thesis long range bond order potential (LCBOP) [147], Tersoff potential [148] and reactive empirical bond order (REBO) [149] potential are used to model graphene, 2D h-BN and molybdenum di-sulphide (MoS_2) respectively. The detailed descriptions will be given at respective chapters.

B2. Solving the equation of motion and determining the new position and velocity: In MD, to integrate the equation of motion several numerical algorithms have been developed. The important ones are Verlet, leapfrog Verlet, velocity Verlet, and Gear predictor corrector algorithms [135, 136]. The objective of all the above algorithms is to compute the position and velocity at a time $t + \triangle t$ from its current state (at time t). A good MD algorithm requires the following features, 1) robustness, 2) fast, 3) take little memory 4) allows longer time step 5) conserve energy, and 6) time-reversibility [137]. In the present studies the velocity Verlet algorithm [150, 151] is used because of its robustness, ease of implementation and its superior energy conservation properties [135, 136]. Verlet algorithm is derived from the two Taylor expansion (third order) of $\mathbf{r}(t)$, one backward and other forward. Let v(velocity), a(acceleration) and b are the first, second and third order derivative of the $\mathbf{r}(t)$ then,

$$\mathbf{r}(t + \triangle t) = \mathbf{r}(t) + \mathbf{v}(t)\,\triangle t + \mathbf{a}(t)\,\frac{\triangle t^2}{2} + \mathbf{b}(t)\,\frac{\triangle t^3}{6} + o(\triangle t^4)$$

$$\mathbf{r}(t - \triangle t) = \mathbf{r}(t) - \mathbf{v}(t)\,\triangle t + \mathbf{a}(t)\,\frac{\triangle t^2}{2} - \mathbf{b}(t)\,\frac{\triangle t^3}{6} + o(\triangle t^4)$$

Adding above two equation and re-arranging leads to

$$\mathbf{r}(t + \triangle t) = 2\mathbf{r}(t) - \mathbf{r}(t - \triangle t) + \mathbf{a}(t)\,\triangle t^2 + o(\triangle t^4)$$

The algorithm essentially does $\{\mathbf{r}(t),\, \mathbf{a}(t),\, \mathbf{r}(t - \triangle t)\} \rightarrow \{\mathbf{r}(t + \triangle t),\, \mathbf{a}(t + \triangle t)\}$. The $\mathbf{a}(t)$ can be calculated from the force divided by mass, which in turn is a function of $\mathbf{r}(t)$. $\mathbf{a}(t) = -\frac{1}{m}\nabla U(\mathbf{r}(t))$, at every instant compute the force, which makes the system to evolve. The truncation error of the algorithm is of the order of $\triangle t^4$. One drawback of Verlet algorithm is that velocities are not directly generated, which is required to compute the kinetic energy of the system and it is mandatory to check the energy conservation criteria. The velocities can be obtained from the positions as follows

$$v(t) = \frac{\mathbf{r}(t + \triangle t) - \mathbf{r}(t - \triangle t)}{2\triangle t}$$

The error involved in the above expression is of the order of $\triangle t^2$ rather than $\triangle t^4$. To overcome the above limitation, another form of Verlet algorithm has been devised, which computes the position, velocity and acceleration at time $t + \triangle t$ from their values at time t. This variant is known as velocity Verlet algorithm and it works in the following way

$$\{\mathbf{r}(t),\, \mathbf{v}(t),\, \mathbf{a}(t)\} \rightarrow \{\mathbf{r}(t + \triangle t),\, \mathbf{v}(t + \triangle t),\, \mathbf{a}(t + \triangle t)\}$$

$$\mathbf{r}(t + \triangle t) = \mathbf{r}(t) + \mathbf{v}(t)\,\triangle t + \mathbf{a}(t)\,\frac{\triangle t^2}{2}$$

$$\mathbf{v}(t + \triangle t) = \mathbf{v}(t) + \Big[\mathbf{a}(t) + \mathbf{a}(t + \triangle t)\Big]\,\frac{\triangle t}{2}$$

The velocity Verlet algorithm is mathematically equivalent to Verlet algorithm. It explicitly includes the velocity at each time step, and it is self-starting from the initial positions and velocities.

B3. Updating the neighbour list : Most time consuming part of MD simulation is the energy or force evaluation. For a system of N particle it is needed to evaluate $\frac{N(N-1)}{2}$ pair interactions. This implies that the time needed for the evaluation of forces scales as N^2 [136]. To speed up the calculations Verlet [150, 151] suggested a technique, in which another cut-off radius (r_v) is defined apart from the potential cut-off radius (r_c) in such a way that $r_v > r_c$. Before one starts the calculations, for a given particle i, a list of all other atoms within r_v is constructed. For further calculation of interactions, only those particles in this list is considered. If the maximum displacement of particles is less than $r_v - r_c$, then only those atom in the list needs to be considered. This is a calculation of the order N. If any particle crosses r_v , the list has to be updated, and this operation is of the order of N^2, but need not be done at all time-steps. The list needs to be updated only at regular intervals [136]. This technique works for systems with short-range interactions, whereas in the case of long range interactions special lattice summation techniques are needed [152].

2.2.2.3 C. Equilibration

C1. Equilibrating the system at desired temperature and/or pressure: Before computing the physical properties one has to equilibrate the system under certain desired conditions. If the equations of motion is integrated as discussed before, the total energy of the system will not change, and the system is said to be in microcanonical ensemble (NVE). In this ensemble, the total number of particles N, system volume V, and total energy E are kept constant. The main limitation of NVE ensemble is that, most of the experiments are not performed under the conditions of constant total energy. To simulate the actual experimental situation one has to use other ensembles such as canonical (NVT) and isobaric-isothermal (NPT), which allows to keep the system under a particular temperature and pressure.

The temperature enters into MD simulation via equipartition theorem. The temperature and particle velocities are related through mean kinetic energy(K) as

$$K = \frac{3}{2} N k_B T = \frac{1}{2} \sum_{i=1}^{N} \left\langle m_i v_i^2 \right\rangle \tag{2.27}$$

where N is the number of particle and k_B is the Boltzmann constant. The initial velocities are assigned from a Maxwell-Boltzmann distribution at the desired temperature. There are several method to control temperatures, the most trivial method is velocity rescaling, in which the velocities of particles are scaled with a factor $\sqrt{\frac{T_{desired}}{T_{current}}}$ to obtain the desired temperature. The inherent problem with this method is that it does not allow the fluctuation in temperature which is always present in canonical ensemble. Another possibility of reproducing the canonical ensemble is coupling the MD system with an external thermostats. In doing so the equations of motion are modified, hence the total energy is not conserved in NVT and NPT ensemble, rather, it fluctuate around the mean value [153]. Several thermostats have been made to control the temperature such as Andersén [154], Berendsen [155] and Nosé-Hoover [156, 157]. In this thesis Nosé-Hoover thermostats are used to control the temperatures.

The definition of the pressure is not straightforward as temperature. The Virial theorem can be used to calculate the pressure, which relates the pressure to the product of the positions and forces as follows

$$P = \frac{N k_B T}{V} + \frac{1}{3V} \left\langle \sum_i \sum_{i<j} (r_{ij} . \mathbf{F}_{ij} \right\rangle \tag{2.28}$$

Where N is the number of atoms, r_{ij} is the distance between a pair of interacting atoms and $\mathbf{F_{ij}}$ is the corresponding force, and sum is over all pairs. The methods used to control the pressure are analogous to the one used for temperature control. The system pressure is set by changing the simulation volume with a scaling factor. The scaling is done for both simulation cell dimensions and the position of particles (Berendsen barostat). Nosé-Hoover scheme is also available to control the pressure [156, 157]. A suitable combination of Nosé-Hoover thermostat and barostat will reproduce the proper NPT ensemble.

2.2.2.4 D. Averaging

D1. Compute the average of the measured quantities of interest: According to statistical mechanics, the macrostates (such as T, P, V, and N) are represented as averages over the microstates ($\mathbf{r}_i$, $\mathbf{p}_i$) of the system (configurations) in an ensemble, known as ensemble average. In MD simulations, instead of ensemble average, time average is used to obtain the thermodynamic variables, this is motivated by ergodic hypothesis. The ergodic hypothesis postulates that for sufficiently long time the phase trajectory of a closed system passes arbitrarily close to every point in phase space. This implies that average over phase space or average over a trajectory are equivalent.

$$\langle A \rangle_{Ensemble} = \langle A \rangle_{Time} \tag{2.29}$$

After ensuring that the system has equilibrated properly in a particular ensemble, one can start the production runs. The system has to evolve for sufficiently long time to hold good the ergodic hypothesis. After that point, averaging among any of the physical quantities of interest can be started.

2.3 Theoretical methods - For vibrational properties of solids

Many important physical properties of materials such as thermal expansions, specific heat, thermal conductivity and phase transitions stems from the dynamics of the atoms [158, 159]. The collective vibrations of atoms in a solid form a traveling wave, called lattice vibrations. The subject which deals with the study of lattice vibrations is known as lattice dynamics (LD). At sufficiently low temperatures (well below Debye temperatures), these traveling waves are decoupled and does not interact with each other. They behave like independent harmonic-oscillators, which are called normal-modes of vibrations and their quanta is known as "phonon". At very low temperature, the phonon properties can be evaluated by harmonic approximation. The anharmonic effects are studied using quasi-harmonic and anharmonic LD methods. In the following section, the harmonic, quasi-harmonic and anharmonic LD methods are reviewed briefly.

2.3.1 Lattice dynamics

In this section, the basic theory of lattice dynamics (LD) is briefly reviewed. The detailed description can be found in the literature [158, 159]. Vibrations occur due to the displacement of atoms from their equilibrium configurations. Assuming that the displacement of atoms, $u\binom{l}{\kappa}$ are small around the equilibrium positions, $r\binom{l}{k}$ {where l is the unitcell index ($l = l_1$, l_2, l_3, set of integers) and κ is basis index (κ=1, 2,... $\mathrm{N_b}$)} the crystal potential energy can be expressed as Taylor series. The Taylor expansion is truncated at second order-term, which is a key approximation in the theory of LD known as harmonic approximation. Under harmonic approximation, the potential energy can be expressed as follows;

$$\Phi = \Phi^{(0)} + \Phi^{(1)} + \Phi^{(2)} \tag{2.30}$$

where

$$\begin{aligned}
\Phi^{(0)} &= \Phi\left(r\begin{pmatrix} l \\ \kappa \end{pmatrix}\right), \\
\Phi^{(1)} &= \sum_{lk\alpha} \frac{\partial \Phi}{\partial u_\alpha\binom{l}{\kappa}} u_\alpha\begin{pmatrix} l \\ \kappa \end{pmatrix}\Bigg|_0 = \sum_{lk\alpha} \Phi_\alpha\begin{pmatrix} l \\ \kappa \end{pmatrix} u_\alpha\begin{pmatrix} l \\ \kappa \end{pmatrix}, \\
\Phi^{(2)} &= \frac{1}{2}\sum_{lk\alpha}\sum_{l'k'\beta} \frac{\partial^2 \Phi}{\partial u_\alpha\binom{l}{\kappa}\partial u_\beta\binom{l'}{\kappa'}}\Bigg|_0 u_\alpha\begin{pmatrix} l \\ \kappa \end{pmatrix} u_\beta\begin{pmatrix} l' \\ \kappa' \end{pmatrix} \\
&= \frac{1}{2}\sum_{lk\alpha}\sum_{l'k'\beta} \Phi_{\alpha\beta}\begin{pmatrix} l & l' \\ \kappa & \kappa' \end{pmatrix} u_\alpha\begin{pmatrix} l \\ \kappa \end{pmatrix} u_\beta\begin{pmatrix} l' \\ \kappa' \end{pmatrix}
\end{aligned}$$

where $\alpha, \beta = x,\ y,\ z$ are the Cartesian components.

The first term ($\Phi^{(0)}$) in equation 2.30 does not depend on displacement, hence can be considered as zero. In equilibrium configuration the force on every atom must vanish, this leads to $\Phi_\alpha\binom{l}{\kappa} = 0$, for every α, κ, l. Hence $\Phi^{(1)} = 0$.

Now the Hamiltonian under harmonic approximation can be written as follows

$$H = T + \Phi \tag{2.31}$$

$$H = \sum \frac{p_\alpha^2\binom{l}{\kappa}}{2m_\kappa} + \frac{1}{2}\sum_{lk\alpha}\sum_{l'k'\beta} \Phi_{\alpha\beta}\begin{pmatrix} l & l' \\ \kappa & \kappa' \end{pmatrix} u_\alpha\begin{pmatrix} l \\ \kappa \end{pmatrix} u_\beta\begin{pmatrix} l' \\ \kappa' \end{pmatrix} \tag{2.32}$$

where $P_\alpha\binom{l}{\kappa}$ is the momentum conjugate to $u_\alpha\binom{l}{\kappa}$. From Hamilton's equations, one can directly obtain the equations of motion as

$$-\dot{p}_\alpha\begin{pmatrix} l \\ \kappa \end{pmatrix} = -m_\kappa \ddot{u}_\kappa\begin{pmatrix} l \\ \kappa \end{pmatrix} = \sum_{l'k'\beta} \Phi_{\alpha\beta}\begin{pmatrix} l & l' \\ \kappa & \kappa' \end{pmatrix} u_\beta\begin{pmatrix} l' \\ \kappa' \end{pmatrix} \tag{2.33}$$

From equation 2.33 it is evident that $\Phi_{\alpha\beta}\begin{pmatrix} l & l' \\ \kappa & \kappa' \end{pmatrix}$ is the negative of the force exerted on $\binom{l}{\kappa}^{th}$atom along α direction due to displacement of $\binom{l'}{\kappa'}^{th}$ atom along β direction.

This quantity ($\Phi_{\alpha\beta}$) is referred as force constant, symbolizing the spring constant in Hook's law.

If an infinitesimal translation is given to a crystal, all the atoms will have same displacement (ϵ_β) and doesn't make any restoring force, hence from equation 2.33 we can write

$$0 = \left[\sum_{l'k'} \Phi_{\alpha\beta} \begin{pmatrix} l & l' \\ \kappa & \kappa' \end{pmatrix} \epsilon_\beta \right] \tag{2.34}$$

where ϵ_β is arbitrary hence

$$\sum_{l'k'} \Phi_{\alpha\beta} \begin{pmatrix} l & l' \\ \kappa & \kappa' \end{pmatrix} = 0 \tag{2.35}$$

This is known as translational sum rule, and it helps to determine the self force constant($l\kappa = l^{'}\kappa^{'}$), which has not been defined in equation 2.33. The diagonal terms is given by

$$\Phi_{\alpha\beta} \begin{pmatrix} l & l \\ \kappa & \kappa \end{pmatrix} = - \sum_{l'k' \neq lk} \Phi_{\alpha\beta} \begin{pmatrix} l & l' \\ \kappa & \kappa' \end{pmatrix} \tag{2.36}$$

Due to the periodicity of crystal, the displacement of the corresponding atoms in different cells are equivalent apart from a phase factor, hence one can assume a wave-like solution to equation 2.33

$$u_\alpha \begin{pmatrix} l \\ \kappa \end{pmatrix} = \frac{1}{\sqrt{m_k}} U_\alpha(\kappa|\bar{q})\, exp \left[i \left((\bar{q}.\bar{r}(l) - \omega(\bar{q})t) \right) \right] \tag{2.37}$$

where $\overline{q}$ is the wave vector and $\omega(\overline{q})$ is the angular frequency associated with the wave. Substituting equation 2.37 into equation 2.33 leads to the following $3n$-coupled equations of motion in the wave amplitude $U_\beta(\kappa'|\overline{q})$;

$$\omega^2(\overline{q}) U_\alpha(\kappa|\overline{q}) = \sum_{k'\beta} D_{\alpha\beta} \begin{pmatrix} \overline{q} \\ \kappa\kappa' \end{pmatrix} U_\beta(\kappa'|\overline{q}) \tag{2.38}$$

where $D_{\alpha\beta}$ is the dynamical matrix and it is given as

$$D_{\alpha\beta}\begin{pmatrix}\bar{q}\\ \kappa\kappa'\end{pmatrix} = \frac{1}{\sqrt{m_{\kappa}m_{\kappa'}}}\sum_{l'}\Phi_{\alpha\beta}\begin{pmatrix} l & l' \\ \\ \kappa & \kappa'\end{pmatrix} exp\left[iq.\left(\bar{r}(l') - \bar{r}(l)\right)\right] \tag{2.39}$$

Equation 2.38 can be written in matrix form as

$$\omega^2(\bar{q})U(\bar{q}) = D(\bar{q})U(\bar{q}) \tag{2.40}$$

From equation 2.40, it is clear that the lattice dynamics now essentially became eigenvalue problem. The frequencies and polarizations of normal modes are obtained by diagonalizing the dynamical matrix. The equation 2.40 will have a non-trivial solution, if the determinant of coefficients vanishes, and the secular equation is

$$det\left|D_{\alpha\beta}\begin{pmatrix}\bar{q}\\ \kappa\kappa'\end{pmatrix} - \omega^2(\bar{q})\delta_{\kappa\kappa'}\delta_{\alpha\beta}\right| = 0 \tag{2.41}$$

Solving 2.41 yields $3n$ eigenvalues, which are labelled as $\omega_j^2(\bar{q})$ (j=1,2,... $3n$). Since the dynamical matrix $\left(D(\bar{q})\right)$ is Hermitian, the eigenvalues $\omega_j^2(\bar{q})$ are real . A negative eigenvalue would lead to a purely imaginary frequency, which implies that the displacements of atoms increases indefinitely with time, leading to destruction of crystal; that means the system under study is dynamically unstable. The eigenvectors $U_{\alpha}\left(\kappa\middle|\begin{matrix}\bar{q}\\ j\end{matrix}\right)$ can be obtained by substituting the eigenvalues $\omega_j^2(\bar{q})$ to equation 2.38. Being Hermitian the eigenvectors of $D(\bar{q})$ can be chosen as orthonormal. We can write the j^{th} eigenvector $U_{\alpha}\left(\kappa\middle|\begin{matrix}\bar{q}\\ j\end{matrix}\right)$ as

$$U_{\alpha}\left(\kappa\middle|\begin{matrix}\bar{q}\\ j\end{matrix}\right) = A\begin{pmatrix}\bar{q}\\ j\end{pmatrix}e_{\alpha}\left(\kappa\middle|\begin{matrix}\bar{q}\\ j\end{matrix}\right) \tag{2.42}$$

where $A\binom{\bar{q}}{j}$ is the amplitude of the mode, $e_{\alpha}\left(\kappa\middle|\begin{matrix}\bar{q}\\ j\end{matrix}\right)$ is the components of eigenvector, which determine the pattern of displacement of atoms in the unitcell for a particular normal mode and hence it is referred as polarization vector. Under some special circumstances the polarization vectors are either parallel (or perpendicular) to $\bar{q}$, then the mode is said to be longitudinal (or transverse) [158].

2.3.2 Quasi-harmonic approximation (QHA)-*incorporates volume dependence of frequency*

LD calculations can be used to obtain the frequencies and polarizations of normal modes under harmonic approximation. For a truly harmonic crystal there will be no thermal expansion and also its thermal conductivity will be infinite [160]. This is contradicting with experimental observations, which predicts a finite value for thermal conductivity at a given temperature. The above contradiction is due to the complete absence of anharmonicity in LD calculations which are always associated with the crystal [158]. To model the finite temperature properties such as thermal expansion, thermal conductivity, and higher order phonon-phonon scattering processes, one has to go beyond harmonic approximation [158, 161, 162]. As temperatures increases the lattice expands/contracts, hence the mean positions of atoms changes from $r^0\binom{l}{\kappa}$ to $r^T\binom{l}{\kappa}$, and the latter can be determined by minimizing the free-energy [161]. In order to device a theory to explain the temperature dependence of vibrations of atoms, Leibfried and Ludwig [163] proposed that the crystal potential energy can be expanded around the mean positions for a given temperature .

$$\Phi_T = \Phi_T^{(0)} + \Phi_T^{(1)} + \Phi_T^{(2)} \tag{2.43}$$

where

$$\begin{aligned}
\Phi_T^{(0)} &= \Phi_T\left(r\begin{pmatrix} l \\ \kappa \end{pmatrix}\right), \\
\Phi_T^{(1)} &= \sum_{lk\alpha} \frac{\partial \Phi_T}{\partial r_\alpha\binom{l}{\kappa}} u_\alpha^T \begin{pmatrix} l \\ \kappa \end{pmatrix}\Bigg|_{mean.posi\,at\,T} = \sum_{lk\alpha} \Phi_\alpha^T \begin{pmatrix} l \\ \kappa \end{pmatrix} u_\alpha^T \begin{pmatrix} l \\ \kappa \end{pmatrix}, \\
\Phi_T^{(2)} &= \frac{1}{2}\sum_{lk\alpha}\sum_{l'k'\beta} \frac{\partial^2 \Phi_T}{\partial r_\alpha\binom{l}{\kappa}\partial r_\beta\binom{l'}{\kappa'}}\Bigg|_{mean.posi\,at\,T} u_\alpha^T \begin{pmatrix} l \\ \kappa \end{pmatrix} u_\beta^T \begin{pmatrix} l' \\ \kappa' \end{pmatrix} \\
&= \frac{1}{2}\sum_{lk\alpha}\sum_{l'k'\beta} \Phi_{\alpha\beta}^T \begin{pmatrix} l & l' \\ \kappa & \kappa' \end{pmatrix} u_\alpha^T \begin{pmatrix} l \\ \kappa \end{pmatrix} u_\beta^T \begin{pmatrix} l' \\ \kappa' \end{pmatrix}
\end{aligned}$$

The potential energy around the means positions corresponds to a particular temperature and the Taylor expansion is truncated at second order. This method is known as quasi-harmonic approximation (QHA). In QHA the atoms are vibrating around the mean positions harmonically. The dynamics of the problem is same as before, and the new force constant is represented as $\Phi^{T}_{\alpha\beta}\begin{pmatrix} l & l' \\ \kappa & \kappa' \end{pmatrix}$. The new force constant is evaluated as the second derivative of potential energy around the mean-positions, which changes with temperature. Since the force constant matrix contains the effect of thermal expansion, unlike harmonic theory, the mode frequencies are temperature dependent here. In QHA, the anharmonicity arises from thermal expansion is incorporated, but anharmonicity due to the movement of atoms are still excluded. The QHA works well at intermediate temperatures and it may not be suitable at higher temperature because of the phonon–phonon interactions which are not included in QHA [134].

2.3.3 Thermodynamic properties

2.3.3.1 *Thermodynamics under harmonic approximation:*

In harmonic model the normal modes of vibrations are treated as independent harmonic oscillator. Within harmonic model, many physical quantities can be derived at low temperatures, where the phonon modes are assumed to be independent [164]. The thermodynamic quantities can be derived by setting up the partition function. The partition function for a single quantum harmonic oscillator with energy $\epsilon_i = \hbar\omega_i$

$$Z_i = \sum_{n=0}^{\infty} exp\left(-\frac{(n+\frac{1}{2})\hbar\omega_i}{k_B T}\right) \tag{2.44}$$

$$Z_i = \frac{exp\left(-\frac{\hbar\omega_i}{2k_B T}\right)}{1 - exp\left(-\frac{\hbar\omega_i}{k_B T}\right)} \tag{2.45}$$

Equation 2.45 is obtained from equation 2.44 by assuming it as a geometric series with constant factor $exp\left(-\frac{\hbar\omega_i}{2k_B T}\right)$. The partition function of a harmonic solid containing N atom can be written as the product of individual partition function [164]

$$Z_N = \prod_i^{3N} Z_i = \prod_i^{3N} \frac{exp\Big(-\frac{\hbar\omega_i}{2k_BT}\Big)}{1 - exp\Big(-\frac{\hbar\omega_i}{k_BT}\Big)} \tag{2.46}$$

Now all other thermodynamic properties of crystal can be derived from the partition function. The vibrational free energy F_{vib} and vibrational entropy S_{vib} are given as

$$F_{vib} = -k_BT \ln Z = \frac{1}{2}\sum_i^{3N} \hbar\omega_i + k_BT \sum_i^{3N} \ln\Bigg(1 - exp\Big(-\frac{\hbar\omega_i}{k_BT}\Big)\Bigg) \tag{2.47}$$

$$S_{vib} = -\frac{dF}{dT} = k_B \sum_i^{3N} \Bigg[-\ln\Bigg(1 - exp\Big(-\frac{\hbar\omega_i}{k_BT}\Big)\Bigg) + \frac{\Big(\frac{\hbar\omega_i}{k_BT}\Big)}{\Big(exp\frac{\hbar\omega_i}{k_BT} - 1\Big)} \Bigg] \tag{2.48}$$

The specific heat at constant volume is

$$C_v = -T\Big(\frac{\partial^2 F}{\partial T^2}\Big) = k_B \sum_i^{3N} \Big(\frac{\hbar\omega_i}{k_BT}\Big)^2 \frac{exp\Big(\frac{\hbar\omega_i}{k_BT}\Big)}{\Big(exp\frac{\hbar\omega_i}{k_BT} - 1\Big)^2} \tag{2.49}$$

2.3.3.2 *Quasi-harmonic thermodynamics:*

In QHA, the phonon frequencies are dependent on the structural parameter $\{a_i\}$, hence $\omega_i \rightarrow \omega_i\{a_i\}$. The free energy in QHA can be written as

$$F\Big(\{a_i\}, T\Big) = E\Big(\{a_i\}\Big) + \frac{1}{2}\sum_i^{3N} \hbar\omega_i\{a_i\} + k_BT \sum_i^{3N} \ln\Bigg(1 - exp\Big(-\frac{\hbar\omega_i\{a_i\}}{k_BT}\Big)\Bigg) \tag{2.50}$$

where $E\Big(\{a_i\}\Big)$ is the ground state energy. The direct minimization of free energy gives the equilibrium structure at a given temperature. This formalism can be used to derive many temperature dependent thermodynamics properties, such as thermal expansion, Grüneisen parameter and heat capacity. The linear thermal expansion coefficient can be determined in two ways, first one is the direct minimization of quasi-harmonic free energy (equation 2.50) for each lattice parameter at a given temperature. This will give a lattice parameter $a(T)$ at that temperature for which free energy is minimum. Now the linear thermal expansion coefficient can be obtained as

$$\alpha(T) = \frac{1}{a(T)}\frac{da(T)}{dT} \tag{2.51}$$

The second formalism is the Grüneisen parameter based, which assumes a linear dependence of the phonon frequencies on three orthogonal cell direction $\{a_i\}$ [165]

$$\alpha = \frac{1}{a_o^2 \frac{\partial^2 E}{\partial a^2}\Big|_0} \sum_i C_{v,i} \frac{-a_0}{\omega_{0,i}} \frac{\partial \omega_i}{\partial a}\Bigg|_0 \tag{2.52}$$

where subscript 0 indicate the quantity computed at equilibrium and $C_{v,i}$ is the specific heat contribution from the i$^{\text{th}}$(i=$\overline{q}$, j) phonon mode

The Harmonic theory yields the specific heat at constant volume C_v. But experimentally we are measuring specific heat at constant pressure C_p , and it can be obtained from the following relationship

$$C_p(T) - C_v(T) = \alpha_v(T)^2 BVT \tag{2.53}$$

where α_v is the volume thermal expansion and B is bulk modulus and it is defined as $B = -V\,\frac{dP}{dV}$.

2.3.4 Anharmonic lattice dynamics - *introduces the interaction between the phonon modes*

Both harmonic and quasi-harmonic approximation treat the phonon modes as decoupled. Once a phonon mode gets excited, it vibrates indefinitely without decaying its energy into the other modes. In anharmonic LD, the interaction between the phonon modes are introduced as a perturbation to the quasi-harmonic solution [166–168], and the anharmonic phonon frequency (ω_A) and lifetime time (τ) can be written as follows

$$\omega_A\begin{pmatrix}\overline{q}\\ j\end{pmatrix} = \omega\begin{pmatrix}\overline{q}\\ j\end{pmatrix} + \Delta\begin{pmatrix}\overline{q}\\ j\end{pmatrix} \tag{2.54}$$

$$\tau\begin{pmatrix}\overline{q}\\ j\end{pmatrix} = \frac{1}{2\Gamma\binom{\overline{q}}{j}} \tag{2.55}$$

where $\Delta\binom{\overline{q}}{j}$ is the shift in the quasi-harmonic mode frequency $\omega\binom{\overline{q}}{j}$ and $\Gamma\binom{\overline{q}}{j}$ is the phonon linewidth. The frequency shift and linewidth are the second order anharmonic corrections to the quasi-harmonic frequencies, which contains the contributions from the three and four phonon processes. The three and four phonon processes depends on the third and fourth order derivative of the potential energy(Φ) [166]. Using this formalism the mode dependent frequency shift and linewidth can be obtained, with which one can compute the thermal conductivity [166]. Density functional perturbation theory (DFPT) [134] formalism has been used to compute the frequency shift and lifetime of phonon modes using anharmonic LD [169, 170]. In anharmonic LD, the potential energy is truncated at third or fourth order (difficult to implement in DFPT) in the displacement of the atoms from their equilibrium position, by assuming that the higher order phonon processes are negligible. This assumption may not be valid in many crystals which shows strong anharmonicity at higher temperatures, where the higher order phonon process are important [171]. The high computational cost involved in DFPT calculations, restrict this studies at Γ point ($\overline{q} = 0$). DFPT based studies can incorporate only few hundreds of atoms, hence the thermal properties (say thermal conductivity) computed using this formalism will be prone to finite size effects.

2.3.5 Phonons from MD simulations - *incorporates the full anharmonicity of interatomic potential*

The lattice dynamics methods are reviewed in detail in section 2.3.1. The LD methods can incorporate at most third (in general) or fourth order phonon process. To incorporate the full anharmonicity of interatomic potential one has to depend on MD simulations. This section discusses the theoretical formalism adapted to compute the phonon frequencies within the classical MD framework.

2.3.5.1 Velocity-Velocity Auto correlation Function (VACF):

Velocity-Velocity auto correlation $\langle v(t)\, v(0)\rangle$ is the most commonly used method to compute the phonon frequencies from MD simulations. The normalized VACF can be defined as

$$C_v(\tau) = \frac{\langle \bar{v}_i(\tau)\, \bar{v}_0(0)\rangle}{\langle \bar{v}_i(0)\, \bar{v}_0(0)\rangle} \tag{2.56}$$

where the expectation value is computed as

$$\langle \bar{v}_i(\tau)\, \bar{v}_0(0)\rangle = \frac{1}{3N\tau'} \sum_t^{\tau'} \sum_i^{3N} \bar{v}_i(t+\tau)\bar{v}_i(t) \tag{2.57}$$

The summation ranges over all the frames in time (from 0 to $\tau' = M\Delta t$) and over the 3N velocity components. The Fourier transform of the equation 2.56 will give the phonon density of states (PDOS) [172–174]

$$g(\omega) = \int \exp(i\omega t) \frac{\langle \bar{v}_i(t)\, \bar{v}_i(0)\rangle}{\langle \bar{v}_i(0)\, \bar{v}_i(0)\rangle} dt \tag{2.58}$$

The VACF is prone to finite size effects hence large simulations cells are required, also simulation has to run for long time to ensure the convergence in the correlation functions.

2.3.5.2 Phonon dispersion from an effective dynamical matrix - *fix-phonon method.*

Ling Ti Kong [104] proposed a method to compute the phonon dispersion directly from MD simulations, and implemented as an extension (known as *fix-phonon* method) to classical MD simulation package LAMMPS. Using this method phonon dispersion and PDOS can be computed at any finite temperature well below the melting point. The theoretical derivation of this method is discussed below

Consider a single particle with mass m which is connected to its equilibrium position by a massless spring with force constant k. Particle will fluctuate around the equilibrium position even in the absence of external force. Let us assume that it vibrates along x-direction only, under equilibrium condition an equipartition of energy will be expected, hence it can be written as

$$\frac{1}{2}k\langle\Delta x^2\rangle = \frac{1}{2}m\langle v^2\rangle = \frac{1}{2}k_BT \tag{2.59}$$

where the $\langle..\rangle$ denotes the ensemble average, Δx is the displacement and v is the velocity of particle. k_B is the Boltzmann constant and T is the temperature. If temperature can be defined for a single particle, then the force constant will be

$$k = \frac{K_BT}{\langle\Delta x^2\rangle} \tag{2.60}$$

The above relationship will be valid only for a real crystal under harmonic approximation. For a real crystal, the lattice Green's function coefficient ($G_{lk\alpha,l'k'\beta}$) is obtained from the second moment of the displacement [175, 176]

$$G_{lk\alpha,l'k'\beta} = \langle u_{lk\alpha}u_{l'k'\beta}\rangle \tag{2.61}$$

Now the force constant can be written as

$$\Phi_{lk\alpha,l'k'\beta} = k_BT\left[G^{-1}\right]_{lk\alpha,l'k'\beta} \tag{2.62}$$

Computing the Green's function coefficient in reciprocal space is more convenient due to the periodic boundary conditions. The displacement in reciprocal space is the Fourier transform of the real space ones

$$\tilde{u}_{lk\alpha}(\overline{q}) = \frac{1}{\sqrt{N}}\sum_l u_{lk\alpha}exp(-i\overline{q}.\bar{r}_l) \tag{2.63}$$

Here N is the total number of unitcells in the crystal. The Green's function in reciprocal space is

$$\tilde{G}_{lk\alpha,l'k'\beta}(\overline{q}) = \langle\tilde{u}_{lk\alpha}\tilde{u^*}_{l'k'\beta}\rangle \tag{2.64}$$

where * denotes the complex conjugate. The force constant is then given by

$$\tilde{\Phi}_{lk\alpha,l'k'\beta}(\overline{q}) = k_BT\left[\tilde{G}^{-1}(\overline{q})\right]_{lk\alpha,l'k'\beta} \tag{2.65}$$

Equation 2.65 gives the force constant matrix in the reciprocal space, which is nothing but the dynamical matrix. Once dynamical matrix is available the mode frequencies and polarization can be obtained by simply solving the eigenvalue problem (equation 2.40).

In summary, the displacement of atoms are extracted during the MD simulation and the Green's function is computed in reciprocal space, which will give the force constant matrices in reciprocal space (dynamical matrices) by simple matrix operations. This method uses harmonic and quasi-harmonic mode frequency relationship to construct the dynamical matrices. At finite temperature the crystal Hamiltonian is replaced with an effective one at an average lattice parameter. Hence this method can be considered as an extension of QHA to MD simulations. More-over this method cannot predict the mode resolved frequency shift and linewidth.

2.3.5.3 Spectral energy density (SED) method

Both the VACF and effective dynamical matrix method cannot predict the mode resolved phonon frequency shift and linewidth at finite temperatures, also the later cannot incorporate the full anharmonicity of interatomic potential. To overcome above limitations, a spectral energy density (SED) based method [177, 178] is adapted and coupled with classical MD simulation package LAMMPS [179]. Several in-house codes were developed, and using those codes one can compute phonon dispersion, Phonon DOS, mode resolved phonon frequencies, linewidths (at any $\bar{q}$ point in the Brillouin zone) and coupling of normal modes of vibrations. The theoretical formalism behind the SED method is discussed below.

Let $\{e_\alpha\left(\kappa\middle|\begin{matrix}\overline{q}\\ j\end{matrix}\right), \alpha = x, y, z;\ \kappa = 1.....N_b\}$ be the polarization vector corresponding to the j^{th} normal mode of vibration of the crystal with wave-vector $\overline{q}$ within the harmonic approximation (here N_b is the number of atoms in the basis). The α^{th}component of displacement of the κ^{th} atom in the l^{th}cell at a time t is given by

$$u_\alpha^{LD}\left(\begin{matrix}l\\ \kappa\end{matrix}\middle| t\right) = \frac{1}{\sqrt{N}} \sum_{\bar{q},j} e_\alpha\left(\kappa\middle|\begin{matrix}\overline{q}\\ j\end{matrix}\right) A\begin{pmatrix}\overline{q}\\ j\end{pmatrix} \exp\left(i\bar{q}.\bar{r}(l) - i\omega\begin{pmatrix}\overline{q}\\ j\end{pmatrix}t\right) \tag{2.66}$$

where $A\binom{\bar{q}}{j}$ is the amplitude of j^{th} mode of frequency $\omega\binom{\bar{q}}{j}$. The corresponding velocity can be written as

$$v_{\alpha}^{LD}\left(\begin{matrix} l \\ \kappa \end{matrix}\middle| t\right) = -\frac{1}{\sqrt{N}} \sum_{\bar{q},j} i\omega\begin{pmatrix} \bar{q} \\ j \end{pmatrix} e_{\alpha}\left(\kappa \middle| \begin{matrix} \bar{q} \\ j \end{matrix}\right) A\begin{pmatrix} \bar{q} \\ j \end{pmatrix} \exp\left(i\bar{q}.\bar{r}(l) - i\omega\begin{pmatrix} \bar{q} \\ j \end{pmatrix} t\right) \tag{2.67}$$

Let $v_{\alpha}\left(\begin{matrix} l \\ \kappa \end{matrix}\middle| t\right)$ be the velocity of the $\binom{l}{\kappa}^{th}$ particle at time t at finite temperature (obtained say from MD simulations or some other means). We can project the velocities of the particles on to the j^{th} normal mode of vibration with wave-vector $\bar{q}$ of the perfect crystal by defining a quantity $\psi\left(\begin{matrix} \bar{q} \\ j \end{matrix}\middle| t\right)$ given by

$$\psi\left(\begin{matrix} \bar{q} \\ j \end{matrix}\middle| t\right) = \sum_{\alpha,\kappa} \left(\sum_{l} v_{\alpha}\left(\begin{matrix} l \\ \kappa \end{matrix}\middle| t\right) \exp\Big(-i\bar{q}.\bar{r}(l)\Big) \right) e_{\alpha}^{*}\left(\kappa \middle| \begin{matrix} \bar{q} \\ j \end{matrix}\right) \tag{2.68}$$

In case the velocities are obtained from time evolution within the harmonic approximation, the corresponding quantity $\psi^{LD}\left(\begin{matrix} \bar{q} \\ j \end{matrix}\middle| t\right)$ is given by

$$\psi^{LD}\left(\begin{matrix} \bar{q} \\ j \end{matrix}\middle| t\right) = \sum_{\alpha,\kappa} \left(\sum_{l} v_{\alpha}^{LD}\left(\begin{matrix} l \\ \kappa \end{matrix}\middle| t\right) \exp\Big(-i\bar{q}.\bar{r}(l)\Big) \right) e_{\alpha}^{*}\left(\kappa \middle| \begin{matrix} \bar{q} \\ j \end{matrix}\right) \tag{2.69}$$

The right hand side of equation (2.69) is given by

$$\begin{aligned} &= \frac{1}{\sqrt{N}} \sum_{\alpha,k} \sum_{\bar{q}',j'} (-i)\omega\begin{pmatrix} \bar{q}' \\ j' \end{pmatrix} A\begin{pmatrix} \bar{q}' \\ j' \end{pmatrix} \exp\left(-i\omega\begin{pmatrix} \bar{q}' \\ j' \end{pmatrix} t\right) \\ &\times e_{\alpha}\left(\kappa \middle| \begin{matrix} \bar{q}' \\ j' \end{matrix}\right) e_{\alpha}^{*}\left(\kappa \middle| \begin{matrix} \bar{q} \\ j \end{matrix}\right) \sum_{l} \exp\Big(i(\bar{q}' - \bar{q}).\bar{r}(l)\Big) \end{aligned}$$

Using the fact that $\sum_l \exp\Big(i(\bar{q}' - \bar{q}).\bar{r}(l)\Big) = N\delta_{\bar{q},\bar{q}'}$ and the ortho-normality condition $\sum_{\alpha,k} e_{\alpha}\left(\kappa \middle| \begin{matrix} \bar{q} \\ j' \end{matrix}\right) e_{\alpha}^{*}\left(\kappa \middle| \begin{matrix} \bar{q} \\ j \end{matrix}\right) = \delta_{j,j'}$ the above equation can be re-written as

$$\psi^{LD}\left(\begin{matrix} \bar{q} \\ j \end{matrix}\middle| t\right) = (-i)\sqrt{N}\,\omega\begin{pmatrix} \bar{q} \\ j \end{pmatrix} A\begin{pmatrix} \bar{q} \\ j \end{pmatrix} \exp\left(-i\omega\begin{pmatrix} \bar{q} \\ j \end{pmatrix} t\right) \tag{2.70}$$

The time Fourier transform of equation 2.70 is

$$\tilde{\psi}^{LD}\left(\begin{matrix}\bar{q}\\ j\end{matrix}\middle|\,\omega\right) = \int dt\ \exp\Big(-i\omega t\Big)\,\psi^{LD}\left(\begin{matrix}\bar{q}\\ j\end{matrix}\middle|\,t\right) = (-i)\,\sqrt{N}\,\omega\begin{pmatrix}\bar{q}\\ j\end{pmatrix}A\begin{pmatrix}\bar{q}\\ j\end{pmatrix}\,2\pi\delta\left(\omega - \omega\begin{pmatrix}\bar{q}\\ j\end{pmatrix}\right) \tag{2.71}$$

The power spectrum $\left|\tilde{\psi}^{LD}\left(\begin{matrix}\bar{q}\\ j\end{matrix}\middle|\,\omega\right)\right|^2$ is infinitely sharply peaked at the mode frequency $\omega\binom{q}{j}$. The $\left|\tilde{\psi}^{LD}\left(\begin{matrix}\bar{q}\\ j\end{matrix}\middle|\,\omega\right)\right|^2$ constructed in this manner should give the spectral density of the vibration of a system at any temperature resolved on to the $\binom{q}{j}^{th}$ normal mode of the harmonic crystal.

2.4 Benchmarking of codes

The lattice dynamics (LD) problem essentially involves the evaluation of force constants and further the dynamical matrices (section 2.3.1). Diagonalizing the dynamical matrix will yield the square of the mode frequencies (eigenvalues) and polarizations (eigenvectors). This is shown schematically in figure 2.2

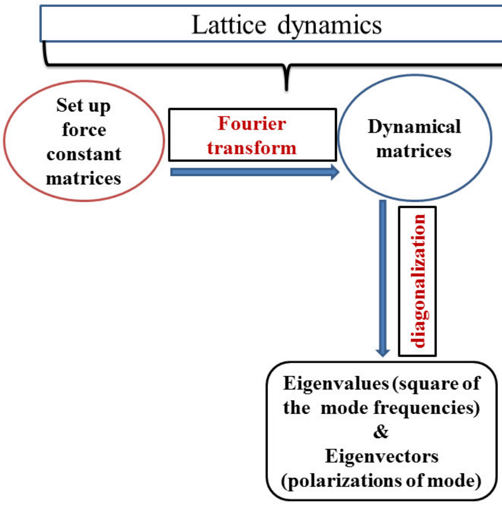

Figure 2.2 – The schematic representation of lattice dynamics method

The objective of the problem is to construct the force constant matrices. Traditionally, analytical models are used to define the interaction between the atoms and evaluate the force constants. Force constants can be derived in various other routes, and most of them essentially involves fitting the theoretical models to experimental data such as phonon dispersion (obtained from in-elastic neutron scattering), specific heat and compressibility. The analytical models were replaced by electronic structure calculations with the development of powerful *ab initio* calculation tools [180]. The *ab initio* methods are tedious and computationally expensive. In order to get a quick and accurate estimation of phonon frequencies and polarization, LD based on empirical potentials is adapted, in which the force constants are computed using empirical potentials rather than the electronic structure calculations. An in-house code has been developed to compute the force constants using a synergetic combination of LAMMPS [179] and Phonopy [181]. The work flow of this method is as follows. A super cell of appropriate size is created, the atoms which are inequivalent by symmetry are displaced along the inequivalent directions by a fixed amount (figure 2.3) and the force acting on each atom is calculated by LAMMPS using empirical potentials. These forces are given to phonopy as FORCE_SETS. Phonopy uses the FORCE_SET to compute the dynamical matrix and then mode frequencies and polarizations.

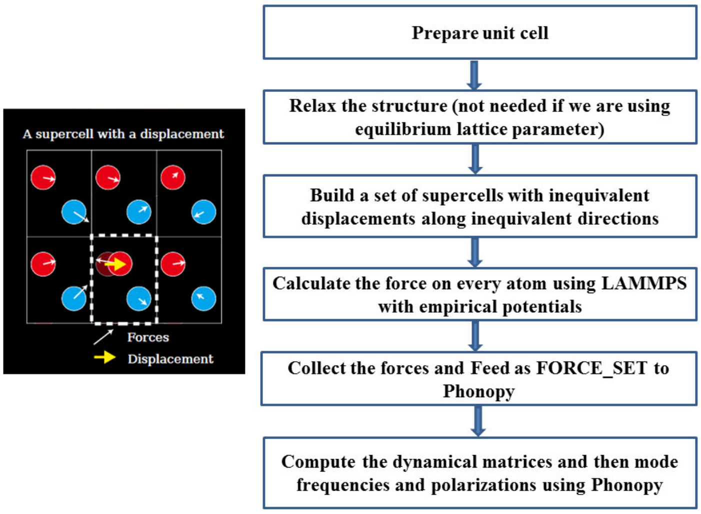

Figure 2.3 – (left) Schematic of supercell with displacements;(right) The work flow of the lattice dynamics based on empirical potential using a combination of LAMMPS and Phonopy

2.4.1 Lattice dynamics of Si

The benchmarking of the code has been done using Si (diamond-structure). LD calculations are done with a supercell of size 3×3×3 using various empirical potentials. Figure 2.4 shows the phonon dispersion and phonon DOS (PDOS) of Si. The unit-cell of Si contains 2 basis atoms hence there will be six modes of vibrations, three of them are acoustic (A) and remaining three are optic (O) modes. The modes are labeled according to their polarizations the letter 'L' and 'T' are used to designate longitudinal and transverse polarizations. The accuracy of the results depends on the quality of empirical potentials, hence to choose a proper empirical potential, calculations are done with SiC-Tersoff [182], Stillinger-Weber (SW) [144] and modified Stillinger-Weber (mod.SW) potentials [183]. The phonon frequencies at high symmetry points in the Brillouin zone are tabulated and compared with experiment (table 2.2). The original SW potential largely overpredict the Γ point degenerate longitudinal optic and transverse (LO/TO) mode frequency by 15.18 %. The Tersoff potential also overpredict the LO/TO mode frequency at Γ point by 3.87 %. At the same time, the modified SW potential predict the Γ point LO/TO mode frequency reasonably accurate and it is 1.50 % smaller than the experimental one. In the case of acoustic modes, the LA mode frequencies are in good agreement with experiments. All three potentials largely under predict the TA mode frequency at the boundary of X and L points. This problem has been already reported with Tersoff potential [184]. Among three potentials, the modified SW reproduces the Γ point LO/TO mode frequency accurately, but it could not reproduce the acoustic mode (LA-mode) as good as Tersoff potential. Over-all analysis shows that the Tersoff potential can reproduce both optic and acoustic modes reasonably well, hence it will be used to predict the finite temperature phonon properties.

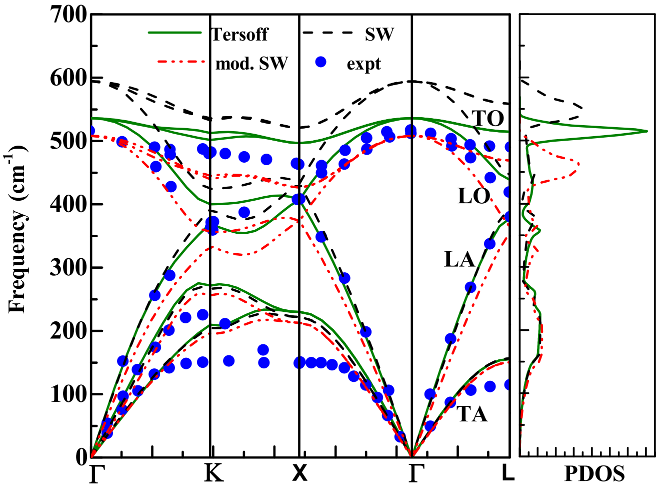

Figure 2.4 – The Phonon dispersion and DOS of Si, computed using lattice dynamics with various empirical potentials. The blue-spheres are experimental data taken from references [185, 186]

Table 2.2 – The phonon frequencies (in cm^{-1}) of Si at different high symmetry point in the Brillouin zone. The Letters S, D and T denotes the single, double and triple degenerate modes.

mode	SiC-Tersoff	SW	mod.SW	Expt.
LO/TO(Γ)	536.01 (T)	594.37(T)	508.30 (T)	516.01
TA (X)	229.59 (D)	221.69 (D)	212.79 (D)	149.03
LA/LO (X)	406.69 (D)	433.08 (D)	373.54 (D)	406.39
TO (X)	496.84 (D)	520.92 (D)	426.68 (D)	465.11
TA (L)	155.55 (D)	156.76 (D)	150.46 (D)	115.41
LA (L)	376.85 (S)	392.24(S)	354.10 (S)	380.42
LO (L)	438.93 (S)	446.57 (S)	364.67 (S)	419.59
TO (L)	514.66 (D)	558.85 (D)	469.27(D)	486.98

2.4.2 Phonon frequencies at finite temperatures from classical MD simulations

The finite temperature phonon properties are computed by resorting to classical MD simulations. The size of the simulation cell is chosen in such a manner that the temperature and pressure of the system stabilizes to the required value. It is found that a 15×15×15 supercell containing 6750 atoms is adequate, in this respect. Periodic boundary condition is employed in all the three directions. The initial geometry is relaxed using the conjugate gradient algorithm to eliminate the residual stresses. The system is equilibrated by coupling it to a Nosé-Hoover thermostat at constant temperature and under ambient pressure (NPT ensemble) for 500 ps. The NPT ensemble allows change in the volume of the cell with respect to temperature and hence incorporates the anharmonic effects without any approximations. The velocities of all atoms are collected in the NVE (micro-canonical) ensemble. How often the velocities of all the atoms should be collected is determined by Nyquist theorem, according to which the sampling frequency should be at least twice the highest frequency contained in the signal. From the LD calculations it is known that the maximum frequency of vibration $\left(\nu_{max}\right)$ in Si is ~540 cm^{-1}(16.21 THz). So the sampling interval can be obtained as $\triangle t = \frac{1}{2\nu_{max}} = 31$ fs. The Nyquist theorem demands that the velocities of all the atoms should be sampled at least every 31 fs. In the present simulations the velocities are sampled at every 5 fs. The simulations are carried out for 3.2 ns.

2.4.2.1 Phonon dispersion and phonon DOS (PDOS)

To study the finite temperature effect on phonon frequencies, the temperature dependent phonon dispersion is computed directly from MD simulations using SED method. The modes of vibration of the crystal at finite temperature are labeled in terms of wavevectors $\bar{q}$ belonging to the Brillouin zone of the perfect crystal. When MD simulations are carried out on a simulation cell comprising of $n_1 \times n_2 \times n_3$ unit cells with periodic boundary condition along all the three directions, the allowed values of $\bar{q}$ are of the form $j_1\bar{A}/n_1 + j_2\bar{B}/n_2 + j_3\bar{C}/n_3$. Here, $\bar{A}$, $\bar{B}$ and $\bar{C}$ are the reciprocal lattice vectors and $0 \leq j_1 < n_1$, $0 \leq j_2 < n_2$ and $0 \leq j_3 < n_3$, thereby giving $n_1 \times n_2 \times n_3$ q-points. If there are n atoms per unit cell, there are $3n \times n_1 \times n_2 \times n_3$ modes of vibration. These modes are organized as $3n$ branches with $n_1 \times n_2 \times n_3$ points along each branch.

Figure 2.5 shows the phonon dispersion computed at 300 K (thick black) from MD simulation using SED method. The LD phonon dispersion (green dash) is also shown here for reference. The phonon dispersion obtained using SED method is in good agreement with LD calculations and experiments, which guarantees the reliability of this method. The acoustic modes (LA and TA) obtained at 300 K, is identical to LD dispersion, indicating its less sensitivity to temperature. The optic modes (LO and TO) show softening at 300 K with respect to LD frequencies, and agreement with experiments became better. This is due to the fact that, the MD simulations and experiments are done at 300 K, whereas the LD frequencies are obtained at 0 K. The phonon DOS is obtained from the Fourier transform of velocity-velocity auto correlation function (VACF) at 300 K is shown in figure 2.5.

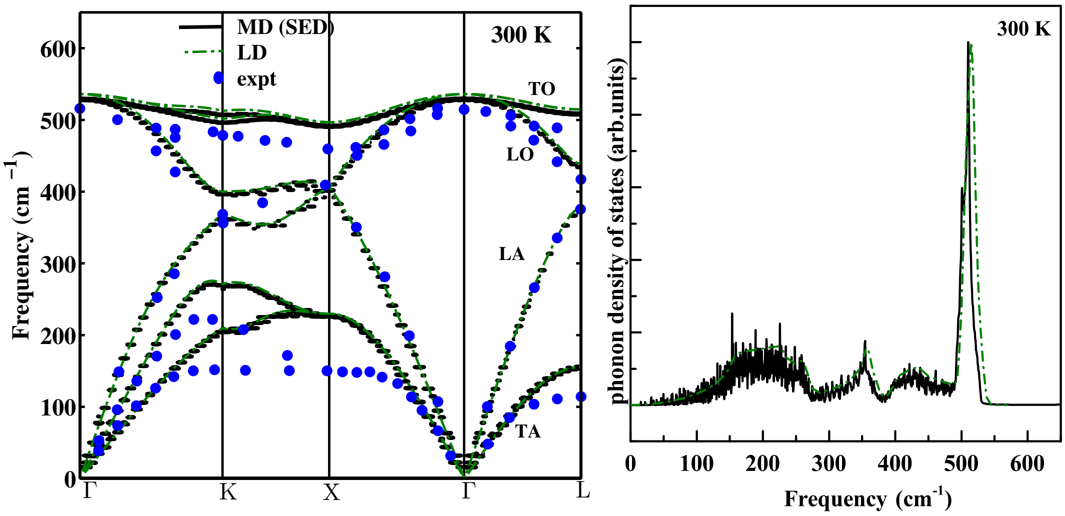

Figure 2.5 – (left) The phonon dispersion of Si computed at 300 K (thick black lines) using spectral energy density (SED) method. The green dash lines are obtained from LD calculations. The blue-spheres are experimental data taken from references [185, 186]. (right) phonon DOS obtained from the Fourier transform of velocity-velocity auto-correlation function (VACF).

2.4.2.2 Mode resolved phonon spectra

To study the softening of LO/TO mode frequencies, mode resolved phonon spectra (at Γ point) is calculated as a function of temperature (Figure 2.6). At 300 K, the LO/TO mode peaks at 530.62 cm^{-1} which is slightly (2.7 %) higher than that of experimental value. The temperature dependent shift and broadening of peaks are clearly visible. The exact peak position and linewidth is obtained by fitting a Lorentzian to the frequency spread.

$$\tilde{\psi}\left(\begin{array}{c}\bar{q}\\ j\end{array}\middle|\,\omega\right) = \frac{A}{(\omega-\omega_c)^2+\gamma^2/4} \tag{2.72}$$

where $4A/\gamma^2$ is the peak height, ω_c is the peak frequency and γ is the full width at half maximum. The LO/TO mode frequency falls with an increase in temperature (Figure 2.7), which is due to the softening of the force constants at higher lattice parameters. The linewidth is increasing in a monotonous fashion with temperatures (Figure 2.7).

To study the anharmonic effect on eigenvectors, the phonon frequency shift and linewidth is computed in two different methods. In first method, the frequency shift and linewidths are extracted by projecting the MD based atomic velocities on to the normal modes of vibrations of a perfect crystal (obtained from LD calculations). In an alternate method, the same quantities are computed directly from the Fourier transform of atomic velocities obtained from the MD simulations. In this method *a priori* knowledge of eigenvector is not necessary. The frequency shift obtained using the above method (black square in figure 2.7) is identical to the one obtained with projection technique (green upper triangle in figure 2.7); the linewidths shows a small deviation.

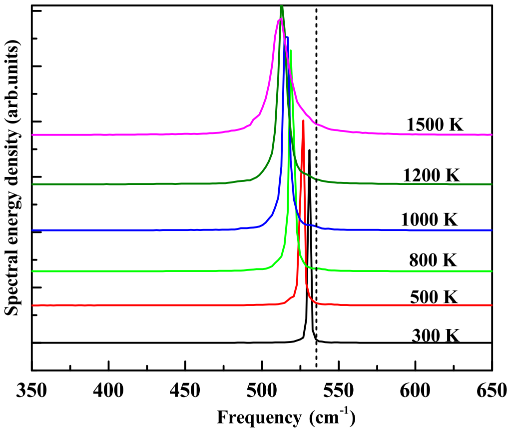

Figure 2.6 – The Γ point LO/TO mode frequency as a function of temperature. The vertical (short dash) line is the LD peak position.

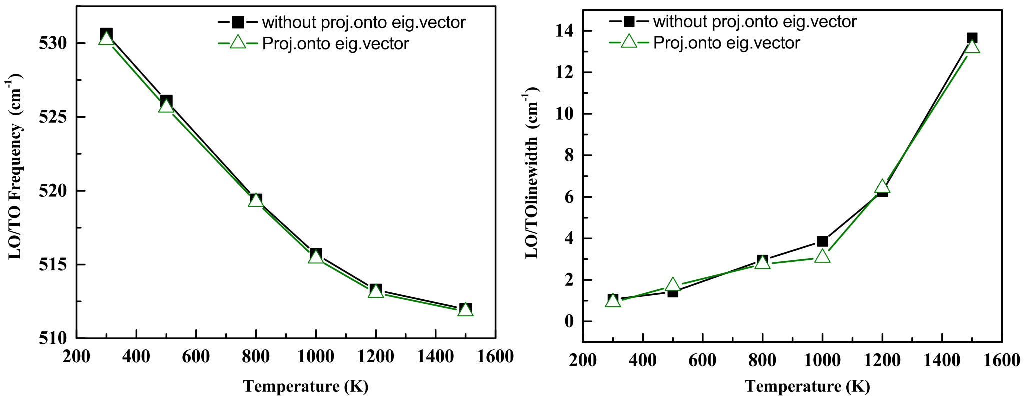

Figure 2.7 – LO/TO mode frequency shift (left) and linewidth (right) as a function of temperatures.

2.4.2.3 Anharmonic coupling of normal modes

The phonon coupling and decay seen in the MD simulations can be modeled in terms of the third and higher order terms in the expansion of lattice potential energy with respect to displacement of atoms from equilibrium [187]. The third order anharmonic term corresponds to three phonon processes and it is the simplest model used to study anharmonic effects [167, 168]. There are two allowed processes in three phonon interactions- in first process, one phonon of momentum $\overline{k}_1$ and energy $\epsilon\left(\overline{k}_1\right)$ decays into two other phonons of momenta $\overline{k}_2$ and $\overline{k}_3$ and energy $\epsilon\left(\overline{k}_2\right)$ and $\epsilon\left(\overline{k}_3\right)$, respectively with $\epsilon\left(\overline{k}_1\right) = \epsilon\left(\overline{k}_2\right) + \epsilon\left(\overline{k}_3\right)$ and $\overline{k}_1 = \overline{k}_2 + \overline{k}_3 + \overline{G}$. In the second type, two phonons combine to form a third one $\epsilon\left(\overline{k}_1\right) + \epsilon\left(\overline{k}_2\right) = \epsilon\left(\overline{k}_3\right)$ and $\overline{k}_1 + \overline{k}_2 = \overline{k}_3 + \overline{G}$, where $\overline{G}$ is a reciprocal lattice vector, which will be zero in a normal process and nonzero in an Umklapp process [187]. Since MD simulations are carried out with the untruncated interaction potential, the anharmonicity is fully incorporated, and hence all the higher order phonon process are included naturally.

Figure 2.8 shows the mode resolved phonon spectra at Γ, X and L point at 300 K. The modes are designated as longitudinal or transverse as per their polarization at the Γ point. The modes are, in general, neither longitudinal nor transverse, but of mixed character, when the propagation is along a general direction. At Γ point, there are three acoustic modes with zero frequency and three optic modes (triply degenerate

LO/TO) with non-zero frequency. The LO/TO modes do not get coupled with other modes at Γ point. At X point, all modes are having non- zero frequency. The TO modes are coupled with LA/LO and TA modes. Similarly at L point, TO modes with certain polarization get coupled with LA and TA, and TO modes with different polarizations are coupled with LO, LA and TA modes. The modes are coupled due to anharmonicity. While laborious calculations can, in principle, be done to analyze the multi-phonon processes associated with decay of each mode for anharmonicity of a particular order, there is no simple way of enumerating the decay channels taking into account all orders of anharmonicity. Our method automatically incorporates decay due to all orders of anharmonicity. This is one of the interesting features of the present method.

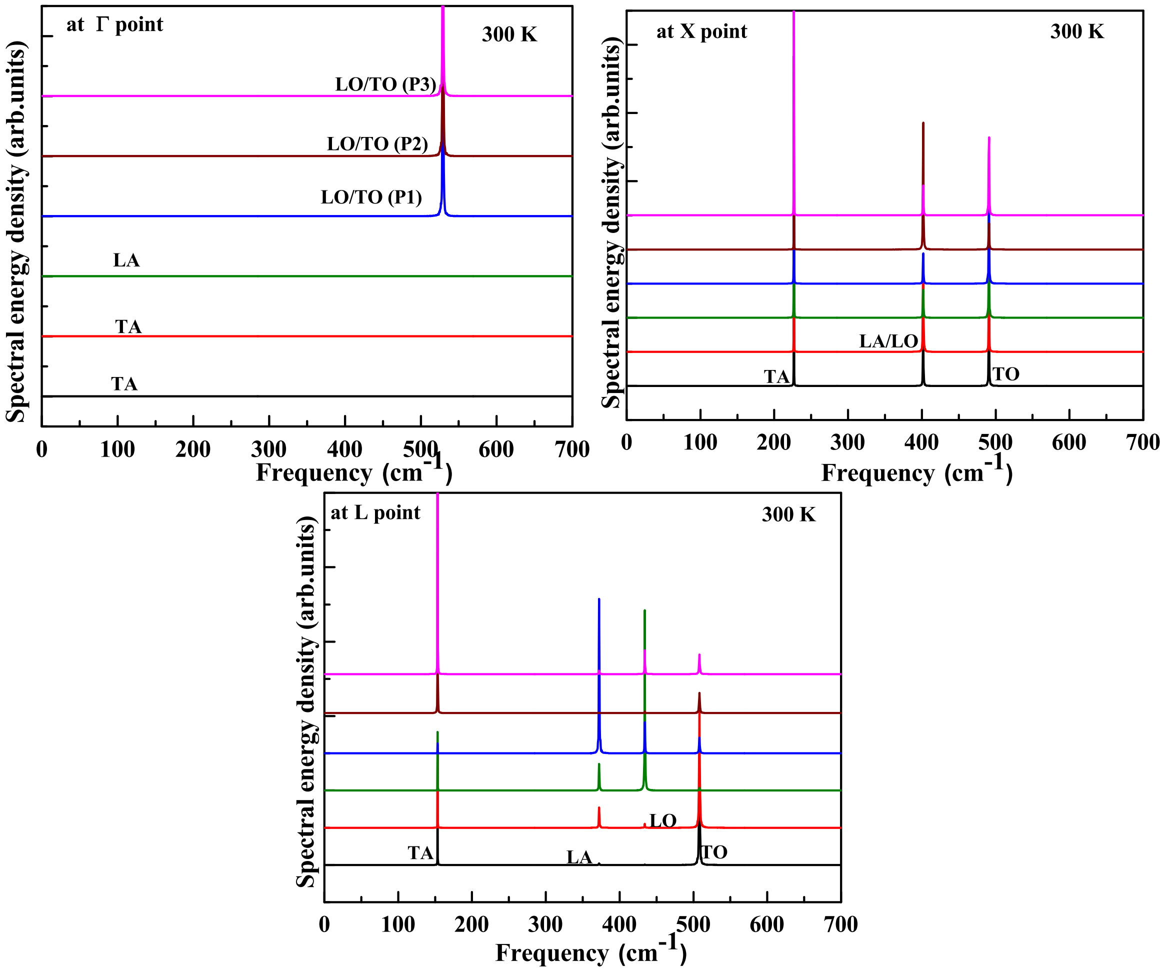

Figure 2.8 – Mode resolved phonon spectra at Γ, X and L point in the Brillouin zone at 300 K. The modes are designated as longitudinal or transverse as per their polarization at the Γ point

2.5 Summary

The general aspects of density functional theory (DFT) and classical molecular dynamics simulations are discussed in the present chapter. The harmonic, quasi-harmonic and anharmonic lattice dynamics theories are reviewed and their merits and demerits are discussed. The above mentioned methods cannot incorporate the anharmonicity of interatomic potential fully, hence a spectral energy density (SED) based method is adapted to compute the phonon transport of materials directly from classical MD simulations at finite temperatures. Several in-house codes were developed and coupled with classical MD simulation package LAMMPS. These codes can be used to compute the (1) Lattice dynamics properties of crystal at 0 K; (2) The phonon dispersion and phonon DOS at finite temperatures; (3) Mode resolved phonon spectra at any point in the Brillouin zone; (4) Anharmonic coupling and decay of normal modes. This technique can complement the results obtained from the optical (Raman and IR) and neutron scattering experiments. Since MD simulation cannot incorporate the electronic contributions, this method can't be used to model the electronic effects, such as electron-phonon coupling and LO-TO splitting. These codes have been benchmarked by computing the phonon dispersion, phonon DOS and mode resolved phonon frequency shift and linewidth of Si (diamond-structure) at 300 K.

CHAPTER 3

Stacking sequences and dynamical stability of graphite structures

---

The electronic, optical and transport properties of few layer graphene or graphite can be tuned by altering the stacking sequences between the graphene layers. In this chapter, the structure and stability of several such plausible stacking sequences in the graphite are investigated using ab inito and classical MD simulations.

3.1 Introduction

Graphite or few layer (FL) graphene is obtained by stacking the graphene sheet one above another in a certain fashion. Based on the stacking sequences between the graphene layers, there are two known forms of graphite (or FL-graphene) such as AB-hexagonal (Bernal) [188] and ABC-rhombohedral strictures [189]. Varying the stacking sequences between the graphene sheets leads to different graphite structures in addition to the AB-hexagonal or ABC-rhombohedral structures. Stacking sequences are used as a probe to tune the electronic band gap, optical conductivity and transport properties of few layer graphene [7]. Charlier *et al* [190] studied the effect of stacking sequences on the electronic properties of graphite and found that the stacking sequence alters the electrical conductivity. From the *ab initio* simulations Andrews *et al* [191] predicted the existence of a structure based on AA stacking with a strong covalent bonding between the layers which are having an inter-planar separation of 1.56 Å. The study further showed that this structure is metastable with respect to the standard AB graphite structure. Okada *et al* [192] studied the electronic structure of multilayer graphene with different stacking sequences using tight binding approximation and found a qualitative agreement with that of graphite having analogous stacking sequences. Savini *et al* [193] made the first detailed study on the mechanical stability of graphite structures. In addition to the structures analyzed by Charlier *et al* [190], they also studied the AB-orthorhombic structure. The authors found that stacking sequences, which are different from the AB-hexagonal and ABC-rhombohedral structures are mechanically unstable even though they are comparable in free energy.

There is no detailed study on the dynamical stability of the stacking altered graphite structures. In addition to the structures analyzed by Savini *et al* [193], one more stacking sequence of type ABC...ABC.... . . is proposed here, which leads to ABC-hexagonal structure with a free energy comparable with that of the other structures. The vibrational properties of hexagonal (AB-bilayer) and rhombohedral (ABC-trilayer) graphite are studied using first principle calculations [44, 56, 194]. The first detailed study on the effect of stacking sequence on phonon dispersion of multilayer graphene was made by Yan *et al* [61]. In their study, they compared the phonon dispersion and vibrational properties of graphene with a few layers stacked in hexagonal or rhombohedral sequences, such as AB, ABA and ABC, via DFPT. In this chapter, the free energy, mechanical and dynamical stability of all stacking altered structures are studied using *ab initio* calculations. Further, the effect of temperatures on the stability of these structures are studied using classical MD simulations.

3.2 Computational methods

In this study, all the calculations are done using *ab initio* DFT as implemented in VASP [131], which also employs pseudopotentials to describe the interaction between the valence electrons and ions. PAW [195] pseudopotentials used in this study helps not only to reduce the size of the basis set considerably, but also to obtain the accuracy of all-electron calculations. Perdew-Zunger [116] version of LDA and GGA of Perdew-Burke-Ernzerhof (PBE) [122] are used to compute the exchange correlation functional. It is seen that while the LDA reproduces the equilibrium structure of bulk 3D graphite reasonably accurately [196], GGA yields poor binding across the layers [44, 197]. The equilibrium in-plane lattice parameter a and the c/a ratio obtained from LDA based calculations are found to be 2.451 Å and 2.712, in good agreement with experimental values ($a = 2.463$ Å, $c/a = 2.725$) [198] and previous calculations [61, 197]. The GGA predicts a (2.467 Å) accurately but over-predicts the c/a ratio (3.335) [44, 62]. DFT does not yet have a completely successful formalism to accurately model the Van der Waals (vdW) interaction across the layers. Incorporating the vdW interaction by DFT-D2 method [199] leads to over binding between the layers for both LDA ($a = 2.446$ Å and $c/a = 2.440$) and GGA ($a = 2.463$ Å and $c/a = 2.601$). A series of convergence tests are done to fix the kinetic energy cut-off that determines the size of the basis set and k-point mesh size that governs sampling of the Brillouin zone in the reciprocal space. A kinetic energy cut-off of 800 eV is found to give free energy convergence of the order 0.025 meV/atom for AB-hexagonal graphite. Integration over the Brillouin-zone is done by using a Monkhorst-Pack [125] grid of 35×35×15 k-points for bilayer graphite structures which contain four atoms in a unit cell. For ABC-rhombohedral/hexagonal structures which contain 6 atoms in a unit cell, a Monkhorst-Pack grid of 35×35×13 k-point mesh is used. Methfessel-Paxton [200] smearing with a smearing width of 0.1 eV is used to incorporate the partial occupancy near the Fermi level. All the structures are relaxed until force on each atom is less than 10^{-5} eV/Å.

The elastic constant tensor is determined by calculating the elastic energy for six finite distortions of the lattice, and relating the elastic energy to elastic constants through the stress-strain relationship [201]. The phonon dispersion for all structures is calculated using DFPT (chapter-2, 2.1.6) as implemented in VASP code. Phonon frequencies and polarizations are calculated by constructing the force constant matrix, from which the dynamical matrix is obtained by Fourier inversion. Eigenvalues of dynamical matrix give the square of the phonon frequencies. Occurrence of a negative eigenvalue in the spectrum of the dynamical matrix signifies imaginary frequency for the corresponding phonon mode, and that indicates dynamical instability in the lattice [158, 202]. DFPT will yield zone center ($\mathbf{q}$=0) phonon frequencies and eigenvectors. Phonon dispersion in the entire Brillouin-zone is computed using the PHONOPY module [181].

3.3 Results and Discussions

3.3.1 Stacking sequences and structural models

Bulk graphite is obtained by stacking of graphene sheets having in-plane C-C nearest neighbor distance of 1.42 Å and a relatively larger inter-planar separation of 3.35 Å due to the weaker van der Waals interaction, which is responsible for holding the planes together. Graphene can be described in terms of a two dimensional lattice with a rhombus containing two basis atoms as the unit cell as seen in Figure 3.1. The two basis atoms are at $(\bar{a}+\bar{b})/3$ and $2(\bar{a}+\bar{b})/3$, where $\bar{a}$ and $\bar{b}$ are the lattice translation vectors. The graphene sheets can be stacked directly one above the other leading to the AA-simple hexagonal structure. Experiments suggest that graphite crystallizes in AB-hexagonal/ABC-rhombohedral structures [188]. The 'B' layer in the AB-hexagonal structure [188] is obtained by shifting the second graphene layer by $(\bar{a}+\bar{b})/3$ (one C-C bond length) with respect to the first layer (the 'A' layer) as shown in Figure 3.1. Thus in the AB-hexagonal structure, half of the carbon atoms in 'B' layer coincide with those in the 'A' layer and the remaining half reside above the center of the hexagons of the 'A' layer. The 'C' layer in the ABC stacking is obtained by shifting a graphene layer by $(\bar{a} + \bar{b})/3$ with respect to the 'B' layer. This stacking produces the rhombohedral structure. In the ABC-rhombohedral structure, half of the carbon atoms in the 'C' layer coincide with those in the 'B' layer and the remaining half sit directly above their hexagonal ring centers. In addition to these three, there are two other stacking sequences. The AB stacking is obtained by shifting 'B' layer by $\bar{a}/2$ along the basis vector $\bar{a}$ with respect to the 'A' layer. This leads to another high symmetric graphite phase known as AB-orthorhombic structure [193]. We propose a new ABC stacking sequence in which the 'C' layer is obtained by shifting by $\bar{b}/2$ along the basis vector $\bar{b}$ with respect to the 'B' layer. In the ABC-hexagonal structure thus obtained, all the carbon atoms in the successive layers remain distinct when compared to the ABC-rhombohedral structure. All the structures are shown in Figure 3.1, which is generated using VESTA [203].

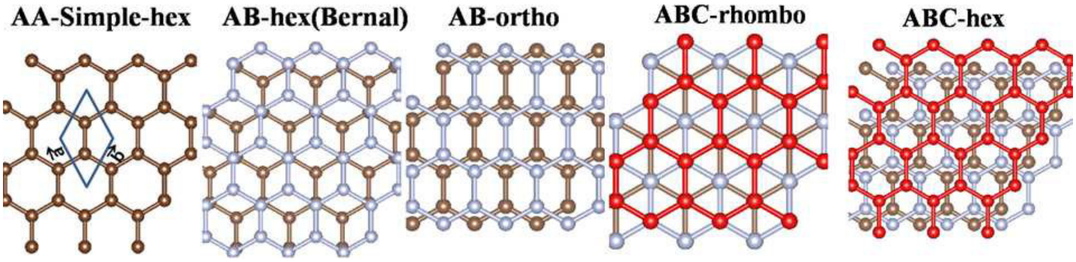

Figure 3.1 – Different stacking sequences leading to different graphite structures . The 2D unit cell of graphene is shown as a rhombus (a = b = 2.456 Å and $\gamma = 60°$) that contains two basis atoms; the successive layers in graphite are held together by a weak van der Waals force with an inter-planar separation (c_{int}) of 3.35 Å.

The geometry of all the structures is relaxed such that the forces acting on all the atoms are $< 10^{-5}$ eV/Å. The free energy of each of the relaxed structures is compared (Table 3.1) with that of the AB-hexagonal structure, which is the ground state structure of bulk graphite. Among the bilayer graphite structures studied here, it is seen that the AA-simple hexagonal and AB-orthorhombic structures are higher in energy with respect to the AB-hexagonal structure, by 9.7 meV/atom and 1.7 meV/atom, respectively. ABC-rhombohedral graphite is higher in energy as compared to the ground state by 0.1 meV/atom. The newly proposed ABC-hexagonal structure is higher in energy with respect to the AB-hexagonal structure by 1.6 meV/atom. These free energy calculations are compared with the results of previous investigations in table 3.1. Since the difference in free energies among the various structures is very small, all these plausible structures can coexist.

Table 3.1 – Comparison of the free energies of different graphite structures with standard AB-hexagonal structures.

Structure	Energy/atom (eV/atom)	Difference in energy with respect to AB-hexagonal (meV/atom)
AA-simple hexagonal	−10.0951	9.70, 9.29 [193] , 17.31 [190]
AB-hexagonal	−10.1048	——
AB-orthorhombic	−10.1031	1.70, 1.66 [193]
ABC-rhombohedral	−10.1047	0.10, 0.10 [193], 0.11 [190]
ABC-hexagonal	−10.1032	1.60

Table 3.2 – The in-plane lattice parameter (a) and inter-planar separation (c_{int}) for the different graphite structures. The quantities inside the curly brackets are calculated with van der Waals (vdW) correction.

	LDA		GGA		
Structure	a (Å)	(c_{int}) (Å)	a (Å)	(c_{int}) (Å)	Space group
AB-hex present study	2.451{2.446}	3.320 {2.984}	2.467 {2.463}	4.070 {3.204}	$P6_3/mmc$ (194)
Literature (*ab initio*)	2.451 [56, 61, 190, 197]	3.350 [190], 3.330 [61], 3.320 [197]			
Experiment	2.463 [198]	3.356 [198]			
AA-sim.hex.	2.450 {2.446}	3.610 {3.201}, 3.34 [190]	2.467 {2.463}	4.291 {3.441}	$P6/mmm$ (191)
AB-ortho	2.451 {2.446}	3.370 {3.020}	2.467 {2.463}	4.141 {3.245}	$Fmmm$ (69)
ABC-rhombo	2.451 {2.446}	3.327{2.989}, 3.340 [190]	2.467 {2.463}	4.073 {3.207}	$R\bar{3}m$ (161)
ABC-hex	2.451 {2.446}	3.361{3.011}	2.467 {2.463}	4.142 {3.236}	$P6_422$ (181)

The structural details of the different graphite phases are summarized in table 3.2. The in-plane lattice parameter (a) and inter-planar separations (c_{int}) are computed using LDA, LDA with vdW correction, GGA and GGA with vdW corrections. From the above calculations, it is found that LDA predicts the equilibrium lattice parameters accurately. Computed in-plane lattice parameter (a) and inter-planar separation (c_{int}) match with previous studies (table 3.2). Bosak and Krisch [198] reported the lattice parameter a = 2.463 Å and c_{int} = 3.356 Å from inelastic X-ray scattering studies on single crystalline graphite. In LDA based simulations we obtain a = 2.451 Å and c_{int} = 3.320 Å for AB-hexagonal graphite. It is seen that the lattice parameter a is under-predicted by 0.5 % whereas the discrepancy is ∼1 % for c_{int}. In fact, the discrepancy between the computed and experimental values is small for a as compared to c_{int} in all the previous studies as well (table 3.2). Higher c_{int} value for the AA-simple hexagonal, AB-orthorhombic and ABC-hexagonal structures as compared to AB-hexagonal and ABC-rhombohedral structures indicates lesser binding across the layers in the former structures as compared to the latter.

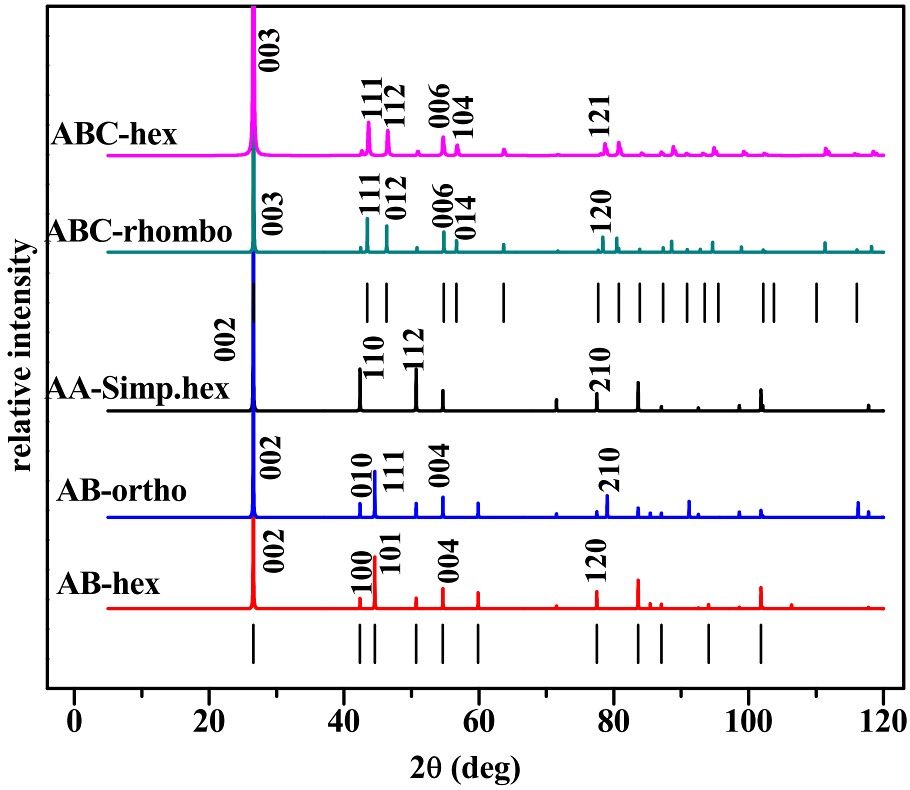

Figure 3.2 – The calculated XRD pattern of different graphite structures with experimental lattice parameters. The peak positions of the standard structures are shown as a stick plot (ICDD data base, PDF Number: 00-056-0159 (hexagonal), 01-075-2078 (rhombohedral)).

Having compared the energetics of the plausible structures, we now proceed to compare the XRD pattern computed for each of these structures with the experimental data available in the ICDD data base (PDF Number: 00-056-0159 (hexagonal), 01-075-2078 (rhombohedral)). Since the lattice parameters obtained from the calculations are not exactly the same as the values obtained from experiment, the positions of the peaks in the computed patterns are not expected to match with those obtained from experiments. Hence the XRD patterns of each of the structures are calculated at the experimental lattice parameters of graphite. The systematic extinction of certain reflections due to symmetry, and the differences in relative intensities can be used to identify which of the proposed structures are actually relevant from the experimental consideration.

Figure 3.2 shows the XRD patterns calculated using Cu-K_α radiation. It can be seen that among the bilayer graphite structures, the peak positions of the AB-hexagonal structures are matching well with experimental XRD pattern. The XRD pattern of AB-orthorhombic structures is very similar to the experimental data, there are significant difference as well at higher angles. In the case of the AA-simple hexagonal structure, the diffraction peaks at $2\theta = 44.56°$, $59.87°$, and many low intensity peaks at higher angles are missing when compared to AB-hexagonal/orthorhombic structures. The calculated XRD patterns of the ABC-rhombohedral and ABC-hexagonal structures are identical and matches with experimental data. Hence, from the structural point of view, it is quite likely that graphite seen in nature contains the newly proposed structures in addition to the AB-hexagonal and ABC-rhombohedral structures.

3.3.2 Elastic constants

The elastic constants are intimately related to the mechanical stability of a crystal and they determine the response of the crystal to external strain. There are five independent elastic constants for graphite, which are C_{11}, C_{12}, C_{13}, C_{33} and C_{44} and they can be categorized into three different classes depending on the nature of the predominant bonding involved. C_{11}, C_{12} belong to first class, where the strong in-plane covalent bonding is involved. C_{33} and C_{44} belong to second class, where the weak Van der Waals bonding across the layers is important. C_{13} forms the third class which depends both on in-plane covalent bonding and inter-layer van der Waals interactions. The elastic constants data is very much essential to predict the mechanical properties of graphite structures. The Born stability criterion, obtained by demanding that the elastic strain energy should be positive definite [161], requires that $2C_{13}^2 < C_{33}(C_{11} + C_{12})$ and C_{11}, C_{12}, C_{33}, $C_{44} > 0$ for mechanical stability of graphite.

Elastic constants of hexagonal graphite have been obtained using different experimental techniques. Blakslee *et al* [204] determined the five independent elastic constants of pyrolytic graphite using ultrasonic and static tests. The value of C_{44} thus obtained is in the range 0.18 – 0.3 GPa, which is very small. Grimsditch [205, 206] found that the value of C_{44} reported by Blakslee *et al* [204] is small due to the low ultrasonic wave velocity propagation along the c-axis caused by movement of dislocations. After neutron irradiation, which arrests the movement of dislocations due to pinning by defects produced by the irradiation, C_{44} increases to 5 GPa. Later Cousins *et al* [207] refined the values of C_{13} and C_{44}. Bosak *et al* [198] determined the elastic constants of graphite single crystals from phonon dispersion obtained by inelastic x-ray scattering and found that the value of C_{11} is slightly higher than that obtained from the ultrasonic experiments, due to the presence of defects in their samples.

Mounet and Marzari [44] calculated the elastic constants of graphite from the sound velocities computed from the slope of the phonon dispersions near the Γ-point by PWSCF using ultrasoft pseudopotentials. The authors found the overall agreement with experiments to be satisfactory. Savini *et al* [193] computed the elastic constants of different graphite structures using linear response theory, as implemented in ABINIT code. The elastic constants obtained using norm-conserving pseudopotentials [208] show good agreement with experimental data. Michel and Verberck [209] made a theoretical investigation and derived the elastic constant data of graphite using Born's long wave method.

Table 3.3 – Elastic constants for all graphite structures

Structure	C_{11}(Gpa)	C_{12}(GPa)	C_{33}(GPa)	C_{13}(GPa)	C_{44}(GPa)
AB-hexagonal (present study)	1109.4	216.6	30.5	-2.7	5.1
Mounet and Marzari [44], *ab initio*	1118.0	235.0	29.0	-2.8	4.5
Andres *et al* [208], *ab initio*	1069.0	204.0	32.0	-2.8	1.0
Michel and Verberck [209], *Theory*	1211.3	275.5	36.79	0.59	4.18
Savini *et al* [193], *ab initio*	1109.0	175.0	29.0	-2.5	4.5
Blakslee *et al* [204], *expt.*	1060.0±20	180.0±20	36.5±1	15±5.0	0.18 - 0.35
Cousins & Heggie [207], *fit to expt.*	1060.0	180.0	36.5	7.9	5.05
Bosak *et al* [198], *expt.*	1109±16	139±36	38.7±7	0±3.0	5±3.0
AA-simple hexagonal	1018.7	202.0	20.0	-2.7	-4.0
AB-orthorhombic	1094.8	211.5	29.3	-1.4	-3.2
ABC-rhombohedral	1108.2	214.9	30.7	-2.6	4.5
ABC-hexagonal	1097.3	213.0	29.2	-2.8	-7.1

The elastic constants computed for all the structures are shown in table 3.3, and the results for AB-hexagonal structure are compared with results of previous calculations and experiments. The qualitative agreement between the present calculations and the previous ones is satisfactory. However, it is worth mentioning that there is a considerable spread in the elastic constant data reported from various *ab initio* simulations (table 3.3). In the present study, the effect of smearing width [210] and the size of the k-grid to sample the Brillouin zone on the convergence of the computed elastic constants has been investigated. The values of C_{11} and C_{12} are found to be very high for all the structures consistent with the strong in plane C-C covalent bonding. Similarly, the values of the computed C_{44} and C_{33} are seen to be small in view of the weak coupling across the layers. The computed Poisson ratio, ($\nu_{xy} = \nu_{yx} = \frac{C_{12}}{C_{11}} = 0.195$) and the Young's modulus ($Y_x = Y_y = 1.1$ TPa) match well with the results of the previous calculations [208] and experiment [204] (0.165 and 1.1 TPa, respectively). C_{13} of all the structures becomes negative in the calculations (meaning that Poisson's coefficient ν_{xz} would be negative [44]) which may be indicative of the inadequacy of the LDA exchange and correlation functional [208]. It is interesting to note that a GGA based calculation also leads to a negative ν_{xz} [44].

The criterion for mechanical stability is that except C_{13}, all the other independent elastic constants mentioned above should be greater than zero [161]. In our calculations, except for the AB-hexagonal and ABC-rhombohedral structures, C_{44} becomes negative and hence violates the stability criterion for all the other structures including the newly proposed ABC-hexagonal structure. Hence, all the newly proposed structures are mechanically unstable, which is in agreement with the conclusions of Savini *et al* [193].

3.3.3 Phonon dispersion

The elastic constant data shows that the new structures are mechanically unstable. The dynamical stability of these new structures is not addressed in the literature. Hence, the dynamical stability of all graphite structures are analyzed by computing the phonon dispersions. Even though LDA predicts the accurate equilibrium lattice parameters, in order to understand the effect of long range van der Waals (vdW) interactions on phonon dispersions, the calculations are done using LDA, LDA with vdW correction and GGA with vdW correction scheme of S. Grimme [199]. The phonon dispersion of all the structures is computed with a 6×6×1 supercell (144 atoms in bilayer graphite, 216 atoms in trilayer graphite), with a Monkhorst-Pack grid of 3×3×7 k-point mesh for bilayer graphite and 3×3×5 k-point mesh for trilayer graphite structures. For smaller supercells, there is a phonon branch with imaginary frequencies even for the AB-hexagonal structure which is the ground state structure of graphite. Also, the dispersion of the ZA mode is not quadratic in q in contrast to what is seen in neutron scattering experiments [59]. The supercell size was therefore increased (upto 6×6x1) until the imaginary frequencies disappears and obtain the quadratic dispersion for the ZA branch, which is a characteristic feature of layered structures[57, 58]. The phonon frequencies are converged to ∼1-2 cm^{-1} with respect to supercell size and energy cut off. The phonon density of states (Phonon DOS) is computed on a dense k-point mesh of 51×51×51.

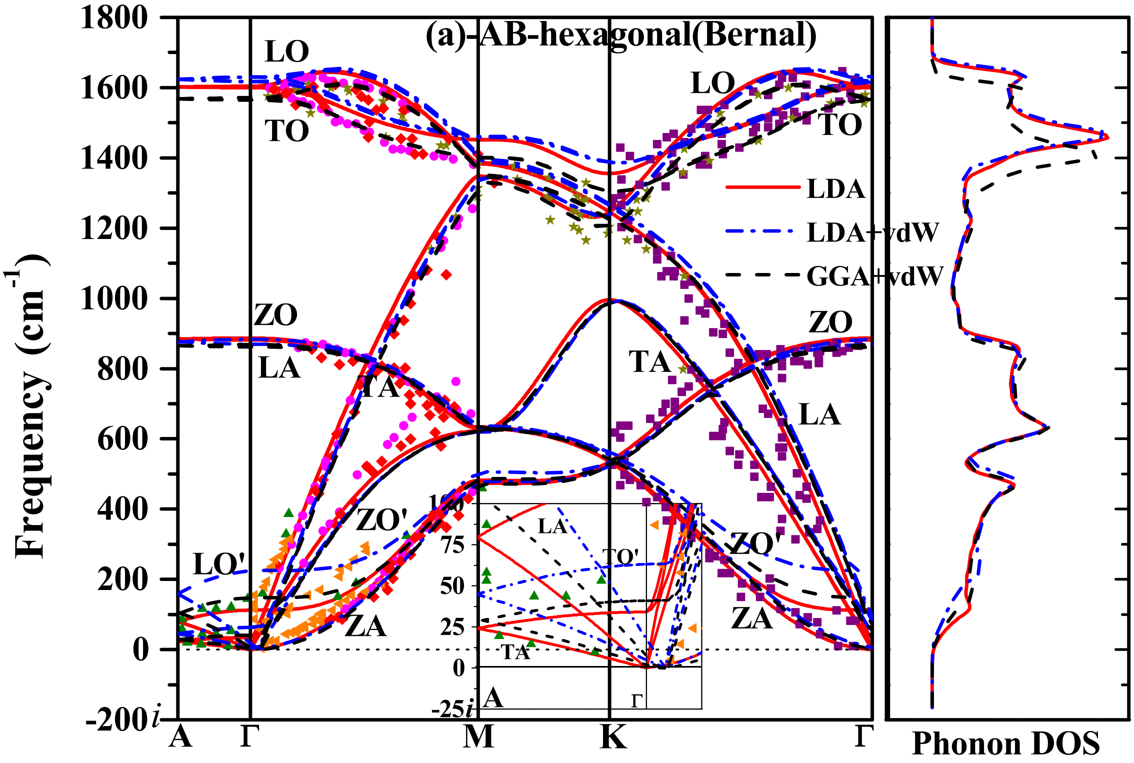

Figure 3.3 – The phonon dispersion of AB-hexagonal structure. The red (solid) lines are calculated using LDA, the blue (dash–dot) lines are calculated using LDA with van der Waals correction (LDA+vdW) and the black (dash) lines are obtained using GGA+vdW. The inset shows the enlarged view along the Γ–A direction. The experimental results [59, 71–75] are shown as symbols for the AB-hexagonal structures and is taken from [70].

The phonon dispersion and phonon DOS for AB-hexagonal structures are computed for the equilibrium lattice parameters and compared with experiments [59, 71–75] (Figure 3.3; the experimental data are taken from reference [70]). The unit cell of AB-hexagonal structure contains four atoms and gives 12 branches in the phonon dispersion, three of them are acoustic (A) and remaining nine are optic (O) branches. The phonon modes are doubly degenerate above ∼400 cm^{-1} due to weak coupling between the layers [56]. As can be seen from Figure 3.3, in LDA based calculations, the low frequency modes are in good agreement with the experimental data , whereas there is a slight deviation from experiments for the LA and ZO high frequency modes. The LDA with vdW correction affects the low frequency phonon modes along Γ-A direction and shows that the low frequency modes harden and deviate from the experimental data. This up-shift in frequency is due to the reduction in the inter-planar separation in the presence of vdW interaction. The frequencies of low lying modes along the Γ-A direction obtained in GGA with vdW corrections falls in between LDA and LDA with vdW corrections. When compared among the above three cases, LDA shows better agreement with experimental data for low lying modes along Γ-A direction. Because of strong C-C in-plane covalent bonding and low atomic weight of carbon atom, some modes vibrate with very high frequency (1596.51 cm^{-1}). The phonon frequencies of degenerate LO/TO and ZO mode at Γ point (1593.17/1596.51 cm^{-1}, 887.24 cm^{-1}) are in good agreement with the calculation results of Mounet and Marzari [44] (1591.84/1603.17 cm^{-1}, 898.58 cm^{-1}) and experiments also (1589.17 [72] /1573.84 [211] cm^{-1}, 860.58 [72] cm^{-1}). The LO/TO and ZO (1617.17/1630.17 cm^{-1}, 883.58 cm^{-1}) modes obtained using LDA with vdW correction deviate slightly from the values predicted by LDA. The increase in frequency of LO/TO mode is due to the decrease in the in-plane lattice parameter in the presence of vdW interaction. The LO/TO and ZO (1568.04/1568.01 cm^{-1}, 864.91 cm^{-1}) mode frequency predicted by GGA with vdW correction is smaller than that given by LDA and LDA with vdW correction. This can be attributed to higher in-plane lattice parameter obtained in GGA with vdW correction. GGA with vdW corrections shows better agreement with experiments for high frequency LO/TO modes.

The phonon dispersion and phonon DOS of ABC-rhombohedral structure are shown in Figure 3.5a. The nature of phonon dispersion of AB-hexagonal and ABC-rhombohedral structures above 400 cm^{-1} are almost similar, which implies that difference in stacking has no significant effect on phonon dispersion above 400 cm^{-1}. There is a slight difference in dispersion below 400 cm^{-1} along Γ-A direction and near the Γ-point [44]. The LO/TO modes show two doubly degenerate branches in AB-hexagonal and three doubly degenerate branches in ABC-rhombohedral structures [61].

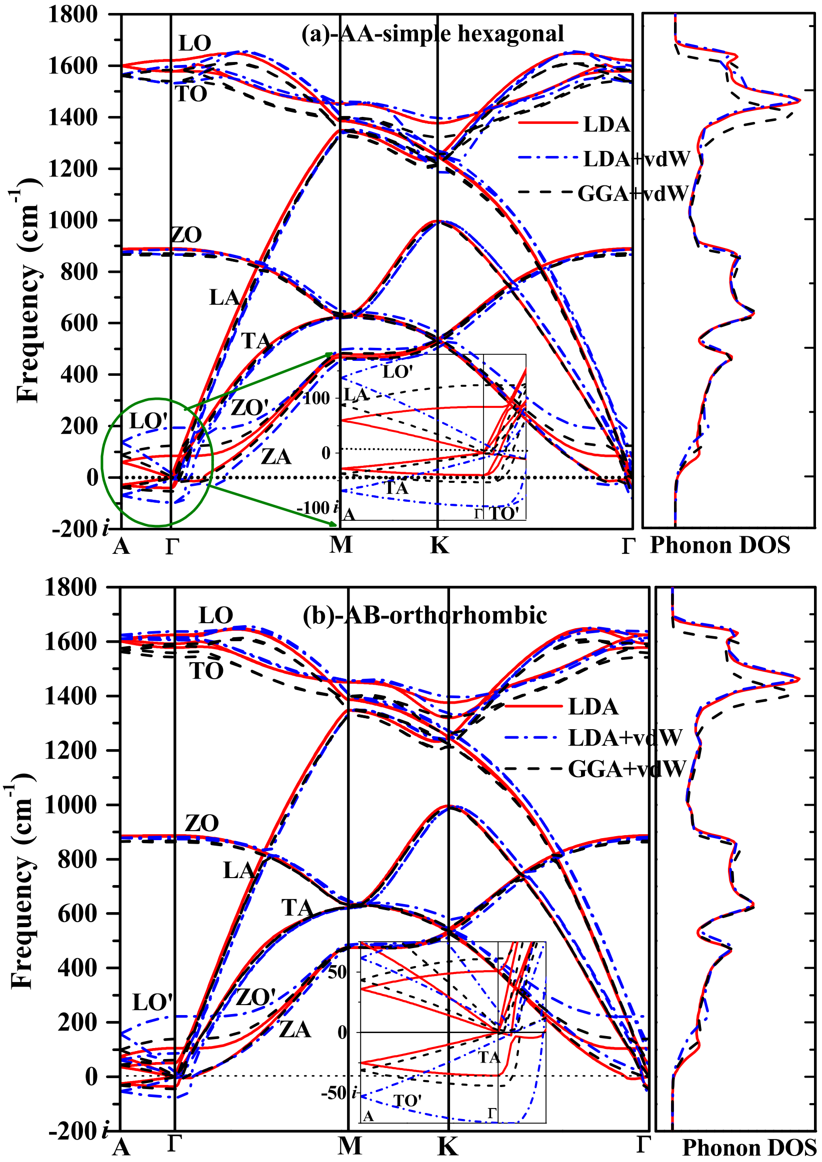

Figure 3.4 – Phonon dispersion of (a) AA-simple hexagonal, (b) AB-orthorhombic structures. The red (solid) lines are calculated using LDA, the blue (dash–dot) lines are calculated using LDA with van der Waals correction (LDA + vdW) and the black (dash) lines are obtained using GGA + vdW. Insets show the enlarged view of the dispersion in the Γ–A direction.

The phonon dispersion of other stacking altered structures such as AA-simple hexagonal, AB-orthorhombic and ABC-hexagonal structures are computed at their optimized lattice parameters and are shown in Figure 3.4a-b &Figure 3.5b, respectively. In all these structures, one or more phonon modes become imaginary along Γ-A direction (out of plane dispersion) in all the three cases (LDA, LDA with vdW and GGA with vdW), indicating a dynamical instability. When compared with AB-hexagonal/ABC-rhombohedral structures, the phonon modes in the new structures have almost similar behavior along Γ-M, M-K and K-Γ directions. The quadratic dispersion of ZA mode and the linear crossing of ZA/ZO, LA/LO modes at K-point are identical to that seen in the AB-hexagonal/ABC-rhombohedral structures. In AB-hexagonal and ABC-rhombohedral structures, the frequency difference between the degenerate LO and TO mode at Γ-point is about ~3 cm^{-1}, and occurs due to the weak binding across the layers [61]. This splitting is more apparent in the new structures. In the AA- simple hexagonal structure, the difference between TO and LO mode rises to 42.32 cm^{-1}, in AB-orthorhombic it is 32.66 cm^{-1}and in ABC-hexagonal it is 18.66 cm^{-1}.

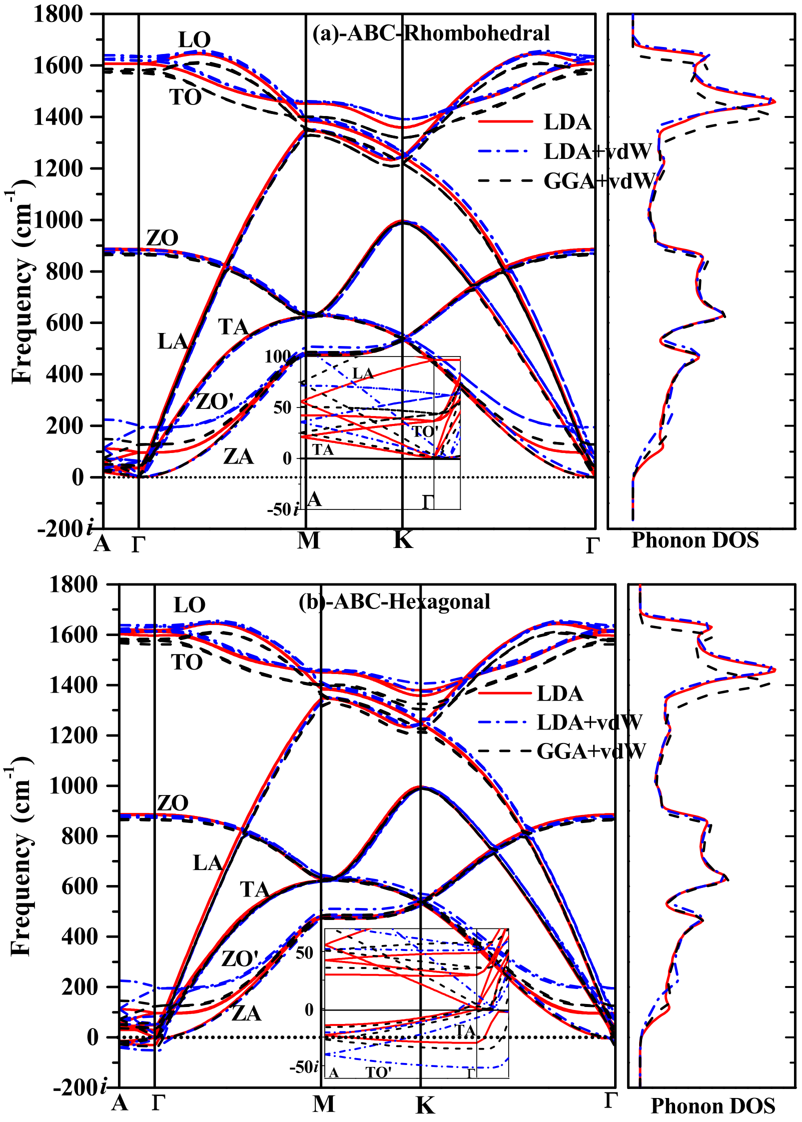

Figure 3.5 – Phonon dispersion of (a) ABC-rhombohedral and (b) ABC-hexagonal structures. The red (solid) lines are calculated using LDA, the blue (dash–dot) lines are calculated using LDA with van der Waals correction (LDA + vdW) and the black (dash) lines are obtained using GGA + vdW. Insets show the enlarged view of the dispersion in the Γ–A direction.

The enlarged view of phonon dispersion along Γ-A direction is shown as an inset in Figure 3.3, Figure.3.4a&b and Figure 3.5 a&b. There are no imaginary modes in the phonon dispersion of AB-hexagonal and ABC-rhombohedral structures. In AA-simple hexagonal, AB-orthorhombic and ABC-hexagonal structures, there are some imaginary modes along Γ-A direction. In AA-simple hexagonal both TA and TO' modes become imaginary. In AB-orthorhombic and ABC-hexagonal structures the degeneracy in TA and TO' is lifted and one of the TA and TO' modes becomes imaginary. Under certain circumstances the dynamical instability can be removed by stabilizing the imaginary phonon modes and this can be achieved by incorporating the effects of zero point vibrational energy to the equilibrium lattice parameters via quasi harmonic approximation [212]. Figure 3.6 shows the phonon dispersion of AB-orthorhombic structure at three different volumes. The volume of the unit cell is varied by ± 5% by varying the in-plane lattice parameter. For all the three volumes the instability associated with the lattice still persists in all the three cases (LDA, LDA with vdW and GGA with vdW). This may be due to the failure of quasi harmonic approximation to describe the strong anharmonicity associated with these lattices [213]. The movement of atoms in AB-orthorhombic structure corresponding to an unstable mode at Γ-point is shown in Figure 3.7. The atoms in A layer (brown spheres with blue arrow) are vibrating in phase, but out of phase with the neighboring B layer atoms (blue sphere with pale green arrow). The polarization associated with this mode is transverse in nature. It can be concluded that the TO' mode frequency becomes imaginary at Γ-point.

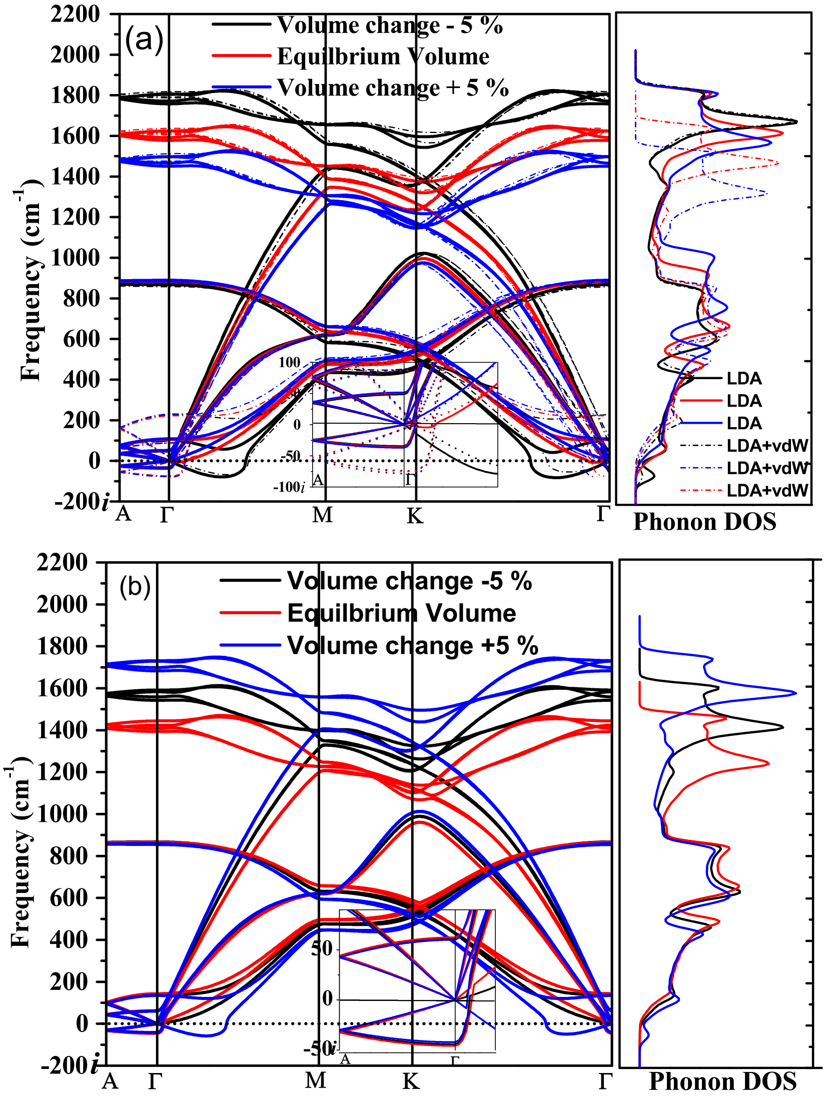

Figure 3.6 – Phonon dispersion of AB-orthorhombic for three different volumes using (a) LDA (solid lines) and LDA + vdW (dash–dot lines), and (b) GGA + vdW.

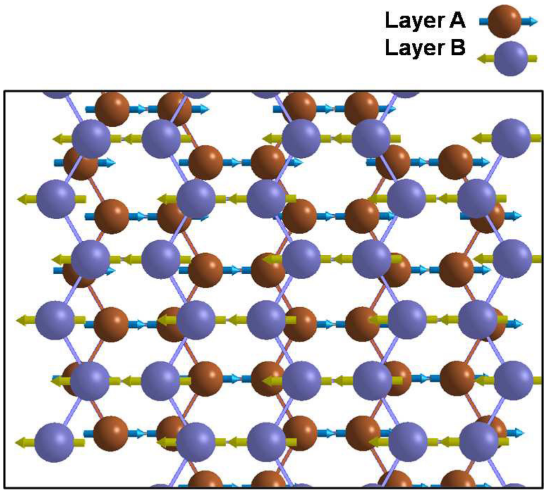

Figure 3.7 – Vibration of atoms in AB-orthorhombic structures corresponding to the unstable mode at the Γ−point.

3.3.4 Potential energy surfaces

In order to further study the nature of instability, the potential energy surfaces are computed by calculating the total energy as a function of the displacement given to all the atoms away from their equilibrium position along the unstable normal mode eigenvector (polarization). The eigenvectors of dynamical matrix contain the information about the relative displacement of atoms in the unit cell. The normalized eigenvector $\vec{\epsilon}$ corresponding to an unstable mode is extracted, and each atom is displaced away from the equilibrium position in accordance with the displacement vector $\vec{\epsilon}d$, so that d is the amplitude of displacement. Then perform a non self-consistent calculation for each incremental displacement d and get the free energy. It is seen from Figure 3.8 that the resultant potential energy surface has the topography of a potential hill, and not a potential well, for all the new structures which confirms that they are inherently unstable. The fact that the potential energy surface is not in the form of a double well when displacements of larger amplitudes are considered implies that the new structures are linearly as well as globally unstable.

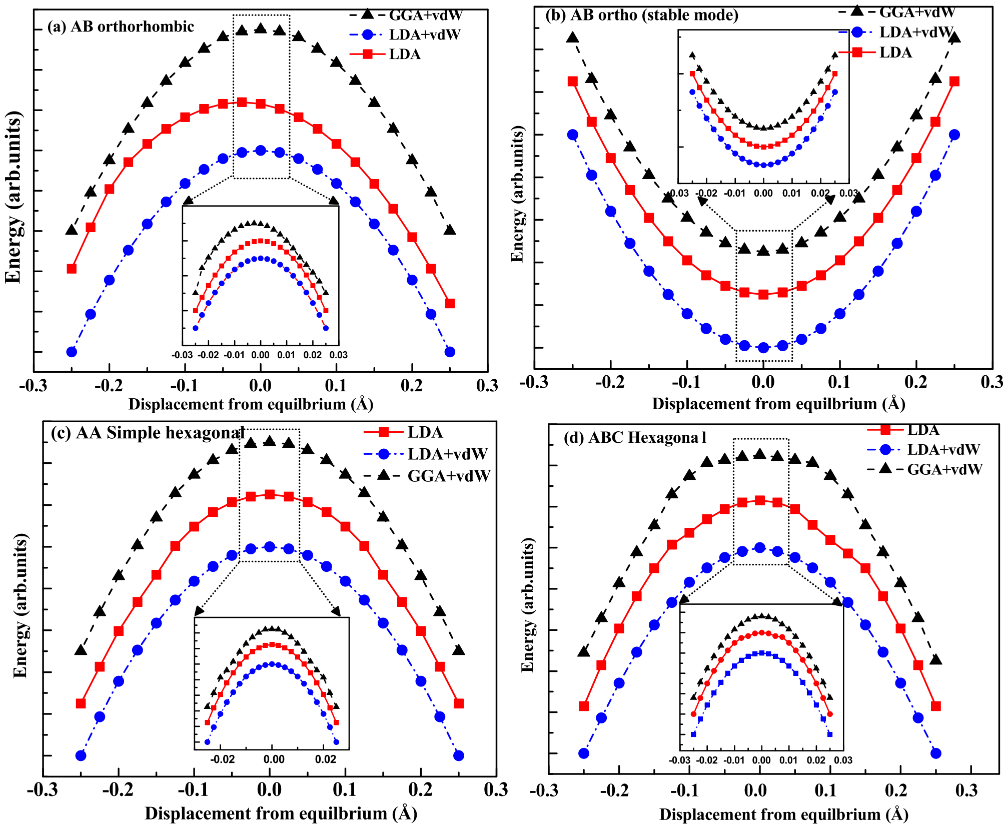

Figure 3.8 – (a) Potential energy surface of AB-orthorhombic for an unstable mode and (b) for a stable mode. (c) and (d) Potential energy surfaces of AA-simple hexagonal and ABC-hexagonal for an unstable mode (d = 0.25 Å). The red (solid) lines are calculated using LDA and the blue (dash–dot) lines are calculated using LDA with van der Waals correction (LDA + vdW). The black (dash) lines are obtained using GGA + vdW. The inset is the potential energy surfaces computed at smaller displacement (d = 0.025 Å).

3.4 Dynamical stability at finite temperatures

In order to understand the effect of temperature on stability of graphite structures, phonon dispersions are computed directly from classical MD simulations using the *fix-phonon* method (chapter-2,2.3.5.2). The phonon dispersions at 0 K are obtained using lattice dynamics method. To compute the phonon dispersion at finite temperature using MD, a triclinic simulation box of size 10×10×1 is used. The interactions between the carbon atoms in in-plane lattice is modeled by a reactive empirical bond order (REBO) potential [214]. The out-of-plane Van der Waals (vdW) forces between the graphite layer is treated using the Lennard–Jones (LJ) potential. Periodic boundary conditions (PBC) are employed in all three directions. In order to eliminate any residual stresses that could be present in the initial configuration, the simulation volume is relaxed using conjugate gradient algorithm. The system is then equilibrated for 500 ps in NPT ensemble at 300 K. After ensuring that the system has equilibrated properly, the instantaneous positions of atoms are extracted at a predefined intervals for 15 ns.

Figure 3.9a&b shows the phonon dispersion of bilayer and trilayer graphite structures obtained from LD calculations at 0 K. The phonon dispersions shares a resemblance with those obtained from DFPT calculations (section 3.3.3). The quadratic dispersion of ZA mode and the linear intersection of ZA/ZO, LA/LO modes at K-point are identical to that seen in the DFPT calculations. In AB-hexagonal structure (green dash lines) all modes are real and positive. The phonon dispersion of AA-simple hexagonal (red solid line) and AB-orthorhombic (blue dot lines) structures contains imaginary modes along $\Gamma - A$ direction, indicating the dynamical instability of these structures, which is in accordance with DFPT calculations. Figure 3.9c shows the phonon dispersion of bilayer graphite structures calculated at 300 K. In contrast to LD results, all the modes are positive and real; the phonon dispersion of all bilayer structures are identical at 300 K. The similar studies are done on trilayer graphite structures (Figure 3.9b&d). The LD results shows that, the ABC- rhombohedral structure is dynamically stable, at the same time the ABC-hexagonal structure have the imaginary modes along $\Gamma - A$ direction, and thus unstable (Figure 3.9c). The instability associated with ABC-hexagonal structure is removed in MD simulation, where all modes are positive and real (Figure 3.9d). The phonon dispersion for ABC-rhombohedral and ABC-hexagonal structures obtained from MD simulations are identical.

In some context, the structures which is dynamically unstable at 0 K can be stabilized at high temperatures due to the anharmonic contributions to the free energy [213, 215]. In such cases the potential energy surfaces would have a topography of double-well. Since the potential energy surfaces (Figure 3.8) are having a shape of inverted

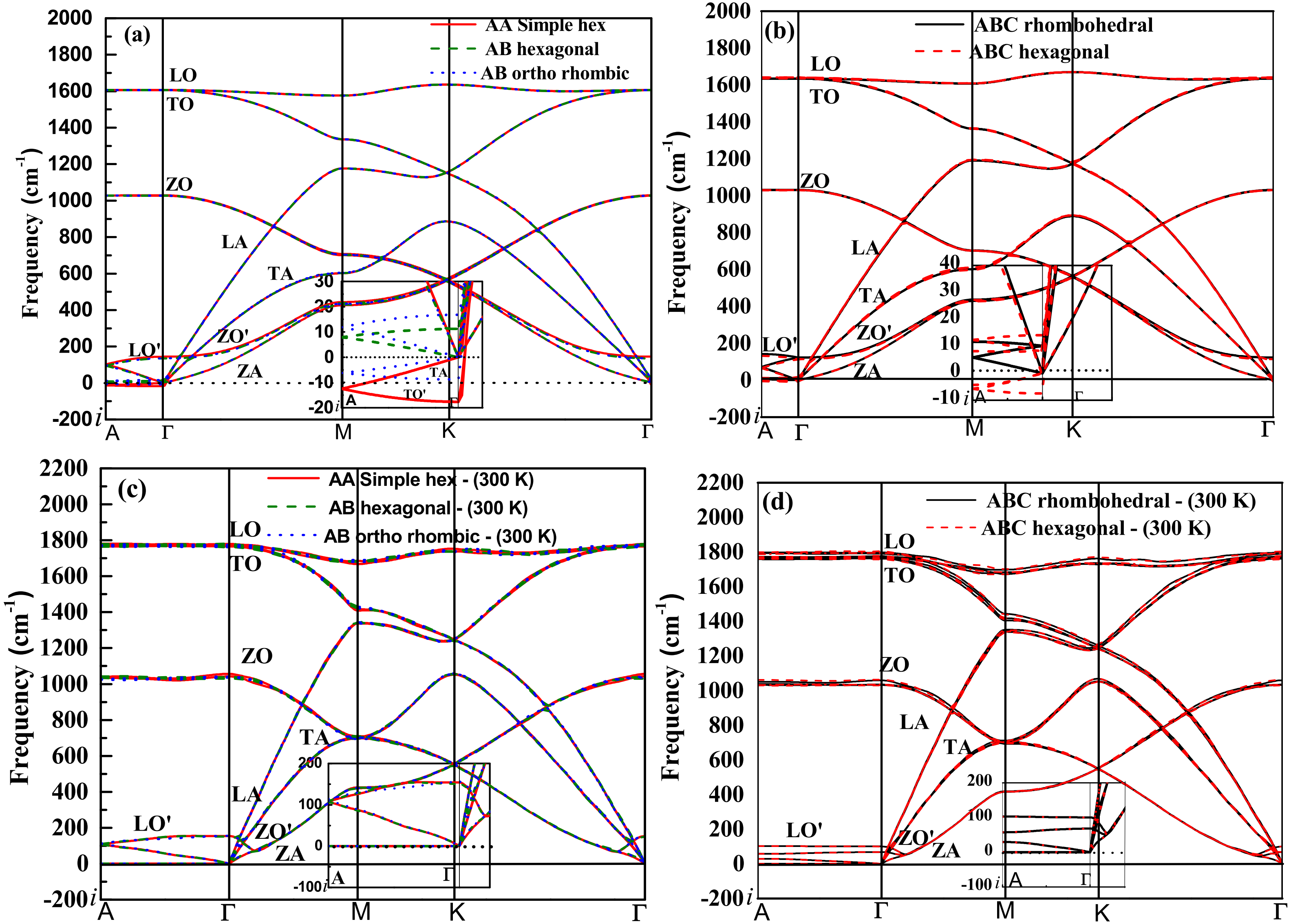

Figure 3.9 – (a&b) Lattice dynamics of bilayer and trilayer graphite structures (at 0 K); (c&d) The phonon dispersion calculated from MD simulations at 300 K. The insets shows the enlarged view along Γ-A direction.

parabola the above possibility is eliminated in these cases. Another possibility is that there may be some structure relaxation at elevated temperatures. To study the structural relaxation at higher temperatures, the radial distribution functions (RDF) are calculated for all the structures. Figure 3.10a shows the RDF of bilayer structures calculated at 300 K. The peak positions of AA-simple hexagonal and AB-orthorhombic structures are identical to that of AB-hexagonal structure, this may lead to a conclusion that the unstable bilayer structures are reverting back to the stable AB-hexagonal structures at 300 K. Hence the imaginary frequencies along the Γ-A direction disappears in all bi-layer structures at 300 K. Similarly the RDF of ABC-hexagonal and ABC-rhombohedral structures are identical (Figure 3.10b), it may tempt to conclude that ABC-hexagonal structures are falling back to ABC-rhombohedral structures. The similarity in phonon dispersion strengthens the above arguments.

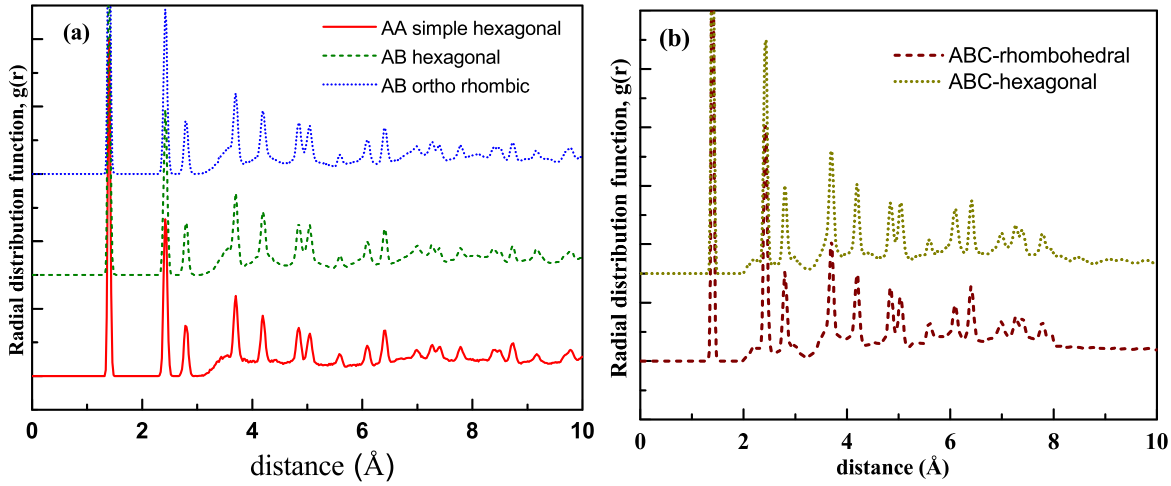

Figure 3.10 – The radial distribution function (RDF) of (a) bilayer graphite structures and (b) trilayer graphite structures computed from MD simulations at 300 K.

3.5 Summary

Ab initio and classical MD simulations have been performed to study the structure, energetics and stability of several plausible stacking sequences in graphite. The key findings of this study are summarized below

- Calculations suggest that in addition to the standard structures, graphite can also exist in AA-simple hexagonal, AB-orthorhombic and ABC-hexagonal type stacking. The free energy difference between these structures is very small ($\sim$1 meV/atom), and hence all structures can coexist from purely energetic considerations.

- Shear elastic constant C_{44} is negative in AA-simple hexagonal, AB-orthorhombic and ABC-hexagonal structures, suggesting that these structures are mechanically unstable. Phonon dispersions show that the frequencies of some modes along the Γ–A direction in the Brillouin zone are imaginary in all of the new structures, implying that these structures are dynamically unstable. Incorporation of zero point vibrational energy via the quasi-harmonic approximation does not result in the restoration of dynamical stability.

- Potential energy surfaces for the unstable normal modes are seen to have the topography of a potential hill for all the new structures, confirming that all of the new structures are inherently unstable. The fact that the potential energy surface is not in the form of a double well implies that the structures are linearly as well as globally unstable.

- The effect of temperature on stability of the above structures are studied using classical MD simulations at 300 K. The phonon dispersion at 0 K is obtained by lattice dynamics methods shows imaginary modes along the Γ- A direction and this is consistent with *ab initio* predictions. The phonon dispersion calculated at 300 K does not have imaginary frequencies along the Γ-A direction. The high temperature structural relaxations are studied from radial distribution functions, and found that the new bilayer/trilayer structures are thermodynamically unstable and revert back to the standard AB-hexagonal/ABC-rhombohedral structures.

Chapter 4

Temperature dependent structural stability and phonon frequency shift of graphene

---

This chapter discusses the temperature dependent structural stability, frequency shift, linewidth and coupling of normal modes of vibrations of free-standing graphene, which are studied using spectral energy density (SED) method. Structural stability of graphene at finite temperatures is analyzed by computing the phonon dispersion using quasi-harmonic, fix-phonon and SED methods. The mode resolved phonon spectra is calculated at Γ*, M and K points in the Brillouin zone to extract the frequency shift, linewidth and coupling of normal modes* of vibrations. *To understand the role of ripples on thermal expansion properties, 2D and 3D simulations are done explicitly at different temperatures.*

4.1 Introduction

Graphene and other allied 2D materials are expected to have tremendous applications in the forthcoming technologies. For such applications, the knowledge on structural, thermal and vibrational properties are mandatory. The thermal expansion of graphene has been studied in detail both theoretically [44–47] and experimentally [48–50]. There are considerable differences between the thermal expansion data obtained from various simulations because of difference in handling anharmonicity in those calculations. Disagreement among experimental data are due to the strain effects induced by substrates. The effect of anharmonicity on phonon frequency shift and linewidth is studied using DFPT calculations [43, 64, 65]. Experimentally, the temperature dependent phonon frequency shift and linewidth of graphene (normally supported on Si/SiO$_2$ substrates) are obtained using Raman spectroscopy [50, 66–68]. The strain effect caused by the substrate prevents a direct comparison of Raman spectra with the results of calculations which pertain to a free-standing graphene.

DFPT based calculations can include anharmonicity upto fourth (maximum) order [43, 64, 65]. Being a strong anharmonic 2D crystal the higher order phonon processes are important in graphene and cannot be neglected [68]. Hence in the present chapter a spectral energy density (SED) formalism (chapter-2, 2.3.5.3) is adapted to probe the complete anharmonicity in free-standing graphene using classical MD simulations. The simulations are done in both isobaric-isothermal (NPT) and canonical (NVT) ensembles to delineate the contributions of thermal expansion and phonon-phonon coupling to the total anharmonic effects. The thermally excited ripples can affect the thermal expansion properties considerably. The quasi-harmonic calculations cannot incorporate the effects of these ripples, where they consider a flat sheet. Moreover quasi-harmonic methods can incorporate only few hundreds of atoms, which is inadequate to model large scale ripples. Hence three-dimensional (3D) and two-dimensional (2D) molecular dynamics (MD) simulations are done to delineate the role of thermally excited ripples on thermal expansion properties explicitly.

4.2 Computational methods

All the simulations are performed using the classical MD simulation package LAMMPS [179]. The interaction between the carbon atoms in the honeycomb lattice of graphene is modeled using the long range bond order potential (LCBOP) [147]. Magnin *et al*

[216] have investigated the finite temperature effect on the $\boldsymbol{a}$-lattice of free-standing graphene using various semi-empirical potentials, and concluded that LCBOP potential shows better agreement with their reference data near the room temperature. The LCBOP potential successfully combines the strong in-plane covalent bonding and weak intermolecular interactions that are significant for describing breaking and making of bonds, and is used to account for the interaction between the carbon atoms in the honeycomb lattice of graphene. The interaction energy defined by LCBOP [147] potential is

$$E_b = \frac{1}{2}\sum_{i,j}^{N} V_{i,j}^{tot} = \frac{1}{2}\sum_{i,j}^{N}\left[f_{c,i,j}V_{i,j}^{SR} + S_{i,j}V_{i,j}^{LR}\right] \tag{4.1}$$

where $f_{c,i,j}V_{i,j}^{SR}$ describes the short range covalent bonding, and the long range interaction is given by $S_{i,j}V_{i,j}^{LR}$. The LCBOP potential is a combination of the short range bond order potential and a long range radial potential. It accurately describes bond distances, conjugation, stretching force constants, elastic constants and interlayer interaction energy in graphite [147].

The 2D unitcell of graphene is as shown in figure 4.1. The graphene sheet forms a honeycomb lattice with a C-C nearest neighbor distance of 1.42 Å. The simulations are carried out in three dimensions with periodic boundary condition along all the three directions. In order to ensure that the interaction of the graphene layer with its replicas is negligible an inter-planar vacuum separation of 25 Å is provided between the layers. A supercell of size 6×6×1 (72 atoms) is used to obtain the phonon dispersion and phonon density of states (Phonon DOS) at 0 K by LD method (chapter-2, 2.4). The finite temperature properties are computed by resorting to classical MD simulations. The size of the simulation cell is chosen in such a manner that the temperature and pressure of the system stabilizes to the required value. A supercell of size 70×70×1 (9800 atoms) is adequate, in this respect, for graphene. Moreover, the 70×70×1 supercell is sufficiently large to incorporate the effect of thermally excited ripples, which are known to stabilize free-standing graphene sheet [41]. The computational procedure is same as given in chapter-2 (2.4.2). The Nyquist theorem demands that the velocities of all the atoms should be sampled at least every 10 fs. In the present simulations the velocities have been sampled at every 5 fs. The simulations are carried out for 3.2 ns.

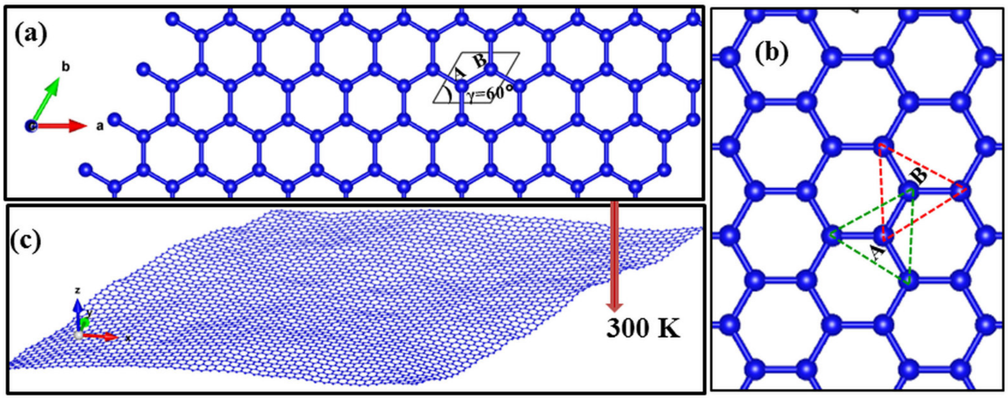

Figure 4.1 – (a) The graphene honeycomb lattice at 0 K. The unitcell is defined using a rhombus; the inequivalent carbon atoms are situated in A and B sites. (b) Alternatively, the unitcell can be visualized as two interpenetrating triangular sub-lattices, the atoms (A and B) are situated at the centers of triangles. (c) The graphene sheet at 300 K with corrugations due to the thermally excited ripples. Such corrugations are seen in the simulations carried out at all nonzero temperatures.

4.3 Results and discussions

4.3.1 Lattice parameter and linear thermal expansion coefficient (LTEC)

The behaviour of in-plane lattice parameter ($\boldsymbol{a}$-lattice) and linear thermal expansion coefficient (LTEC) of graphene are studied as a function of temperature. The simulation box contains 9800 atoms, and the dimensions of the box are L_x=172.15 Å, L_y=149.09 Å and L_z=25 Å. The variation of lattice parameters are monitored in NPT ensemble. Figure 4.2 displays the temperature dependence of $\boldsymbol{a}$-lattice. The LTEC is computed by direct numerical differentiation of the above data.

$$\alpha\left(T\right)=\frac{1}{a\left(T\right)}\frac{da\left(T\right)}{dT} \tag{4.2}$$

The $\boldsymbol{a}$-lattice *contracts* with increasing temperature upto ∼1300 K, and it *expands* thereafter. The LTEC remains negative upto ∼1300 K and then changes its sign from negative to positive. The LTEC is $\alpha_a = -4.300\times10^{-6}\,\mathrm{K}^{-1}$ at 300 K, which matches well with the previous reports [45]. Based on DFPT calculations in conjunction with QHA, Mounet and Marzari [44] reported that the in-plane thermal expansion coefficient of graphene continues to be *negative* up to 2300 K. Zakhrchenko *et al* [45] calculated the finite temperature properties of graphene by MC simulations using LCBOPII potential and predict that both the $\boldsymbol{a}$-lattice and average nearest neighbor distance (R_{nn}) *decrease* when temperature increases and this trend continues up to 900 K. They attribute this anomalous behavior to low frequency bending phonon modes [58]. The thermal expansion coefficient matches with the results of Mounet and Marzari [44] up to 500 K, it continues to be negative up to 900 K and then changes the sign. The above disagreement between the quasi-harmonic theory and MC simulations may be due to the strong anharmonicity associated with the graphene lattice which is not incorporated properly in the quasi-harmonic approximation [45]. Pozzo *et al* [46] performed *ab initio* MD simulations on free-standing and supported graphene and found that the average C-C distance increases with temperature in both free-standing and supported graphene sheets. The authors observed that unlike the increasing trend shown by the C-C nearest neighbor distance, the $\boldsymbol{a}$-lattice *decreases* with temperature (up to 2000 K) in free-standing graphene [41]. They also observed a simulation cell size dependence arising from the presence of long wave length ripples. At low temperatures our LTEC data matches qualitatively with the predictions of Mounet [44] and Zakhrchenko [45] *et al.* The disagreement among the high temperature data obtained through quasi-harmonic, MC and MD simulations is due to the difference in handling the anharmonicity, which is more pronounced at higher temperatures. The behaviour of LTEC is also sensitive to type of interaction between the C-C atoms, which has been discussed in reference [216].

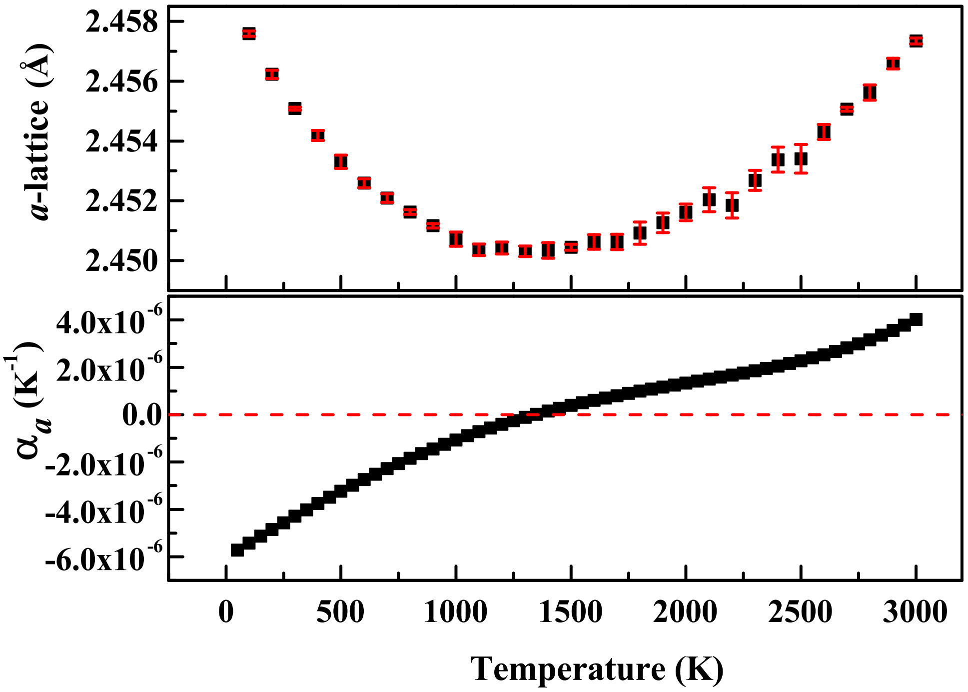

Figure 4.2 – (top) temperature dependent in-plane lattice parameter (***a***-lattice) and (bottom) linear thermal expansion coefficient (LTEC)

4.3.2 Phonon dispersion and structural stability

Lattice dynamics calculations are done at equilibrium ***a***-lattice (2.459 Å) to obtain the phonon dispersion and polarization vectors at 0 K. The dynamical matrix and phonon frequencies are obtained using LCBOP potential under harmonic approximation. The unitcell of graphene contains 2 basis atoms, and hence there are six modes in the phonon dispersion (three acoustic (A) + three optic (O) modes, Figure 4.3). The letters L, T and Z are used to represent the longitudinal, transverse and out-of-plane modes. The ZO modes are considerably softer than LO and TO modes due to the higher freedom of the basis atoms to move along the Z direction [63]. The LO and TO modes are degenerate at Γ point, and they are designated as LO/TO. The LO and LA, ZO and ZA modes are degenerate and show a linear crossing at K point. The doubly degenerate phonon modes arise as a consequence of the C_{3v} symmetry. Since graphene is a non-polar material, any splitting of ZA/ZO or LA/LO modes at K point is in violation of C_{3v} symmetry. However, the ZA/ZO degeneracy at K point may be lifted if there is a reduction of C_{3v} symmetry. Allard *et al* [217] showed that such a reduction in symmetry and the consequent lifting of the degeneracy occurs in graphene on Ni(111) substrate. From the symmetry considerations it is found that bending (out-of-plane) modes are not coupled with in-plane vibrations [218].

Figure 4.3 shows the phonon dispersion of graphene, where the green dot-dash curve is obtained from LD, the red solid curves are computed using quasi-harmonic lattice dynamics (QH-LD) (the terminology QH-LD is used to represent the phonon frequencies computed at temperature dependent lattice parameter, which is obtained from MD simulations), the blue dash lines and thick black lines are calculated from MD simulations (at 300 K) using *fix-phonon* and SED methods (chapter-*2*, 2.3.5.3). The recent experimental data of graphene are shown as symbols [76–80]. The LD frequencies match with previous calculations [63] and the agreement with the experiments is satisfactory. The in-plane acoustic modes (LA and TA) show very good agreement with experimental data, whereas the optic modes (LO/TO) slightly deviate from the experiments at Γ point. Table 4.1 shows the comparison of LD and MD with experiments at high symmetry points in the Brillouin zone. The LCBOP potential underestimates the ZO mode frequency by 0.4 % at Γ point. Similarly the computed LO/TO modes frequency is 3 % lower with respect to experimental data at Γ point. The LCBOP potential reproduced the quadratic dispersion of ZA mode, but there is a significant reduction in the frequency along Γ-M direction, and this may be due to the strong temperature dependence of this mode [63]. While the LA and TA modes show excellent agreement with experimental data along Γ -M direction, the TA modes are overestimated by 14 % at M point. Similarly the frequency of linear crossing of ZA/ZO modes at K point is underestimated by 13 %.

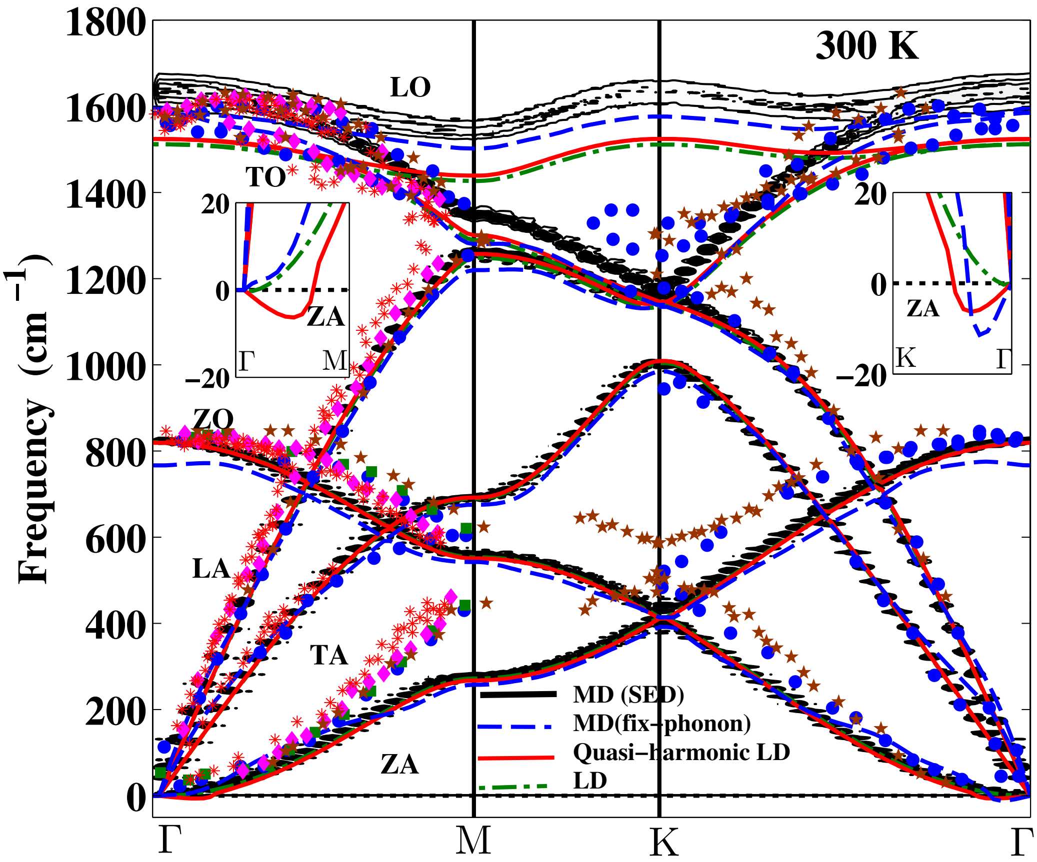

Figure 4.3 – The phonon dispersion of graphene. The green dot-dash lines are from LD calculations at equilibrium lattice parameter, the red solid curves are computed using quasi-harmonic lattice dynamics, the blue dash lines and thick black lines are obtained directly from MD simulations (at 300 K) using *fix-phonon* and SED method respectively. Insets shows the instability of ZA mode along Γ-M (quasi-harmonic LD) and K-Γ (quasi-harmonic LD and *fix-phonon* method) direction. The experimental data corresponding to blue circles, green squares, magenta diamonds, red stars, and brown pentagons are obtained respectively from the references [76–80]. There is an upshift of LO/TO phonon frequencies at 300 K (from MD) with respect to the 0 K frequencies (from LD).

The phonon dispersion obtained by MD simulations (at 300 K) shows a blue-shift of LO/TO mode with respect to the LD calculations. This blue-shift in frequency is due to the thermal contraction of $\boldsymbol{a}$-lattice and/or anharmonic phonon-phonon coupling. The thermal contraction of $\boldsymbol{a}$-lattice causes an increase in the in-plane force constants and hence there is an upshift in the LO/TO mode frequency. Unlike to the quasi-harmonic and *fix-phonon* method the phonon dispersion obtained using SED method shows a temperature dependent broadening of each branch (Figure 4.3). The width of

Table 4.1 – The phonon frequencies at high symmetry points in the Brillouin zone. The frequencies are expressed in cm^{-1} units. The results of LD calculations are compared with those obtained from MD simulations using SED method (at 300 K) and experiments.^{a}Reference [76], ^{b}Reference [77], ^{c}Reference [78], ^{d}Reference [79], ^{e}Reference [80]

	Γ			**M**			**K**		
Mode	LD	MD	expt.	LD	MD	expt.	LD	MD	expt.
ZA	0	0		272.39	277.72	422.91^{a}, 437.56^{b}	414.58	422.91	475.86^{a}, 483.18^{e}
TA	0	0		689.31	692.00	604.06^{a}, 628.70^{e}	1003.66	1008.99	944.06^{a}
LA	0	0		1248.08	1262.07	1253.41^{a}, 1239.76^{c}	1136.20	1172.16	1193.14^{a}
ZO	820.20	825.17	823.18^{a}, 822.84^{b}	553.45	558.44	620.71^{b}, 604.06^{d}	414.59	422.91	521.15^{a}, 592.07^{e}
LO	1511.82	1637.30	1555.44^{a}, 1577.75^{d}	1285.38	1348.00	1382.00^{a}, 1383.95^{c}	1136.20	1172.16	1298.7^{a}, 1225.77^{e}
TO	1511.82	1630.03	1555.44^{a}, 1577.75^{d}	1426.90	1541.80	1389.28^{a}	1510.16	1631.7	1321.34^{a}, 1309.23^{e}

each branch is inversely proportional to the lifetime of the corresponding mode. The increase in width of LO and TO modes at 300 K is a result of higher order phonon scattering processes. The ZO mode frequency obtained from MD simulation is 0.2 % higher than the experimental value. Similarly the LO/TO mode frequency is 5.2 % higher when compared to experiments at Γ point.

At 300 K, the quasi-harmonic ZA (bending) mode shows an instability along Γ-M and K-Γdirection (Figure 4.3). Similarly the ZA mode obtained from *fix-phonon* method is also shows an instability along K-Γdirection (Figure 4.3). This indicates a structural instability of flat 2D-graphene sheets, which arises when the $\boldsymbol{a}$-lattice is reduced below the equilibrium value as reported in *ab initio* calculations [219]. But the ZA mode obtained from MD simulations using SED method doesn't show the above structural instability. This is due to the fact that the quasi-harmonic and *fix-phonon* methods includes only the anharmonic effect that arises from the thermal contraction/expansion of $\boldsymbol{a}$-lattice. In addition to the thermal contraction/expansion of $\boldsymbol{a}$-lattice, the entire phonon-phonon scattering processes are included naturally in MD phonon dispersion obtained using SED method; this strong phonon-phonon coupling stabilizes the structure of graphene at higher temperatures. This exemplifies the Mermin-Wagner theorem [39]. In the case of graphene sheet, the strong coupling between the in-plane stretching and out-of-plane bending mode suppresses the effect of thermal fluctuations and leads to ripples on the surface. These ripples stabilize a free-standing graphene sheet [41].

Figure 4.4 shows the phonon dispersions of graphene at different temperatures (100, 1000 and 2000 K)[1]. The instability of quasi-harmonic ZA mode along Γ-M and K-Γ directions are conspicuous at these temperatures (Figure 4.4d&e). As discussed earlier, the phonon dispersions obtained from SED method at these temperatures restores the dynamical stability of the system, by incorporating the higher order

---

[1] The *fix-phonon* methods is used to compute the phonon dispersion only at 300 K, since it fails to incorporate the full anharmonicity, we didn't use this method in further calculations

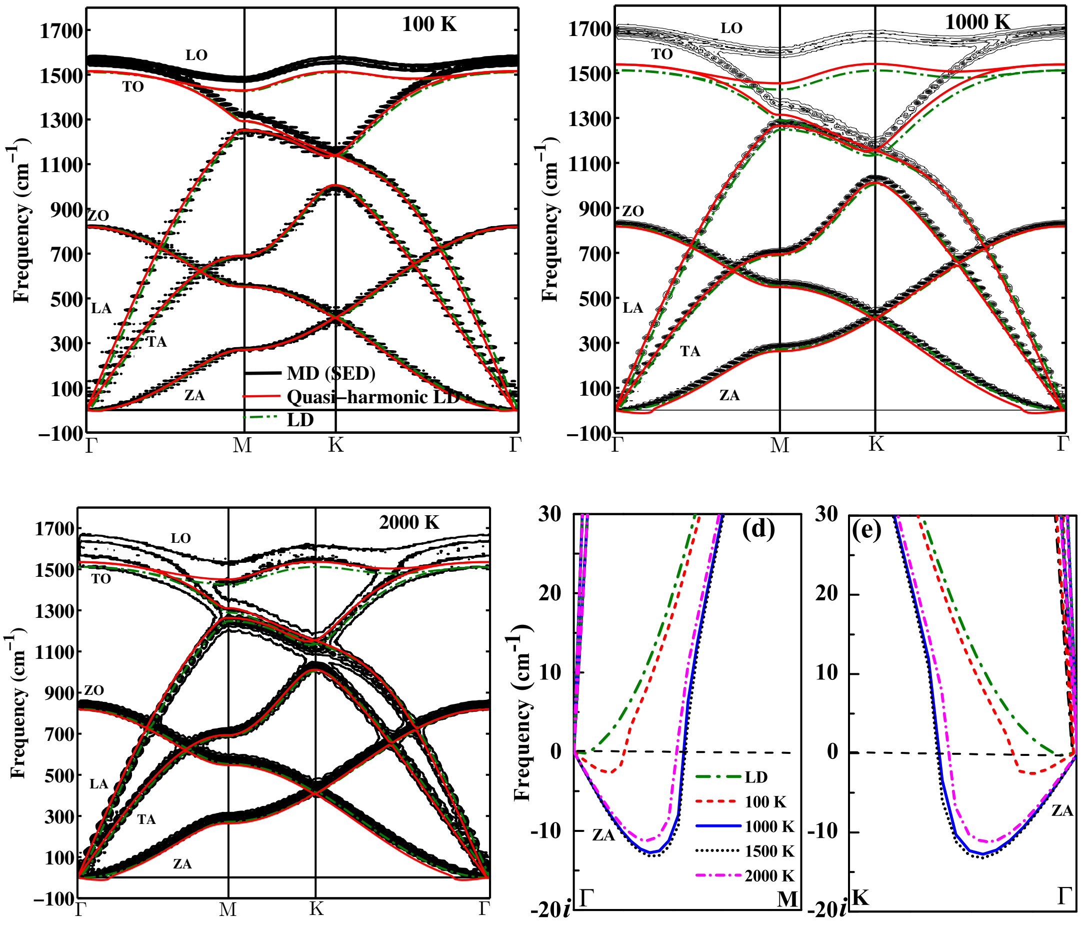

Figure 4.4 – The phonon dispersion of graphene at different temperatures. The green dot-dash line is from LD calculation at equilibrium in-plane lattice parameter ($\boldsymbol{a}$-lattice). The red solid curves are obtained from quasi-harmonic lattice dynamics. The thick black curve is obtained directly from MD simulations using SED method. There is an upshift of LO/TO mode frequency (obtained from MD simulations) with temperature. The quasi-harmonic ZA mode becomes imaginary along Γ−M and K-Γ directions. (d&e) quasi-harmonic ZA mode (zoomed along Γ−M and K-Γ directions) at different temperatures.

phonon-phonon coupling processes. As temperature increases from 100 K to 2000 K, there is an upshift of LO/TO optic modes with respect to the frequency obtained from LD and quasi-harmonic calculations. The ZO mode also shows a blue-shift in frequency, but not as significant as in the case of the LO/TO modes.

The Phonon DOS of graphene is calculated by computing the Fourier transform of the velocity-velocity auto correlation function (VACF) (chapter-2, 2.3.5.1). Figure 4.5 shows the phonon DOS at different temperature. The dotted lines represent the frequency of different branches at various high symmetry points. The shoulder at frequency ω = 0 cm^{-1} is coming from ZA branch at Γ point, which is flat around this point. The ZA mode at M point peaks at ω = 277.72 cm^{-1}, and the ZA mode frequency shifts to higher frequencies as the temperature increases. The degenerate ZA/ZO mode at K point shows a dip around 422.91 cm^{-1}, which shifts to higher frequency as temperature increases. The out-of-plane optic mode (ZO) peaks around 558.44 cm^{-1} (at M point) and 829.17 cm^{-1}(Γ point) also exhibits a blue- shift in frequency with temperature. The in-plane optic modes (LO/ TO) show a clear shift to the higher frequency side of the spectrum upto ∼1300 K .

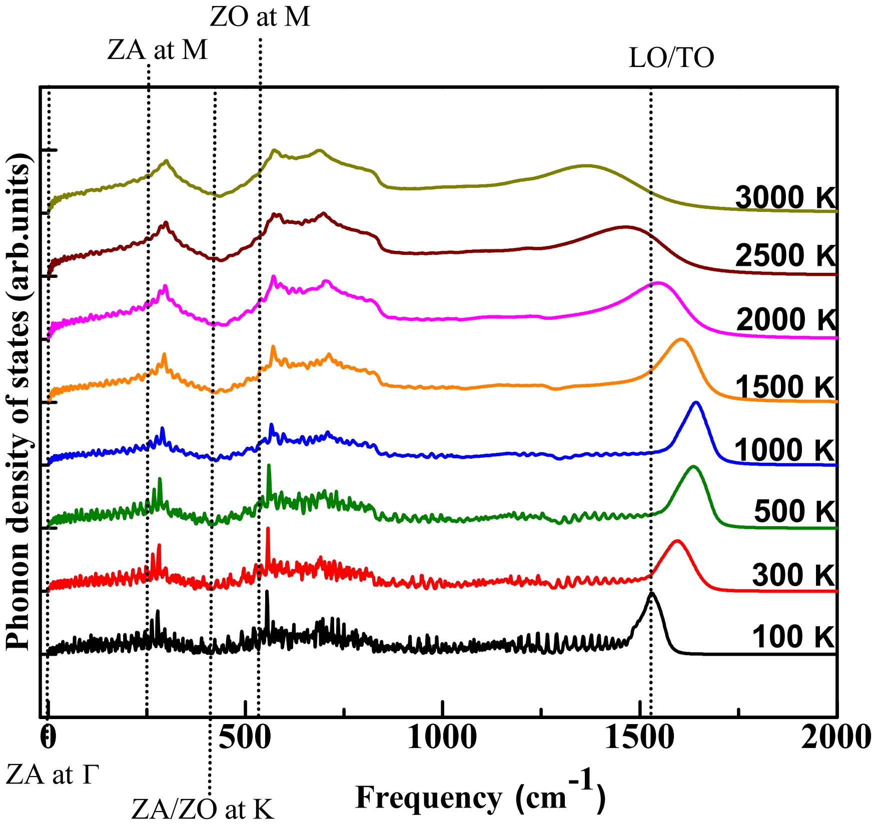

Figure 4.5 – The phonon density of states of graphene at different temperatures. The high frequency optic modes get blue shifted with temperature upto ∼1300 K. The vertical lines (short dash) represent the peak positions obtained from LD calculations.

4.3.3 Temperature dependence of Γ point optic phonon modes

In the previous section, a blue-shift of LO/TO and ZO mode frequencies is observed with an increase in temperature. To analyze the above blue-shift, the mode-resolved phonon spectra at Γ point is computed as a function of temperature. It is found from group theoretical analysis of graphene that the degenerate LO/TO modes at Γ point involve vibrations of atoms in sublattice A against those in sublattice B (Figure 4.1b) and they belong to the E_{2g} representation [66]. The G peak (E_{2g} symmetry) at ∼1580 cm^{-1} is the only Raman active mode at Γ point and it arises from the first order Raman scattering process. The defect induced D peak at ∼1350 cm^{-1} arises from the breathing modes of six-membered rings of carbon atoms, and involves a TO mode and a defect near the K point of Brillouin zone. The D' peak at ∼1620 cm^{-1} is the weak disorder induced peak, which comes from the intra-valley double-resonance process. The G' (2D) peak at ∼2700 cm^{-1} is the overtone of D peak and comes from the second order Raman scattering process of zone boundary phonons. The D and G' peaks arise from the inter-valley double resonance process, in which the phonon wave-vectors ($\overline{q}$) associated with D and G' peaks will couple to electronic states with wave-vectors ($\overline{k}$) at K point in the Brillouin zone [66, 220]. Since electron-phonon coupling cannot be incorporated in classical MD simulations, the G' peak will not be considered in this study. The simulations are done using perfect graphene sheet, and hence the defect induced D and D' peaks will not appear in these simulations.

In the case of graphite, the E_{2g} mode splits into two nearly degenerate modes such as E_{2g} (Raman active, at 1580 cm^{-1}) and E_{1u} (IR active mode, at 1588 cm^{-1}) [221]. The ZO mode corresponds to out-of-plane atomic displacement and belongs to B_{2g} representation and it is neither Raman nor IR active. In graphite the degeneracy in the B_{2g} mode is lifted and it splits into the B_{2g} mode and an A_{2u} mode (IR active, 868 cm^{-1}) [221]. In table 4.2 we compare the results of simulations with those from Raman and IR scattering experiments at 300 K.

Table 4.2 – Comparison of the frequencies of Γ point LO/TO and ZO modes (in units of cm^{-1}) at 300 K with IR and Raman scattering experiments for graphene and graphite. ^{a}Reference [220], ^{b}Reference [221]

mode	simulation	graphene-Raman	graphene-IR	graphite-Raman	graphite-IR
LO/TO (E_{2g} or G-peak)	1637.03	1580.09^a (E_{2g})	inactive	1580.09^a (E_{2g})	1588.08^b(E_{1u})
ZO	825.17	inactive	inactive	inactive	867.80^b (A_{2u})

LD calculations using LCBOP potential predicts the peak position of LO/TO modes at Γ point to be 1511.72 cm^{-1} at 0 K. As temperature increases the LO/TO mode frequency shows a blue-shift (Figure 4.6). Similarly the ZO mode at 0 K peaks at 820.18 cm^{-1} and shows a slight blue-shift with temperature. The shift in phonon frequency and change in phonon linewidth with temperature are due to the anharmonicity in the effective interaction between the atoms. Effect of anharmonicity can be separated into two parts: one that comes from the anharmonic coupling of phonon modes (self-energy change) and the other that arises from the thermal expansion/contraction of the crystal. Thermal expansion/contraction leads to decrease/increase in the values of the force constants and hence a shift in the mode frequencies. On the other hand, the coupling between the phonon modes leads to finite lifetime (nonzero width) apart from a shift in the mode frequency. The phonon frequency shift with temperature that arises purely due to anharmonic coupling of phonon modes, can be obtained from the constant volume simulations/experiments [67, 222]. Since most of experiments are performed at constant pressure, the observed frequency shift arises from the combination of thermal expansion and self-energy change. In the present work we decouple this self energy change and thermal expansion contributions by performing constant volume (NVT ensemble) and constant pressure (NPT ensemble) simulations.

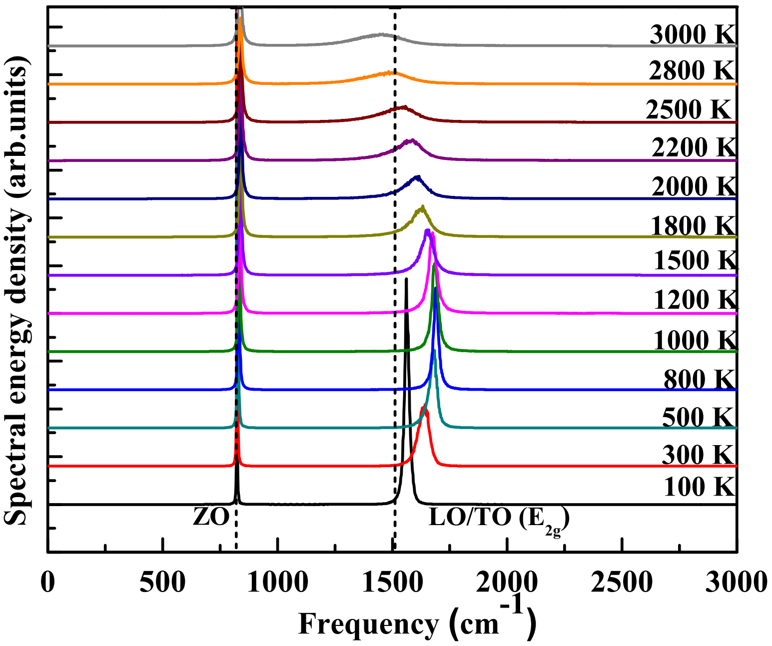

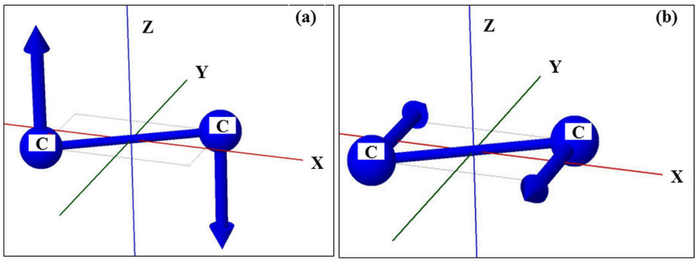

Figure 4.6 – The ZO and LO/TO frequencies at Γ point as a function of temperature. The vertical lines (short dash) represent the peak positions of ZO and LO/TO frequency obtained from LD calculations. The ZO and LO/TO mode frequencies show a blue shift with temperature when compared to LD calculations. (bottom) The eigenvectors corresponds to (a) ZO and (b)/LO/TO mode

The exact peak position and linewidth is computed by fitting a Lorentzian to the frequency spread (chapter-2, equation 2.72). Figures 4.7 a&b show the shift in LO/TO and ZO frequency with temperature. The quasi-harmonic frequencies computed at temperature dependent ***a***-lattices, showing a blue-shift in the LO/TO mode frequency, and it peaks at ∼1300 K, where the thermal contraction of ***a***-*lattice is a maximum.* This sensitive behavior of LO/TO mode frequency with respect to small change in the ***a***-lattice was reported by Wirtz *et al* [56] using *ab initio* calculations. Both NVT and NPT ensemble simulations are showing a blue-shift of LO/TO mode frequencies. The NVT ensemble shift is purely due to anharmonic phonon-phonon coupling, while NPT ensemble shift is an outcome of anharmonic phonon-phonon coupling as well as the thermal contraction of $\boldsymbol{a}$-lattice. The difference between NVT and NPT simulations is more apparent in the temperature range of 700 K - 1300 K which indicates that thermal contraction of graphene is maximum in this temperature range. From the above discussion it can be concluded that the thermal contraction of inpane lattice leads to a blue-shift in quasi-harmonic mode frequency, but when only phonon-phonon coupling is introduced (NVT ensemble) the blue shift becomes more prominent than quasi-harmonic shift. When phonon-phonon coupling and thermal contraction operates together (NPT ensemble), the blue-shift is even more prominent due to additional contribution from thermal contraction. *Hence we can conclude that the strong anharmonic phonon-phonon coupling is the major cause for the observed blue-shift of LO/TO mode frequencies.* There is a cross-over of quasi-harmonic, NVT and NPT ensemble frequencies above 2500 K, which indicates that the effect of phonon-phonon coupling becomes weak when compared to thermal-contraction for temperatures >2500 K.

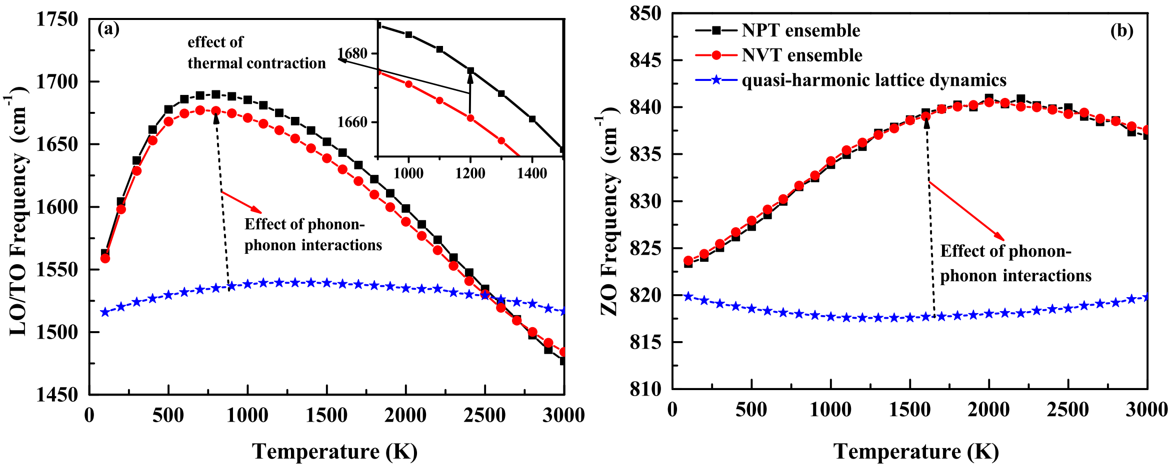

Figure 4.7 – (a) The LO/TO frequency shift with temperature. The inset depicts the contribution from in-plane thermal contraction in the temperature range 900 - 1500 K. (b) The shift in ZO frequency with temperature. *Legends are common for both plots*

A fifth order polynomial fit to describe the variation of phonon frequency with temperature shows a maximum at ~800 K in NPT ensemble. The relative change in the $\boldsymbol{a}$-lattice is small (-0.3%) at 800 K, and it causes 1.5 % shift (23 cm^{-1}) in quasi-harmonic LO/TO frequency. But when we compare the NPT ensemble LO/TO frequency with quasi-harmonic data (at 800 K), there is a considerable upshift (10 %) which is due to strong phonon-phonon scattering process. Bonini *et al* [64] studied the frequency shift of E_{2g} mode as a function of temperature using DFPT implemented in the PWSCF package. These authors found that even though the $\boldsymbol{a}$-lattice contraction would imply an upward shift in frequency, the 3-phonon and 4-phonon scattering processes cause a downward shift. They further showed that the total shift (both from lattice contraction and anharmonic phonon coupling) is downward with temperature (0 K - 800 K). In our simulations the anharmonicity is fully included, and hence all the multi-phonon processes have been taken into account. However, we did not observe any downward shift in the frequency with respect to the values predicted by LD calculation. On the experimental front, a red-shift of the G-peak (E_{2g} mode) is seen in the temperature dependent Raman spectra of graphene sheets [50, 67, 68] which is in qualitative agreement with the above mentioned DFPT calculations. The *ab initio* MD simulations carried out in the temperature range 0 K - 2000 K by Pozzo *et al* [46] show thermal contraction of free-standing graphene for various system sizes. On the other hand, Pozzo *et al* show that thermal expansion occurs for supported graphene sheets in the entire temperature range of simulation, and this might be one of the reasons for the red shift seen in the experiments. In support of this argument, we can see the previous observation of Aizawa *et al* [223], who reported that the in-pane lattice parameter of graphene over TaC(111) substrate is 3 % larger than the bulk graphite, which leads to a considerable softening of zone-centre optical phonons. Later, Rieder *et al* [224], also observed similar softening of optical phonon of monolayer graphite on Ni(111) substrate. Recently, Allard *et al* [217] measured the phonon dispersion of graphene supported on Ni(111) surfaces, and found significant softening of optical phonon for Ni over which graphene layer bonded strongly. The strong coupling between the graphene and substrate causes an increase in $\boldsymbol{a}$-lattice ($\sim$3 %). Yoon *et al* [50] found that the thermal expansion mismatch between the graphene and substrate leads to a strain which also alters the physical properties. Hence we can conclude that the strong binding between the graphene sheet and substrate causes a significant softening of in-plane lattice, and alter the phonon-transport mechanism, and their combined effect may lead to substantial changes in the phonon frequency shift when compared to free-standing graphene.

In graphene the ZO mode is inactive in both Raman and IR scattering experiments. There are no studies to understand the effect of temperature on ZO mode both experimentally and theoretically. Figure 4.7b shows the variation of ZO mode frequency with temperature. The quasi-harmonic ZO mode frequencies show a behaviour opposite to that of LO/TO mode. The mode frequencies decrease with temperature upto ∼1300 K and further increases with temperature. This red-shift of ZO mode quasi-harmonic frequency can be explained using membrane effect [58]. When the thermal contraction occurs the tension in the in-plane lattice grows, which restricts the out-of-plane motion of atoms, leading to a softening of out-of-plane force constants and fall in the mode frequency [44]. Unlike to quasi-harmonic data, the NVT and NPT ensemble frequencies are showing a blue-shift, which is again a consequence of phonon-phonon coupling. The NPT ensemble mode frequency shows a maximum at ∼2060 K and it is slightly lower than the NVT ensemble frequencies due to the membrane effect induced by thermal contraction.

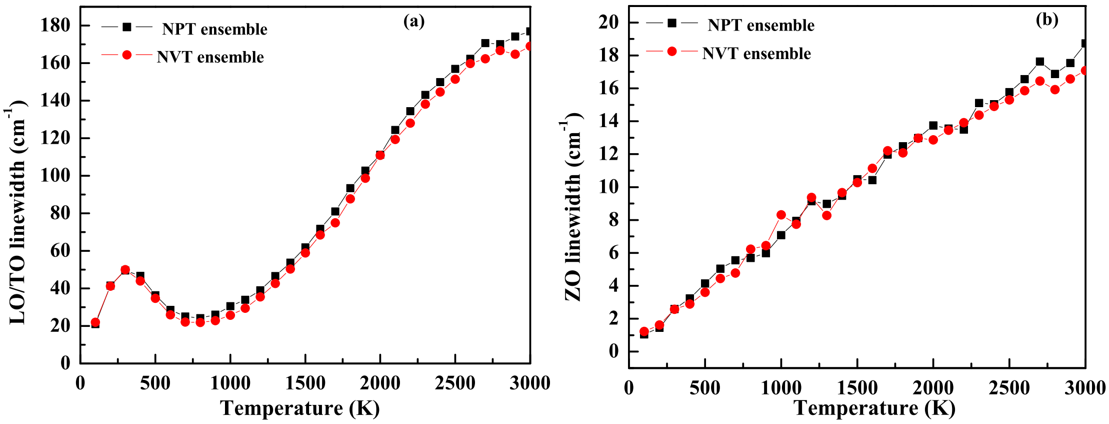

Figure 4.8 – The Phonon linewidth as a function of temperature in NVT and NPT ensemble (a) LO/TO mode (b) ZO mode

Figure 4.8 a&b shows the width of LO/TO and ZO phonon modes at Γ point as a function of temperature. The width of the LO/TO phonons increases with temperature in a non-monotonic manner. There is a local maximum in the temperature range 0 K - 500 K followed by a local minimum in the temperature range 500 K - 1000 K. This unusual behavior is seen in the results obtained with both NVT and NPT ensemble simulations. The phonon processes responsible for such a behavior are currently not known. Furthermore, the pronounced nonlinear increase in width seen at all temperatures is in disagreement with Bonini *et al* [64], who showed that the E_{2g} linewidth decreases with temperature. This occurs in their calculations due to the strong electron-phonon coupling which reduces the linewidth and more than nullifies the increase in linewidth of E_{2g} mode that occurs due to three-phonon process. The temperature dependent Raman spectra of graphene sheets show an increase in linewidth of G peak as a function of temperature [68, 171]. The model calculations including the three-phonon, four-phonon and electron-phonon scattering processes predict an increase in phonon linewidth with temperature which is in agreement with experimental observations [68]. These model calculations suggest that four-phonon scattering process should be incorporated to study the linewidth of G peak at high temperatures. Even though we did not consider the electron-phonon coupling, the phonon linewidth increases with temperature in our simulations, which may be due to the contribution from higher order phonon scattering processes. This is in agreement with previous experimental result [171], where it was found that the broadening of G peak as a function of temperature is an outcome of higher order anharmonic phonon coupling which becomes more pronounced at higher temperature. The linewidth of ZO mode increases with temperature, and the broadening is less when compared to LO/TO mode. Since ZO mode is inactive in Raman and IR scattering experiments, no experimental results are available for comparison.

To study the anharmonic effect on eigenvectors, the phonon frequency shift and linewidths of ZO and LO/TO modes are computed with and without eigenvectors (chapter-2, 2.4.2.2). Figure 4.9 displays the results obtained in both methods. For LO/TO mode the frequency shift and linewidths computed with and without eigenvectors are identical. In the case of ZO mode the second method predicts a slightly lower frequency shift and linewidth at a given temperature. But this difference ($\triangle\omega_{300\,K}$= -1.5 cm^{-1} and $\triangle\Gamma_{300\,K}$ = -0.47 cm^{-1}) is too small to be significant.

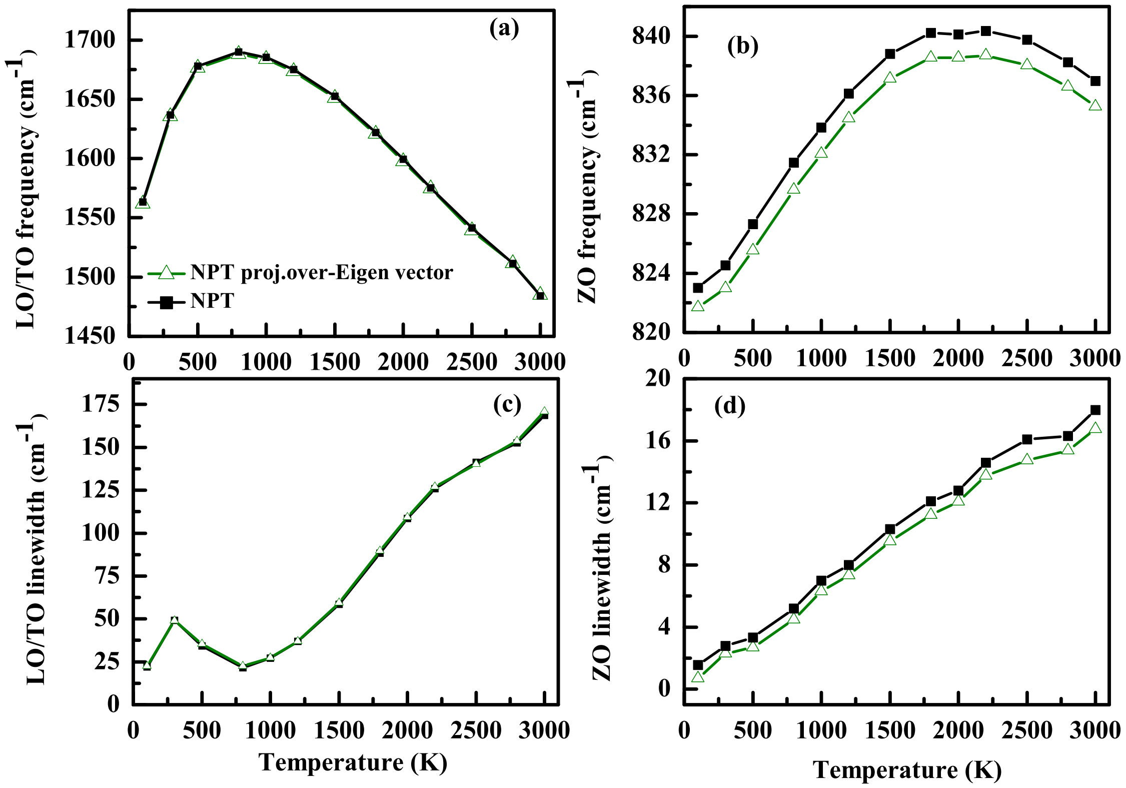

Figure 4.9 – The temperature dependent frequency shift and linewidth of LO/TO and ZO mode. The black squares are computed directly from the Fourier transform of MD based atomic velocity. The green open triangles are obtained by projecting the atomic velocity on to the normal modes of vibration. *Legends are common for all plots*

4.3.4 Anharmonic phonon coupling at Γ, M and K point

In harmonic approximation, the normal modes of vibration of a crystal are, by definition, decoupled from each other. Once such a normal mode is excited, the crystal will continue to vibrate for ever in that mode without any decrease in the amplitude. However, at finite temperature, the modes get coupled due to anharmonicity. This coupling leads to sharing of energy between the modes, thereby causing decay of the vibrational excitations leading to reduction in the intensity of the spectral lines. Furthermore, lifetime of the modes become finite, which is manifested as a finite width of the spectral line. Thus anharmonic coupling of a mode with other modes leads to a decrease in intensity and increase in width of that particular mode. In order to understand the anahrmonic coupling between the phonon modes, we computed the temperature dependent phonon spectra at 500 K and 1000 K at Γ, M and K points and are shown in figure 4.10. LO/TO modes do not get coupled with the other modes at Γ implying that their decay occurs by coupling with phonons at other points in Brillouin zone. At M point, the out-of-plane vibrations (ZO and ZA) are coupled. The high frequency LO and TO optic modes are coupled to LA and TA acoustic modes. At K point, the ZA/ZO and LA/LO modes are not coupled with other modes, and the TO mode gets coupled with TA mode.

4.3.5 Temperature evolution of acoustic phonon modes

To study the temperature evolution of acoustic phonon modes, the mode resolved phonon spectra is computed at M-point in the Brillouin zone. Figure 4.11 shows the frequency shift and linewidth of acoustic modes as a function of temperature. The quasi-harmonic LD frequencies of out-of-plane acoustic (ZA) mode falls with temperature up to ∼1300 K and increases thereafter, this is due to the membrane effect [58]. The ZA-mode frequencies obtained from both NVT and NPT ensemble simulations show a blue-shift. The phonon-phonon coupling effects dominates over the membrane effect, leads to an upshift in ZA-mode frequencies in NVT and NPT ensemble simulations. For transverse acoustic (TA) mode (Figure 4.11b), the quasi-harmonic frequencies increases with temperature upto ∼1300 K, and decreases thereafter. Both NPT and NVT ensemble simulations predicts a large and identical upshift in TA mode frequencies with respects to quasi-harmonic calculations, which is again due to higher order phonon-phonon coupling effects. For longitudinal acoustic (LA) mode (Figure 4.11c), the upshift in quasi-harmonic mode frequencies (upto ∼1000 K) are due to thermal contraction effects. LA mode frequencies obtained from NVT ensemble are

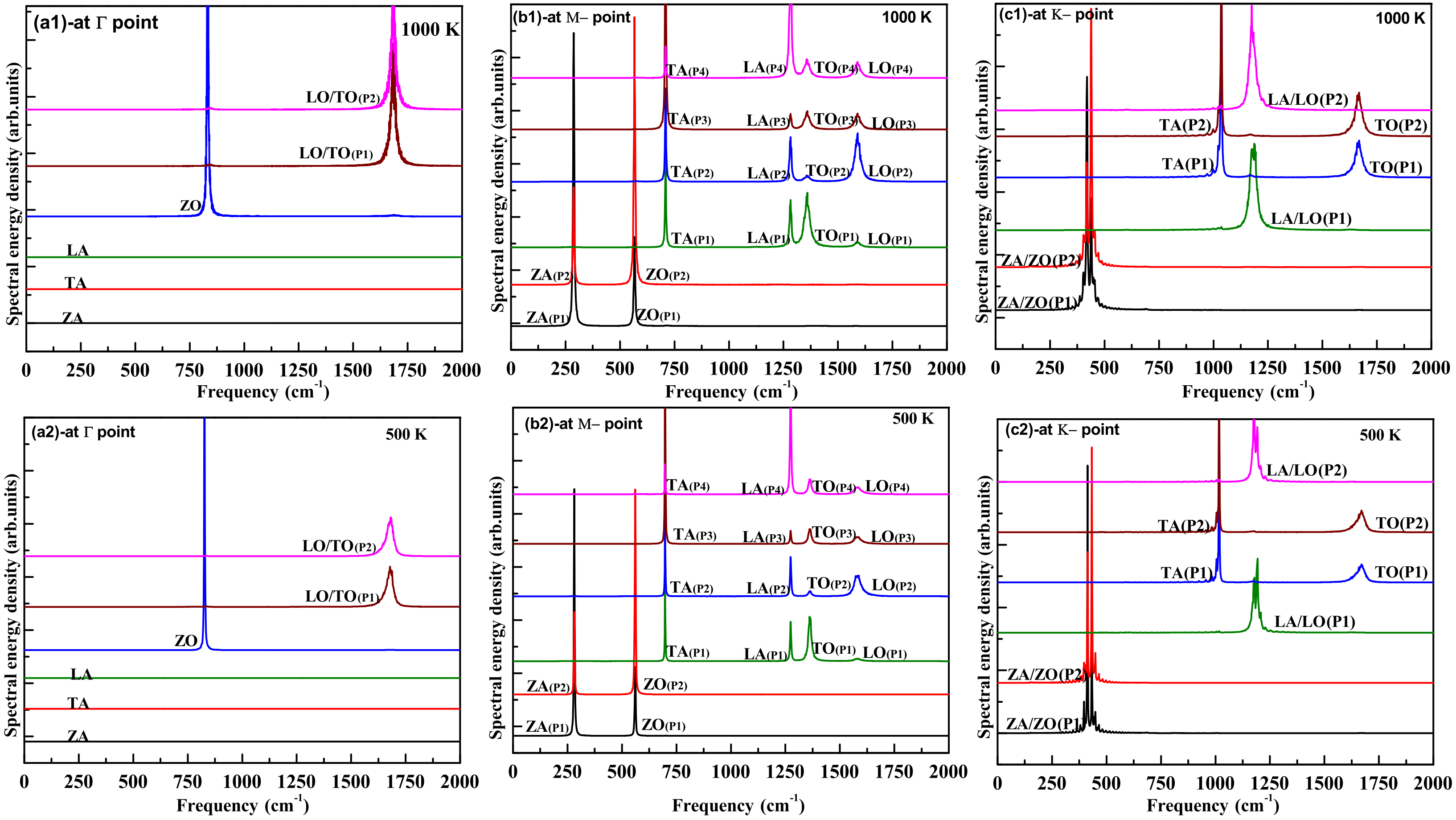

Figure 4.10 – Spectral density is shown at some special points in the Brillouin zone to obtain information about anharmonic coupling of each of the six phonon modes. The modes are labeled as per their polarization at the Γ point and P1, P2, P3 and P4 represent different polarizations. (a) Spectral density at Γ point, which shows that the width of LO/TO modes is higher at 500 K as compared to 1000 K, and LO/TO modes are not coupled with other modes at the Γ point. (b) Spectral density at M point shows that LO-TO modes are getting coupled with LA-TA, and ZO modes are coupled with ZA (c) Spectral density at K point; the ZA/ZO and LA/LO modes are not coupled with other modes and TO mode is coupled with TA mode.

further shifted up with respect to quasi-harmonic predictions. NPT ensemble LA mode frequencies show even higher shift in mode frequencies, this is due to the combined effects of thermal contraction and phonon-phonon coupling. Figure 4.11a1-c1 shows the linewidth of the corresponding acoustic modes. The linewidths of all modes are increasing in a monotonous fashion.

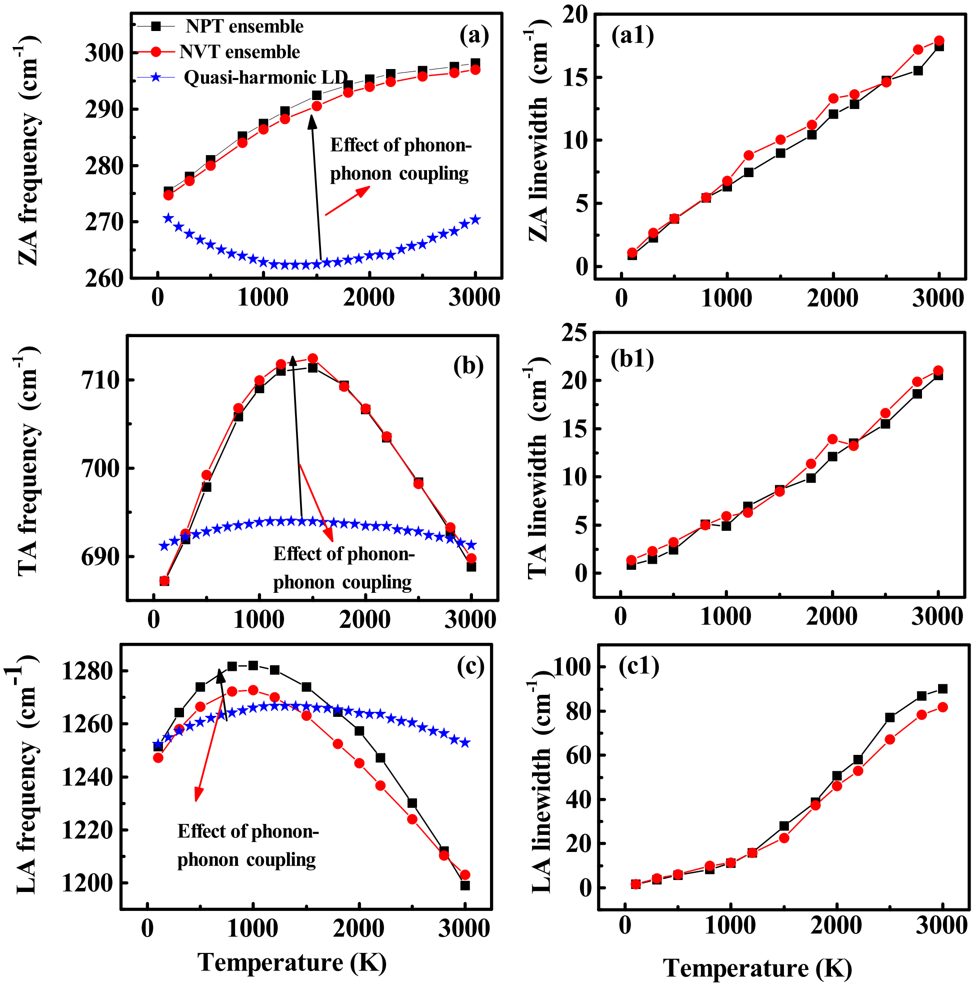

Figure 4.11 – The temperature evolution of acoustic mode at M point in the Brillouin zone. The left panel (a-c) shows the mode frequency shift computed in quasi-harmonic lattice dynamics (blue-star), NVT ensemble (red-sphere) and NPT ensemble (black squares) simulations. The right panel (a1-c1) shows the linewidth of the corresponding modes. *Legends are common for all plots*

4.3.6 Effects of ripples on thermal expansion properties

In order to understand the role of ripples on thermal expansion properties, we explicitly carried out 2D and 3D simulations of very same system at different temperatures. In 2D simulations, we arrested the movement of atoms along the direction normal to the sheet and prevented the formation of thermally excited ripples using *fix enforce2d* command [179]. Ripples are naturally included in 3D simulations and leads to a corrugated surface instead of flat 2D sheet (figure 4.12a). We used simulation cells of various sizes (10×10×1, 30×30×1, 50×50×1, 70×70×1, 100×100×1, 150×150×1) to incorporate the effect of long wavelength ripples. Figure 4.12b&c displays the temperature dependence of ***a***-lattice and linear thermal expansion coefficient (LTEC) of free-standing graphene. In 3D simulations, we found that the a-lattice decreases with an increase in temperature. Fourth order polynomial fit to the above data shows that minima occurs in the temperature range 1300 K - 1400 K, and further it expands with an increase in temperature.

Noteworthy, the temperature evolution of ***a***-lattice is system size dependent (Figure 4.12 b&c). For the simulation cell of size 10×10×1 (contains only 200 atoms) ***a***-lattice shows relatively less contraction with respect to bigger cells and minima occurs around T = 1100 K. The ***a***-lattice shows a convergence from simulation cell of size 70×70×1 (9800 atoms) onwards, and the minima falls in the temperature range of 1300 K - 1400 K (dependence on system size). The similar system size dependence was reported by Pozzo *et al* [46], they used simulation cells of sizes 8×8×1, 10×10×1 and 16×16×1 contains 128, 200 and 512 atoms respectively. The authors found that the thermal contraction of ***a***-lattice is identical at low temperatures for simulations employing cells of various sizes. At 1000 K, ***a***-lattice slightly increases for two smaller simulation cells, while it decreases for the cell of bigger size. This system size dependence of ***a***-lattice is due to the existence of large scale ripples [42] in the actual physical context, which cannot be fitted adequately inside the small simulation cells [46] . Fasolino *et al* [41] observed fluctuations with wavelength of the order of 80 Å at 300 K from their Monte Carlo simulations. To incorporate such long wave length fluctuations bigger simulation cells are required, which makes *ab initio* Car-Parinello simulations prohibitive. In the present study, we used a simulation cell of size 150×150×1 (45000 atoms), is adequate to incorporate all long-wavelength rippling effects.

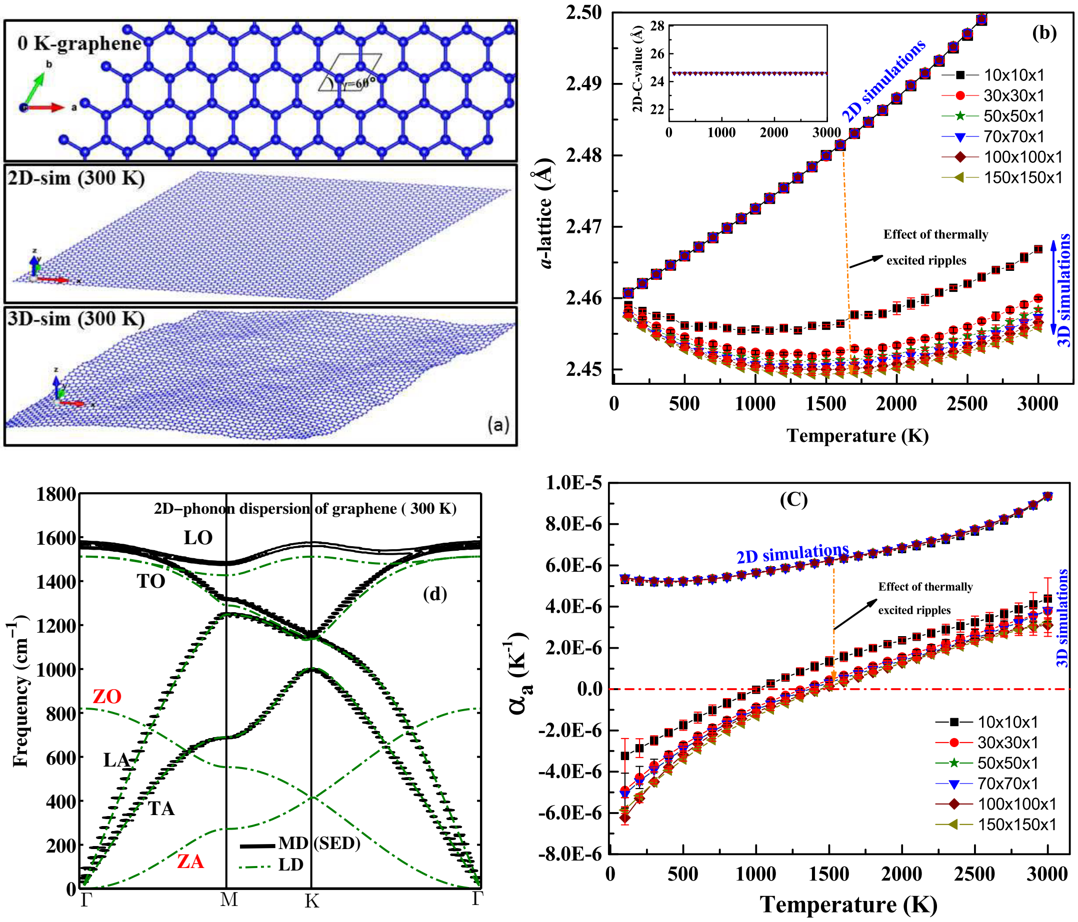

Figure 4.12 – clockwise; (a) snapshots of the sheets obtained from 2D and 3D simulations at 300 K. (b) The temperature evolution of in-plane lattice parameter (***a***-lattice) obtained from 2D and 3D simulations. Inset shows that in 2D simulations the C-value doesn't change with temperature. (c) The linear thermal coefficient (LTEC) as a function of temperature. (d) The phonon dispersion curve of graphene obtained from 2D simulations. The green-dot-dash lines are obtained from lattice dynamics calculations (LD) at 0 K, the thick black line is computed directly from 2D-molecular dynamics simulations using SED method at 300 K.

In 3D simulations, the LTEC is negative for all simulation cells. The LTEC also shows a system size dependence and its value for 10×10×1 simulation cell is roughly half of the value of 150×150×1 cell (table 4.3). The value of LTEC at 300 K ($\alpha_a = -4.300 \times 10^{-6} K^{-1}$) is in qualitative agreement with previous calculations [44, 45, 52]. All simulations predict the LTEC roughly half of the experimental value [48, 50] (table 4.3). Unlike DFPT calculations, present study incorporated the full anharmonicity of interatomic potential, hence the disagreement with experiments may not be due to the strong anharmonic nature of graphene. Though the above experiments has taken care to eliminate the strain effect induced by substrate, more accurate analysis is needed to get a clear picture. To support the above arguments, we can see the previous observation of Pozzo *et al* [46], when the graphene sheet was supported on Ir (111) substrate it shows thermal expansion instead of thermal contraction. Jiang *et al* [47] used Green's function technique and reported that the LTEC is very sensitive to substrate layer interaction. They found that a weak substrate-layer interaction can cause a significant change in the value of LTEC, and if the substrate effects are strong enough, the LTEC can become positive in the whole computed temperature range. Later, Pan *et al* [225], used temperature dependent Raman spectroscopy and measured a lower bound of LTEC (at 300 K ($\alpha_a = -5.5 \times 10^{-6} K^{-1}$)) of graphene which was supported on BN, while Bao *et al* [48] and Yoon *et al* [50] used Si and SiO_2 substrates to support their graphene sheet respectively; this may be one of the reason to have different LTEC in these experiments. Our results, along with the earlier theoretical predictions[44, 45, 52] are in qualitative agreement with Pan *et al* [225].

Table 4.3 – The system size dependence of linear thermal expansion coefficient (LTEC) of graphene at 300 K. In 2D simulations the LTEC are positive and does not show any system size dependence. The LTEC obtained from 3D simulations are negative and show a system size dependence. The data has been compared with the experiments. [a]Reference[225], [b]Reference[48], [c]Reference[49], [d]Reference [50]

simulation cell size	2D simulation $\alpha_a(\times 10^{-6} K^{-1})$	3D simulation $\alpha_a(\times 10^{-6} K^{-1})$	expt. $\alpha_a(\times 10^{-6} K^{-1})$
10×10×1 (200 atoms)	5.178	-2.486	-5.500[a], -7.000[b, c], -8.000[d]
30×30×1 (1800 atoms)	5.226	-3.706	
50×50×1 (5000 atoms)	5.235	-3.907	
70×70×1 (9800 atoms)	5.230	-4.300	
100×100×1 (20000 atoms)	5.243	-4.490	
150×150×1 (45000 atoms)	5.241	-4.524	

Further the 2D simulation results are analyzed (Figure 4.12a&b). In contrast to 3D simulations, ***a***-lattice increases with an increase in temperature for 2D simulation, and it does not show any system size dependence. We compared the LTEC at 300 K in table 4.3. The LTEC obtained from 2D simulations are all positive in sign and does not have any system size dependence (table 4.3). Since there is no movement of atoms along Z direction, rippling effects are absent in 2D simulations, hence ***a***-lattice shows a thermal expansion, and the sign of LTEC is positive in the whole computed temperature range. Here it is concluded that, the long-wavelength ripples have significant effect on thermal expansion properties of free-standing graphene.

Grüneisen theory has been widely used to understand the underlying mechanism behind the thermal contraction or expansion of solids [44, 52, 226]. According to Grüneisen theory, modes with positive Grüneisen parameters will encourage the thermal expansion, while modes with negative Grüneisen parameter will aid thermal contraction. A solid is undergoing thermal expansion or contraction is determined by the balance between the modes with positive and negative Grüneisen parameters [226]. For graphene, the Grüneisen parameters of low lying bending mode (ZA) become large negative (as low as -80). At low temperature only low frequency acoustic modes will be excited, (high frequency optic modes with positive Grüneisen parameters are frozen) and contributes to thermal contraction [44, 52]. The competition between the modes with positive and negative Grüneisen parameters leads to an initial fall of ***a***-lattice and a crossover at a particular temperature (for graphene it is around 1100 K-1400 K). The mode dependent Grüneisen parameters are computed by strain derivative of phonon frequencies which obtained using quasi-harmonic approximation (QHA) [44]. One drawback of above method is that, under certain compressive strain, it is difficult to keep the crystal stable. When compressive strain is large enough, it leads to imaginary frequencies around the Γ point which cannot be used to compute the mode Grüneisen parameters. Due to above limitation, wavevectors are computed with less accurate finite difference algorithm around the Γ point [219] . Moreover in QHA we are using a flat 2D sheet, which is devoid of ripples. Despite the above limitations, Grüneisen theory predicts the thermal expansion of honeycomb structures reasonably well .

Instead of Grüneisen theory based analysis, we computed the phonon dispersion separately from 2D simulations to get a clear picture about the role of each phonon modes on thermal contraction (Figure 4.12d). In 2D dispersion, the in-plane acoustic modes LA and TA shows similar behavior as reported in 3D dispersion (Figure 4.3). The most important point here to note the absence of out-of-plane modes (ZA and ZO). Since we arrested the movement of atoms along Z directions, the branches corresponding to out-of-plane motions are missing in phonon dispersion. This complete absence of ZA and ZO mode, which is responsible for thermal contraction of $\boldsymbol{a}$-lattice at low temperature, is the reason behind the continuous thermal expansion of $\boldsymbol{a}$-lattice in 2D simulations, and this observation is completely agreeing with Grüneisen theory based analysis.

4.4 Summary

A spectral energy density (SED) based formalism is adapted to probe the temperature dependent structural stability, frequency shift, linewidth and coupling of normal modes of vibrations of free-standing graphene. The key findings of this study are summarized below.

- The in-plane lattice parameter ($\boldsymbol{a}$-lattice) of graphene shows thermal contraction upto 1300 K and it expands thereafter.

- Frequency of the bending mode (ZA) becomes imaginary in the quasi-harmonic and *fix-phonon* dispersions at higher temperatures, suggestive of a structural instability. However, the frequency of the ZA mode becomes real in the dispersion obtained from molecular dynamics (MD) simulations using SED method. Dynamical stability to the structure is restored by strong anharmonic coupling of phonon modes which is automatically incorporated in the MD simulations using SED method, whereas it is ignored in the quasi-harmonic and *fix-phonon* dispersion.

- The mode resolved phonon spectra at Γ point show a blue-shift of degenerate longitudinal and transverse (LO/TO) optic modes. The blue-shift observed in canonical (NVT) and isobaric-isothermal (NPT) ensembles are more prominent than the shift predicted by quasi-harmonic approximation due to the additional contribution from phonon-phonon coupling. The out-of-plane optic (ZO) mode frequencies are red-shifted in the quasi-harmonic approximation due to membrane-effect, whereas MD simulations show that the strong phonon-phonon coupling dominates the membrane effect leading to a blue-shift. The linewidth of LO/TO and ZO modes increases non-monotonically with temperature.

- Temperature evolution of acoustic modes are studied at M point in the Brillouin zone. Similar to optic phonon modes, the strong phonon-phonon coupling causes the upshift of ZA, TA and LA mode frequencies.

- The role of ripples on thermal expansion properties of graphene is delineated by performing 2D and 3D simulations of very same system at different temperatures. The 2D $\boldsymbol{a}$-lattice, which is devoid of ripples, shows continuous thermal expansion. At the same time, the $\boldsymbol{a}$-lattice obtained from 3D simulations shows thermal contraction upto 1300 K and further it expands. The discrepancy between 2D and 3D simulations of graphene is due to the absence of out-of-plane bending mode (ZA) in 2D simulations, which is responsible for thermal contraction of $\boldsymbol{a}$-lattice at low temperatures.

Chapter 5

Effect of strong phonon-phonon coupling on structural and vibrational properties of 2D h-BN

2D-h-BN is isostructural to graphene and used as a substrate to graphene based electronics. Knowledge on temperature dependent phonon transport, structural stability and thermal expansion of 2D h-BN is crucial to fabricate graphene/h-BN hybrid nanodevices. This chapter discusses the temperature dependent structural stability, thermal expansion, frequency shift and linewidth of 2D h-BN, which are studied using SED method. The effects of ripples on thermal expansion properties is also discussed.

5.1 Introduction

The 2D h-BN is structural analog of graphene, with B and N atoms located at the corners of hexagons of honeycomb lattice. 2D h-BN geometrically supports graphene due to identical structure, is hence used as a substrate, which retains the quality of suspended graphene sheets [24]. The thermal and vibrational properties of 2D h-BN are studied both theoretically [82–84] and experimentally [87–91]. Being a 2D crystal and analogue of graphene, it is expected to have strong anharmonicity in 2D h-BN also. The thermally excited ripples are inevitable in 2D h-BN, and they can affect the thermal and phonon transport. The temperature dependent structural and vibrational properties of 2D h-BN are not studied in detail, knowledge of these properties is crucial to fabricate nano-devices with better heat dissipation capability. This chapter is devoted to study the finite temperature structural, thermal and vibrational properties of 2D h-BN using spectral energy density (SED) method (chapter-2, 2.3.5.3). The effects of ripples on thermal expansion are analyzed and compared with graphene at end of this chapter.

5.2 Computational methods

All simulations are done using the classical MD simulation package LAMMPS [179]. The interaction between B and N atoms in a honey-comb lattice (Figure 5.1) is modeled using a Tersoff-type [182] interatomic potential, and its functional form can be written as

$$E = \frac{1}{2}\sum_{i}\sum_{j\neq i} V_{ij} \tag{5.1}$$

$$V_{ij} = f_C(r_{ij})\Big[f_R(r_{ij}) + b_{ij} f_A(r_{ij})\Big]$$

,

$$f_C(r) = \begin{cases} 1 & r < R - D, \\ \frac{1}{2} - \frac{1}{2}\, sin\,(\frac{\pi}{2}\frac{r-R}{D} & R - D < r < R + D \\ 0 & r > R + D \end{cases}$$

$$f_R(r) = Aexp(-\lambda_1 r),$$

$$f_A(r) = -Bexp(-\lambda_2 r),$$

$$b_{ij} = (1 + \beta^n \zeta_{ij}^n)^{-\frac{1}{2n}},$$

$$\zeta_{ij} = \sum_{k\neq i,j} f_C(r_{ik}) g(\theta_{ijk}) exp\big[\lambda_3^3 (r_{ij} - r_{ik})^3\big],$$

$$g(\theta) = \left(1 + \frac{c^2}{d^2} - \frac{c^2}{[d^2 + (cos\theta - h)^2]}\right)$$

where f_R and f_A are two-body and three-body terms respectively. The summation is over all the neighbors j and k of atom i within a cut-off radius of $R + D$. The modified cut-off functions f_c guarantees the first nearest neighbour interaction. The bond angle term b_{ij} depends on local coordination of atoms around atom i and angle between atoms i, j, and k (θ_{ijk}). Sevik *et al* [148], developed a set of Tersoff-type potential parameters, that reproduces the experimental phonon dispersion of 2D h-BN effectively. This potential also models the structural, mechanical and thermal properties of 2D h-BN reasonably well [148]. The parametrization of Sevik *et al* [148] is used in this study for further calculations. A supercell of size 70×70×1 (9800 atoms) is created and periodic boundary conditions are employed in all the three directions. A vacuum separation of 25 Å is provided along Z-direction to avoid the unphysical interactions between the periodic images of the 2D h-BN layers. The computational procedure is same as discussed in chapter-2 (2.4.2). The velocities of all atoms are collected at every 5 fs interval. The whole simulations are done for 3.2 ns.

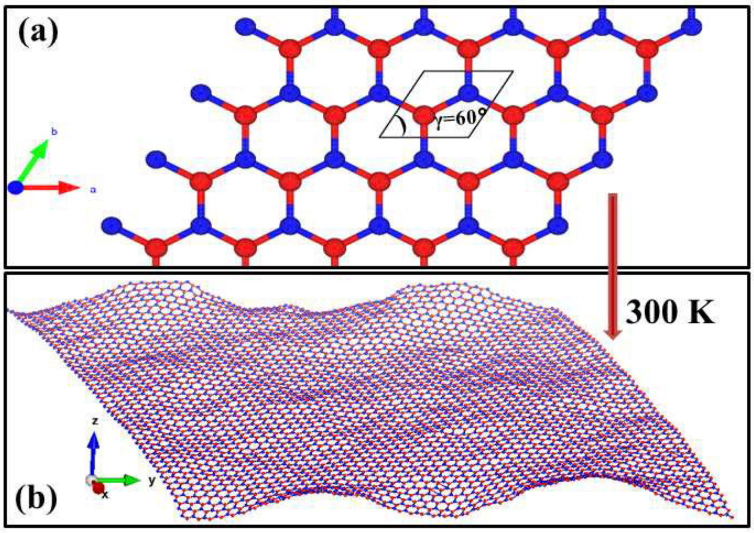

Figure 5.1 – (a) The 2D h-BN at 0 K; the red and blue balls are B and N atoms, respectively. (b) The 2D h-BN sheet at 300 K. Similar to graphene, the 2D flat surface becomes corrugated due to thermally excited ripples

5.3 Results and Discussions

5.3.1 Lattice dynamics (LD) and quasi-harmonic lattice dynamics (QH-LD)

The interatomic potential predicts the equilibrium in-plane lattice parameter (***a***-lattice) of 2D h-BN to be 2.498 Å at T = 0 K, which is close to the experimental value 2.500 Å [227, 228]. The LD calculations (chapter-2, 2.4) are done with various supercells of size 4×4×1, 5×5×1, 6×6×1 and 8×8×1, and the convergence is found in the spectrum of the order of 0.03 cm^{-1} for a supercell of size 6×6×1 (72 atoms) and larger. Hence, we adapted 6×6×1 supercell for LD and quasi-harmonic LD (QH-LD) calculations. The results obtained at equilibrium ***a***-lattice parameter (2.498 Å) (Figure 5.2a) show a very good agreement with previous calculation [148]. The acoustic phonon frequencies around the Γ point obtained using Tersoff potential show an excellent matching with experiment [91], while the optic mode frequencies show deviation from experiments. This is due to the partial ionic nature of h-BN, which can affect optic mode frequencies around the Γ point [82]. This effect is not incorporated in the present potential. This shows that the empirical potential used in the present simulation, albeit being the best in the literature, still needs revision to be able to capture all structural and dynamical aspects of 2D h-BN. Analogous to graphene, the unit cell of 2D h-BN contains 2 basis atom, and hence there are six modes of vibrations. The LA and TA modes are showing linear dispersion around the Γ point, while ZA mode exhibits quadratic dispersion, as found in graphene. Even though BN is a polar material, the macroscopic electric field due to electrostatic interaction does not cause an LO-TO splitting at Γ point because of its 2D nature [85, 86, 229].

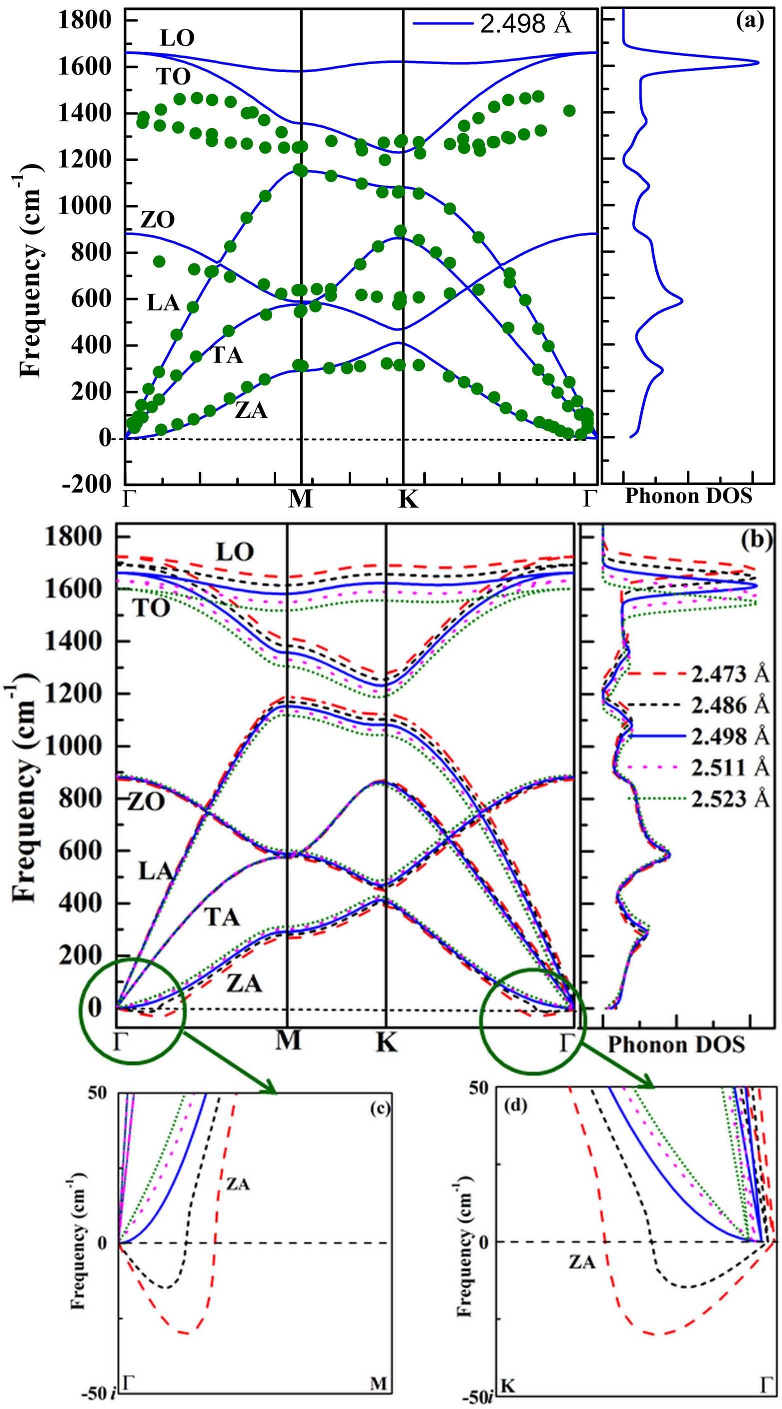

Figure 5.2 – (a) The phonon dispersion of 2D h-BN along high symmetry directions, the experimental data are shown as solid (green) circles taken from reference [91](b) Quasi-harmonic frequencies obtained by varying the equilibrium in-plane lattice parameter ($\boldsymbol{a}$-lattice) by ±1%. (c&d) The ZA (bending) mode is imaginary around the Γ point along Γ-M (c) and K-Γ (d) directions for the in-plane lattice parameter which is smaller than the equilibrium value ($a_{eq} = 2.498$ Å). *Legends are common for plots b, c and d.*

In order to include the anharmonicity that arises from thermal contraction/expansion of $\boldsymbol{a}$-lattice we used QH-LD, in which dependence of phonon frequency on the lattice parameter is studied by varying the equilibrium $\boldsymbol{a}$-lattice by ±1 % ($\boldsymbol{c}$-value kept fixed as 25 Å). In a single layer of h-BN, there is no interaction along c-axis, hence the phonon frequencies do not have any dependence on the value of $\boldsymbol{c}$. Figure 5.2b shows the quasi-harmonic phonon dispersion curves obtained at different $\boldsymbol{a}$-lattices. The degenerate longitudinal and transverse (LO/TO) optic mode at Γ point arises from the in-plane atomic displacement, so any change in $\boldsymbol{a}$-lattices will have an influence on LO/TO mode frequency. When $\boldsymbol{a}$-lattice decreases/increases the in-plane force constants will increase/decrease, hence there will be an upshift/downshift in the LO/TO mode frequency.

From figure 5.2b we can see that when $\boldsymbol{a}$-lattice parameter decreases there is an upshift of LO/TO mode frequency and vice-versa. The variation in $\boldsymbol{a}$-lattice affects the ZO mode frequency also, but this change is not significant as in the case of the LO/TO mode. The LO/TO and ZO mode frequency shift as a function of $\boldsymbol{a}$-lattice parameter is shown in figure 5.3. The LO/TO mode frequency shows a linear increase in mode frequency with decrease in $\boldsymbol{a}$-lattice parameter. The ZO mode frequency shows an opposite behaviour. This is due to membrane effect [58], and it has already reported in the case of graphene [44, 219]. For $\boldsymbol{a}$ = 2.473 Å (1 % smaller than $\boldsymbol{a}_{\mathrm{eq}}$), the LO/TO mode frequency increases by $\sim$ 3.76 % and for $\boldsymbol{a}$ = 2.523 Å (1 % larger than $\boldsymbol{a}_{\mathrm{eq}}$) there is a downshift in the LO/TO mode phonon frequency by $\sim$ 3.68 %. The ZO mode shows an upshift ($\sim$ 0.68 %) for 1 % increase and a downshift of ($\sim$ 0.89 %) for 1 % decrease in the $\boldsymbol{a}$-lattice parameter.

Similar to graphene, the ZA mode (bending mode) shows an instability around the Γ-point along Γ-M and K-Γ directions when the $\boldsymbol{a}$-lattice parameter is smaller than the equilibrium value (a_{eq} = 2.498 Å). The imaginary ZA mode suggests an instability of 2D-flat h-BN sheet. This is a shortcoming of approximation we used, namely, we considered the h-BN sheet to be a flat 2D surface in QH-LD. Since the anharmonic couplings are not included in QH-LD, the ZA mode is unstable as reported in the case of graphene (chapter-4, 4.3.2). Thus strong anharmonicity is envisaged in 2D-h-BN sheet also, which cannot be incorporated in QH-LD, and hence we have to go beyond quasi-harmonic method to include the full anharmonicity.

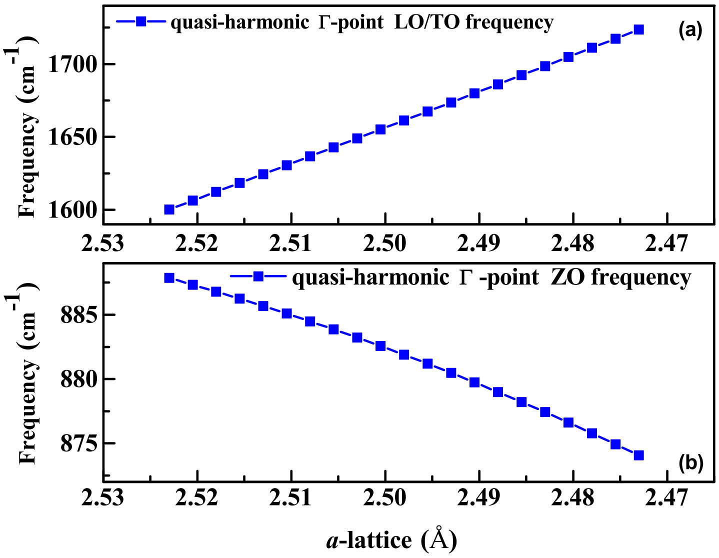

Figure 5.3 – The quasi-harmonic Γ point (a) LO/TO and (b) ZO optic mode frequencies as a function of in-plane lattice parameter (***a***-lattice)

5.3.2 Negative thermal expansion of *a*-lattice

The variation of ***a***-lattice parameter and linear thermal expansion coefficient (LTEC) are studied as a function of temperature. MD simulations are done with a 2D h-BN sheet containing 9800 atoms, and the dimensions of the simulation box are L_x=174.86 Å, L_y=151.43 Å and L_z=25 Å. Though the melting point of 2D h-BN is quite high (∼3000 K), in this study, the simulations are restricted upto 2000 K, above this temperature the system shows an instability with the present potential [148]. Figure 5.4 displays the simulations results for ***a***-lattice parameter and LTEC. The ***a***-lattice decreases with an increase in temperature, and its magnitude reduces to 0.84 % of the equilibrium value at 2000 K. The experimental data of bulk h-BN shows a thermal contraction with an increase in temperature upto 300 K [230]. The LTEC is computed by direct numerical differentiation of the above data. The LTEC is negative in the whole computed temperature interval upto 2000 K and this is consistent with previous prediction [231]. The negative thermal expansion of h-BN is more prominent at low temperatures, and it is due to the large negative Grüneisen parameter of out-of-plane bending mode (ZA) [52]. The room temperature LTEC $\alpha_a = -5.32\times10^{-6}\,\mathrm{K}^{-1}$, is comparable with the quasi-harmonic predictions [52]. Both the quasi-harmonic and MD results are lower than the experimentally reported values of bulk h-BN, $-2.72\times 10^{-6}\,\mathrm{K}^{-1}$ [230], $-2.76\times10^{-6}\,\mathrm{K}^{-1}$ [51] and $-2.90\times10^{-6}\,\mathrm{K}$ [232].

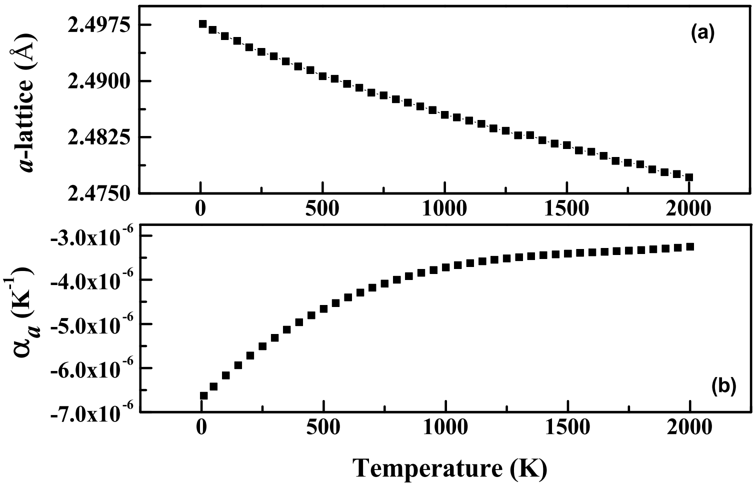

Figure 5.4 – The temperature dependent (a) in-plane lattice parameter (***a***-lattice) and (b) the linear thermal expansion coefficient (LTEC)

5.3.3 Structural stability at finite temperatures

The effect of temperature on structural stability is studied by computing the phonon dispersion directly from MD using SED method. Figure 5.5 displays the phonon dispersion curves computed at different temperatures. The LD dispersion (green dot dashed line) is calculated at equilibrium ***a***-lattice parameter. The red solid lines are obtained from quasi-harmonic LD calculations. The thermal contraction of ***a***-lattice parameter increases the in-plane force-constants and hence there is an upshift in the LO and TO quasi-harmonic LD frequencies. The overall appearance of phonon dispersion curves obtained from MD simulation (thick black curve) is similar to LD and quasi-harmonic dispersion. As temperature increases the LO and TO optic mode frequencies obtained from MD simulations are showing an unusual downshift (mode softening). This unusual downshift contradicts with the quasi-harmonic predictions. The out-of-plane optic (ZO) mode frequencies also show a downshift and this is consistent with quasi-harmonic calculations.

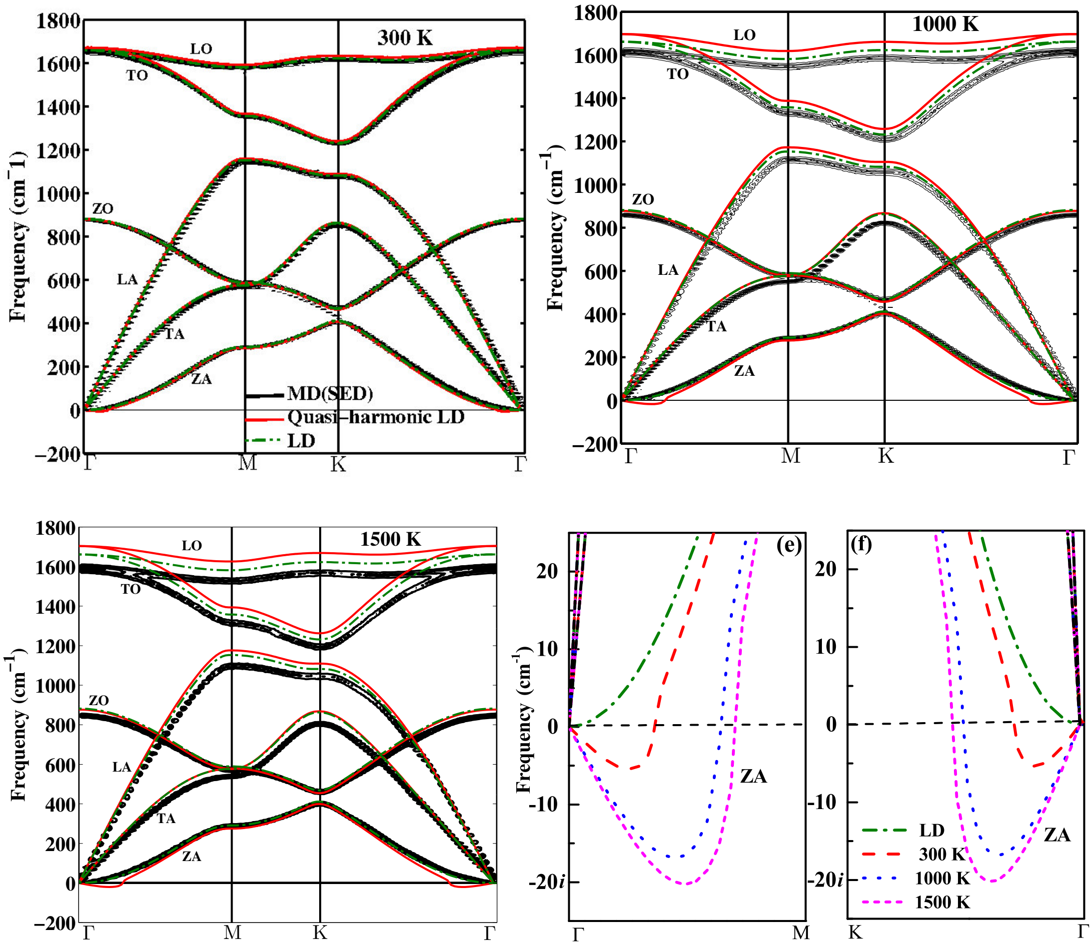

Figure 5.5 – The phonon dispersion of 2D h-BN at different temperatures. The green dot dashed lines are obtained from the lattice dynamics at equilibrium in-plane lattice parameter (***a***-lattice). The red solid lines are the quasi-harmonic dispersion curve computed at temperature dependent in-plane lattice parameter (obtained from MD simulations), and the thick black lines are MD dispersion curves. The quasi-harmonic ZA modes becomes imaginary along Γ-M and K-Γ directions, and it is more apparent at higher temperature. (d&e) quasi-harmonic ZA mode (zoomed along Γ-M & K-Γ directions) at different temperatures.

From figure 5.5 we can see that the low energy quasi-harmonic ZA bending mode (red solid lines) computed at temperature dependent ***a***-lattice parameter is unstable along Γ-M and K-Γ directions at finite temperatures. Due to the thermal contraction, the value of ***a***-lattice parameter falls below that of the equilibrium value, causing a structural instability. We have already seen this in section 5.3.1, where we arbitrarily varied the ***a***-lattice parameter. At the same time the phonon dispersion obtained from MD simulations does not have any such instability. All the ZA mode frequencies are real at finite temperatures. The dynamical stability has been restored in MD simulations. This behaviour is analogous to that of graphene (chapter-4, 4.3). The strong anharmonic coupling between the phonon modes is absent in quasi-harmonic methods where we consider a flat 2D sheet, whereas all the phonon-phonon interactions were naturally included in MD simulations, and it leads to the formation of thermally excited ripples, which makes the 2D sheet stable. The above result explains the role of strong anharmonic phonon-phonon coupling on the structural stability of 2D h-BN sheet at finite temperatures, and this is in concurrence with the findings on graphene. Experimental [233, 234] and theoretical [84] efforts have been made to quantify the dimension and role of ripples on electronic and thermo-mechanical properties of 2D h-BN sheet and nanotube.

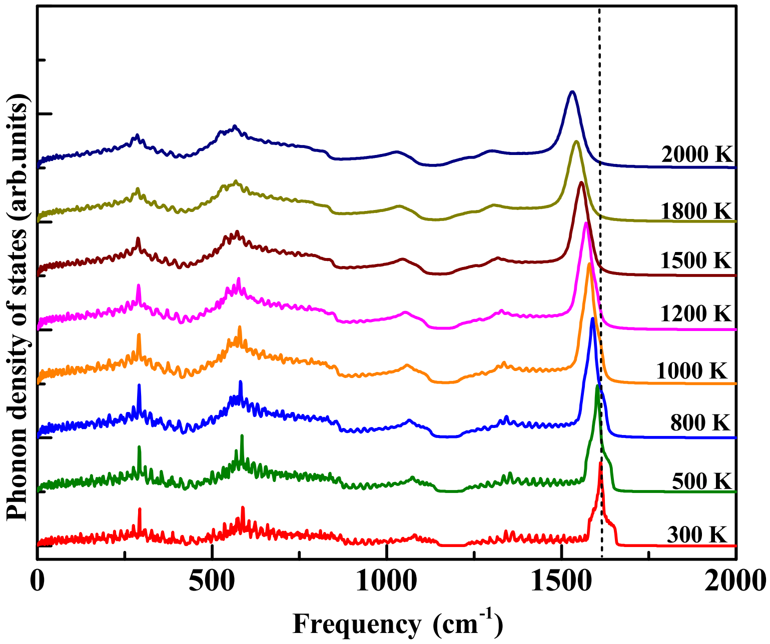

Figure 5.6 – The temperature dependent phonon DOS of 2D h-BN. The high frequency optic modes show a red-shift with an increase in temperature. The vertical dash lines is the peak position of LO/TO mode obtained from LD calculation.

Figure 5.6 shows the phonon DOS of 2D h-BN as a function of temperature. The vertical (black dash) line represents the peak position of high frequency optic modes at 300 K. As temperature increases the optic modes shifts towards the lower frequency side of the spectrum and exhibits a red-shift. This is concurrent with the downshift of optic branches observed in phonon dispersion (Figure 5.5).

5.3.4 Temperature dependence of Γ point optic modes

In the previous section we observed an unusual downshift of LO/TO optic mode frequencies with temperature. In order to analyze this unusual downshift we computed the mode resolved phonon spectra at Γ point. The bulk h-BN belongs to a point group D_{6h}(space group, $P6/mmm$), according to the factor group analysis the Γ point optic mode frequencies can be classified as [81].

$$\Gamma_{optic}(bulk) = 2E_{2g}(Raman) + 2B_{2g}(inactive) + 2A_{2u}(IR) + 2E_{1u}(IR) \tag{5.2}$$

The E_{2g} and E_{1u} modes are doubly degenerate, while B_{2g} and A_{2u} modes are non-degenerate. The Raman and IR active modes are assigned. The 2D h-BN structure is having D_{3h} (space group, $P\overline{6}2m$) point group symmetry and the corresponding Γ point optic mode frequencies are [81] ,

$$\Gamma_{optic}(2D) = A2^{''}[ZO](IR) + E^{'}[LO/TO](IR + Raman) \tag{5.3}$$

In equation 5.3 the quantity inside the square bracket represents the polarization based designation of the corresponding mode. The $E^{'}$ and $A2^{''}$ are the group theory notations of LO/TO and ZO mode respectively.

In order to delineate the contributions of thermal contractions and phonon-phonon coupling to the total frequency shift and linewidth, we performed quasi-harmonic LD, NVT and NPT ensemble simulations of the very same system at different temperatures. Figure 5.7 displays the temperature dependent frequency shift and linewidth of LO/TO and ZO modes. Both ZO and LO/TO modes are exhibiting a red-shift with respect to LD predicted peak positions. The temperature induced broadening of the modes is clearly visible. In order to obtain the exact peak position and linewidth we fit a Lorentzian to the frequency spread (chapter-2, equation 2.72).

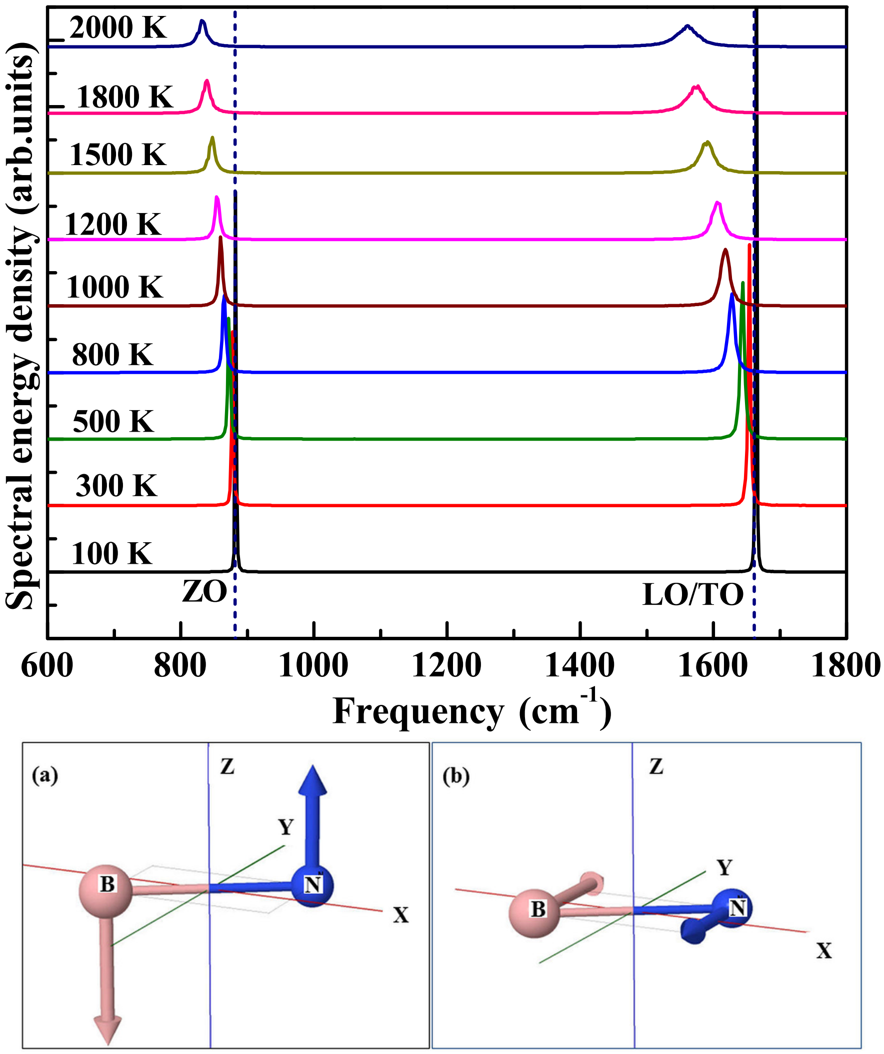

Figure 5.7 – The Γ-point ZO and LO/TO modes as a function of temperature. The dot-dashed lines are the LD predicted peak positions. Both ZO and LO/TO modes are showing a red-shift in the mode frequency. (bottom) The eigenvectors of (a) ZO and (b) LO/TO modes.

Figure 5.8a shows the variation of LO/TO mode frequency with temperature. The quasi-harmonic LO/TO frequencies (blue star) computed at the temperature dependent ***a***-lattice parameter shows a blue shift in the mode frequency as expected. The NPT ensemble simulations (black square) shows a reverse trend, the mode frequencies are falling with temperature (red-shift), which contradicts the well known assumptions that for shorter bond-lengths, the bonds becomes stiffer leading to larger force constants and mode frequencies. In the NPT (constant pressure) ensemble simulations, the volume change is allowed, hence the observed frequency shift is an outcome of both thermal contraction of ***a***-lattice parameter and the coupling of phonon modes. While in NVT ensemble, the simulation volume is fixed, hence the frequency shift is purely due to anharmonic coupling of phonon modes. To analyze the above unusual shift we studied the same system using NVT ensemble. NVT ensemble (red circle) simulations also predict the red-shift in the LO/TO mode frequency and it is much more prominent than NPT ensemble simulations. *From these results we can conclude that, even-though the thermal contraction of* ***a****-lattice parameter leads to an upshift in the LO/TO quasi-harmonic mode frequency, the strong anharmonic phonon-phonon coupling dominates over this weak thermal contraction effects and pulls down the LO/TO mode frequency in NVT and NPT ensemble simulations.* This behaviour contradicts with the observations made in graphene, where the strong phonon-phonon coupling causes blue-shift of LO/TO mode frequency along with thermal contraction effects (chapter-4, 4.3.3). This discrepancy may be due to the difference in masses of basis atoms (B and N) in 2D h-BN, whereas it is identical in graphene.

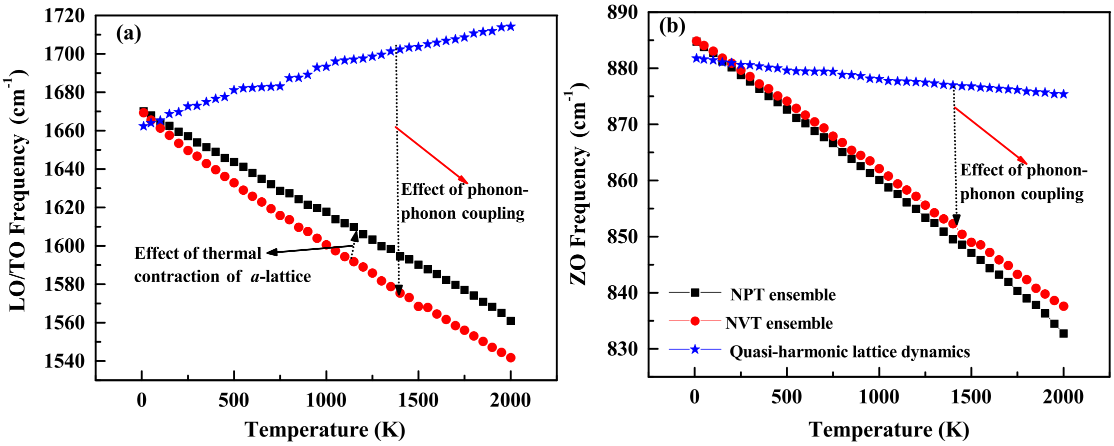

Figure 5.8 – The temperature dependent frequency shift of Γ-point (a) LO/TO and (b) ZO modes. The quasi-harmonic frequencies (blue star) are computed at temperature dependent in-plane lattice parameter $\boldsymbol{a}$ obtained from MD simulations, and it includes a weaker type of anharmonicity that arises from the thermal contraction of $\boldsymbol{a}$-lattice parameter. The NVT (red) and NPT (black) ensemble simulations are done to delineate the contributions of phonon-phonon coupling and thermal contraction to the total peak shift. *Legends are common for both plots*

Figure 5.8b shows the temperature dependence of ZO mode; the temperature dependent quasi-harmonic frequency exhibits a slight red-shift. Both NPT and NVT ensemble simulations are showing a red-shift in the ZO mode frequency. In NVT ensemble the ZO mode frequency falls with temperature due to strong phonon-phonon coupling. But when we switch the NPT ensemble the thermal contraction of ***a***-lattice also comes into picture, and it has a reverse effect here (with respect to LO/TO mode). The thermal contraction further pulls down the ZO mode frequency, this is due to the membrane effect [58]. *Hence the combined effect of phonon-phonon coupling and membrane effect leads to a red-shift in the ZO mode frequency.*

5.3.5 Anharmonic effects on eigenvectors

The anharmonic effect on the Γ-point optic mode frequencies were studied in the previous section. Here we are studying the non-linear effects on eigenvectors (polarization) of the dynamical matrix due to temperature driven anharmonicity. Recalling the discussions in the section on theoretical formulations (chapter-2, 2.4.2.2), the phonon properties are evaluated by projecting the MD based atomic velocity on to the j^{th} normal mode of vibrations of a perfect crystal, assuming that the eigenvectors will remain the same at all temperatures. In order to validate this assumption we compute the Γ-point optic mode frequency and linewidth using with and without eigenvectors. Figure 5.9a&b displays the LO/TO and ZO mode frequencies obtained from both methods. The mode frequencies computed with and without eigenvectors are identical and match with the previous predictions. Figure 5.9c&d shows the linewidth of LO/TO and ZO mode. Unlike the mode frequency, the linewidth of the LO/TO modes obtained from both methods are different. The linewidths computed using eigenvectors are lower in magnitude than the direct calculations in both NPT and NVT ensemble simulations. At low temperature (10 K - 300 K) both NPT and NVT ensemble simulations predict similar linewidths; but as temperature increases further, there is a significant difference in the variation of linewidths. The NPT ensemble simulations shows higher linewidths (in both methods) than NVT ensemble simulations at higher temperatures. This shows that the thermal contraction of ***a***-lattice parameter has an effect on LO/TO linewidths at higher temperatures. But in the case of ZO mode the change in linewidth is too small to distinguish the effect of eigenvectors. Both NPT and NVT ensemble simulations predict almost similar behaviour of linewidths at all temperature.

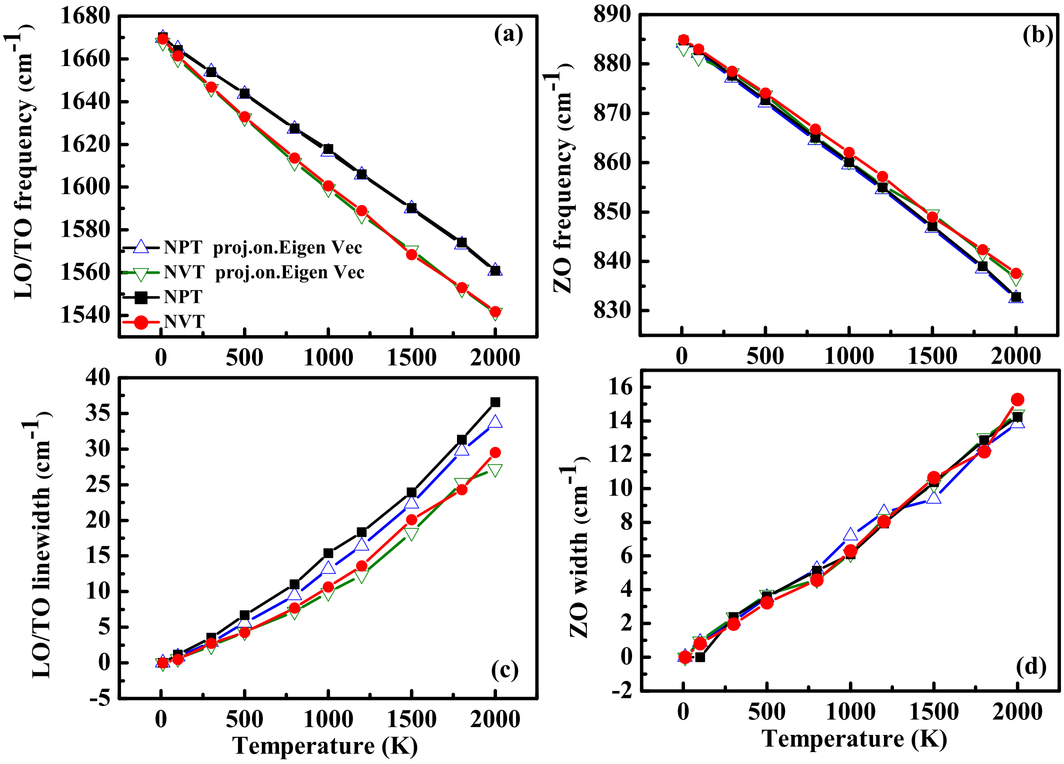

Figure 5.9 – The temperature dependent frequency shift and linewidth of LO/TO and ZO mode. The black squares (NPT-ensemble) and red circles (NVT-ensemble) are computed directly from the Fourier transform of velocities. The blue upper triangle and green lower triangle are calculated by projecting the velocity to the normal modes of vibrations in NPT and NVT ensemble simulations. *Legends are common for all plots*

5.3.6 Anharmonic coupling of normal modes

To understand the anharmonic coupling and decay of normal modes, phonon spectra is computed at Γ, M and K point in the Brillouin zone. Figure 5.10 shows the mode resolved phonon spectra at 500 K and 1000 K. At Γ point, there are six normal modes of vibrations, three acoustic modes with zero frequency, and three optic modes with non-zero frequency (Figure 5.10 a1&a2). The ZO and LO/TO mode do not get coupled with any other modes at Γ point, implying that their decay occurs by coupling with modes at other point in the Brillouin zone. This behaviour is analogous with graphene (chapter-4, 4.3.4). At M point (Figure 5.10b1&b2) all six normal modes have non-zero frequency. The ZO modes are coupled with ZA modes. Similarly the LO and TO modes are coupled with LA and TA modes at M point. At K point (Figure 5.10 c1&c2) the ZA and ZO modes coupled each other, similarly the LO modes with certain polarizations couple with TO and LA modes, LO modes with different polarization couple only with TA mode. This observation contradicts with graphene, where the ZA/ZO and LA /LO modes are degenerate and do not couple with any other modes (chapter-4, 4.3.4) .

5.3.7 Temperature dependence of acoustic (ZA, TA and LA) phonon modes

To study the temperature dependence of acoustic phonon modes, we analyzed the ZA, TA and LA modes at M point in the Brillouin zone. Figure 5.11 shows the frequency shift and linewidth of ZA, TA and LA modes. The quasi-harmonic frequencies are computed as a function of temperature dependent $\boldsymbol{a}$-lattice parameter. The ZA mode quasi-harmonic frequencies are decreasing with temperatures. While the NVT ensemble frequencies are showing a blue-shift, the NPT ensemble frequencies are red-shifted. The red-shift observed in NPT ensemble frequencies are not as prominent as that of the quasi-harmonic shift. From this we can conclude that for ZA mode the thermal contraction of $\boldsymbol{a}$-lattice parameter (quasi-harmonic) leads to a red-shift, while the anharmonic phonon-phonon coupling pull the mode frequencies up (NVT ensemble). But when thermal contraction and phonon-phonon coupling operates together, (NPT ensemble) the thermal contraction effect slightly dominates over the phonon-phonon coupling and leads a red-shift in the mode frequency. For TA mode, there is a small blue-shift in the quasi-harmonic mode frequency. At the same time, both NVT and NPT ensemble simulations are predicting a red-shift and it is identical in magnitude. Since the red-shift observed in NVT and NPT simulations are identical, we can conclude that the phonon-phonon scattering is the cause of observed red-shift. This behaviour of TA mode is analogous to that of Γ-point

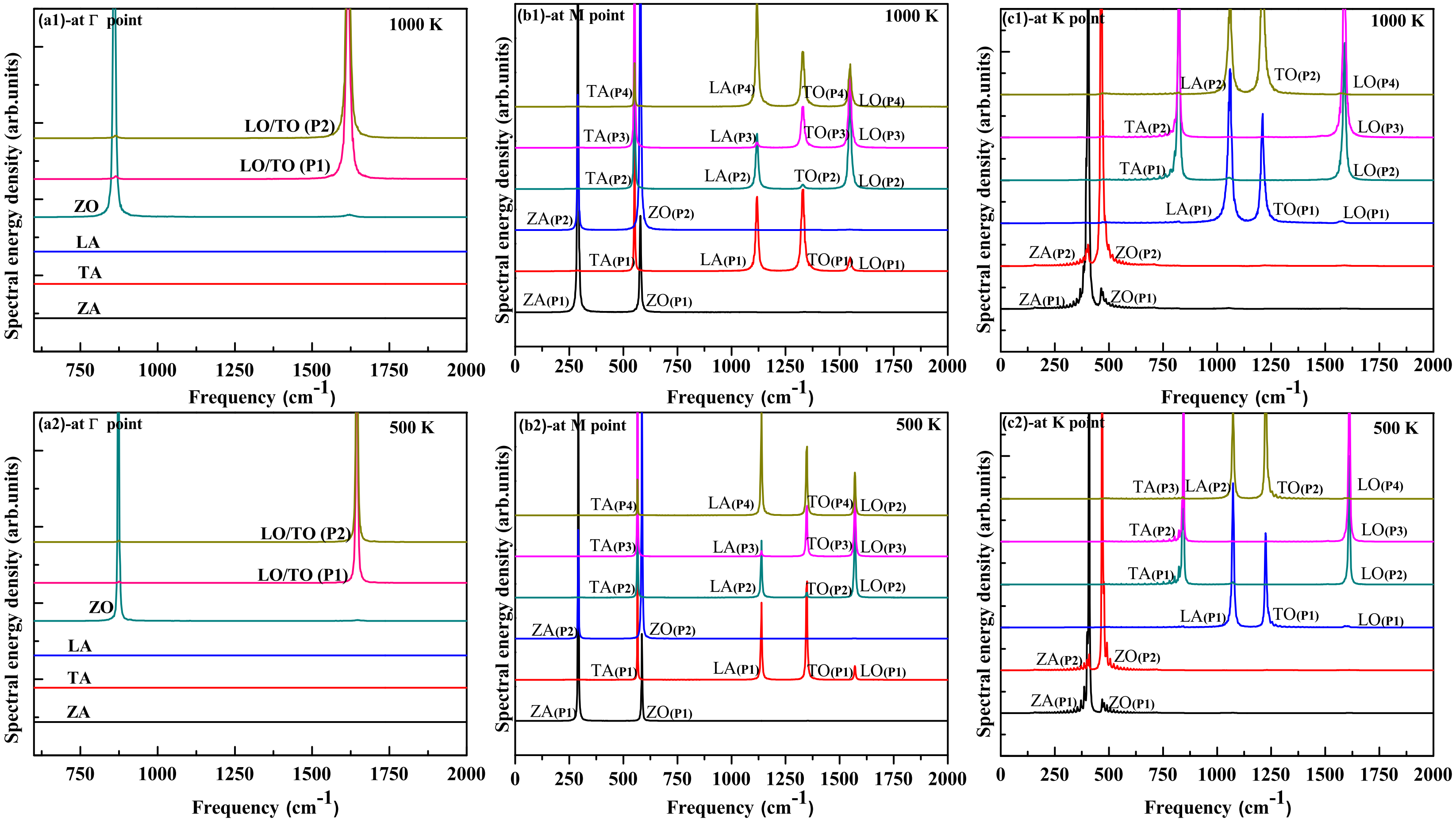

Figure 5.10 – The spectral density at (a) Γ, (b) M and (c) K point in the Brillouin zone. The modes are labeled as per their polarization at Γ−point and P1, P2, P3 and P4 represent different polarizations. Top panel is at 1000 K and bottom panel is at 500 K.

ZO mode studied in the previous section (5.3.4). In the case of LA mode the quasi-harmonic frequencies are blue-shifted. Both NVT and NPT ensemble frequencies are red-shifted, and it is more significant in NVT ensemble. This again leads to a similar conclusion as we made for Γ point LO/TO mode in the previous section, the strong anharmonic phonon-phonon coupling dominates over the thermal contraction effects and pulls down the mode frequency. The above explanations clearly bring out the role of strong anharmonic phonon-phonon scattering effect in the mode frequency shift of M point acoustic phonon modes. The phonon modes are deviating strongly from the quasi-harmonic predictions, due to their strong anharmonic nature, which was introduced in MD simulations and we captured their true anharmonic behaviour. The linewidth of all modes are monotonically increasing with temperature as shown in figure5.11 a1-c1.

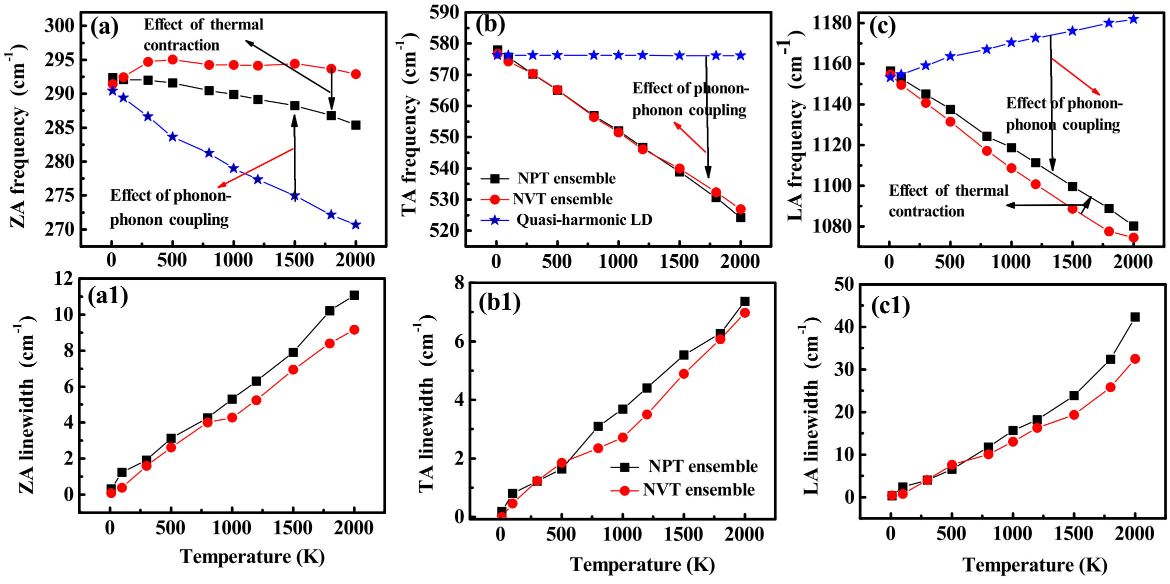

Figure 5.11 – The temperature dependent frequency shift (a,b and c) and linewidths (a1,b1 and c1) of ZA (bending), TA (transverse acoustic) and LA (longitudinal acoustic) phonon modes at M point in the Brillouin zone. The blue stars are quasi-harmonic frequencies, the black squares and red spheres are NPT and NVT ensemble simulations. *Legends are common for all plots*

5.3.8 Delineating the effects of ripples on thermal expansion

In order to delineate the role of ripples on thermal expansion properties, 2D and 3D simulations has been carried out separately. Figure 5.12 displays the temperature dependence of ***a***-lattice for different system sizes. As found in section 5.3.2, in 3D simulations, ***a***-lattice decreases with an increase in temperature. To incorporate the effect of long wavelength ripples, simulations are done with various supercells of size 10×10×1, 30×30×1, 50×50×1, 70×70×1, 100×100×1 and 150×150×1. Similar to graphene (chapter-4, 4.3.6), ***a***-lattice shows a system size dependence in 2D h-BN also, and we found a convergence for the simulation cell of size larger than 70×70×1 (9800). In 2D simulation, the ***a***-lattice increases with an increase in temperature and shows thermal expansion in the whole computed temperature range. The ***a***-lattice does not show any system size dependence in 2D simulations and it is consistent with our earlier observations for graphene (chapter 4, Figure-4.12b)

The LTEC obtained at 300 K are shown in table 5.1, the LTEC is negative in 3D simulations and their system size dependence is discernible. The LTEC at 300 K ($\alpha_a = -5.508 \times 10^{-6} K^{-1}$) is matching with previous quasi-harmonic predictions [52]. The computed values of LTEC are showing significant difference with experimental values (table 5.1). The LTEC obtained from 2D simulations all are positive in sign and does not have any system size dependence. To understand the effect of phonon modes on thermal expansion, the phonon dispersion is computed from 2D simulations (Figure 5.12). The out-of-plane modes (ZO and ZA) are absent in 2D phonon dispersion of 2D h-BN and is analogous with graphene (chapter-4, Figure-4.12). The ZA mode which is responsible for thermal contraction of lattice [52] is absent in 2D simulation, which leads to the thermal expansion of ***a***-lattice in the whole computed temperature range. Here we can conclude that, similar to graphene, the effect of ripples are quite strong in 2D h-BN also.

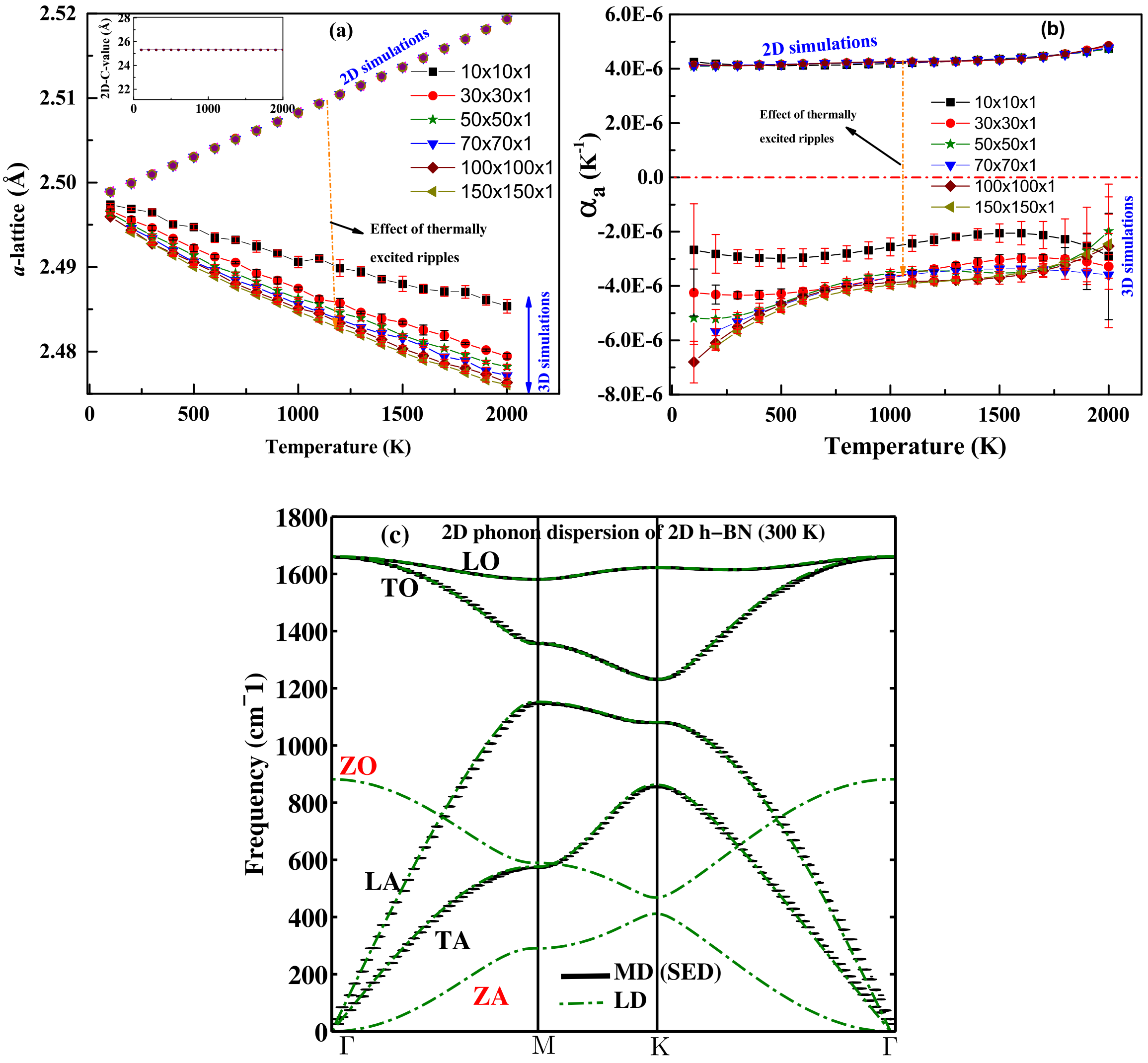

Figure 5.12 – (a) The temperature dependence of in-plane lattice parameter (***a***-lattice) of 2D h-BN; (b) Linear thermal expansion coefficient (LTEC) as a function of temperature. (c) The 2D phonon dispersion of 2D h-BN at 300 K

Table 5.1 – The linear thermal expansion coefficients (LTECs) of 2D h-BN at 300 K, the system size dependence of LTECs obtained from 3D simulations are discernible. The data has been compared with available experiments. [a]Reference [230],[b]Reference [51],[c]Reference [232]

simulation cell size	2D simulation $\alpha_a(\times 10^{-6} K^{-1})$	3D simulation $\alpha_a(\times 10^{-6} K^{-1})$	expt. $\alpha_a(\times 10^{-6} K^{-1})$
10×10×1 (200 atoms)	4.145	-2.905	-2.720[a] , -2.760[b], -2.900[c]
30×30×1 (1800 atoms)	4.130	-4.330	
50×50×1 (5000 atoms)	4.124	-5.105	
70×70×1 (9800 atoms)	4.129	-5.508	
100×100×1 (20000 atoms)	4.114	-5.516	
150×150×1(45000 atoms)	4.107	-5.670	

5.4 Summary

Temperature dependent structural stability, frequency shift and linewidth of 2D hexagonal boron nitride (h-BN) are computed using SED method. The major findings of this study are summarized below.

- The in-plane lattice parameter ($\boldsymbol{a}$-lattice) calculated from MD simulations shows negative thermal expansion in the whole computed temperature range (0 K - 2000 K).

- When the in-plane lattice parameter falls below the equilibrium value, the quasi-harmonic bending (ZA) mode frequency becomes imaginary along Γ-M and K-Γ directions in the Brillouin zone, leading to a structural instability of the 2D sheet. The ZA mode is seen to be stabilized in the dispersion obtained from MD simulations, due to automatic incorporation of higher order phonon scattering processes in MD, which are absent in quasi-harmonic dispersion. These observations are analogous to graphene.

- The mode resolved phonon spectra computed with quasi-harmonic method predicts a blue-shift of longitudinal and transverse (LO/TO) optic mode frequencies with temperature. On the other hand, both canonical (NVT) and isobaric-isothermal (NPT) ensembles predict a red-shift with temperature, that is more prominent in NVT ensemble. The strong phonon-phonon coupling dominates over thermal contraction effect and leads to a red-shift in LO/TO mode frequency in NPT ensemble simulations. This is contradicting with the observations made in graphene, where the strong-phonon coupling along with thermal contraction causes a blue-shift in LO/TO mode frequency. The out-of-plane (ZO) optic mode quasi-harmonic frequencies are red-shifted due to membrane effect. The phonon-phonon coupling effects in NVT and NPT ensemble simulations lead to a further reduction in the ZO mode frequencies. The linewidth of

LO/TO and ZO mode frequencies increases in a monotonic fashion.

- Temperature dependence of acoustic modes is analyzed at M point in the Brillouin zone. The frequencies of ZA, TA and LA modes obtained from MD simulations deviate significantly from quasi-harmonic predictions. This is again a consequence of strong phonon-phonon coupling in MD simulations.
- The role of ripples on thermal expansion properties is delineated by carrying out 2D and 3D simulations. The 2D $\boldsymbol{a}$-lattice shows continuous thermal expansion, at the same time the $\boldsymbol{a}$-lattice obtained from 3D simulation shows thermal contractions. This discrepancy is due to the absence of ZA mode in 2D simulations, and it is in agreement with the observations made in graphene.

Chapter 6

Thermal expansion, structural stability and anharmonicity of monolayer (ML)-MoS$_2$

The monolayer(ML)-MoS$_2$ is an emerging 2D honeycomb material similar to graphene and 2D h-BN. This chapter discusses the thermal expansion, structural stability and temperature evolution of Γ-point optic phonon modes of free-standing ML-MoS$_2$, and the results are compared with graphene and 2D h-BN.

6.1 Introduction

The monolayer(ML)-MoS$_2$ is an atomically thin layered material similar to graphene and 2D h-BN, which shows striking optical, electronic and mechanical properties [25, 26]. ML-MoS$_2$ posses a special S-Mo-S symmetric sandwich structure which makes it differ from graphene and 2D h-BN. Unlike graphene, ML-MoS$_2$ is a direct band gap semiconductor with a band gap of ~1.8 eV [25]. This special property puts ML-MoS$_2$ in the front-end of electronic and opto-electronic industry [25, 26]. To devise ML-MoS$_2$ based electronic devices knowledge about the thermal and vibrational properties is essential. *Ab initio* simulations are used to obtain the phonon frequencies of monolayer and bulk MoS$_2$ [33, 52, 93, 94]. Experimentally, among four Raman active modes, the evolution of $E^1_{2g}(E^{'})$ and $A_{1g}(A^{'}_1)$ modes in bulk (monolayer) MoS$_2$

was studied as a function of layer number [95–97] or temperature [98–101]. The evolution of other Raman active modes $E_{1g}(E'')$ and E^2_{2g} (absent in mono layer) are not reported in the literature due to the constraints imposed either by the selection rules on the scattering geometry($E_{1g}(E'')$) [95] or Rayleigh rejection filter(E^2_{2g}) [96]. The temperature evolution of IR active $A_{2u}(A''_2)$ modes is also not reported in the literature.

Though the melting point of MoS_2 is 1498 K [53], most of the Raman spectroscopy studies measured the spectra upto a maximum temperature of 550 K [98–101]. This is due to the decomposition of MoS_2 sample above this temperature [98]. Further, experimental/theoretical investigations are needed over a wide range of temperatures to get a clearer picture about the temperature evolution of Raman peaks. In this chapter, the temperature driven anharmonic effects on all four Γ point optic phonon modes are analyzed, irrespective of experimental constrains. The structural stability and thermal expansion properties are studied and compared with graphene and 2D h-BN, the effects of ripples and system size on thermal expansion are also discussed.

6.2 Computational methods

The ML-MoS_2 is made up of three atomic layers (Figure 6.1). The middle Mo atom layer is sandwiched between two S atom layers in a trigonal prismatic fashion, and held together by a strong covalent bond. Liang *et al* [235] parametrized a many body reactive empirical bond order (REBO) potential for Mo-S system and its functional form can be written as

$$\begin{aligned} E_{REBO} &= \frac{1}{2}\sum_{i\neq j} f^c_{ij}(r_{ij})\Big[V^R(r_{ij}) - b_{ij}V^A(r_{ij})\Big] \\ &= \frac{1}{2}\sum_{i\neq j} f^c_{ij}(r_{ij})\Big[\Big(1+\frac{Q_{ij}}{r_{ij}}\Big)A_{ij}e^{-\alpha_{ij}r_{ij}} - b_{ij}B_{ij}e^{-\beta_{ij}r_{ij}}\Big] \end{aligned} \qquad (6.1)$$

where r_{ij} is the distance between atoms i and j, $f^c_{ij}(r_{ij})$ is the cutoff function. $V^R(r_{ij})$ and $V^A(r_{ij})$ are the pairwise repulsive and attractive interactions. b_{ij} is the many-body bond-order function. The α, β, A, B, and Q are the pairwise parameters which depends on the chemical species of the interacting atoms. This potential could successfully model the structural and mechanical properties of Mo-S and MoS_2 systems. Later, Stewart and Spearot [149] refined the parametrization of Liang *et al* and implemented it into MD simulation package LAMMPS. We used the parametrization of Stewart and Spearot [149] to model the interaction between the Mo and S atoms in MoS_2 monolayer. The present potential predicts the equilibrium $\boldsymbol{a}$-lattice, $\boldsymbol{a_0}$ = 3.17 Å which is close to the experimentally reported value (3.16 Å) [93]. Simulations are done using the classical MD simulation package LAMMPS [179]. A supercell of size 25×25×1 (1875 atoms), has been created. Periodic boundary conditions are employed in all the three direction to eliminate the surface effects. A vacuum separation of 15 Å is provided along Z-direction to avoid the un-physical interactions between the periodic images of the layers. The general computational procedure is same as discussed in chapter 2 (2.4.2). The velocities of all atoms are collected at every 5 fs. The whole simulations are done for 1.6 ns.

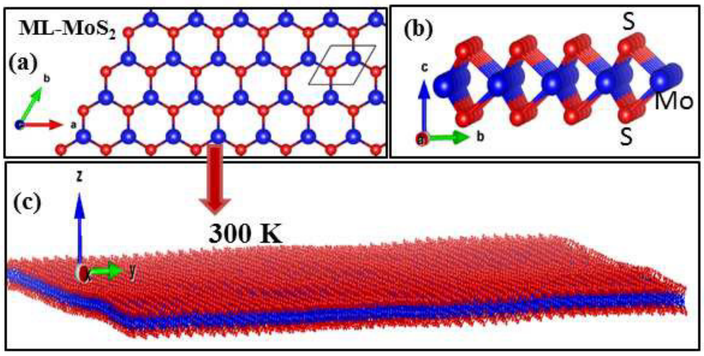

Figure 6.1 – (a) Top view of the honeycomb lattice of ML-MoS_2. The honeycomb lattice contains one Mo atom and two S atoms located at the corners of hexagons. (b) Side view of ML-MoS_2 ; Mo atomic layer sandwiched between the two S atom layers in a trigonal prismatic fashion. (c) ML-MoS_2 at 300 K, similar to graphene and 2D h-BN, the thermally excited ripples are present in ML-MoS_2 also.

6.3 Results and Discussions

6.3.1 Thermal expansion

In order to understand the thermal expansion behaviour of ML-MoS_2, the variation of in-plane lattice parameter ($\boldsymbol{a}$-lattice) is studied as a function of temperature. The $\boldsymbol{a}$-lattice is found to be increasing in the whole computed temperature range (Figure 6.2), and this behaviour is consistent with the previously reported experiments on the bulk MoS_2 [54, 55]. The linear thermal expansion coefficients (LTEC) increases quickly with temperatures and becomes fairly stable for temperatures greater than 400 K, and approaches an asymptotic value of $8.0\times10^{-6}\mathrm{K}^{-1}$, and this is in agreement with quasi-harmonic predictions [53]. In contrast to other 2D layered materials, such as graphene and h-BN, which shows a thermal contraction of $\boldsymbol{a}$-lattice upto a wide range of temperature [44, 45, 83], MoS_2 shows a thermal contraction in the temperature range of 0 K - 20 K, and thereafter it expands. This phenomena is explained by small negative Grüneisen parameters (-10) of out of plane bending (ZA) mode around the Γ point, which is smaller than that of graphene and h-BN (as small as -80), and leads to a relatively small negative LTEC in the range of 0 K - 20 K in MoS_2 [52, 53]. This difference in thermal expansion coefficient of the 2D layered materials can be utilized to fabricate graphene/MoS_2 based hybrid devices for better performance. MD simulations will not be meaningful at very low temperature because of the manifestation of quantum effects, so we studied the properties of the system above 100 K, hence we can not observe the thermal contraction effect in these simulations.

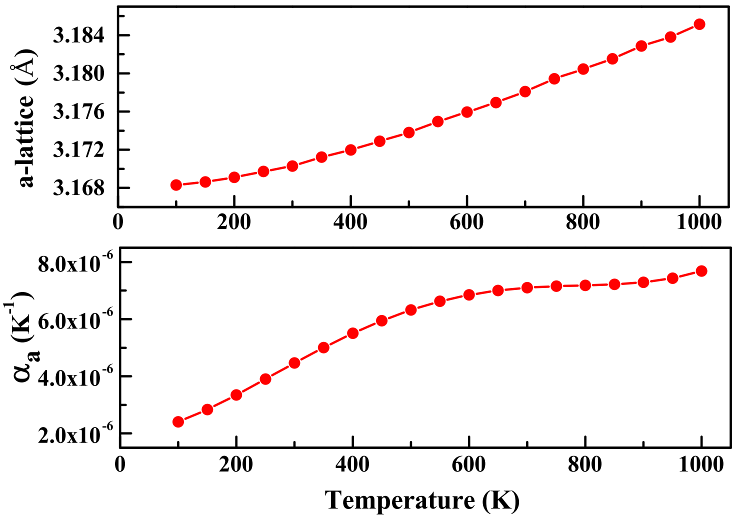

Figure 6.2 – (top)Temperature dependence of in-plane lattice parameter (***a***-lattice); (bottom) linear thermal expansion coefficient (LTEC).

6.3.2 Phonon dispersion and structural stability

In ML-MoS$_2$, due to the trigonal prismatic arrangement of Mo and S atoms, vibrational modes behaves quite differently from that of graphene and 2D h-BN. The unitcell of ML-MoS$_2$ contains three basis atoms, hence there will be nine modes of vibrations (3 acoustic+6 optic). Figure 6.3 displays the phonon dispersion in ML-MoS$_2$. The LA and TA modes show linear dispersion, while ZA mode exhibits quadratic dispersion around the Γ point, analogous to graphene and h-BN. The six optic branches are two in-plane longitudinal (LO1, LO2), two in-plane transverse (TO1, TO2) and two out-of plane optic (ZO1, ZO2). These six optic branches belongs to irreducible representation of E''(LO1, TO1), E'(LO2, TO2), A_2''(ZO1)and A_1'(ZO2) at Γ point [92]. The gap between the acoustic and optic modes is discernible, three acoustic branches TA, LA and ZA are separated below the optic branches (TO1 and LO1) by ∼55 cm^{-1}, and it is in agreement with *ab initio* calculations [94]. Since MoS$_2$ is a polar insulator, an LO-TO splitting is expected in the long wave length limit (q=0) due to the coupling of the lattice to macroscopic electric field created by relative displacement of Mo and S atom. The born effective charges of Mo and S are small and hence the polarized field associated with IR modes are weak, this leads to a small

LO-TO splitting (2 cm^{-1}) in bulk MoS_2 [236]. In ML-MoS_2 the electronic screening is weaker than bulk MoS_2, hence the splitting will be even smaller [94].

The LD calculations (green dot dash curves) are done with various supercells of sizes 2×2×1, 2×2×2, 3×3×1, 3×3×2 and 3×3×3, and found convergence in the spectrum of the order of 0.2 cm^{-1} for simulation cell of size 3×3×2 (contains 54 atoms) onwards. The LD calculations are in good agreement with previous reports [33, 94]. The LD frequency of LO2/TO2 (E') mode at Γ point is 426.87 cm^{-1}, which is 9 % higher than the experimental value (384.62 cm^{-1}) [95, 96]. Similarly the ZO2 (A_1') mode LD frequency (461.87 cm^{-1}) is 12 % higher than the experimental one (384.62 cm^{-1}) [95, 96].

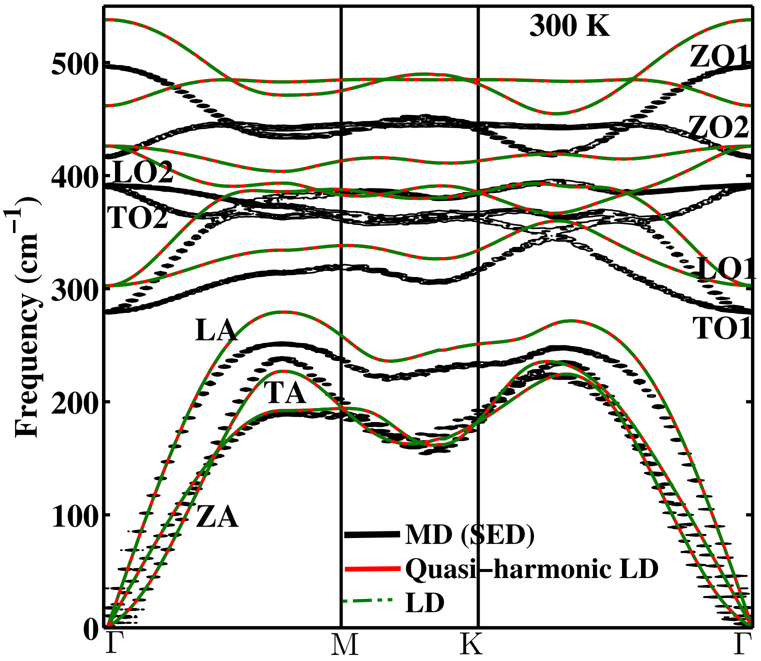

Figure 6.3 – phonon dispersion of ML-MoS_2. The quasi-harmonic LD (red) and MD (thick black lines) phonon frequencies are real and positive, indicates the structural stability at 300 K.

In order to understand the structural stability of free-standing monolayer, the quasi-harmonic LD calculations are performed. The quasi-harmonic LD dispersion (red curve) is computed with $\boldsymbol{a}$-lattice obtained from MD simulation at 300 K, and it predicts that all phonon modes are real and positive at all q-points in the Brillouin zone, which indicates the structural stability of free-standing ML-MoS$_2$. These observations differ from that of graphene and 2D h-BN, where the quasi-harmonic LD frequencies are imaginary along Γ−M direction and that led to a structural instability of the free-standing graphene and 2D h-BN. The phonon dispersion is also computed from MD simulation (thick black curve) using SED method. Similar to quasi-harmonic calculations, all modes are real and positive in MD phonon dispersion curve, and it again confirms the structural stability at 300 K. MD phonon dispersion shows softening of high frequency optic modes with respect to quasi-harmonic predictions, and its agreement with experiments becomes more satisfactory (table 6.1). This is analyzed and discussed in detail in the subsequent sections.

In the case of graphene and 2D h-BN, the stability of sheet has been ascribed to strong coupling between in-plane stretching and out-of-plane bending modes which re-normalizes the long wavelength ripples and stabilizes the 2D sheets (chapter-4, 4.3.2 and chapter-5, 5.3.3). The internal modes in ML-MoS$_2$ (arising from the vibrations of Mo-S bond) are activated at lower energy with respect to C-C bond in graphene, hence there will be less coupling between the in-plane and out-of-plane modes in ML-MoS$_2$ [237]. Therefore in ML-MoS$_2$, unlike graphene and 2D h-BN, the finite temperature structural stability can be attributed to its finite thickness effect, which counteract against the membrane effects and makes the crystal stable and prevents the crumpling transition.

6.3.3 Anharmonicity of Γ point optic modes

To address the anharmonic effect on optic modes we computed the mode resolved phonon spectra at Γ point as a function of temperature. Bulk MoS$_2$ belongs to point group D_{6h}, using group theoretical analysis the Γ point optic mode frequencies can be classified as [93, 94]

$$\Gamma_{optic}(bulk) = A_{1g}(R)+A_{2u}(IR)+2B_{2g}+B_{1u}+E_{1g}(R)+E_{1u}(IR)+2E_{2g}(R)+E_{2u} \quad (6.2)$$

For fewlayer(FL)-MoS_2, there is a lack of translational symmetry along z-axis, which leads to a reduction in the symmetry [92]. The ML-MoS_2 belongs to a point group of D_{3h}, and the corresponding Γ point optic mode frequencies are given below [93, 94]

$$\Gamma_{optic}(ML - MoS_2) = A_2^{''}[ZO1](IR) + E^{'}[LO2/TO2](IR + R) + A_1^{'}[ZO2](R) + E^{''}[LO1/TO1](R) \quad (6.3)$$

The Raman (R) and IR active modes are assigned. The quantity inside the square bracket is the polarization based designation. Since most of the literature follows the group theoretical notations, in the subsequent discussions, we follow the group theoretical based designation to avoid ambiguity when compare with experimental data. The modes labelled using letter E are doubly degenerate. The $E^{'}$ mode in the monolayer is both Raman and IR active due to absence of inversion center in monolayer and denoted as E_{2g}^1 in bulk [95], similarly the A_{1g} mode in bulk, which used to identify the layer number in FL-MoS_2 is identical to $A_1^{'}$ mode in the monolayer [94, 95].

Figure 6.4 displays the Γ point phonon spectra at different temperature. The frequency shift and linewidth of all four modes are captured irrespective of the selection rule or scattering geometry constraints of the Raman spectroscopy. The frequency and linewidth of E' and $A_1^{'}$ modes at 300 K are in qualitative agreement with experiments (table 6.1). The E' and $A_1^{'}$ modes are showing a red-shift with an increase in temperature, which is consistent with experimental observations [98–101]. The newly reported $E^{''}$ and $A_2^{''}$ modes also show a red-shift in mode frequency (Figure 6.4). The temperature dependent peakshift and broadening of peaks are due to the manifestation of anharmonic effects. The peakshift arises from the combined effect of thermal expansion and phonon-phonon coupling (self-energy change). The thermal expansion/contraction of lattice will cause a change in effective force constants leading to a softening/hardening in the mode frequency. The peakshift induced by self-energy change cannot be predicted *a priori*, it is intrinsic to material properties.

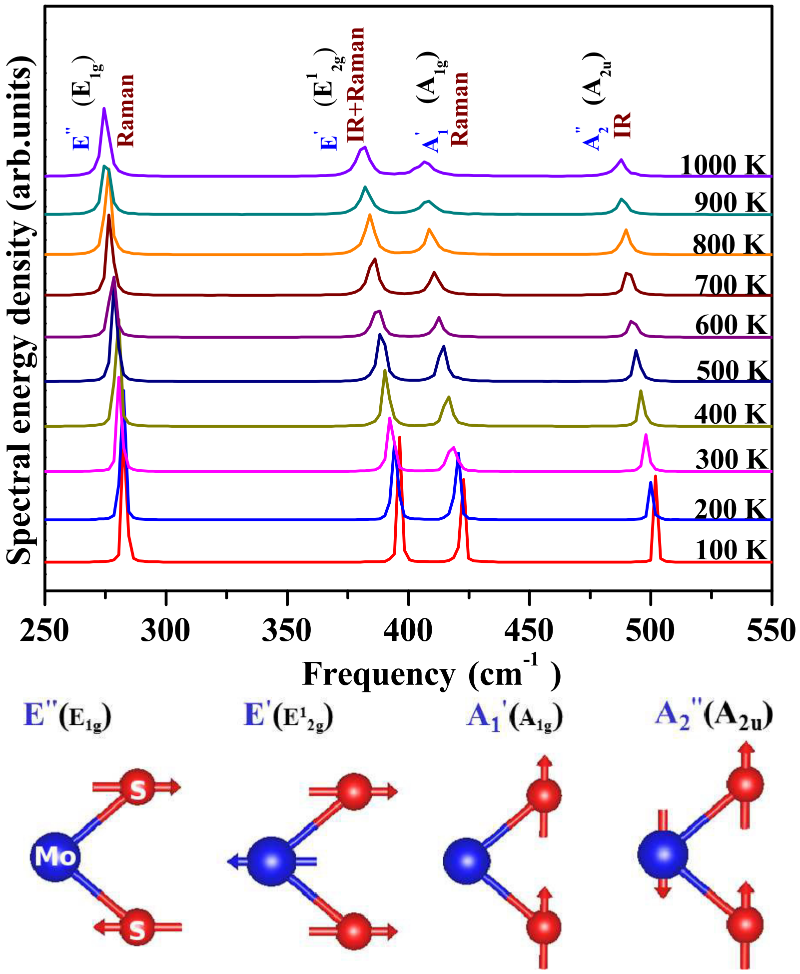

Figure 6.4 – (top)The Γ-point optic phonon modes as a function of temperature. The modes are labelled, the notations inside the bracket corresponds to bulk representation. Infrared (IR) and Raman active modes are indicated. (bottom) Eigenvectors of the corresponding modes.

Table 6.1 – The Γ point optic mode frequencies and linewidth at 300 K (expressed in cm^{-1}) compared with experiments. Reference a,b,c, and d are from [95, 96, 98, 238] respectively

	peak position		linewidth	
Mode	MD	expt.	MD	expt.
E''	280.96	....	1.35±0.09	....
E'	392.96	$384.28^{a,b}$, 391.7^{c}, 385^{d}	2.1±0.20	2.0^{b}, 2.0^{c}
A_1'	418.11	$402.93^{a,b}$, 408.9^{c}, 405^{d}	3.3±0.33	4.0^{b}, 5.5^{c}
A_2''	498.25	....	1.75±0.13	....

The peakshifts and linewidths are extracted by fitting a Lorentzian to the frequency spread (chapter-2, equation 2.72). Figure 6.5 displays the temperature dependent frequency shift of all four Γ point optic modes over a wide range of temperatures (100 K - 1000 K). To study the underlying mechanism of observed peakshift, we computed the mode frequency shift using quasi-harmonic lattice dynamics (QH-LD), canonical (NVT) and isobaric-isothermal (NPT) ensembles. In QH-LD, we compute the mode frequencies at temperature dependent lattice parameters obtained from MD simulations. The quasi-harmonic (blue star) frequencies of all modes are falling with an increase in temperature, and this red-shift in mode frequencies is due to the softening of force constants with an increase in lattice parameters. The mode frequencies are further reduced in NVT ensemble simulations (red sphere). Since the simulation volume is fixed here, the enhanced red-shift is purely due to anharmonic coupling of phonon modes. NPT ensemble (black square) simulations incorporate the combined effect of thermal expansion and coupling of phonon modes, and predicts a similar downshift as we observed in NVT ensemble.

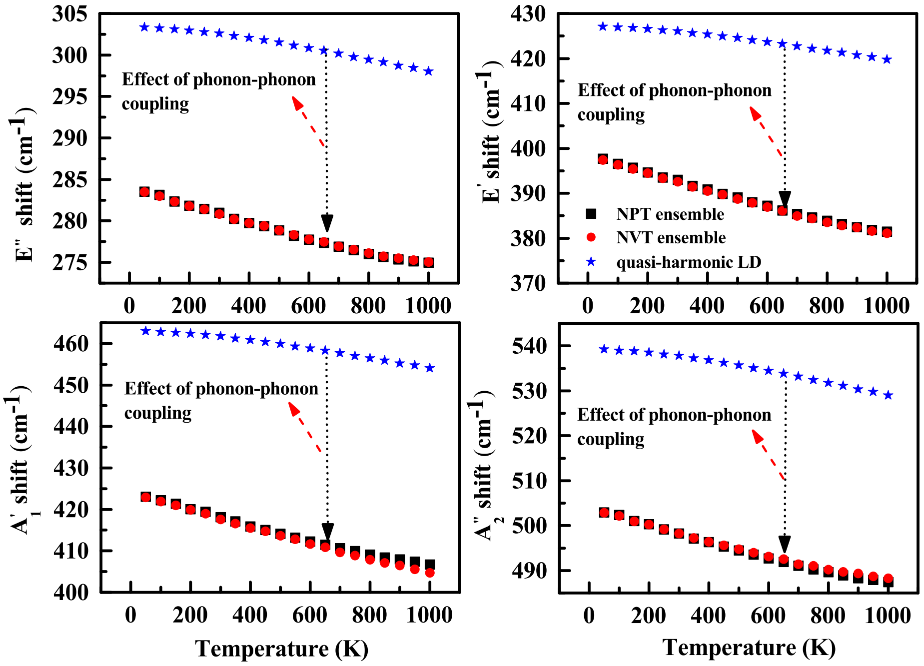

Figure 6.5 – The temperature dependent peak shifts of Γ point optic phonon modes in ML-MoS_2. The quasi-harmonic lattice dynamics (blue-stars) calculations includes only the effect of thermal expansions. The NVT ensemble (red spheres) mode frequency shifts are purely due to anharmonic coupling of phonon modes. NPT ensemble (black squares) mode frequency shift contains the combined effect of thermal expansion and anharmonic coupling of phonon modes. *Legends are common for all plots*

The three types of simulations carried out here help us to delineate the contributions of thermal expansion and phonon-phonon coupling effects to the total frequency shift. The red-shift of quasi-harmonic mode frequencies arises purely from thermal expansion of $\boldsymbol{a}$-lattice, and it does not contain the effects of phonon-phonon coupling. The NVT and NPT ensemble simulations predict a large downshift in mode frequencies with more steeper variation, and their magnitudes are identical. *This leads to the conclusion that the observed red-shifts at finite temperatures are essentially due to strong anharmonic coupling of phonon modes. Although thermal expansion contributes, its effect is masked by strong anharmonic coupling of phonon modes, and it is true for all four optic modes including the newly reported* $E^{''}$ *and* $A_2^{''}$.

Najmaei *et al* [98], used temperature dependent Raman spectroscopy to study the vibrational modes. The authors found that four phonon process is the major source of observed red-shift of $E_{2g}^1(E^{'})$ and $A_{1g}(A_1^{'})$ modes. Thermal expansion also contributes to the latter mode. Lanzillo *et al* [99] computed the temperature dependent phonon density of states of ML-MoS$_2$ using first principle MD simulations, and found that the temperature dependent red-shift of $E_{2g}^1(E^{'})$ and $A_{1g}(A_1^{'})$ modes are due to anharmonic coupling of phonon modes. Later, Taube *et al* [238] also made a similar conclusion about the observed red-shift of Raman active modes. Huang *et al* [53] performed first principle simulations and found that the observed red-shift of optic modes are due to multi-phonon scattering process with an insignificant contribution from thermal expansion. Present results are in qualitative agreement with the above reports in the case of all optic phonon modes.

The anharmonic coupling of phonon modes leads to decay of vibrational excitation from one mode to other causing a finite width of normal modes. Here we are analyzing the variation of linewidth as a function of temperature. The evolution of linewidth with layer numbers has been reported in various studies [95, 239]. However, temperature evolution of linewidth is not studied in detail. Taube *et al* [238] measured the linewidth of $E^1_{2g}(E^{'})$ and $A_{1g}(A^{'}_1)$ modes at temperatures between 70 K to 350 K and found that the change in linewidth of $E^1_{2g}(E^{'})$ mode is insignificant, while $A_{1g}(A^{'}_1)$ mode shows a strong temperature dependence. Figure 6.6 displays the computed linewidth of all four optic modes as a function of temperature. All modes are showing a monotonous increase in linewidth with an increase in temperature, except $A^{'}_1$ mode, which shows a small non-linearity in the initial portion, the similar trend has been reported by Taube *et al* [238]. Our data for E' also shows narrow spread in linewidth (~1 - 2 cm^{-1}) in the temperature range 50 K - 300 K, and matches with Taube *et al* [238]. But for temperature higher than 300 K, E' mode linewidth varies considerably. Unfortunately there are no high temperature Raman data for comparison. The newly reported $E''$and $A^{''}_2$ mode linewidth also shows a monotonous increase with an increase in temperatures. However, their magnitude is less compared to their in-plane (E') and out-of-plane ($A^{'}_1$) counter parts.

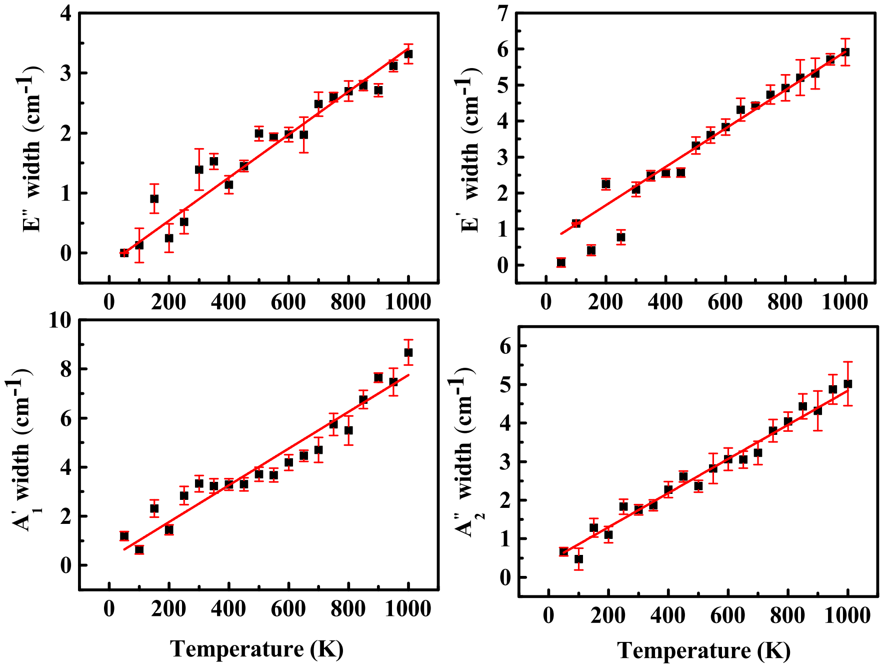

Figure 6.6 – The temperature dependent linewidth of Γ point optic modes in ML-MoS$_2$.

To understand the non-linear effect on eigenvectors, we computed the mode frequency shift and linewidth of all modes with and without using eigenvectors (chapter-2, 2.4.2.2). The peakshifts of modes obtained using both methods are identical (Figure 6.7), while linewidths are showing little difference (Figure 6.7). The linewidths obtained using eigenvectors (green-open triangle) are slightly lower in magnitude with respect to the one obtained without eigenvectors. But these differences are too small to be significant, as found in the case of graphene and 2D h-BN.

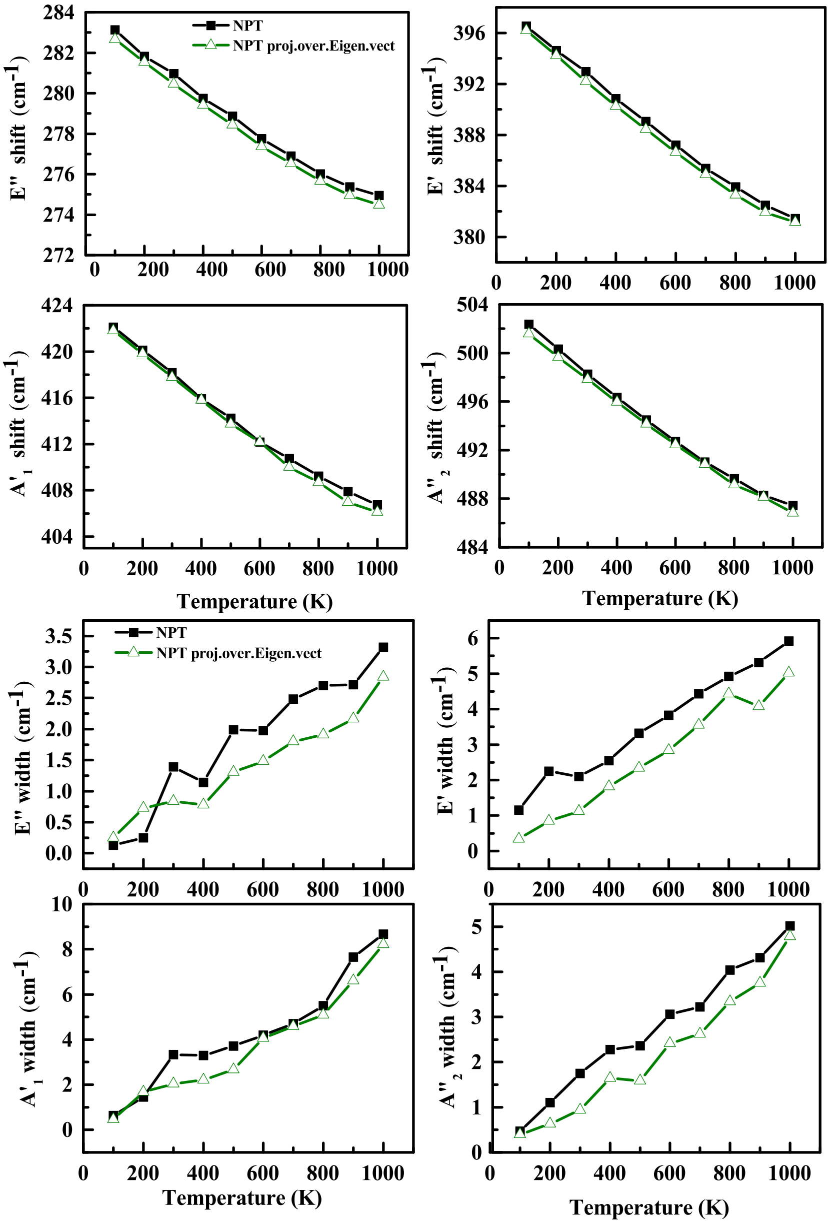

Figure 6.7 – (top)The peakshift and (bottom) linewidth of all modes computed with (green-open-upper triangle) and with out eigenvecotrs (black square) as a function of temperatures in NPT ensemble. *Legends are common for all plots*

From figure 6.5 we found that the peak positions evolve linearly with an increase in temperature, and this can be represented by the relationship [98],

$$\omega = \omega_0 + \chi T \tag{6.4}$$

where ω_0 is the extrapolated peak-position at 0 K, and χ is the first order temperature coefficient. The value of χ will be used to quantify the linear dependency, and it can be obtained from the slope of linear fit to ω vs T plot (Figure 6.8). The extracted values of χ for E' and $A_1^{'}$ modes are in qualitative agreement with experiment (table 6.2). The value of χ for $A_1^{'}$ mode is slightly higher than that of E' mode, which is an indication of higher temperature sensitivity of the corresponding mode. The smallness of the value of the temperature coefficient of E'' mode implies that it is less sensitive to temperature changes compared to the other in-plane (E') mode. Among the out-of-plane modes, $A_1^{'}$ and $A_2^{''}$ modes are having almost similar temperature coefficient.

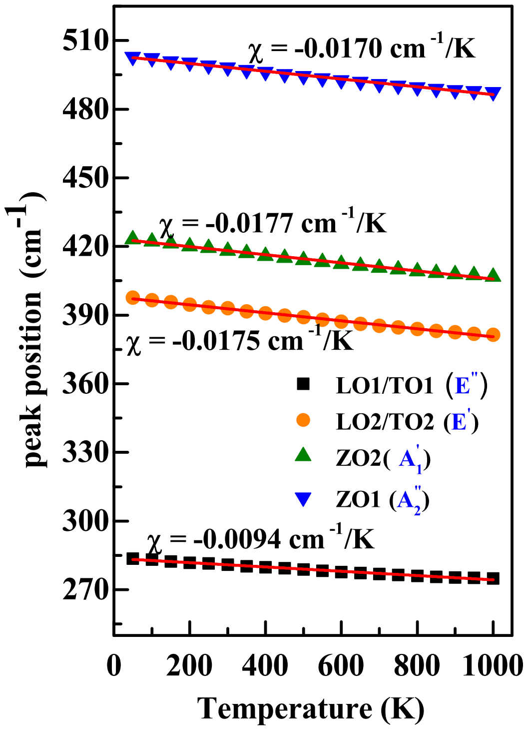

Figure 6.8 – The first order temperature coefficient (χ) of Γ point optic modes.

Table 6.2 – The first order temperature coefficient (χ) of all optic modes (expressed in cm^{-1}/K). Reference a, b, c and d are from [98–100, 238] respectively.

Mode	simulation	experiment
E''	-0.0094	———
E'	-0.0175	-0.0179^{a}, -0.013^{b}, -0.011^{c}, -0.0124^{d}
A_1'	-0.0177	-0.0143^{a}, -0.016^{b}, -0.013^{c}, -0.0143^{d}
A_2''	-0.0170	———

6.3.4 Effects of ripples and system size on thermal expansion

Similar to graphene and 2D h-BN, thermally excited ripples are present in ML-MoS$_2$ also. In order to understand the effect of thermally excited ripples we performed 2D and 3D simulation of very same system with simulation cells of different sizes. Figure 6.9 displays the thermal expansion of $\boldsymbol{a}$-lattice and linear thermal expansion coefficient (LTEC). As seen in the previous section (6.3.1) $\boldsymbol{a}$-lattice is expanding in the whole computed temperature range. This monotonous increase in $\boldsymbol{a}$-lattice with temperature is almost similar in both 2D and 3D simulations, and its system size dependence is marginal. The linear thermal expansion coefficients (LTEC) are positive in both 2D and 3D simulations (table 6.3), and its magnitude is slightly higher in 2D simulations at low temperatures ($T < 300$ K). Though ML-MoS$_2$ shares the same hexagonal honeycomb lattice with graphene and 2D h-BN, the $\boldsymbol{a}$-lattice of ML-MoS$_2$ shows a positive thermal expansion. This contradiction with graphene and h-BN can be visualized as an effect of S-Mo-S sandwich structure in ML-MoS$_2$, which reduces the thermally excited rippling behavior considerably [237].

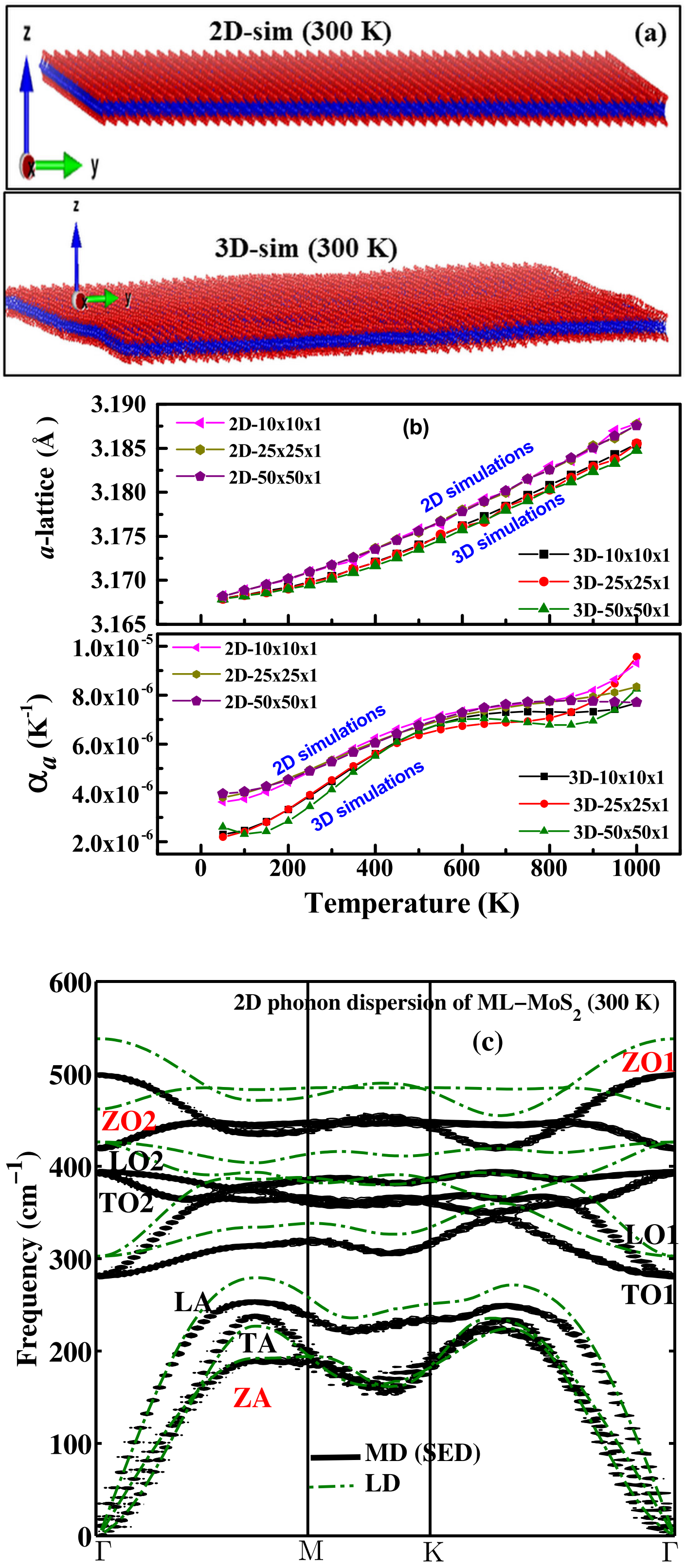

Figure 6.9 – (a) The snapshots of sheets obtained from 2D and 3D simulations at 300 K. (b) Temperature dependence of of in-plane lattice parameter (***a***-lattice) and linear thermal expansion coefficient (LTEC). The system size dependence of ***a***-lattice is marginal in ML-MoS_2 . (c) The phonon dispersion obtained from 2D simulations using SED method. The 2D phonon dispersion curve (thick black curve) share resemblance with LD dispersion curve (green dot dash). Unlike graphene (chapter-4, Figure-4.12) and 2D-h-BN (chapter-5, Figure-5.12), the out-of-plane vibrations (ZA, ZO1 and ZO2) are present here.

Figure 6.9c displays the phonon dispersion of ML-MoS$_2$ obtained from 2D simulations, and it shares a resemblance with LD calculations. Unlike graphene and 2D h-BN, all the out-of-plane modes are present in the 2D dispersion of ML-MoS$_2$. Though we arrested the out-of-plane movement of atoms, the ZA and ZO branches are still persisting in ML-MoS$_2$ dispersion curve, and this can be ascribed to the finite thickness effect. The graphene and 2D h-BN are one atom thick structure and have more flexibility along out-of-plane direction, the S-Mo-S sandwich structure of ML-MoS$_2$ makes it a more rigid material along out-of-plane direction and leads to less rippling. The magnitude of thermally excited ripples can be quantified using the height-height correlation function $\langle h^2 \rangle$, and its value is much smaller for ML-MoS$_2$ (∼1 Å^{2}at 300 K) in comparison with graphene(∼3.5 Å^{2}at 300 K), and it is an outcome of its less rippling behaviour [237]. The finite thickness of ML-MoS$_2$ counteracts the membrane effects, and hence the origin of bending mode (ZA) is not purely due to the out-of-plane movement of atoms. From the above results, it is clear that, the special S-Mo-S sandwich structure of ML-MoS$_2$ lowers the rippling behaviour, and its effect on thermal expansion is not prominent as found in graphene and 2D h-BN.

Table 6.3 – The linear thermal expansion coefficient LTEC of ML-MoS$_2$ at 300 K. The system size dependence of LTEC is insignificant in both 3D and 2D simulations. [a]Reference [55]

simulation cell size	2D simulation $\alpha_a(\times 10^{-6} K^{-1})$	3D simulation $\alpha_a(\times 10^{-6} K^{-1})$	expt. $\alpha_a(\times 10^{-6} K^{-1})$
10×10×1 (300 atoms)	5.340	4.469	
25×25×1 (1875 atoms)	5.343	4.530	4.922[a]
50x×50×1 (7500 atoms)	5.261	4.140	

6.4 Summary

Thermal expansion, structural stability and anharmonicity of free-standing ML-MoS$_2$ are computed using SED method. The important findings of this study are given below

- Unlike graphene and 2D h-BN the in-plane lattice parameter (***a***-lattice) of ML-MoS_2 shows thermal expansion in the whole computed temperature range (100 K - 1000 K).

- The phonon dispersion computed from quasi-harmonic lattice dynamics and molecular dynamics doesn't have any imaginary modes, which confirms the finite temperature structural stability. In graphene and 2D h-BN the structural stability can be ascribed to strong coupling between in-plane and out-of-plane modes, but in ML-MoS_2 it owes to its special S-Mo-S symmetric sandwich structure.

- Temperature evolution of Γ point optic modes are studied. Here we probed the temperature evolution of experimentally forbidden $E^{''}$ and $A_2^{''}$ modes in addition to the Raman active E' and $A_1^{'}$ modes. All the Γ point optic modes are showing a red-shift with an increase in temperature. We delineated the contributions of thermal expansion and anharmonic coupling of phonon modes to the total frequency shift and linewidth, and found that anharmonic coupling of phonon modes is the dominant source of observed red-shift and broadening of peaks.

- The effect of thermally excited ripples on thermal expansion are studied. Contrary to graphene and 2D h-BN, the ***a***-lattice of ML-MoS_2 shows thermal expansion in both 3D and 2D simulations and their system size dependence is marginal. The special S-Mo-S sandwich structure of ML-MoS_2 lowers the rippling behaviour, and its effect on thermal expansion is not prominent as found in graphene and 2D h-BN.

CHAPTER 7

Summary and future outlook

7.1 Summary

2D materials are the potential candidates in future electronic and opto-electronic industry due to their novel electronic, thermal and mechanical properties. Among 2D materials graphene has been studied extensively due its unique physical properties. The absence of finite band gap in graphene's electronic band structure is the major bottleneck in graphene based electronics. The 2D h-BN and monolayer(ML)-MoS_2 are other high interesting 2D honeycomb materials, they show fascinating electronic and optical properties. 2D materials based technologies makes the electronic devices smaller and more efficient in comparison with conventional Si based electronics. Heat removal is a crucial issue in such miniaturized and nano-size electronic devices. To fabricate electronic devices with better heat dissipation capability, knowledge of thermal and vibrational properties is essential. The ability of a material to transport heat is related to its atomic structure. However, it is difficult to understand heat transport phenomena at the atomistic level by experimentation. Computer simulations can be used in such situations to understand the fundamental issues associated with thermal and vibrational properties at atomistic level.

The structural, thermal and vibrational properties of 2D materials were reported elaborately in literature using *ab initio* calculations in conjunction with DFPT. However, there were no attempts to understand the temperature dependent structural stability and anharmonicity of these materials, which takes into account the full anharmonicity of the effective interaction between the atoms. The main reason behind this situation is that appropriate computational tools were not available to probe the complete anharmonicity of materials. We tackled this problem by adapting a spectral energy density (SED) method and investigated the structural stability, thermal expansion and anharmonicity of different 2D materials (graphite, graphene, 2D h-BN and monolayer (ML)-MoS$_2$) using *ab initio* and classical MD simulations. The present chapter discusses the major findings of this thesis and scope for future work.

Spectral energy density (SED) method to compute the phonon frequencies from MD simulations

A spectral energy density formalism is adapted to compute the phonon transport from MD simulations with full anharmonicity of effective interactions between the atoms. Several in-house codes were developed and coupled with classical MD simulation package LAMMPS. Using these codes one can readily compute the 1)phonon dispersion, 2)phonon DOS, 3)mode resolved frequency shift and linewidth at any point in the Brillouin zone, 4)anharmonic coupling and decay of normal modes. These codes were benchmarked using Si as a reference material. The phonon dispersion computed using SED method shows good agreement with experimental data. The Γ point longitudinal or transverse (LO/TO) optic mode frequency is ∼2.7 % higher than that of experimental value. The above agreement with experimental data is reasonably accurate, which guarantees the reliability of this method. After that, these codes were extensively used to study the finite temperature structural and vibrational properties of strong anharmonic 2D crystals such as graphene, 2D h-BN and ML-MoS$_2$. These studies show significant difference from quasi-harmonic predictions, due to inclusion of higher order phonon-phonon scattering processes. The key findings are given below.

Structural stability of 2D materials at finite temperatures

To understand the finite temperature structural stability of different 2D materials, phonon dispersions are computed using lattice dynamics (LD), quasi-harmonic LD and SED method. The computed phonon dispersions show reasonable agreement with experiments. In graphene, the out-of-plane optic (ZO) mode frequency is ∼0.4 % smaller than the experimental value at Γ point. Similarly the in-plane LO/TO modes frequency is ∼3 % lower with respect to experimental data at Γ point.

The quasi-harmonic out-of-plane bending mode (ZA) frequency of graphene and 2D h-BN becomes imaginary at higher temperatures, suggestive of a structural instability. However, in MD simulations using SED method, the frequency of the ZA mode becomes real. The dynamical stability of the system is restored due to the incorporation of phonon-phonon coupling processes of all orders in MD simulations, which were absent in the quasi-harmonic dispersion. The strong coupling between the phonon modes leads the formation of thermally excited ripples, which makes the 2D sheet stable at finite temperatures. The above results explain the role of strong anharmonic phonon–phonon coupling on the structural stability of free-standing graphene and 2D h-BN sheet at finite temperatures.

The phonon dispersion of ML-MoS$_2$ computed from LD, quasi-harmonic LD and MD (using SED method) doesn't have any imaginary modes, which confirms its finite temperature structural stability. Unlike graphene and 2D h-BN, where the structural stability is ascribed to strong coupling between phonon modes, in ML-MoS$_2$ it owes to its special S-Mo-S symmetric sandwich structure, which counteract against the membrane effects and makes the crystal stable and prevents the crumpling transition.

Anharmonicity of Γ point optic phonon modes

To understand the temperature dependent phonon frequency shift and linewidth of optic phonon modes, mode resolved phonon spectra is computed at Γ point. The contributions of thermal expansion and anharmonic coupling of phonon modes to the frequency shift and linewidth are delineated using quasi-harmonic LD, canonical (NVT), and isobaric-isothermal (NPT) ensemble based MD simulations. In graphene, along with thermal contraction effects, the strong phonon-phonon coupling causes a blue-shift of LO/TO and ZO mode frequencies with increase in temperature. At the same time, the phonon-phonon coupling causes a reverse effect in 2D h-BN. Though the thermal contraction of ***a***-lattice causes a blue-shift in LO/TO mode frequency, the strong phonon–phonon coupling dominates over it and decreases the mode frequency, eventually leading to a red-shift. This discrepancy between the graphene and 2D h-BN is due to the difference in masses of basis atoms (B and N) in 2D h-BN. The ZO mode also got red-shifted due to strong phonon-phonon coupling effects. Similar studies in ML-MoS_2 showed that the phonon-phonon coupling between the phonon modes is the predominant source of observed redshift of optic mode phonon frequencies, the thermal expansion contribution is insignificant.

From the above results, we concluded that the higher order phonon-phonon coupling processes have significant role in determining the temperature dependent peak shift of phonon modes in all 2D materials studied here.

Thermal expansion of 2D materials - role of thermally excited ripples

The variation of in-plane lattice parameter (***a***-lattice) and linear thermal expansion coefficient (LTEC) are studied as a function of temperature using 3D MD simulations. The ***a***-lattice of graphene shows a thermal contraction upto ∼1300 K and further it expands. The linear thermal expansion coefficient is $\alpha_a = -4.300\times10^{-6}$ K^{-1} at 300 K, which is in agreement with experimental data (-5.500×10^{-6} K^{-1}). From the experimental front, graphene shows thermal contraction upto 400 K. Above this temperature graphene sheet slips on SiO_2 substrate surface because the tensile strain increases significantly over the weak Van der Waals (vdW) force which pins the sheet on the substrate, hence high temperature experimental data is not available for comparison. In 2D h-BN, the ***a***-lattice shows thermal contraction in the whole computed temperature range (100 K - 2000 K). Contrary to graphene and 2D h-BN, the ***a***-lattice of ML-MoS_2 shows a thermal expansion in the interval of 100 K - 1000 K. This difference in thermal expansion of the 2D layered materials can be utilized to devise graphene/MoS_2 based hybrid devices for better performance.

We delineated the role of thermally excited ripples on thermal expansion properties of aforementioned 2D materials, by explicitly carrying out 3D and 2D MD simulations. In 3D simulations, the in-plane lattice parameter ($\boldsymbol{a}$-lattice) of graphene and 2D h-BN shows thermal contraction over a wide range of temperatures and exhibits a strong system size dependence. The 2D simulations of the very same system show a reverse trend, where the $\boldsymbol{a}$-lattice is expanding in the whole computed temperature range.

Contrary to graphene and 2D h-BN, the $\boldsymbol{a}$-lattice of ML-MoS$_2$ shows thermal expansion in both 2D and 3D simulations and their system size dependence is marginal. By analyzing the phonon dispersion at 300 K, we found that the discrepancy between 2D and 3D simulations of graphene and 2D h-BN is due to the absence of out-of-plane bending mode (ZA) in 2D simulations, which is responsible for thermal contraction of $\boldsymbol{a}$-lattice at low temperature. Meanwhile, all the phonon modes are present in 2D phonon dispersion of ML-MoS$_2$, which indicates that the origin of ZA mode is not purely due to out-of-plane movement of atoms and also its effect on thermal expansion is not significant as found in graphene and 2D h-BN.

Though ML-MoS$_2$ possess the same hexagonal honeycomb lattice of graphene and 2D h-BN, the a-lattice of ML-MoS$_2$ shows a positive thermal expansion. This contradiction with graphene and h-BN can be visualized as an effect of S-Mo-S sandwich structure in ML-MoS$_2$, which reduces the thermally excited rippling behavior considerably.

Mechanical and dynamical stability of stacking altered graphite structures

Ab initio simulations have been performed to study the structure, energetics and stability of several plausible stacking sequences in graphite. These calculations suggest that, in addition to the standard structures (AB-hexagonal and ABC-rhombohedral), graphite can also exist in AA-simple hexagonal, AB-orthorhombic and ABC-hexagonal type stacking. The free energy difference between these structures is very small ($\sim$1 meV/atom), and hence all the structures can coexist from purely energetic considerations. From elastic constant and phonon dispersion calculation we found that these stacking altered structures are mechanically as well as dynamically unstable. The stability of these structures at finite temperature is studied by computing the phonon dispersion (at 300 K) directly from classical MD simulations. These studies indicates that all the stacking altered bilayer/trilayer structures are reverting back to thermodynamically stable AB-hexagonal/ABC-rhombohedral structures.

7.2 Future outlook

The following studies can be carried as an extension to the present study.

1. The stacking altered graphite structures are found to be unstable. It is worth studying whether the incorporation of planar defects or intercalates will stabilize the stacking altered graphite structures or not. MD results indicates that the unstable bilayer/trilayer structures are reverting back to thermodynamically stable AB-hexagonal/ABC-rhombohedral structure at 300 K. Nudged elastic band (NEB) [240] calculation can be done to confirm the above transition and to get the information on transition pathways.

2. In the present study, we didn't investigate the isotope effects on the structural and anharmonic properties. This study needs to be undertaken to understand the role of isotopes on thermal and vibrational properties of 2D materials at different temperatures.

3. The presence of defects can alter the phonon transport mechanism. This can't be studied in conventional LD method. The SED method can be used to study the effects of various defects on vibrational properties of materials at finite temperatures. Hence this method can be used to understand the thermal and vibrational properties of 2D materials with different types of topological defects.

4. Recently, several van der Waals (vdW) hetero-structures have been fabricated by stacking different types of 2D materials one above another. These hetero-

structures revealed many intriguing electronic phenomena. It will be interesting to study their finite temperature structural stability and anharmonicity using SED method.

5. SED method can be further extended to develop a code which can predict the mode resolved contribution to the lattice thermal conductivity. This information will help to control and manipulate the heat flow and will aid in the development of promising thermo-electric materials with higher ZT values.

References

[1] A. F. Morpurgo, Nat. Phys. **11**, 625 (2015).

[2] F. Iacopi, J. Boeckl, and C. Jagadish, *2D Materials*, Semiconductors and Semimetals (Elsevier Science, 2016).

[3] K. S. Novoselov, A. K. Geim, S. V. Morozov, D. Jiang, Y. Zhang, S. V. Dubonos, I. V. Grigorieva, and A. A. Firsov, Science **306**, 666 (2004).

[4] A. K. Geim and K. S. Novoselov, Nat. Mater. **6**, 183 (2007).

[5] L. Zhang, Y. Zhang, J. Camacho, M. Khodas, and I. Zaliznyak, Nat. Phys. **7**, 953 (2011).

[6] C. H. Lui, Z. Li, K. F. Mak, E. Cappelluti, and T. F. Heinz, Nat. Phys. **7**, 944 (2011).

[7] W. Bao, L. Jing, J. Velasco, Y. Lee, G. Liu, D. Tran, B. Standley, M. Aykol, S. B. Cronin, D. Smirnov, et al., Nat. Phys. **7**, 948 (2011).

[8] A. H. Castro Neto, F. Guinea, N. M. R. Peres, K. S. Novoselov, and A. K. Geim, Rev. Mod. Phys. **81**, 109 (2009).

[9] A. K. Geim and I. V. Grigorieva, Nature **499**, 419 (2013).

[10] A. K. Geim, Rev. Mod. Phys. **83**, 851 (2011).

[11] A. C. Ferrari, F. Bonaccorso, V. Fal'ko, K. S. Novoselov, S. Roche, P. Boggild, S. Borini, F. H. L. Koppens, V. Palermo, N. Pugno, et al., Nanoscale **7**, 4598 (2015).

[12] A. A. Balandin, Nat. Mater. **10**, 569 (2011).

[13] C. Lee, X. Wei, J. W. Kysar, and J. Hone, Science **321**, 385 (2008).

[14] R. R. Nair, P. Blake, A. N. Grigorenko, K. S. Novoselov, T. J. Booth, T. Stauber, N. M. R. Peres, and A. K. Geim, Science **320**, 1308 (2008).

[15] K. Watanabe, T. Taniguchi, and H. Kanda, Nat. Mater. **3**, 404 (2004).

[16] Y. Shi, C. Hamsen, X. Jia, K. K. Kim, A. Reina, M. Hofmann, A. L. Hsu, K. Zhang, H. Li, Z.-Y. Juang, et al., Nano Lett. **10**, 4134 (2010).

[17] D. Golberg, Y. Bando, Y. Huang, T. Terao, M. Mitome, C. Tang, and C. Zhi, ACS Nano **4**, 2979 (2010).

[18] M. S. Bresnehan, M. J. Hollander, M. Wetherington, M. LaBella, K. A. Trumbull, R. Cavalero, D. W. Snyder, and J. A. Robinson, ACS Nano **6**, 5234 (2012).

[19] E. H. Hwang, S. Adam, and S. D. Sarma, Phys. Rev. Lett. **98**, 186806 (2007).

[20] D. L. Duong, G. H. Han, S. M. Lee, F. Gunes, E. S. Kim, S. T. Kim, H. Kim, Q. H. Ta, K. P. So, S. J. Yoon, et al., Nature **490**, 235 (2012).

[21] M. Ishigami, J. H. Chen, W. G. Cullen, M. S. Fuhrer, and E. D. Williams, Nano Lett. **7**, 1643 (2007).

[22] M. I. Katsnelson and A. K. Geim, Proc. R. Soc. A **366**, 195 (2008).

[23] S. V. Morozov, K. S. Novoselov, M. I. Katsnelson, F. Schedin, D. C. Elias, J. A. Jaszczak, and A. K. Geim, Phys. Rev. Lett. **100**, 016602 (2008).

[24] C. R. Dean, A. F. Young, I. Meric, C. Lee, L. Wang, S. Sorgenfrei, K. Watanabe, T. Taniguchi, P. Kim, K. L. Shepard, et al., Nat Nano **5**, 722 (2010).

[25] M. Chhowalla, H. S. Shin, G. Eda, L.-J. Li, K. P. Loh, and H. Zhang, Nat. Chem. **5**, 263 (2013).

[26] X. Huang, Z. Zeng, and H. Zhang, Chem. Soc. Rev. **42**, 1934 (2013).

[27] B. Radisavljevic, A. Radenovic, J. Brivio, V. Giacometti, and A. Kis, Nat Nano **6**, 147 (2011).

[28] M. Buscema, M. Barkelid, V. Zwiller, H. S. J. van der Zant, G. A. Steele, and A. Castellanos-Gomez, Nano Lett. **13**, 358 (2013).

[29] D. Jariwala, A. Srivastava, and P. Ajayan, ArXiv e-prints,1108.4141 (2011).

[30] J. M. H. Kroes, A. Fasolino, and M. I. Katsnelson, Phys. Chem. Chem. Phys. **18**, 19359 (2016).

[31] R.-F. Liu and C. Cheng, Phys. Rev. B **76**, 014405 (2007).

[32] A. K. Geim and A. H. MacDonald, Phys. Today **60**, 35 (2007).

[33] A. Molina-Sánchez and L. Wirtz, Phys. Rev. B **84**, 155413 (2011).

[34] A. Kuc, N. Zibouche, and T. Heine, Phys. Rev. B **83**, 245213 (2011).

[35] A. Splendiani, L. Sun, Y. Zhang, T. Li, J. Kim, C.-Y. Chim, G. Galli, and F. Wang, Nano Lett. **10**, 1271 (2010).

[36] S.-L. Li, K. Tsukagoshi, E. Orgiu, and P. Samori, Chem. Soc. Rev. **45**, 118 (2016).

[37] R. E. Peierls, Ann. I. H. Poincare **5**, 177 (1935).

[38] L. Landau and D. Zur, Phys. Z. Sowjetunion **11**, 26 (1937).

[39] N. D. Mermin, Phys. Rev. **176**, 250 (1968).

[40] J. Evans, P. Thiel, and M. Bartelt, Surf. Sci. Rep. **61**, 1 (2006).

[41] A. Fasolino, J. Los, and M. I. Katsnelson, Nat. Mater. **6**, 858 (2007).

[42] J. C. Meyer, A. K. Geim, M. I. Katsnelson, K. S. Novoselov, T. J. Booth, and S. Roth, Nature **446**, 60 (2007).

[43] N. Bonini, J. Garg, and N. Marzari, Nano Lett. **12**, 2673 (2012).

[44] N. Mounet and N. Marzari, Phys. Rev. B **71**, 205214 (2005).

[45] K. V. Zakharchenko, M. I. Katsnelson, and A. Fasolino, Phys. Rev. Lett. **102**, 046808 (2009).

[46] M. Pozzo, D. Alfè, P. Lacovig, P. Hofmann, S. Lizzit, and A. Baraldi, Phys. Rev. Lett. **106**, 135501 (2011).

[47] J.-W. Jiang, J.-S. Wang, and B. Li, Phys. Rev. B **80**, 205429 (2009).

[48] W. Bao, F. Miao, Z. Chen, H. Zhang, W. Jang, C. Dames, and C. N. Lau, Nat. Nanotechnol. **4**, 562 (2009).

[49] V. Singh, S. Sengupta, H. S. Solanki, R. Dhall, A. Allain, S. Dhara, P. Pant, and M. M. Deshmukh, Nanotechnology **21**, 165204 (2010).

[50] D. Yoon, Y.-W. Son, and H. Cheong, Nano Lett. **11**, 3227 (2011).

[51] B. Yates, M. J. Overy, and O. Pirgon, Philos. Mag. **32**, 847 (1975).

[52] C. Sevik, Phys. Rev. B **89**, 035422 (2014).

[53] L. F. Huang, P. L. Gong, and Z. Zeng, Phys. Rev. B **90**, 045409 (2014).

[54] S. H. El-Mahalawy and B. L. Evans, J. Appl. Crystallogr. **9**, 403 (1976).

[55] R. Murray and B. Evans, J. Appl. Crystallogr. **12**, 312 (1979).

[56] L. Wirtz and A. Rubio, Solid State Commun. **131**, 141 (2004).

[57] H. Zabel, J. Phys.: Condens. Matter **13**, 7679 (2001).

[58] M. Lifshitz, Zh. Eksp. Teor. Fiz **22**, 475 (1952).

[59] R. Nicklow, N. Wakabayashi, and H. G. Smith, Phys. Rev. B **5**, 4951 (1972).

[60] G. Saito, R. Dresselhaus and M. Dresselhaus, *Physical Properties of Carbon Nanotubes* (London: Imperial College Press, 1998).

[61] J.-A. Yan, W. Y. Ruan, and M. Y. Chou, Phys. Rev. B **77**, 125401 (2008).

[62] S. K. Saha, U. V. Waghmare, H. R. Krishnamurthy, and A. K. Sood, Phys. Rev. B **78**, 165421 (2008).

[63] L. Karssemeijer and A. Fasolino, Surf. Sci. **605**, 1611 (2011).

[64] N. Bonini, M. Lazzeri, N. Marzari, and F. Mauri, Phys. Rev. Lett. **99**, 176802 (2007).

[65] L. Paulatto, F. Mauri, and M. Lazzeri, Phys. Rev. B **87**, 214303 (2013).

[66] L. Malard, M. Pimenta, G. Dresselhaus, and M. Dresselhaus, Phys. Rep. **473**, 51 (2009).

[67] I. Calizo, A. A. Balandin, W. Bao, F. Miao, and C. N. Lau, Nano Lett. **7**, 2645 (2007).

[68] J. Lin, L. Guo, Q. Huang, Y. Jia, K. Li, X. Lai, and X. Chen, Phys. Rev. B **83**, 125430 (2011).

[69] M. Omar, *Elementary Solid State Physics: Principles and Applications* (Addison-Wesley, 1975).

[70] I. I. Al-Qasir, Ph.D. thesis, North Carolina State University, North Carolina (2007).

[71] G. Benedek, G. Brusdeylins, C. Heimlich, J. Toennies, and U. Valbusa, Surf. Sci. **178**, 545 (1986).

[72] C. Oshima, T. Aizawa, R. Souda, Y. Ishizawa, and Y. Sumiyoshi, Solid State Commun. **65**, 1601 (1988).

[73] J. Wilkes, R. Palmer, and R. Willis, J. Electron Spectrosc. Relat. Phenom. **44**, 355 (1987).

[74] S. Siebentritt, R. Pues, K.-H. Rieder, and A. M. Shikin, Phys. Rev. B **55**, 7927 (1997).

[75] J. Maultzsch, S. Reich, C. Thomsen, H. Requardt, and P. Ordejón, Phys. Rev. Lett. **92**, 075501 (2004).

[76] M. Endlich, A. Molina-Sánchez, L. Wirtz, and J. Kröger, Phys. Rev. B **88**, 205403 (2013).

[77] M. Endlich, H. P. C. Miranda, A. Alejandro Molina-Sánchez, L. Wirtz, and J. Kröger, Ann. Phys. **526**, 1 (2014).

[78] T. Aizawa, Y. Hwang, W. Hayami, R. Souda, S. Otani, and Y. Ishizawa, Surf. Sci. **260**, 311 (1992).

[79] A. Politano, A. R. Marino, D. Campi, D. Farias, R. Miranda, and G. Chiarello, Carbon **50**, 4903 (2012).

[80] H. Yanagisawa, T. Tanaka, Y. Ishida, M. Matsue, E. Rokuta, S. Otani, and C. Oshima, Surf. Interface Anal. **37**, 133 (2005).

[81] M. Topsakal, E. Aktürk, and S. Ciraci, Phys. Rev. B **79**, 115442 (2009).

[82] K. H. Michel and B. Verberck, Phys. Rev. B **83**, 115328 (2011).

[83] G. J. Slotman and A. Fasolino, J. Phys.: Condens. Matter **25**, 045009 (2013).

[84] S. K. Singh, M. Neek-Amal, S. Costamagna, and F. M. Peeters, Phys. Rev. B **87**, 184106 (2013).

[85] D. Sánchez-Portal and E. Hernández, Phys. Rev. B **66**, 235415 (2002).

[86] L. Wirtz, A. Rubio, R. A. de la Concha, and A. Loiseau, Phys. Rev. B **68**, 045425 (2003).

[87] R. Geick, C. H. Perry, and G. Rupprecht, Phys. Rev. **146**, 543 (1966).

[88] R. J. Nemanich, S. A. Solin, and R. M. Martin, Phys. Rev. B **23**, 6348 (1981).

[89] C. Oshima and A. Nagashima, J. Phys.: Condens. Matter **9**, 1 (1997).

[90] E. Rokuta, Y. Hasegawa, K. Suzuki, Y. Gamou, C. Oshima, and A. Nagashima, Phys. Rev. Lett. **79**, 4609 (1997).

[91] J. Serrano, A. Bosak, R. Arenal, M. Krisch, K. Watanabe, T. Taniguchi, H. Kanda, A. Rubio, and L. Wirtz, Phys. Rev. Lett. **98**, 095503 (2007).

[92] X. Zhang, X.-F. Qiao, W. Shi, J.-B. Wu, D.-S. Jiang, and P.-H. Tan, Chem. Soc. Rev. **44**, 2757 (2015).

[93] C. Ataca, M. Topsakal, E. Aktürk, and S. Ciraci, J. Phys. Chem. C **115**, 16354 (2011).

[94] Y. Cai, J. Lan, G. Zhang, and Y.-W. Zhang, Phys. Rev. B **89**, 035438 (2014).

[95] C. Lee, H. Yan, L. E. Brus, T. F. Heinz, J. Hone, and S. Ryu, ACS Nano **4**, 2695 (2010).

[96] H. Li, Q. Zhang, C. C. R. Yap, B. K. Tay, T. H. T. Edwin, A. Olivier, and D. Baillargeat, Adv. Funct. Mater. **22**, 1385 (2012).

[97] X. Zhang, W. P. Han, J. B. Wu, S. Milana, Y. Lu, Q. Q. Li, A. C. Ferrari, and P. H. Tan, Phys. Rev. B **87**, 115413 (2013).

[98] S. Najmaei, P. M. Ajayan, and J. Lou, Nanoscale **5**, 9758 (2013).

[99] N. A. Lanzillo, A. Glen Birdwell, M. Amani, F. J. Crowne, P. B. Shah, S. Najmaei, Z. Liu, P. M. Ajayan, J. Lou, M. Dubey, et al., Appl. Phys. Lett. **103**, (2013).

[100] R. Yan, J. R. Simpson, S. Bertolazzi, J. Brivio, M. Watson, X. Wu, A. Kis, T. Luo, A. R. Hight Walker, and H. G. Xing, ACS Nano **8**, 986 (2014).

[101] S. Sahoo, A. P. S. Gaur, M. Ahmadi, M. J.-F. Guinel, and R. S. Katiyar, J. Phys. Chem. C **117**, 9042 (2013).

[102] B. J. Robinson, C. E. Giusca, Y. T. Gonzalez, N. D. Kay, O. Kazakova, and O. V. Kolosov, 2D Mater. **2**, 015005 (2015).

[103] S. Najmaei, Z. Liu, P. M. Ajayan, and J. Lou, Appl. Phys. Lett. **100**, 013106 (2012).

[104] L. T. Kong, Comput. Phys. Commun. **182**, 2201 (2011).

[105] M. Born and R. Oppenheimer, Ann. Phys. **389**, 457 (1927).

[106] L. H. Thomas, Math. Proc. Cambridge Philos. Soc. **23**, 542 (1927).

[107] E. Fermi, Rend. Accad. Naz. Lincei **6**, 602 (1927).

[108] E. Teller, Rev. Mod. Phys. **34**, 627 (1962).

[109] P. Hohenberg and W. Kohn, Phys. Rev. **136**, B864 (1964).

[110] J. Kohanoff, *Electronic Structure Calculations for Solids and Molecules: Theory and Computational Methods* (Cambridge University Press, 2006).

[111] R. Martin, *Electronic Structure: Basic Theory and Practical Methods* (Cambridge University Press, 2004).

[112] M. C. Payne, M. P. Teter, D. C. Allan, T. A. Arias, and J. D. Joannopoulos, Rev. Mod. Phys. **64**, 1045 (1992).

[113] W. Kohn and L. J. Sham, Phys. Rev. **140**, A1133 (1965).

[114] D. M. Ceperley and B. J. Alder, Phys. Rev. Lett. **45**, 566 (1980).

[115] W. Kohn, Rev. Mod. Phys. **71**, 1253 (1999).

[116] J. P. Perdew and A. Zunger, Phys. Rev. B **23**, 5048 (1981).

[117] S. H. Vosko, L. Wilk, and M. Nusair, Can. J. Phys. **58**, 1200 (1980).

[118] J. P. Perdew and Y. Wang, Phys. Rev. B **45**, 13244 (1992).

[119] D. C. Langreth and M. J. Mehl, Phys. Rev. B **28**, 1809 (1983).

[120] J. P. Perdew, J. A. Chevary, S. H. Vosko, K. A. Jackson, M. R. Pederson, D. J. Singh, and C. Fiolhais, Phys. Rev. B **46**, 6671 (1992).

[121] A. D. Becke, Phys. Rev. A **38**, 3098 (1988).

[122] J. P. Perdew, K. Burke, and M. Ernzerhof, Phys. Rev. Lett. **77**, 3865 (1996).

[123] C. Kittel, *Introduction to Solid State Physics* (John Wiley & Sons, Inc., New York, 1986).

[124] N. Ashcroft and N. Mermin, *Solid State Physics* (Saunders College, Philadelphia, 1976).

[125] H. J. Monkhorst and J. D. Pack, Phys. Rev. B **13**, 5188 (1976).

[126] D. J. Chadi and M. L. Cohen, Phys. Rev. B **8**, 5747 (1973).

[127] W. E. Pickett, Comput. Phys. Rep. **9**, 115 (1989).

[128] URL http://en.wikipedia.org/wiki/Pseudopotential.

[129] G. Kresse and D. Joubert, Phys. Rev. B **59**, 1758 (1999).

[130] P. E. Blöchl, Phys. Rev. B **50**, 17953 (1994).

[131] G. Kresse and J. Hafner, Phys. Rev. B **47**, 558 (1993).

[132] H. Hellmann, *Einführung in die Quantenchemie* (Franz Deuticke, 1937).

[133] R. P. Feynman, Phys. Rev. **56**, 340 (1939).

[134] S. Baroni, S. de Gironcoli, A. Dal Corso, and P. Giannozzi, Rev. Mod. Phys. **73**, 515 (2001).

[135] M. P. Allen and D. J. Tildesley, *Computer Simulation of Liquids* (Clarendon Press, New York, NY, USA, 1987).

[136] D. Frenkel and B. Smit, eds., *Understanding Molecular Simulation: From Algorithms to Applications* (Academic Press, Inc., Orlando, FL, USA, 1996).

[137] K. Nordlund and D. F. Djurabekova, *Molecular dynamics simulations*, University Lecture (2015), URL `http://www.acclab.helsinki.fi/~knordlun/moldyn/`.

[138] N. Zabaras, *Introduction to molecular dynamics simulations*, University Lecture (2012), URL `http://www.zabaras.com/Courses/MAE715/MAE715.html`.

[139] F. Ercolessi, *A molecular dynamics primer*, Spring College in Computational Physics (1997).

[140] L. Zhigilei, *Introduction to interatomic potentials*, Lecture notes (2016), URL `http://www.people.virginia.edu/~lz2n/mse627/`.

[141] M. S. Daw and M. I. Baskes, Phys. Rev. Lett. **50**, 1285 (1983).

[142] M. S. Daw and M. I. Baskes, Phys. Rev. B **29**, 6443 (1984).

[143] M. Mendelev, D. Srolovitz, S. Han, A. Barashev, and G. Ackland, J. Phys.: Condens. Matter **16**, S2629 (2004).

[144] F. H. Stillinger and T. A. Weber, Phys. Rev. B **31**, 5262 (1985).

[145] J. Tersoff, Phys. Rev. Lett. **56**, 632 (1986).

[146] D. W. Brenner, Phys. Rev. B **42**, 9458 (1990).

[147] J. H. Los and A. Fasolino, Phys. Rev. B **68**, 024107 (2003).

[148] C. Sevik, A. Kinaci, J. B. Haskins, and T. Çağ ın, Phys. Rev. B **84**, 085409 (2011).

[149] J. A. Stewart and D. E. Spearot, Modell. Simul. Mater. Sci. Eng. **21**, 045003 (2013).

[150] L. Verlet, Phys. Rev. **159**, 98 (1967).

[151] L. Verlet, Phys. Rev. **165**, 201 (1968).

[152] P. P. Ewald, Ann. Phys. **369**, 253 (1921).

[153] M. Tuckerman, *Statistical Mechanics: Theory and Molecular Simulation*, Oxford Graduate Texts (OUP Oxford, 2010).

[154] H. C. Andersen, J. Chem. Phys. **72**, 2384 (1980).

[155] H. J. C. Berendsen, J. P. M. Postma, W. F. van Gunsteren, A. Dinola, and J. R. Haak, J. Chem. Phys. **81**, 3684 (1984).

[156] S. Nosé, J. Chem. Phys. **81**, 511 (1984).

[157] W. G. Hoover, Phys. Rev. A **31**, 1695 (1985).

[158] G. Venkataraman, L. Feldkamp, and V. Sahni, *Dynamics of perfect crystals* (MIT Press, 1975).

[159] A. Maradudin, *Lattice dynamics*, Progress in physics (Benjamin, 1969).

[160] R. Peierls, *Quantum Theory of Solids*, International Series of Monographs on Physics (Clarendon Press, 1996).

[161] M. Born and K. Huang, *Dynamical Theory of Crystal Lattices*, International series of monographs on physics (Clarendon Press, 1998).

[162] P. Brüesch, *Phonons: Theory and Experiments I: Lattice Dynamics and Models of Interatomic Forces*, Springer Series in Solid-State Sciences (Springer Berlin Heidelberg, 1982).

[163] G. Leibfried and W. Ludwig, *Theory of Anharmonic Effects in Crystals* (Academic Press, 1961).

[164] B. Fultz, Prog. Mater Sci. **55**, 247 (2010).

[165] T. Barron, J. Collins, and G. White, Adv. Phys. **29**, 609 (1980).

[166] J. E. Turney, E. S. Landry, A. J. H. McGaughey, and C. H. Amon, Phys. Rev. B **79**, 064301 (2009).

[167] D. Wallace, *Thermodynamics of Crystals* (Dover Publications, 1998).

[168] A. A. Maradudin and A. E. Fein, Phys. Rev. **128**, 2589 (1962).

[169] A. Debernardi, S. Baroni, and E. Molinari, Phys. Rev. Lett. **75**, 1819 (1995).

[170] G. Deinzer, G. Birner, and D. Strauch, Phys. Rev. B **67**, 144304 (2003).

[171] S. Berciaud, M. Y. Han, K. F. Mak, L. E. Brus, P. Kim, and T. F. Heinz, Phys. Rev. Lett. **104**, 227401 (2010).

[172] M. T. Dove, *Introduction to Lattice Dynamics* (Cambridge University Press, 1993).

[173] J. M. Dickey and A. Paskin, Phys. Rev. **188**, 1407 (1969).

[174] P. Heino, EPJ B **60**, 171 (2007).

[175] C. Campañá and M. H. Müser, Phys. Rev. B **74**, 075420 (2006).

[176] V. Tewary, Adv. Phys. **22**, 757 (1973).

[177] J. A. Thomas, J. E. Turney, R. M. Iutzi, C. H. Amon, and A. J. H. McGaughey, Phys. Rev. B **81**, 081411 (2010).

[178] B. Qiu, H. Bao, G. Zhang, Y. Wu, and X. Ruan, Comput. Mater. Sci. **53**, 278 (2012).

[179] S. Plimpton, J. Comput. Phys. **117**, 1 (1995), URL http://lammps.sandia.gov.

[180] G. J. Ackland, M. C. Warren, and S. J. Clark, J. Phys.: Condens. Matter **9**, 7861 (1997).

[181] A. Togo, F. Oba, and I. Tanaka, Phys. Rev. B **78**, 134106 (2008).

[182] J. Tersoff, Phys. Rev. B **39**, 5566 (1989).

[183] Y. Lee and G. S. Hwang, Phys. Rev. B **85**, 125204 (2012).

[184] D. Powell, Ph.D. thesis, University of Sheffield (2006).

[185] G. Nilsson and G. Nelin, Phys. Rev. B **6**, 3777 (1972).

[186] P. Giannozzi, S. de Gironcoli, P. Pavone, and S. Baroni, Phys. Rev. B **43**, 7231 (1991).

[187] A. J. McGaughey and M. Kaviany, Advances in Heat Transfer **39**, 169 (2006).

[188] J. D. Bernal, Proc. R. Soc. A **106**, 749 (1924).

[189] H. Lipson and A. R. Stokes, Proc. R. Soc. A **181**, 101 (1942).

[190] J.-C. Charlier, X. Gonze, and J.-P. Michenaud, Carbon **32**, 289 (1994).

[191] P. L. de Andres, R. Ramírez, and J. A. Vergés, Phys. Rev. B **77**, 045403 (2008).

[192] S. Okada and T. Kobayashi, Jpn. J. Appl. Phys. **48**, 050207 (2009).

[193] G. Savini, Y. J. Dappe, S. Öberg, J.-C. Charlier, M. I. Katsnelson, and A. Fasolino, Carbon **49**, 62 (2011).

[194] G. Kresse, J. Furthmüller, and J. Hafner, Europhys. Lett. **32**, 729 (1995).

[195] G. Kresse and J. Furthmüller, Phys. Rev. B **54**, 11169 (1996).

[196] S. Latil and L. Henrard, Phys. Rev. Lett. **97**, 036803 (2006).

[197] N. Ooi, A. Rairkar, and J. B. Adams, Carbon **44**, 231 (2006).

[198] A. Bosak, M. Krisch, M. Mohr, J. Maultzsch, and C. Thomsen, Phys. Rev. B **75**, 153408 (2007).

[199] S. Grimme, J. Comput. Chem. **27**, 1787 (2006).

[200] M. Methfessel and A. T. Paxton, Phys. Rev. B **40**, 3616 (1989).

[201] Y. Le Page and P. Saxe, Phys. Rev. B **65**, 104104 (2002).

[202] G. A. de Wijs, C. M. Fang, G. Kresse, and G. de With, Phys. Rev. B **65**, 094305 (2002).

[203] K. Momma and F. Izumi, J. Appl. Crystallogr. **44**, 1272 (2011).

[204] O. L. Blakslee, D. G. Proctor, E. J. Seldin, G. B. Spence, and T. Weng, J. Appl. Phys. **41**, 3373 (1970).

[205] M. Grimsditch, physica status solidi (b) **193**, K9 (1996).

[206] M. Grimsditch, J. Phys. C: Solid State Phys. **16**, L143 (1983).

[207] C. S. G. Cousins and M. I. Heggie, Phys. Rev. B **67**, 024109 (2003).

[208] P. L. de Andres, F. Guinea, and M. I. Katsnelson, Phys. Rev. B **86**, 245409 (2012).

[209] K. H. Michel and B. Verberck, Phys. Rev. B **78**, 085424 (2008).

[210] M. J. Mehl, Phys. Rev. B **61**, 1654 (2000).

[211] F. Tuinstra and J. L. Koenig, J. Chem. Phys. **53**, 1126 (1970).

[212] Y.-S. Lee, Y. Kim, Y. W. Cho, D. Shapiro, C. Wolverton, and V. Ozoliņš, Phys. Rev. B **79**, 104107 (2009).

[213] O. Hellman, I. A. Abrikosov, and S. I. Simak, Phys. Rev. B **84**, 180301 (2011).

[214] D. W. Brenner, O. A. Shenderova, J. A. Harrison, S. J. Stuart, B. Ni, and S. B. Sinnott, J. Phys.: Condens. Matter **14**, 783 (2002).

[215] L. Dubrovinsky, N. Dubrovinskaia, O. Narygina, I. Kantor, A. Kuznetzov, V. B. Prakapenka, L. Vitos, B. Johansson, A. S. Mikhaylushkin, S. I. Simak, et al., Science **316**, 1880 (2007).

[216] Y. Magnin, G. D. Förster, F. Rabilloud, F. Calvo, A. Zappelli, and C. Bichara, J. Phys.: Condens. Matter **26**, 185401 (2014).

[217] A. Allard and L. Wirtz, Nano Lett. **10**, 4335 (2010).

[218] L. Falkovsky, Phys. Lett. A **372**, 5189 (2008).

[219] L. Karssemeijer and A. Fasolino, Master's thesis, Theory of Condensed Matter, Institute for Molecules and Materials,Radboud University Nijmegen (2010).

[220] A. C. Ferrari and D. M. Basko, Nat. Nanotechnol. **8**, 235 (2013).

[221] R. Nemanich, G. Lucovsky, and S. Solin, Mater. Sci. Eng. **31**, 157 (1977).

[222] C. Postmus, J. R. Ferraro, and S. S. Mitra, Phys. Rev. **174**, 983 (1968).

[223] T. Aizawa, R. Souda, S. Otani, Y. Ishizawa, and C. Oshima, Phys. Rev. Lett. **64**, 768 (1990).

[224] A. M. Shikin, D.Farias, and K. H. Rieder, Europhys. Lett. **44**, 44 (1998).

[225] W. Pan, J. Xiao, J. Zhu, C. Yu, G. Zhang, Z. Ni, K. Watanabe, T. Taniguchi, Y. Shi, and X. Wang, Sci. Rep. **2**, 893 (2012).

[226] P. K. Schelling and P. Keblinski, Phys. Rev. B **68**, 035425 (2003).

[227] D. Pacilé, J. C. Meyer, c. O. Girit, and A. Zettl, Appl. Phys. Lett. **92**, 133107 (2008).

[228] A. Nag, K. Raidongia, K. P. S. S. Hembram, R. Datta, U. V. Waghmare, and C. N. R. Rao, ACS Nano **4**, 1539 (2010).

[229] E. J. Mele and P. Král, Phys. Rev. Lett. **88**, 056803 (2002).

[230] W. Paszkowicz, J. Pelka, M. Knapp, T. Szyszko, and S. Podsiadlo, Appl. Phys. A **75**, 431 (2002).

[231] S. Thomas, K. M. Ajith, S. Chandra, and M. C. Valsakumar, J. Phys.: Condens. Matter **27**, 315302 (2015).

[232] R. S. Pease, Acta Crystallogr. **5**, 356 (1952).

[233] P. Gallagher, M. Lee, F. Amet, P. Maksymovych, J. Wang, S. Wang, X. Lu, G. Zhang, K. Watanabe, T. Taniguchi, et al., ArXiv e-prints,1504.05253 (2015).

[234] H. M. Ghassemi, C. H. Lee, Y. K. Yap, and R. S. Yassar, Nanotechnology **22**, 115702 (2011).

[235] T. Liang, S. R. Phillpot, and S. B. Sinnott, Phys. Rev. B **79**, 245110 (2009).

[236] T. J. Wieting and J. L. Verble, Phys. Rev. B **3**, 4286 (1971).

[237] S. K. Singh, M. Neek-Amal, S. Costamagna, and F. M. Peeters, Phys. Rev. B **91**, 014101 (2015).

[238] A. Taube, J. Judek, C. Jastrzebski, A. Duzynska, K. Świtkowski, and M. Zdrojek, ACS Appl. Mater. Interfaces **6**, 8959 (2014).

[239] B. Chakraborty, H. S. S. R. Matte, A. K. Sood, and C. N. R. Rao, J. Raman Spectrosc. **44**, 92 (2013).

[240] G. Henkelman and H. Jónsson, J. Chem. Phys. **113**, 9978 (2000).